Electrostatic problem for a thin, unclosed ellipsoidal shell and disk

G. Ch. Shushkevich

Ya. Kupala Grodno State University, 230023 Grodno, Belarus
(Submitted November 28, 1997)
Zh. Tekh. Fiz. **69**, 1–5 (February 1999)

The axisymmetric electrostatic problem of a thin, unclosed ellipsoidal shell and disk is solved. The capacitance coefficients are calculated for a representative set of values of the geometrical parameters of the conductors. © *1999 American Institute of Physics.* [S1063-7842(99)00102-6]

The necessity of calculating the capacitance of a system of conductors of various configuration arises in the solution of a number of problems which engineers and scientists of the most diverse specializations must contend. The aim of the present work is to solve the axisymmetric electrostatic problem for a thin, unclosed ellipsoidal shell and disk and calculate the capacitance coefficients for a representative set of values of the geometrical parameters of the conductors.

Let us consider the axisymmetric problem of finding the potential of the electrostatic field of a system of conductors consisting of a thin, unclosed prolate ellipsoidal shell S and a circular disk Γ of radius a (the axial cross section of the conductors is shown in Fig. 1). The shell S is located on the surface of the prolate ellipsoid of revolution S_1, where b and d are the large and small semi-axis of the ellipse, respectively, and $c=\sqrt{b^2-d^2}$ is half the interfocal distance. To solve the problem, we locate the origin of the cylindrical coordinates $\{\rho,z,\varphi\}$ at the point O (Ref. 1):

$$x=\rho\cos\varphi,\quad y=\rho\sin\varphi,\quad z=z$$

$$(0\leqslant\rho<\infty,\quad 0\leqslant\varphi\leqslant 2\pi,\quad -\infty<z<\infty),$$

and the degenerate ellipsoidal coordinates $\{\alpha,\beta,\varphi\}$ at the point O_1 (Ref. 1)

$$x=c\sinh\alpha\sin\beta\cos\varphi;\quad y=c\sinh\alpha\sin\beta\sin\varphi;$$

$$z=c\cosh\alpha\cos\beta(0\leqslant\alpha<\infty,\quad 0\leqslant\beta\leqslant\pi,\quad 0\leqslant\varphi\leqslant 2\pi).$$

The conducting bodies under discussion are now described as

$$S=\left\{\alpha=\alpha_0=\cosh^{-1}\frac{b}{c},\quad 0\leqslant\beta\leqslant\beta_0<\pi,\quad 0\leqslant\varphi\leqslant 2\pi\right\},$$

$$\Gamma=\{0\leqslant\rho\leqslant a,\quad 0\leqslant\varphi\leqslant 2\pi,\quad z=0\}.$$

We denote the distance between the points O and O_1 as h and arbitrarily divide all space E_3 by the ellipsoid S_1 and the plane $z=0$ into three regions: $D_1(z<0)$, $D_2(\alpha<\alpha_0)$, and $D_3=E_3\backslash(D_1\cup D_2)$. We denote the electrostatic potential in the regions D_j as U_j, $j=1,2,3$. The electrostatic potential U_j should satisfy the Laplace equation $\Delta U_j(M)=0$ in the regions D_j, $j=1,2,3$, and the boundary conditions

$$U_3(M)=|_{M\in S}=V_s-\text{const},\tag{1}$$

$$U_3(M)|_{M\in\Gamma}=V_d-\text{const}\tag{2}$$

and the boundary condition at infinity

$$U_j(M)\to 0\ \text{ as }\ M\to\infty,\quad j=1,3,\tag{3}$$

where M is any point in space.

In addition, the following continuity conditions on the potential and the field must be satisfied:

$$U_2|_{\alpha=\alpha_0}=U_3|_{\alpha=\alpha_0},\quad U_1|_{z=0}=U_3|_{z=0},\tag{4),(5}$$

$$\frac{\partial}{\partial\alpha}U_2\bigg|_{\alpha=\alpha_0,\beta>\beta_0}=\frac{\partial}{\partial\alpha}U_3\bigg|_{\alpha=\alpha_0,\beta>\beta_0},\tag{6}$$

$$\frac{\partial}{\partial z}U_1\bigg|_{z=0,\rho>a}=\frac{\partial}{\partial z}U_3\bigg|_{z=0,\rho>a}.\tag{7}$$

We seek the electrostatic potential U_j in the form of a superposition of cylindrical and ellipsoidal harmonic functions[1,2] such that the boundary condition at infinity (3) is fulfilled

$$U_1(\rho,z)=\int_0^\infty B(\lambda)\exp(\lambda z)J_0(\lambda\rho)d\lambda\ \text{ in }\ D_1,\tag{8}$$

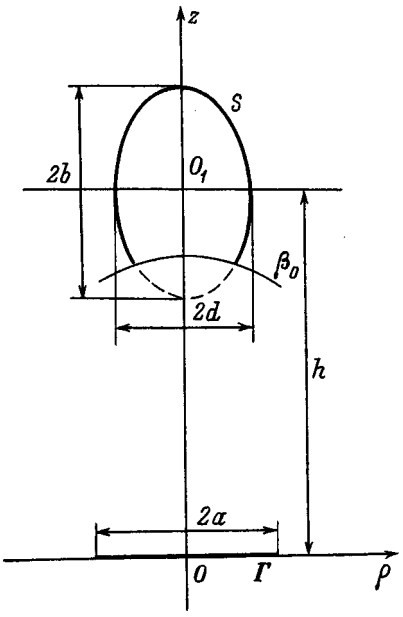

FIG. 1.

$$U_2(\alpha,\beta)=\sum_{n=0}^{\infty} b_n \frac{P_n(\cosh\alpha)}{P_n(\cosh\alpha_0)} P_n(\cos\beta) \quad \text{in} \quad D_2, \tag{9}$$

$$U_3=U_3^{(1)}(\rho,z)+U_3^{(2)}(\alpha,\beta) \quad \text{in} \quad D_3, \tag{10}$$

where

$$U_3^{(1)}(\rho,z)=\int_0^{\infty} A(\lambda)\exp(-\lambda z)J_0(\lambda\rho)d\lambda, \quad z>0,$$

$$U_3^{(2)}(\alpha,\beta)=\sum_{n=0}^{\infty} a_n \frac{Q_n(\cosh\alpha)}{Q_n(\cosh\alpha_0)} P_n(\cos\beta), \quad \alpha>\alpha_0,$$

$P_n(\cosh\alpha)$ and $Q_n(\cosh\alpha)$ are the Legendre functions of the first and second kind, respectively, $P_n(\cos\beta)$ are the Legendre polynomials, and $J_0(\lambda\rho)$ is the zeroth-order Bessel function of the first kind.[1,3–6]

The unknown coefficients a_n and b_n and the functions $A(\lambda)$ and $B(\lambda)$ are to be determined from conditions (1)–(7). To satisfy conditions (1), (4), and (6), we expand the potential $U_3^{(1)}(\rho,z)$ in the ellipsoidal harmonic functions in the coordinate system with origin at O_1, utilizing the formula[2]

$$J_0(\lambda\rho)\exp(\mp\lambda z)=\sum_{n=0}^{\infty} (\pm i)^n(2n+1)j_n(ic\lambda) \times P_n(\cosh\alpha)P_n(\cos\beta),$$

where i is the imaginary unit and $j_n(ic\lambda)$ are the spherical Bessel functions.[3–6]

Thus,

$$U_3^{(1)}(\alpha,\beta)=\sum_{n=0}^{\infty} d_n P_n(\cosh\alpha)P_n(\cos\beta), \tag{11}$$

where

$$d_n=i^n(2n+1)\int_0^{\infty} A(\lambda)\exp(-\lambda h)j_n(ic\lambda)d\lambda. \tag{12}$$

Taking representations (9), (10), and (11) into account and imposing the boundary condition (1) on the surface of the unclosed ellipsoidal shell S and the conditions of continuity (4) and (6), we obtain a pair of summation equations in the Legendre polynomials of the form

$$\sum_{n=0}^{\infty} a_n P_n(\cos\beta)=V_s-\sum_{n=0}^{\infty} d_n P_n(\cosh\alpha_0)P_n(\cos\beta), \quad \beta<\beta_0,$$

$$\sum_{n=0}^{\infty} \frac{a_n P_n(\cos\beta)}{\sinh\alpha_0 P_n(\cosh\alpha_0)Q_n(\cosh\alpha_0)}=0, \quad \beta>\beta_0. \tag{13}$$

To satisfy boundary condition (2) on the disk Γ, we expand the potential $U_3^{(2)}(\alpha,\beta)$ in cylindrical harmonic functions in the coordinate system with origin at O, applying the integral representation[2,6]

$$Q_n(\cosh\alpha)P_n(\cos\beta)=ci^n\int_0^{\infty} j_n(ic\lambda)J_0(\lambda\rho_1) \times\exp(\lambda z_1)d\lambda, \quad z_1<c.$$

Then

$$U_3^{(2)}(\rho,z)=\int_0^{\infty} d(\lambda)\exp(\lambda z)J_0(\lambda\rho)d\lambda, \tag{14}$$

where

$$d(\lambda)=c\exp(-\lambda h)\sum_{n=0}^{\infty} \frac{i^n j_n(ic\lambda)}{Q_n(\cosh\alpha_0)}a_n. \tag{15}$$

Using the representations for the potentials (8), (10), and (14) and imposing boundary condition (2) and the conditions of continuity (5) and (7), we obtain a pair of integral equations of the form

$$\int_0^{\infty} A(\lambda)J_0(\lambda\rho)d\lambda=V_d-\int_0^{\infty} d(\lambda)J_0(\lambda\rho)d\lambda, \quad \rho>a,$$

$$\int_0^{\infty} \lambda A(\lambda)J_0(\lambda\rho)d\lambda=0, \quad \rho>a. \tag{16}$$

To solve the paired summation equations (13), we introduce a new function $\varphi(t)$, $\varphi(t)\in C^{(1)}_{[0,\beta_0]}$, which is related to the coefficients a_n by the equation

$$a_n=(2n+1)\sinh\alpha_0 P_n(\cosh\alpha_0)Q_n(\cosh\alpha_0) \times\int_0^{\beta_0}\varphi(t)\cos\left(n+\frac{1}{2}\right)t\,dt. \tag{17}$$

Thus, the paired summation equations (13) transform into a Fredholm integral equation of the second kind[7]

$$\varphi(x)-\int_0^{\beta_0} K(x,t)\varphi(t)dt = \frac{2}{\pi}\left[V_s\cos\frac{x}{2}-\sum_{n=0}^{\infty} d_n P_n(\cosh\alpha_0) \times\cos\left(n+\frac{1}{2}\right)x\right], \quad 0\leqslant x\leqslant\beta_0, \tag{18}$$

where

$$K(x,t)=\frac{2}{\pi}\sum_{n=0}^{\infty} g_n\cos\left(n+\frac{1}{2}\right)t\cos\left(n+\frac{1}{2}\right)x, \tag{19}$$

$g_n=1-(2n+1)\sinh\alpha_0 P_n(\cosh\alpha_0)Q_n(\cosh\alpha_0)$, and $g_n\to O\times(n^{-2})$ as $n\to\infty$.

To solve the pair of integral equations (16), we introduce the function $\omega(t)$, related to the function $A(\lambda)$ by the equation

$$A(\lambda)=\int_0^a \omega(t)\cos\lambda t\,dt. \tag{20}$$

After some manipulations[8] we obtain

$$\omega(t)=\frac{2}{\pi}\left[V_d-\int_0^\infty d(\lambda)\cos\lambda t d\lambda\right]$$

or, according to representation (15),

$$\omega(t)=\frac{2}{\pi}\left[V_d-\sum_{n=0}^{\infty}\frac{a_n}{Q_n(\cosh\alpha_0)}B_n(t)\right], \tag{21}$$

where

$$B_n(t)=ci^n\int_0^\infty \exp(-\lambda h)j_n(ic\lambda)\cos\lambda t d\lambda. \tag{22}$$

Substituting the coefficients a_n from Eqs. (17) into the right-hand side of Eq. (21), we establish a relationship between the functions $\omega(t)$ and $\varphi(x)$:

$$\omega(t)=\frac{2}{\pi}\left[V_d-\sinh\alpha_0\int_0^{\beta_0}S(t,x)\varphi(x)dx\right], \tag{23}$$

where

$$S(t,x)=\sum_{n=0}^{\infty}(2n+1)P_n(\cosh\alpha_0)B_n(t)\cos\left(n+\frac{1}{2}\right)x. \tag{24}$$

Taking representations (12) and (20) successively into account, we can transform the Fredholm equation of the second kind (18) into the form

$$\varphi(x)-\int_0^{\beta_0}K(x,t)\varphi(t)dt = \frac{2}{\pi}\left[V_s\cos\frac{x}{2}-\frac{1}{c}\int_0^a S(u,x)\omega(u)du\right]. \tag{25}$$

Now, we eliminate the function $\omega(u)$ from the right-hand side of Eq. (25) with the help of the representation (23) and finally obtain a Fredholm integral equation of the second kind for the function $\varphi(x)$ of the form

$$\varphi(x)-\int_0^{\beta_0}[K(x,t)+K_1(x,t)]\varphi(t)dt = \frac{2}{\pi}\left[V_s\cos\frac{x}{2}-\frac{2}{\pi c}V_d F(x)\right], \quad 0\leqslant x\leqslant\beta_0, \tag{26}$$

where

$$K_1(x,t)=\frac{4\sinh\alpha_0}{\pi^2 c}\int_0^a S(u,x)S(u,t)du,$$

$$F(x)=\int_0^a S(t,x)dt.$$

The charges on the thin, unclosed ellipsoidal shell S and disk Γ are calculated from the solution of the Fredholm integral equation of the second kind (26) via the respective formulas

$$Q_s=4\pi\varepsilon d\int_0^{\beta_0}\varphi(x)\cos\frac{x}{2}dx, \tag{27}$$

TABLE I. Values of the normalized capacitance coefficients $\frac{C_{ik}}{4\pi\varepsilon}$ for $b/d=2$, $d/a=1$, $h/b=2$.

β_0, deg	$\frac{C_{11}}{4\pi\varepsilon}$	$\frac{C_{22}}{4\pi\varepsilon}$	$\frac{C_{12}}{4\pi\varepsilon}$
30	0.3086	0.6033	0.0374
60	0.6287	0.5633	0.0832
90	0.9016	0.5189	0.1361
120	1.0782	0.4785	0.1889
150	1.1508	0.4542	0.2258

$$Q_d=4\pi\varepsilon\left[\frac{2}{\pi}aV_d-\frac{2}{\pi}\sinh\alpha_0\int_0^{\beta_0}F(x)\varphi(x)dx\right], \tag{28}$$

where ε is the dielectric constant of the medium.

The capacitance coefficients C_{ik} can be calculated in terms of the charges on the conductors by the formulas[9]

$$C_{11}=Q_s(V_s=V_d=1),\quad C_{22}=Q_d(V_s=V_d=1),$$

$$C_{12}=Q_s(V_s=0,\ V_d=-1),$$

$$C_{21}=Q_d(V_s=-1,\ V_d=0),\quad C_{12}=C_{21}.$$

Table I displays the normalized capacitance coefficients $C_{ik}/4\pi\varepsilon$, calculated for the following geometrical parameters of the conductors: $b/d=2$, $d/a=1$, $h/b=2$, $\beta_0=30,60,90,120,150°$. The Legendre function $P_n(x)$ was calculated using the recursion formula[3]

$$P_{n+1}(x)=\frac{1}{n+1}[(2n+1)xP_n(x)-nP_{n-1}(x)]$$

with the starting values $P_0(x)=1$, $P_1(x)=x$.

The Legendre functions $Q_n(x)$ were calculated in terms of the hypergeometric function ${}_2F_1(a,b,c,x)$ according to the formula[3]

$$Q_n(x)=\frac{\sqrt{\pi}n!}{\Gamma(n+1{,}5)(2x)^{n+1}} \times {}_2F_1\left(\frac{2+n}{2},\ \frac{1+n}{2},\ \frac{3+2n}{2},\ x^{-2}\right),$$

where

$${}_2F_1(a,b,c,x)=\sum_{k=0}^{\infty}\frac{(a)_k(b)_k}{k!(c)_k}x^k, \tag{29}$$

$\Gamma(x)$ is the gamma function and $(a)_k=a(a+1)\ldots(a+k-1)$ is the Pochhammer symbol.[3–5]

Employing the series expansion of the spherical Bessel function[3–5]

$$j_n(ic\lambda)=2^n i^n\sum_{s=0}^{\infty}\frac{(n+s)!}{s!(2s+2n+1)!}(c\lambda)^{2s+n}$$

and the integral[10]

$$\int_0^\infty x^{\alpha-1}\exp(-px)\cos bx dx=\frac{\Gamma(\alpha)}{(b^2+p^2)^{\alpha/2}}\cos\left(\alpha\tan^{-1}\frac{b}{p}\right),$$

the improper integral (22) $B_n(x)$ is converted into the sum

$$B_n(x)=(-2)^n\sum_{s=0}^{\infty}\frac{(n+s)!(2s+n)!}{s!(2n+2s+1)!}\left(\frac{c}{\sqrt{x^2+h^2}}\right)^{2s+n+1}\times\cos\left[(2s+n+1)\tan^{-1}\frac{x}{h}\right]. \quad (30)$$

The Fredholm integral equation of the second kind (26) was transformed into a finite system of linear algebraic equations using Simpson's rule with a step equal to 0.1. The infinite sums (19), (29), and (30) were calculated with accuracy to 10^{-5}. The calculations were performed with the help of the software package MathCAD 6.0 (Ref. 11).

If $\beta_0=\pi$ (the unclosed shell S goes over to the ellipsoid S_1), then instead of the integral equation (26) we have a Fredholm integral equation for the function $\omega(x)$ of the form

$$\omega(x)-\frac{2}{\pi c}\int_0^a L(x,t)\omega(t)dt=\frac{2}{\pi}\left[V_d-V_s\frac{B_0(x)}{Q_0(\cosh\alpha_0)}\right],$$

$$0\leqslant x\leqslant a, \quad (31)$$

where

$$L(x,t)=\sum_{n=0}^{\infty}(2n+1)\frac{P_n(\cosh\alpha_0)}{Q_n(\cosh\alpha_0)}B_n(x)B_n(t).$$

In the preceding integral equation (31) we make the following substitutions: $x=\tau a$, $t=\sigma a$, $v(\tau)=(\pi/2)\omega(x)$, $v(\sigma)=(\pi/2)\omega(t)$, $\delta=a/d$, $\eta=d/b$, and $\mu=b/h<1$. Then the integral equation (31) takes the form

$$v(\tau)-\frac{2\eta\delta}{\sqrt{1-\eta^2}}\int_0^1 L(\tau,\sigma)v(\sigma)d\sigma=V_d-V_s\frac{B_0(\tau)}{Q_0(\cosh\alpha_0)},$$

$$0\leqslant\tau\leqslant 1, \quad (32)$$

where

$$L(\tau,\sigma)=\sum_{n=0}^{\infty}(2n+1)\frac{P_n(\cosh\alpha_0)}{Q_n(\cosh\alpha_0)}B_n(\tau)B_n(\sigma),$$

$$B_n(\tau)=(-2)^n\sum_{s=0}^{\infty}\sum_{k=0}^{\infty}\frac{(-1)^k(n+s)!}{s!(2n+2s+1)!}\frac{(2s+2k+n)!}{(2k)!}\times(\tau\eta\delta)^{2k}(1-\eta^2)^{\frac{2s+n+1}{2}}\mu^{2k+2s+n+1}.$$

The charge on the prolate ellipsoid S_1 is calculated using the formula

$$Q_1=4\pi c\varepsilon\frac{a_0}{Q_0(\cosh\alpha_0)}=4\pi b\varepsilon a_0 M, \quad (33)$$

where

$$M=\frac{\sqrt{1-\eta^2}}{\cosh^{-1}\frac{1}{\eta}}, \quad a_0=V_s-\frac{2}{\pi}\frac{\eta\delta}{\sqrt{1-\eta^2}}\int_0^1 B_0(\sigma)v(\sigma)d\sigma.$$

The charge on the disk is calculated in terms of the solution of the integral equation (32) according to the formula

$$Q_d=8a\varepsilon\int_0^1 v(\tau)d\tau. \quad (34)$$

If the geometrical parameter μ is sufficiently small ($\mu^n\approx 0$ for $n\geqslant 4$), then it is possible to obtain a solution of the integral equation (32) in the form of a series in the small parameter μ (Ref. 8):

$$v(\tau)=V_d-V_sM\mu+\frac{2}{\pi}V_d\eta\delta M\mu^2+\left[(\tau\eta\delta)^2-\frac{1}{3}(1-\eta^2)-\frac{2}{\pi}\eta\delta M\right]V_sM\mu^3+\ldots.$$

Substituting this expansion into the formulas for the charge on the disk (34) and the charge on the ellipsoid (33), we obtain the following expressions for the charges on these conducting bodies in the form of a series in the small parameter

$$v(\tau)=V_d-V_sM\mu+\frac{2}{\pi}V_d\eta\delta M\mu^2+\left[(\tau\eta\delta)^2-\frac{1}{3}(1-\eta^2)+\frac{2}{\pi}\eta\delta M\right]V_sM\mu^3+\ldots,$$

$$Q_1=4\pi\varepsilon b\left\{V_sM-\frac{2\eta\delta}{\pi}V_dM\mu+\frac{2\eta\delta}{\pi}V_sM^2\mu^2-\frac{2\eta\delta}{\pi}\left[\frac{1}{3}(1-\eta^2)+\frac{2\eta\delta}{\pi}M-\frac{1}{3}(\eta\delta)^2\right]V_dM\mu^3+\ldots\right\}.$$

The electrostatic problem for an oblate unclosed ellipsoidal shell and disk is solved in a similar way.

[1] N. N. Lebedev, *Special Functions and Their Applications* [in Russian], GIITL, Moscow, 1953, 380 pp.
[2] S. V. Shushkevich and G. Ch. Shushkevich, Vestsi ANB Ser. Fiz. Mat. Navuk [Bulletin of the Belorussian Academy of Sciences, Ser. Phys. Math. Sciences, in Belorussian], No. 1, 118 (1993).
[3] *Handbook of Special Functions with Formulas, Graphs, and Mathematical Tables* [in Russian], Nauka, Moscow, 1979, 832 pp.
[4] V. Ya. Arsenin, *Methods of Mathematical Physics, and Special Functions* [in Russian], Nauka, Moscow, 1984, 384 pp.
[5] A. F. Nikiforov and V. B. Uvarov, *Special Functions of Mathematical Physics* [in Russian], Nauka, Moscow, 1984, 344 pp.
[6] S. M. Apollonskiĭ and V. I. Erofeenko, *Electromagnetic Fields in Screening Shells* [in Russian], Minsk University Press, Minsk, 1988, 248 pp.
[7] G. Ch. Shushkevich, Elektrichestvo, No. 6, 51 (1988).
[8] G. Ch. Shushkevich, Zh. Tekh. Fiz. **54**, 1801 (1984) [Sov. Phys. Tech. Phys. **29**, 1050 (1984)].
[9] Yu. Ya. Iossel', É. S. Kochanov, and M. L. Strunskiĭ, *Calculation of Electrical Capacitance* [in Russian], Énergoizdat, Leningrad, 1981, 288 pp.
[10] A. P. Prudnikov, Yu. A. Brychkov, and O. I. Marichev, *Integrals and Series. Elementary Functions* [in Russian], Nauka, Moscow, 1981, 800 pp.
[11] MathCAD 6.0 PLUS. Business, Engineering, and Scientific Calculations in Windows 95 [in Russian], Filin', Moscow, 1996, 698 pp.

Translated by Paul F. Schippnick

Electron-impact excitation cross sections of atomic silver

Yu. M. Smirnov

Moscow Power Institute, 111250 Moscow, Russia
(Submitted October 20, 1997)
Zh. Tekh. Fiz. **69**, 6–10 (February 1999)

The method of extended crossed beams is used to measure excitation cross sections of atomic silver. The results, together with theoretical data on the transition probabilities of AgI, are used to calculate the excitation cross sections of the energy levels of the silver atom and the contribution of cascade population of states. It is found that the dependence of the cross sections on the principal quantum number of the upper level for five spectral series can be expressed as a power law. © *1999 American Institute of Physics.* [S1063-7842(99)00202-0]

INTRODUCTION

A study of inelastic collisions of electrons with silver atoms is of significant interest for a number of reasons. First of all, the silver atom has one electron above the filled shells, similar to atoms of alkali metals. However, in contrast to the latter, in the silver atom the preceding completely filled shell consists of ten *d* electrons, not six *p* electrons as for the alkali metals. In this case, excitation of one of the *d* electrons can take place at a comparatively low energy of the incoming electron, so there is a significant overlap of the shifted and unshifted terms. Second, laser generation in silver vapor has been achieved (see, e.g., Ref. 1). Here pumping, as a rule, is carried out by an electron beam, and information about the corresponding electron–atom collisions is needed in order to understand the mechanisms of creation of a population inversion in silver-vapor lasers.

So far, theoretical studies of inelastic collisions of electrons with silver atoms are lacking. Experimentally, such collisions have been investigated in works by only one research group. Reference 2 reported a study of excitation of the singly charged silver ion from the ground state of the atom, and Ref. 3 reported a study of excitation cross sections of the silver atom. The information reported in these two works is extremely limited due to imperfections of the experimental technique and the extremely small quantity of available silver. After removing these obstacles, a more detailed study was published[4] on excitation of autoionizing states of AgI. In the present study the method of extended crossed beams was used to carry out a more detailed study of excitation of normally excited (unshifted) terms of the silver atom.

EXPERIMENT

A detailed description of the method of extended crossed beams has been presented more than once in the literature;[5–7] therefore its repetition in the present paper would not be useful. Let us dwell here only on some circumstances which are relevant specifically for experiments with silver.

Because of the need to conserve the metal as much as possible, its evaporation was carried out from a tubular molybdenum crucible suspended in vacuum from thin molybdenum cross-beams. The outer surface of the crucible was heated by an electron beam expanded to provide a more uniform temperature field. The geometry of the crucible and its surrounding panels and screens ensured that the secondary emitted and scattered beam electrons would be localized around the crucible in the space bounded by the exit diaphragm adjacent to it. This precluded bombardment of the atomic beam by primary and secondary beam electrons. Since the ground state of the silver atom $4d^{10}5s^2S_{1/2}$ has only one level and is separated from the nearest excited level by an interval of almost $30\,000\,\mathrm{cm}^{-1}$, thermal population of excited levels is essentially excluded, and all of the silver atoms in the beam are found in the ground state before their interaction with the monoenergetic electrons.

At a crucible temperature of 1300 K the density of silver atoms in the intersection region of the atomic beam with the electrons reached $1.2\times10^{10}\,\mathrm{cm}^{-3}$ and was lowered by more than an order of magnitude in order to examine the leading resonance lines. The current density of the electron beam did not exceed $1.0\,\mathrm{mA/cm}^2$ anywhere in the working energy range. In contrast to Refs. 2 and 3, to set up a scale of absolute cross section values, as the reference radiation intensity (or, more accurately, directly as the reference cross section) we used spectral lines of the helium atom. To calibrate the absolute values of the cross sections, helium was let into the chamber at an unknown pressure, instead of silver vapor, while the remaining conditions of the experiment were kept the same as far as possible. Cross section values were recorded for four HeI lines which were measured in Ref. 8 with an error of 9% at an electron energy of 50 eV. The error of the relative values of the cross sections in the present study is 5–12%, and the absolute values were determined with an error of ±23 to $\pm30\%$. A more detailed description of the experiment and technique with analysis of error sources is contained in Ref. 6.

RESULTS AND DISCUSSION

More than 200 lines of the silver atom were recorded, located in the spectral range 200–850 nm. As I noted in an earlier paper,[4] a significant fraction of the low-intensity lines of the silver atom have not been classified; therefore, within

TABLE I. Excitation cross sections of doublet levels of atomic silver.

Term	J	E, cm^{-1}	Configuration	ΣQ^*_{50}, $10^{-18}\,cm^2$	ζ	ΣQ_{50}, $10^{-18}\,cm^2$	$\Sigma Q'$, $10^{-18}\,cm^2$	q, $10^{-18}\,cm^2$	$\frac{\Sigma Q'}{\Sigma Q_{50}}$,%
$6s^2S$	1/2	42556	$4d^{10}6s$	39.6	1.000	39.6	11.4	28.2	28.8
$7s^2S$	1/2	51887	$4d^{10}7s$	16.9	1.435	25.3	3.17	22.1	12.5
$8s^2S$	1/2	55581	$4d^{10}8s$	6.56	1.545	10.2			
$9s^2S$	1/2	57425	$4d^{10}9s$	4.18	1.565	6.55	0.29	6.26	4.43
$10s^2S$	1/2	58478	$4d^{10}10s$	2.17	1.575	3.42			
$11s^2S$	1/2	59136	$4d^{10}11s$	1.46[1]	1.540	2.24			
$12s^2S$	1/2	59575	$4d^{10}12s$	0.84[1]	1.513	1.27			
$5p^2P^0$	1/2	29552	$4d^{10}5p$	743.9			93.5	650.4	12.6
	3/2	30473		1254.4			173.2	1081.2	13.8
	Σ			1998.3			266.7	1731.6	13.3
$6p^2P^0$	1/2	48297	$4d^{10}6p$	5.98			14.5[3]	(−8.5)	242.
	3/2	48501		13.28			23.9[3]	(−10.6)	180.
	Σ			19.3			38.4	(−19.1)	199.
$7p^2P^0$	1/2	54041	$4d^{10}7p$				3.64[3]	(−3.64)	
	3/2	54121		1.62			6.24[3]	(−4.62)	385.
	Σ			1.62			9.88	(−8.26)	611.
$8p^2P^0$	1/2	56618	$4d^{10}8p$	3.27			1.35[3]	1.92	41.2
	3/2	56660		7.14			2.14[3]	5.00	30.0
	Σ			10.41			3.49	6.92	33.5
$9p^2P^0$	1/2	–	$4d^{10}9p$				0.44[3]	(−0.44)	
	3/2	58027		0.38			0.71[3]	(−0.33)	187.
	Σ			0.38			1.15	(−0.77)	302.
$5d^2D$	3/2	48744	$4d^{10}5d$	41.5[2]	1.0001	41.5	4.28	37.2	10.3
	5/2	48764		55.2[2]	1.00002	55.2	1.01	54.2	1.83
	Σ					96.7	5.29	91.4	5.47
$6d^2D$	3/2	54203	$4d^{10}6d$	20.0	1.23	24.6	1.22	23.4	4.07
	5/2	54214		26.5	1.23	32.6	0.44	32.2	1.35
	Σ					57.2	1.66	55.5	2.90
$7d^2D$	3/2	56700	$4d^{10}7d$	10.9[2]	1.395	14.7	0.54	14.2	3.68
	5/2	56706		11.8	1.41	16.6	0.16	16.4	0.96
	Σ					31.3	0.70	30.6	2.24
$8d^2D$	3/2	58050	$4d^{10}8d$	6.58	1.415	9.30	0.54	8.76	5.80
	5/2	58053		7.10	1.585	11.25		11.25	
	Σ					20.55	0.54	20.0	2.63
$9d^2D$	3/2	58862	$4d^{10}9d$	4.37[2]	1.545	6.44	0.38	6.06	5.91
	5/2	58865		4.84	1.565	7.56	0.10	7.46	1.32
	Σ					14.0	0.48	13.5	3.43
$10d^2D$	3/2	59389	$4d^{10}10d$	2.47	1.605	3.96			
	5/2	59391		2.70	1.685	4.55			
	Σ					8.51			
$11d^2D$	3/2	59751	$4d^{10}11d$	1.69	1.59	2.68			
	5/2	59752		1.95	1.61	3.14			
	Σ					5.82			
$4f^2F^0$	5/2,7/2	54205	$4d^{10}4f$	0.39			0.25	0.14	64.1
$5f^2F^0$	5/2,7/2	56709	$4d^{10}5f$	0.13			0.25	(−0.12)	192.

the framework of the present work dozens of spectral lines of AgI have been classified using information about the lines of the silver atom contained in Ref. 9 and later confirmed in Ref. 10. Simultaneously, typographical errors discovered in these works, and also in the ground-breaking work of Shenstone,[11] have been corrected. The main spectrograms were recorded at an electron energy of 50 eV, as a consequence of which, along with the atomic lines, around 150 lines of the singly charged silver ion were also recorded.

Although the electron–atom scattering experiments in which the optical signal of the excited atoms is recorded give information about excitation cross sections of the spectral lines Q_{ki}, more useful for comparison with theoretical studies and for practical purposes is information about the excitation cross sections of the energy levels q_k. These two quantities are related by the well-known formula

$$Q_{ki}=\left(q_k+\sum_l Q_{lk}\right)\frac{A_{ki}}{\Sigma_m A_{km}}, \tag{1}$$

where A_{ki} and A_{km} are the probabilities of the radiative transitions $k\to i$ and $k\to m$, respectively; the sum in parentheses gives the total cross section of the radiative transitions participating in the cascade population of the level k, and the fractional factor on the right takes account of branching of transitions from the level k.

Using the equality

$$\frac{Q_{ki}}{Q_{km}}=\frac{A_{ki}}{A_{km}}, \tag{2}$$

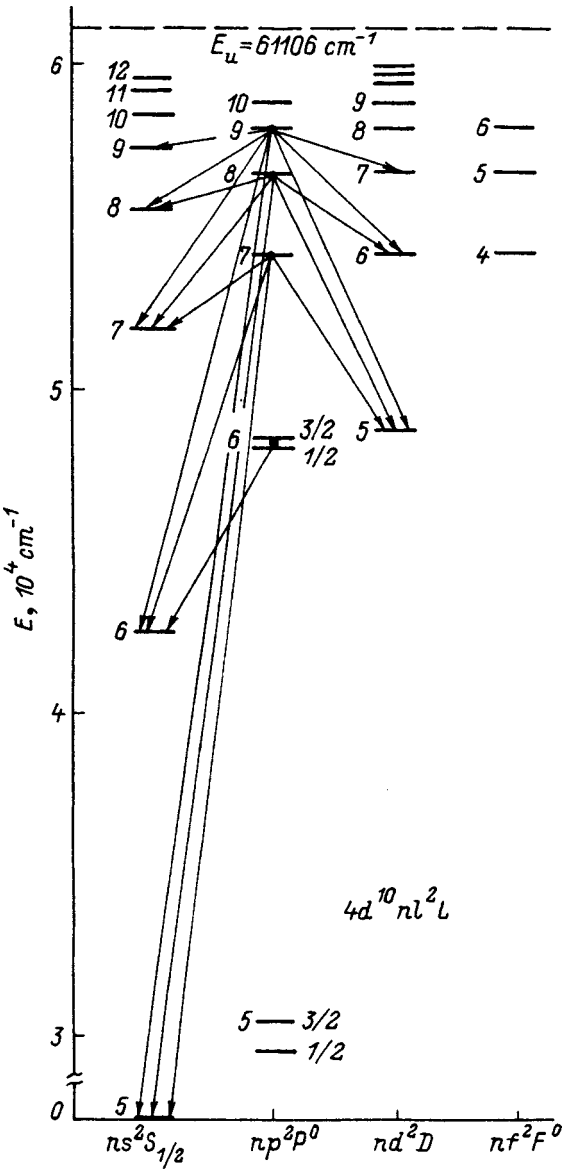

FIG. 1. Energy level diagram of atomic silver (unshifted terms), with the uninvestigated transitions indicated.

which interrelates the cross sections and the transition probabilities, one can write relation (1) in the form

$$q_k=\sum_m Q_{km}-\sum_l Q_{lk}. \tag{3}$$

Relation (3) is useful because it allows us to calculate the excitation cross sections of energy levels completely on the basis of the experimental data on the excitation cross sections of the spectral lines. At the same time, the use of equality (2) allows us to take into account a wider group of lines in the not-infrequently encountered situation in which the excitation cross sections of some transitions with a common upper level cannot be measured but the radiation constants for these transitions are known from independent sources.

Just such a situation arises in the study of the excitation of the valence electron of the silver atom. The one-electron transition $4d^{10}5s^2S_{1/2}\rightarrow 4d^{10}nl^2L_J$ takes place, where $l=s,p,df$; levels of the silver atom with higher values of the angular momentum have not yet been found experimentally.

TABLE II. Excitation cross sections of transitions from the np^2P^0 levels of AgI.

λ, nm	Transition	J	E_H, cm^{-1}	E_B, cm^{-1}	Q_{50}, 10^{-18} cm^{-2}
206.117	$5s^2S-6p^2P^0$	1/2−3/2	0	48501	13.3
206.983	$5s^2S-6p^2P^0$	1/2−1/2	0	48297	5.77
328.068	$5s^2S-5p^2P^0$	1/2−3/2	0	30473	1250.
338.289	$5s^2S-5p^2P^0$	1/2−1/2	0	29552	742.
359.806	$5s^2\,^2D-9p^2P^0$	5/2−3/2	30242	58027	0.38
378.418	$5s^2\,^2D-8p^2P^0$	5/2−3/2	30242	56660	0.76
418.664	$5s^2\,^2D-7p^2P^0$	5/2−3/2	30242	54121	1.62
456.402	$5s^2\,^2D-8p^2P^0$	3/2−1/2	34714	56618	0.38
533.362	$5p^2P^0-6p^2P^0$	1/2−1/2	29552	48297	0.21
547.538	$5s^2\,^2D-6p^2P^0$	5/2−3/2	30242	48501	3.61
553.707	$5s^2\,^2D-6p^2P^0$	5/2−1/2	30242	48297	0.23
708.810	$6s^2S-8p^2P^0$	1/2−3/2	42556	56660	6.38
710.95	$6s^2S-8p^2P^0$	1/2−1/2	42556	56618	2.91
725.153	$5s^2\,^2D-6p^2P^0$	3/2−3/2	34714	48501	0.83
735.996	$5s^2\,^2D-6p^2P^0$	3/2−1/2	34714	48297	1.69

At the same time, the authors of Ref. 12 calculated the probabilities of radiative transitions from the levels $ns^2S_{1/2}$ and $nd^2D_{3/2,5/2}$, where for the levels with $n\leqslant 12$ they took into account all possible allowed transitions in this system of terms. It should also be borne in mind that, so far, both theory and experiment, as a rule, allow one to determine the radiation constants with a higher accuracy than the cross sections.

Results obtained on the basis of cross section measurements by the method of extended crossed beams with application of data on the probabilities of radiative transitions from Ref. 12 are listed in Table I. Here ΣQ_{50}^* is the sum of cross sections measured in the present work, $\zeta=A_{\rm tot}/A_{\rm var}$ is a correction factor taking into account the branching factors of all the known transitions from the level in question according to the data of Ref. 12. We have used the following notation for the total excitation cross section of the level k (without subtracting out the contribution of the cascade transitions):

$$\sum_m Q_{km}=\zeta\sum Q'_{50}=\sum Q_{50}. \tag{4}$$

The superscripts on some of the numerical values denote the following: 1 — The transition $5p^2P^0_{1/2}-11s^2S_{1/2}$ (337.9 nm) is blinded out by the 338.3 nm line, which exceeds it in intensity by three orders of magnitude, the transition $5p^2P^0_{1/2}-12s^2S_{1/2}$ (332.995 nm) is blinded out by the 332.948 nm line. In both cases the cross sections of the $5p^2P^0_{1/2}-11,12s^2S_{1/2}$ transitions were calculated from the measured cross sections of the more intense components of the $5p^2P^0_{3/2}-ns^2S_{1/2}$ doublets; the ratio of the cross sections $Q(3/2)/Q(1/2)$ for $n\leqslant 10$ is 1.69. 2 — The contribution of the transitions to the shifted levels $4d^95s^2\,^2D$, not considered in Ref. 12, were subtracted from the values of Q_{50}^* given in Table I, before multiplying these latter values by the coefficient ζ. 3 — The cross sections of the cascade transitions populating the levels np^2P^0 with $n\geqslant 6$ were determined from the branching factors from the ^2S and ^2D levels according to Ref. 12; in the present work only cascade transitions from the $5p^2P^0_{1/2,3/2}$ level were recorded.

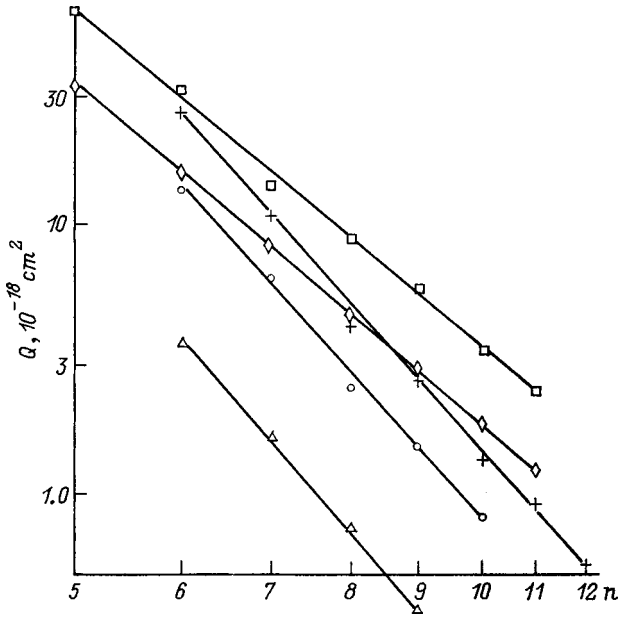

FIG. 2. Dependence of cross sections on n for spectral series of AgI: ○ — $5p^2P^0_{1/2}-ns^2S_{1/2}$, + — $5p^2P^0_{3/2}-ns^2S_{1/2}$, ◇ — $5p^2P^0_{1/2}-nd^2D_{3/2}$, □ — $5p^2P^0_{3/2}-nd^2D_{5/2,3/2}$, Δ — $5s^2\,{}^2D_{5/2}-np^2P^0_{3/2}$.

An energy-level diagram of the silver atom is shown in Fig. 1. All of the levels of the configuration $4d^{10}nl^2L$ considered in Ref. 12 are shown. The $10p^2P^0$ levels are not considered in the present work, because of the extremely small values of the associated cross sections, and likewise for the $12d^2D$ levels. Transitions from the latter levels to the $5p^2P^0$ levels, like the previously mentioned transition from the $11s^2S_{1/2}$ level, are blinded out by the leading resonance lines of AgI.

Transitions from the np^2P^0 levels were not investigated in Ref. 12, nor could analogous information be found in other sources. Therefore, branching is taken into account for the np^2P^0 levels only on the basis of the experimental data of the present work, presented in Table II. As can be seen, the only measured transition from the $7p^2P^0$ levels is to the metastable shifted term $4d^95s^2\,{}^2D$. Transitions from the $7p^2P^0$ levels to the $6s^2S_{1/2}$ level are located in the infrared around 870 nm, and to $5s^2S_{1/2}$ (resonance transitions)—in the vacuum ultraviolet. Because of the shift into the vacuum ultraviolet, resonance transitions from the higher-lying np^2P^0 levels were also not examined. So as not to complicate the energy-level diagram, only those transitions not recorded in the present work and not investigated in Ref. 12 are indicated.

As follows from the data of Table I, for the majority of ns^2S and nd^2D levels, the contribution of cascade population is around 10% or less; only for the $6s^2S_{1/2}$ level does it approach 30%. Despite the incompleteness of the data on cascade population of these levels, it is highly unlikely that taking them completely into account will lead to a significant increase in the cascade contribution. For the majority of np^2P^0 levels the situation is the reverse: the cascade contribution is taken fairly completely into account whereas the available information is clearly insufficient for an account of branching. This latter situation leads to the result that for the

TABLE III. Values of A_i and α_i for spectral series of atomic silver. $2.51(-13)=2.51\times10^{-13}$.

Series	n	α_i	A_i, cm^2
$5p^2P^0_{1/2}-ns^2S_{1/2}$	6−10	5.47	2.51(−13)
$5p^2P^0_{3/2}-ns^2S_{1/2}$	6−12	5.64	6.17(−13)
$5p^2P^0_{1/2}-nd^2D_{3/2}$	5−11	4.16	2.70(−14)
$5p^2P^0_{3/2}-nd^2D_{5/2,3/2}$	5−11	4.14	5.13(−14)
$5s^2\,{}^2D_{5/2}-np^2P^0_{3/2}$	6−9	7.58	6.46(−12)

$^2P^0$ levels with $n=6,7,9$, the calculated cascade population cross sections turn out to be larger than the measured total excitation cross section of the level, and the contribution of cascade population exceeds 100%. Note that the calculations take into account the transitions involving shifted terms measured in the present study and contributing mainly to cascade processes.

As is well known (see, e.g., Ref. 13), in unperturbed spectral series the excitation cross sections vary with the principal quantum number n of the upper level according to a power-law dependence

$$Q=A_i\cdot n^{-\alpha_i}, \tag{5}$$

where A_i and α_i are constants having characteristic values for each of the spectral series.

The dependence $Q=f(n)$ for five spectral series of the silver atom is plotted in Fig. 2 using data obtained in the present work. Power-law dependences on a log–log scale show up as straight lines whose slopes allow one to determine the constant α_i. This latter constant characterizes the rate of variation of the cross sections in each of the spectral series. The other constant $A_i=Q$ for $n=1$; since the cross section for $n=1$ has no real meaning, the constant A_i can be considered only as a conversion factor. Numerical values of A_i and α_i for the investigated series for the silver atom are given in Table III.

Comparison of these data with the results of theoretical calculations is impossible in view of the absence of published works on the theoretical determination of the excitation cross sections of atomic silver.

[1] B. Wernsman, J. J. Rocca, and H. Z. Mancini, IEEE Photon. Technol. Lett. **2**, 12 (1990).
[2] A. Yu. Krasavin, A. I. Kuchenev, and Yu. M. Smirnov, Zh. Prikl. Spektrosk. **36**, 543 (1982).
[3] A. Yu. Krasavin, A. N. Kuchenev, and Yu. M. Smirnov, Opt. Spektrosk. **54**, 20 (1983) [Opt. Spectrosc. **54**, 11 (1983)].
[4] Yu. M. Smirnov, Zh. Prikl. Spektrosk. **59**, 425 (1993).
[5] Yu. M. Smirnov, *Physics of Electron–Atom Collisions* [in Russian], Izdat. FTI AN SSSR, Leningrad, 1985, pp. 183–193.
[6] Yu. M. Smirnov, J. Phys. II **4**, 23 (1994).
[7] Yu. M. Smirnov, Phys. Scr. **49**, 689 (1994).
[8] B. Van Zyl, G. H. Dunn, G. Chamberlain, D. W. O. Heddle, Phys. Rev. A **22**, 1916 (1980).
[9] H.-U. Johannesen and R. Lincke, Z. Phys. A **272**(2), 147 (1975).
[10] S. Baier, M. Martins, B. R. Muller *et al.*, J. Phys. B **23**, 3095 (1990).
[11] A. G. Shenstone, Phys. Rev. **57**, 894 (1940).
[12] N. Bordel, G. Garcia, and J. Campos, Anal. Fis. Ser. A **85**, 201 (1989).
[13] A. N. Kuchenev and Yu. M. Smirnov, Phys. Scr. **51**, 578 (1995).

Translated by Paul F. Schippnick

Rayleigh decay of a highly charged bubble in a dielectric liquid

A. I. Grigor'ev, S. O. Shiryaeva, and A. N. Zharov

Yaroslavl State University, 150000 Yaroslavl, Russia
(Submitted November 3, 1997)
Zh. Tekh. Fiz. **69**, 11–15 (February 1999)

Proceeding from the Onsager principle of minimum energy dissipation, we find the dimensions, charges, and total number of daughter bubbles emitted during an instability of a highly charged bubble in a dielectric liquid. © *1999 American Institute of Physics.* [S1063-7842(99)00302-5]

In diverse problems of applied physics, one encounters the instability of bubbles in a liquid dielectric relative to their self-surface charge or the surface charge induced on them in an external field. In particular, such a problem is of significant interest for the theory of the breakdown of a liquid dielectric.[1–5] The breakdown process is related to the appearance, growth, and decay of a gas microbubble near the cathode. One possible scenario of the development of breakdown involves the release of the self- or polarization charge as a consequence of the development of an instability of the bubble's surface.[6,7] The instability of a gas bubble in an external electric field was investigated in detail experimentally in Ref. 1, where the electrostatic decay of a bubble in a dielectric was recorded photographically. During decay of the parent bubble, small daughter bubbles are thrown off, forming two agglomerations — one each in the vicinity of each emitting protrusion at the vertices of a spheroidal bubble (the equilibrium shape of a gas bubble in a uniform external electric field is a spheroid). The present study presents a theoretical analysis of the electrostatic decay of a highly charged bubble (according to the scheme employed earlier in Refs. 8 and 9 to examine the decay of charged drops) as the first step of a study of the regularities of the decay of bubbles which are unstable to their self-charge or an induced charge.

1. Let us consider an initially spherical bubble of radius R in a liquid dielectric possessing a large specific heat (by virtue of which we will neglect variation of the temperature of the system during decay), where this bubble has on its surface a charge Q (the gas–liquid interface) which is a bit larger than its limiting value in the sense of Rayleigh stability. Two paths of development of the bubble instability are possible: in the one the volume of the bubble will increase until the condition of pressure balance is satisfied, and in the second, thanks to exponential growth of the amplitudes of the capillary waves associated with the thermal motion of the molecules of the liquid medium, the bubble can experience an instability similar to the Rayleigh instability of a free, highly charged drop.[8,9] In this case, the parent bubble is stretched into a shape close to a spheroid of revolution with eccentricity e_1 (in Ref. 1 it was found that $e_1^2 \approx 0.7$). Following this, daughter bubbles are formed on opposite vertices of the bubble, joined by narrow necks to the parent bubble. After rupture of the necks, the daughter bubbles change their volume, contracting or expanding in synchrony with changes in the balance of pressures created by variation of the shape of the daughter bubbles after detachment from the parent bubble. Thanks to viscous dissipation of kinetic energy of the daughter bubbles and the braking influence of the electric field of the daughter bubbles emitted earlier, opposite the vertices of the spheroidal parent bubble, agglomerations of daughter bubbles are formed at a distance $L = ma$ (a is the length of the semimajor axis of the parent bubble) from the vertices of the parent bubble. In the discussion that follows, within the framework of the above qualitative analysis, to simplify the calculations we replace the electric field of the agglomeration of daughter bubbles by the field of an equivalent point charge located a distance L from the vertex of the parent bubble and having charge equal to the total charge of the previously emitted daughter bubbles.

We assume by virtue of the symmetry of the problem that as a result of the nth emission event two daughter bubbles with equal charges q_n ($q_n \ll Q$) and equal radii r_n ($r_n \ll R$) are formed. We also assume that the nth daughter bubble, finding itself in the field of the parent bubble and the field of the agglomeration of daughter bubbles, has the shape of an ellipsoid of revolution with eccentricity e_2 (Ref. 10), which we then determine by an iteration procedure. During decay the energy of the system varies. This variation is composed of the variation of the free energy of the forces of surface tension, the variation of the electrostatic self-energy of the bubbles and the energy of the electrostatic interaction of the bubbles, and also the work performed in contraction or expansion of the bubbles due to a nonproportional variation of the electric pressure and the Laplace pressure in the bubbles upon emission.

We assume that a daughter bubble contains gas and saturated vapor, whose partial pressures are constant and equal respectively to P_2^g and P^v. Taking the temperature of the liquid, the total electric charge, and the radius of the parent bubble to be constant, it is not hard to find from the charge of the daughter bubble the variation of the energy of the system in the linear approximation as a result of the n th decay

$$\Delta U = 8\pi\sigma r_n^2 A(e_2) - 2Q_{n-1}q_n\frac{B(e_1)}{R} + q_n^2\frac{B(e_2)}{r_n}$$
$$+ 2q_nQ_{n-1}\frac{K(\nu_n)}{R} + 2\frac{q_n}{L}\sum_{k=1}^{n-1} q_k - \frac{8\pi}{3}r_n^3P_2^g$$
$$\times\ln\left[\frac{r_n}{r_n^b}\right]^3 + \frac{8\pi}{3}P^v[(r_n^b)^3 - r_n^3];$$

$$A(e_i) = \frac{1}{2}\left[(1-e_i^2)^{1/2} + \frac{\sin^{-1}e_i}{e_i}\right](1-e_i^2)^{-1/\sigma}; \quad i=1,2;$$

$$B(e_i) = \frac{(1-e_i^2)^{1/3}}{e_i}\tanh^{-1}(e_i); \quad i=1,2;$$

$$\nu_n = \left(1+\frac{\xi_n}{a^2}\right)^{1/2};$$

$$K(\nu_n) = \frac{(1-e_1^2)^{1/3}}{e_1}\tanh^{-1}\left(\frac{e_1}{\nu_n}\right), \tag{1}$$

σ is the coefficient of surface tension of the liquid–gas interface, Q_{n-1} is the charge of the parent bubble before the nth decay, ξ_n is the ellipsoidal coordinate of the nth daughter bubble, and r_n^b is the radius of the daughter bubble immediately before contraction or expansion.

In expression (1) the first term is the surface energy of the two daughter bubbles, the second term is the variation of the electrostatic self-energy of the parent bubble, the third term is the electrostatic self-energy of the daughter bubbles, the fourth is the interaction energy of the daughter bubbles with the parent bubble, the fifth is the interaction energy of the agglomeration of bubbles with an nth-generation daughter bubble, the sixth is the work of the gas during isothermal variation of the volume of the daughter bubbles, and the seventh is the work of the vapor during isobaric variation of their volume. The appearance of the last two terms has to do with the fact that the surface charge density at the emitting protrusions during separation of a daughter bubble is large, while the gas pressure inside the entire system is of the same order as the pressure in the parent bubble. After formation of a daughter bubble, because of its ability to change its volume, a balance of pressures at the surface of the bubble will be established in a short time.

It is clear that, as in the problem of the breakup of a highly charged drop,[8,9] the process of division of a bubble will continue until the Coulomb force tearing off a daughter bubble exceeds the Laplace force $2\pi\sigma r_*$ (r_* is the neck radius) holding it in place. Assuming that the field strength at the breakoff point is determined by the field of the parent bubble and by the field of the previously separated daughter bubbles, it is not hard to obtain the condition for breakaway of a daughter bubble from the parent bubble[8,9]

$$\frac{\alpha X_n(1-e_2^2)^{1/\sigma}}{8} \leqslant WY_n\left\{\left[1-2\sum_{k=1}^{n} Y_k\right]\frac{(1-e_1^2)^{2/3}}{(\nu_n^2-e_1^2)}\right.$$
$$\left. - \frac{(1-e_1^2)^{2/3}}{m^2}\sum_{k=1}^{n-1} Y_k\right\}, \tag{2}$$

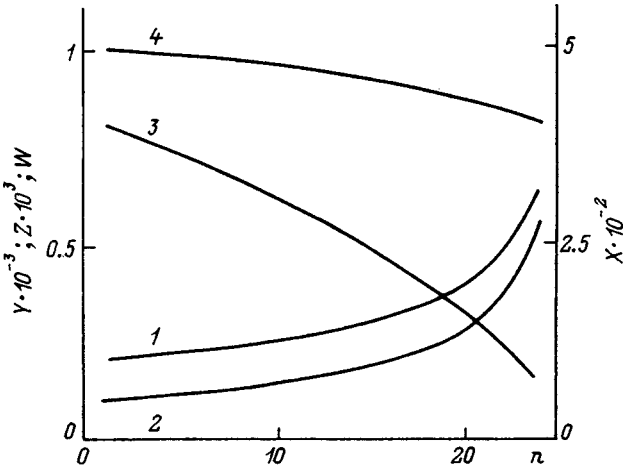

FIG. 1.

where $Y_k = q_k/Q$ and $X_k = r_k/R$ ($k=1,2,\ldots,n$) are respectively the dimensionless charge and radius of the kth daughter bubble, $\alpha = r_*/b_n$, b_n is the length of the semiminor axis of the nth daughter bubble, and $W = Q^2/(16\pi\sigma R^3)$ is the Rayleigh parameter of the initial parent bubble before the first decay.

Note that the instability of the bubble is realized for $W + \beta \geqslant 1$, where $\beta = (P^g + P^v)R/2\sigma$, P^g is the partial pressure of the gas in the parent bubble before breakup whereas the instability of a drop is realized for $W \geqslant 1$ (Ref. 11). In Eq. (2) the first term in braces characterizes the electric field strength of an nth-generation daughter bubble created by the parent bubble at the breakoff point, and the second term takes account of weakening of the field by the agglomeration of daughter bubbles formed earlier.

We require by virtue of the Onsager principle of minimum energy dissipation that its variation be extremal, i.e., that the condition $\partial(\Delta U)/\partial q_n = 0$, $\partial(\Delta U)/\partial r_n = 0$ be fulfilled.[12] Finding the partial derivative of expression (1) with respect to q_n and r_n, we obtain two more equations in addition to Eq. (2) for the three unknowns X_n, Y_n, and ν_n:

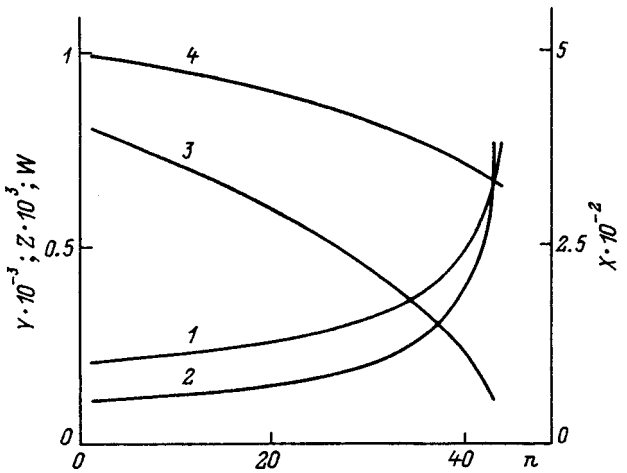

FIG. 2.

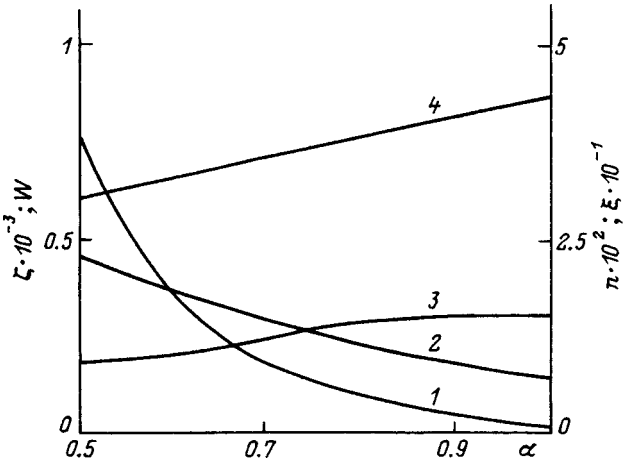

FIG. 3.

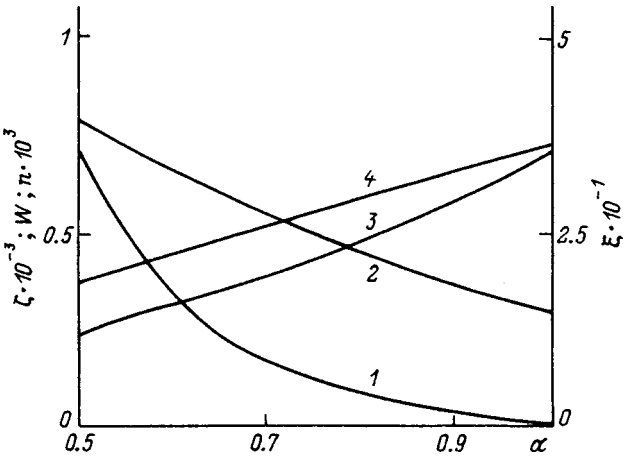

FIG. 4.

$$Y_n\frac{B(e_2)}{X_n}+\left[1-2\sum_{k=1}^{n-1}Y_k\right][K(\nu_n)-B(e_1)]+\frac{(1-e_1^2)^{1/3}}{m}\sum_{k=1}^{n-1}Y_k=0, \tag{3}$$

$$X_nA(e_2)-WY_n^2\frac{B(e_2)}{X_n^2}-\eta\beta X_n^2=0,$$

$$\eta=\frac{P_2^g+P^v}{P^g+P^v}. \tag{4}$$

2. By solving the system of equations (2)–(4) numerically, it became clear that the presence in the vicinity of the emitting protrusions of clouds of previously emitted daughter bubbles has a substantial effect on the characteristics of the breakup process. This can be seen in Figs. 1 and 2, which plot the dependence of the dimensionless radius X (curve *1*), dimensionless charge Y (curve *2*), and the dimensionless specific charge Z (curve *3*) for the daughter bubbles, and also the Rayleigh parameter W for the parent bubble (curve *4*) as functions of the ordinal number of the emitted bubble n for $W=1$, $e_1^2=0.7$, $\alpha=0.9$, $\eta=1.1$, $\beta=0.5$, $m=1$ (Fig. 1) and $m\gg1$ (Fig. 2). The value $\alpha=0.9$ adopted in the calculations was chosen on the basis of data on the decay of highly charged drops, since the best agreement of experiment and theory is noted for this value.[9] The values of the eccentricities of the daughter bubbles in all cases is exceedingly small, i.e., the shape of the daughter bubbles differs very little from spherical.

To illustrate the possible trends of variation of the breakup parameters, Figs. 3 and 4 show plots of the number of emitted bubbles n (curve *1*), the relative charge loss by the parent bubble $\xi=\Delta Q/Q$ (curve *2*), the relative mass loss $\zeta=\Delta M/M$ (curve *3*), and the Rayleigh parameter for the remnant of the parent bubble W (curve *4*) as functions of the undetermined parameter α for $W=1$, $e_1^2=0.7$, $\eta=1.1$, $\beta=0.5$, $m=1$ (Fig. 3) and $m\gg1$ (Fig. 4).

In a number of situations the case can be realized in which the charge of the parent bubble is several times greater than the critical charge for realization of instability. For this case, we calculated the dimensionless radii X (curve *1*), charges Y (curve *2*), and specific charges Z (curve *3*) for the daughter bubbles, and the Rayleigh parameter W for the parent bubble (curve *4*) as functions of the decay number n for $W=10$, $e_1^2=0.7$, $\alpha=0.9$, $\eta=1.1$, $\beta=0.5$, $m=1$ (Fig. 5) and $m\gg1$ (Fig. 6). It can be seen that an increase in the initial value of W leads to an increase in the number of daughter bubbles and a decrease in their characteristic linear dimensions and charges.

3. The fact that the last two terms in Eq. (1) describe the variation of the size of a daughter bubble as a consequence of equalization of the pressures on its surface causes us to ask just how large is this change in the size of the daughter bubble. If we repeat the above calculations but without these two terms, then we can find the dimensionless radius and charge of the daughter bubble immediately before its volume changes as a result of equalization of pressure. The condition of equality of pressures for a spherical bubble in dimensional form is easily written:

$$\frac{q^2}{8\pi r^4}+(P_2^g+P^v)-\frac{2\sigma}{r}=0. \tag{5}$$

It can be rewritten in dimensionless form as

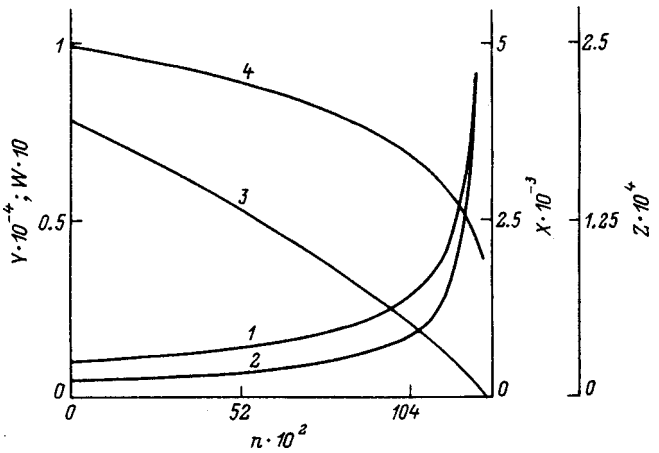

FIG. 5.

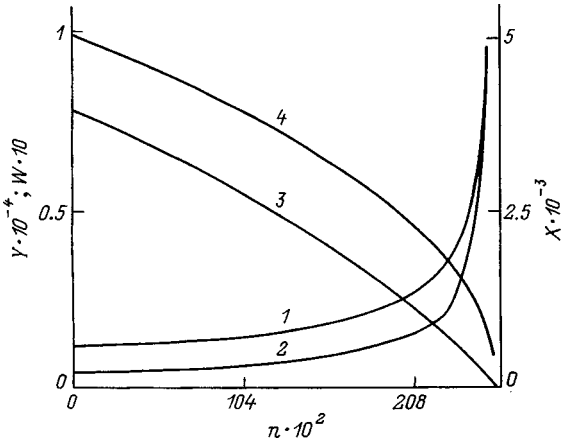

FIG. 6.

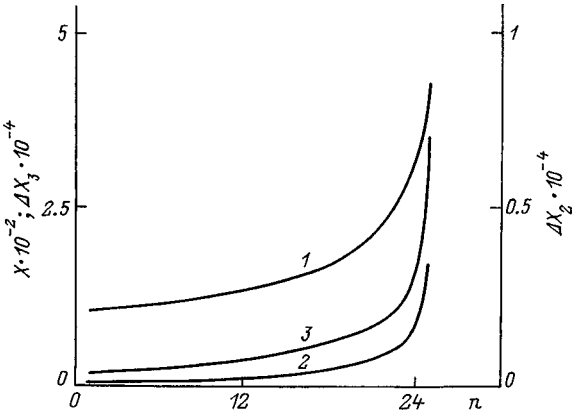

FIG. 7.

$$\frac{WY^2}{X^4} + \eta\beta - \frac{1}{X} = 0. \tag{6}$$

In these equations the first term is the electric pressure, the second term is the total pressure of the gas and vapor, and the third is the Laplace pressure. Calculating Eqs. (2)–(4) numerically without allowance for the last term in Eq. (4), which describes the contribution to the variation of the energy from the variation of the volume, we can find the dimensionless radii and charges of the daughter bubbles. The charges found in this way were substituted into Eq. (6), from which we found the dimensionless radii of the daughter bubbles after the establishment of balance of pressures. The dimensionless radius X of the daughter bubble before expansion (curve *1*) and the change in its radius for two different values of the ratio of the pressure inside the daughter bubble to the pressure inside the parent bubble [ΔX_2 for $\eta = 0.11$ (curve *2*) and ΔX_3 for $\eta = 1.1$ (curve *3*)] are plotted in Fig. 7 as functions of the ordinal number (decay number) of the daughter bubble n for $e_1^2 = 0.7$, $\alpha = 0.9$, $W = 1$, $\beta = 0.5$, and $m = 1$. It is not hard to see that the bubble always expands, and the change in its radius depends on the decay number and the ratio of the pressure inside the daughter bubble to the pressure inside the parent bubble. But the change in the radius is two orders of magnitude smaller than the radius itself.

4. In conclusion we note the following. We have calculated the decay parameters (size, charge, and number of daughter bubbles) of a highly charged parent bubble in a dielectric liquid. In comparison with the situation of decay of a highly charged drop, the number of emitted daughter bubbles is roughly an order of magnitude less. The integrated characteristics of decay (total charge and mass loss of the parent bubble) are roughly the same as for a drop.

[1] C. G. Garton and Z. Krasucki, Trans. Faraday Soc. **60**, 211 (1964).
[2] N. N. Ogus and A. Prospereti, J. Fluid Mech. **219**, 143 (1990).
[3] F. McIntyre, J. Geophys. Res. **77**, 5211 (1972).
[4] M. Khaleeq-Ur-Rahman and C. P. R. Saunders, Atmos. Res. **26**, 329 (1991).
[5] K. J. Cheng and J. B. Chaddock, Phys. Lett. A **106**, 51 (1984).
[6] V. V. Glazkov, O. A. Sinkevich, and P. V. Smirnov, Teplofiz. Vys. Temp. **29**, 1095 (1991).
[7] I. V. Pylaeva, O. A. Sinkevich, and P. V. Smirnov, Teplofiz. Vys. Temp. **30**, 367 (1992).
[8] A. I. Grigor'ev and S. O. Shiryaeva, J. Phys. D **23**, 1361 (1990).
[9] A. I. Grigor'ev and S. O. Shiryaeva, Zh. Tekh. Fiz. **61**, No. 3, 19 (1991) [Sov. Phys. Tech. Phys. **36**, 258 (1991)].
[10] A. I. Grigor'ev, S. O. Shiryaeva, and E. I. Belavina, Zh. Tekh. Fiz. **59**, No. 6, 27 (1989) [Sov. Phys. Tech. Phys. **34**, 602 (1989)].
[11] L. D. Landau and E. M. Lifshitz, *Electrodynamics of Continuous Media*, 2nd ed., with L. P. Pitaevskii (Pergamon Press, Oxford, 1984; Nauka, Moscow, 1982, 620 pp.).
[12] S. O. Shiryaeva and A. I. Grigor'ev, Zh. Tekh. Fiz. **65**(2), 11 (1995) [Tech. Phys. **40**, 122 (1995)].

Translated by Paul F. Schippnick

Generation of electromagnetic waves by a rotating plasma

V. V. Dolgopolov, M. V. Dolgopolov, and Yu. V. Kirichenko

National Science Center, Kharkov Physicotechnical Institute, 310108 Kharkov, Ukraine
(Submitted January 8, 1997)
Zh. Tekh. Fiz. **69**, 16–21 (February 1999)

Generation of electromagnetic waves by an annular shell of plasma rotating in crossed radial electrostatic and axial magnetic fields in a cylindrical resonator is investigated theoretically. Dispersion relations are obtained describing the interaction of the waves with the plasma. It is shown that generation of waves by a narrow plasma shell is possible due to a cyclotron resonance, Čerenkov resonance, or plasma resonance. Here we consider a Čerenkov resonance, where the velocities of the plasma components and the phase velocities of the waves are perpendicular to the constant magnetic field. The frequencies and growth rates of the waves are found under conditions of the above-mentioned resonances in a uniform and in a nonuniform plasma shell. Advantages and disadvantages of wave generation under various conditions are noted. © *1999 American Institute of Physics.* [S1063-7842(99)00402-X]

INTRODUCTION

A number of theoretical works (see Refs. 1–4 and the literature cited therein) have investigated the instabilities arising in a rotating plasma, i.e., in a plasma located in constant electrostatic and axial magnetic fields. The source of the instabilities examined in these works was the relative azimuthal motion of various components of the plasma and radial oscillations of the ions in a strong radial electrostatic field. The interaction of the rotating plasma (i.e., of its components) with the natural oscillations of the resonator filled with the plasma (the metal cylinder in which the plasma is located) remained outside of consideration. A study of this interaction is of both theoretical and practical interest, since it can be used to generate electromagnetic waves. It turns out that an instability can also arise when relative azimuthal motion of different components of the plasma is absent, e.g., in a one-component plasma. The experimental work, Ref. 5, describes a generator whose operation is based on the interaction of the natural oscillations of a cylindrical resonator with a rotating ring of electrons confined by the radial electrostatic field. The use of a rotating plasma instead of a rotating shell of electrons can substantially increase the output power of the generator.

The present paper investigates generation of electromagnetic waves (natural oscillations of the cylindrical resonator) by an annular shell of rotating plasma.

BASIC EQUATIONS

As the resonator, we consider a cavity unbounded in the z direction (we use the cylindrical coordinate system r,φ,z) bounded only by metal walls forming the cylindrical surfaces $r=a$ and $r=b$ ($a\leqslant r\leqslant b$). The potential difference between the central rod ($r<a$) and the sheath ($r>b$) creates a constant radial electrostatic field $E_0(r)$ ($\partial E_0/\partial\varphi=0$, $\partial E_0/\partial z=0$). A constant axial magnetic field B can be created by azimuthal currents flowing in coils surrounding the resonator.

The density of charged particles (plasma components) n_α, when unperturbed by an electromagnetic field, depends only on the coordinate r

$$n_\alpha(r)\neq 0 \quad \text{for} \quad r_-<r<r_+,$$

$$n_\alpha(r)=0 \quad \text{for} \quad r\leqslant r_- \quad \text{and} \quad r\geqslant r_+,$$

$$a<r_-<r_+<b, \quad \delta r=r_+-r_-\ll r_-. \tag{1}$$

Assuming that the fields and the perturbations of the density and velocity of the charged particles do not depend on the axial coordinate z and that the dependence of these quantities on the azimuthal coordinate φ and time t is expressed by the complex exponential factor $\exp\{i(m\varphi-\omega t)\}$, we obtain from the linearized equations of motion of the charged particles

$$\mathcal{V}_{\alpha r}^{(1)}=-\frac{e_\alpha}{m_\alpha w_\alpha}\left\{-i\bar{\omega}_{m\alpha}\left(E_r+\frac{\mathcal{V}_\alpha}{c}H_z\right)+\left(\omega_{c\alpha}+2\frac{\mathcal{V}_\alpha}{r}\right)E_\varphi\right\}, \tag{2}$$

$$\mathcal{V}_{\alpha\varphi}^{(1)}=\frac{e_\alpha}{m_\alpha w_\alpha}\left\{\left(\omega_{c\alpha}+\frac{\partial\mathcal{V}_\alpha}{\partial r}+\frac{\mathcal{V}_\alpha}{r}\right)\left(E_r+\frac{\mathcal{V}_\alpha}{c}H_z\right)+i\bar{\omega}_{m\alpha}E_\varphi\right\}, \tag{3}$$

where

$$\mathcal{V}_\alpha=-\frac{\omega_{c\alpha}r}{2}\left\{1-\left(1-\frac{4e_\alpha E_0}{m_\alpha\omega_{c\alpha}^2 r}\right)^{1/2}\right\},$$

$$\bar{\omega}_{m\alpha}=\omega_\alpha-\frac{m\mathcal{V}_\alpha}{r}, \quad \omega_\alpha=\omega+i\nu_\alpha, \quad \mathrm{Re}(\omega)>0,$$

$$w_\alpha=\bar{\omega}_{m\alpha}^2-\left(\omega_{c\alpha}+2\frac{\mathcal{V}_\alpha}{r}\right)\left(\omega_{c\alpha}+\frac{\partial\mathcal{V}_\alpha}{\partial r}+\frac{\mathcal{V}_\alpha}{r}\right), \tag{4}$$

$\omega_{c\alpha}=Be_\alpha/m_\alpha c$ is the gyrofrequency of particles of species α; e_α and m_α are the charge and mass of the particles of species α; ν_α is the effective collision frequency of particles of species α with other particles; c is the speed of light; E_r, E_φ, and H_z are the components of the electric and magnetic fields of the wave; $\mathcal{V}^{(1)}_{\alpha r}$ and $\mathcal{V}^{(1)}_{\alpha\varphi}$ are the components of the perturbation of the velocity of the particles of species α by the wave field; m is a nonzero integer; and $\mathcal{V}_\alpha$ is the velocity of rotation of the particles of species α, unperturbed by the wave field.

The linearized equations of continuity yield the following expressions for the perturbations of the density n_α of particles of species α:

$$n^{(1)}_\alpha=\frac{1}{r\omega_{m\alpha}}\left\{mn_\alpha\mathcal{V}^{(1)}_{\alpha\varphi}-i\frac{\partial}{\partial r}(rn_\alpha\mathcal{V}^{(1)}_{\alpha r})\right\}, \tag{5}$$

where $\omega_{m\alpha}=\omega-m\mathcal{V}_\alpha/r$.

Substituting Eqs. (2), (3), and (5) into the expressions for the perturbations of the charge density $\rho=\Sigma_\alpha e_\alpha n^{(1)}_\alpha$ and the radial current density $j_r=\Sigma_\alpha e_\alpha n_\alpha\mathcal{V}^{(1)}_\alpha r$, we obtain from Maxwell's equations an equation for the azimuthal component of the electric field of the wave field E_φ in the region $r_-<r<r_+$

$$\begin{aligned}&\frac{d}{dr}\left\{\varepsilon r\frac{d}{dr}(rE_\varphi)+mr\sum_\alpha\frac{\Omega^2_\alpha}{w_\alpha\omega_{m\alpha}}\left(\omega_{c\alpha}+2\frac{\mathcal{V}_\alpha}{r}\right)E_\varphi\right\}\\&\quad=m\sum_\alpha\frac{\Omega^2_\alpha}{w_\alpha\omega_{m\alpha}}\left(\omega_{c\alpha}+2\frac{\overline{\mathcal{V}}_\alpha}{r}\right)\frac{d}{dr}(rE_\varphi)\\&\qquad+m^2\left\{\varepsilon-\sum_\alpha\frac{\Omega^2_\alpha}{w_\alpha\omega^2_{m\alpha}}\left(\frac{\mathcal{V}_\alpha}{r}-\frac{\partial\mathcal{V}_\alpha}{\partial r}\right)\right.\\&\qquad\left.\times\left(\omega_{c\alpha}+2\frac{\mathcal{V}_\alpha}{r}\right)\right\}E_\varphi,\end{aligned} \tag{6}$$

$$\varepsilon=1-\sum_\alpha\frac{\Omega^2_\alpha}{w_\alpha}\frac{\overline{\omega}_{m\alpha}}{\omega_{m\alpha}}, \tag{7}$$

$$2\overline{\mathcal{V}}_\alpha=\left(1+\frac{\overline{\omega}_{m\alpha}}{\omega_{m\alpha}}\right)\mathcal{V}_\alpha+\left(1-\frac{\overline{\omega}_{m\alpha}}{\omega_{m\alpha}}\right)r\frac{\partial\mathcal{V}_\alpha}{\partial r}, \tag{8}$$

$\Omega_\alpha=\{4\pi e^2_\alpha n_\alpha(r)/m_\alpha\}^{1/2}$ is the Langmuir frequency of the particles of species α.

In the regions of vacuum $a\leqslant r\leqslant r_-$ and $r_+\leqslant r\leqslant b$ the components of the electromagnetic field satisfy the equations

$$\begin{aligned}&E_r=-\frac{mc}{\omega r}H_z,\quad E_\varphi=-i\frac{c}{\omega}\frac{\partial H_z}{\partial r},\\&\frac{1}{r}\frac{\partial}{\partial r}\left(r\frac{\partial H_z}{\partial r}\right)+\left(\frac{\omega^2}{c^2}-\frac{m^2}{r^2}\right)H_z=0.\end{aligned} \tag{9}$$

DISPERSION RELATION

It is convenient to write the solutions of the last of Eqs. (9) in the form

$$H_z=A_-J(kr)+B_-N(kr)\quad\text{for}\quad a\leqslant r\leqslant r_-, \tag{10}$$

$$H_z=A_+J(kr)+B_+N(kr)\quad\text{for}\quad r_+\leqslant r\leqslant b, \tag{11}$$

where $k=\omega/c$, and $J(x)=J_{|m|}(x)$ and $N(x)=N_{|m|}(x)$ are Bessel and Neumann functions, and $A_\mp$ and $B_\mp$ are integration constants.

It is impossible to find the solutions of Eq. (6) analytically in the general case. However, in the case under consideration of a narrow shell of plasma Eq. (6) can be solved approximately by invoking the smallness of the parameter $\delta r/r_-$. If terms higher than the first order of smallness in this parameter are neglected, Eq. (6) yields (a similar method is used in Refs. 6–8)

$$\begin{aligned}r_+E_\varphi(r=r_+)-r_-E_\varphi(r=r_-)&=\int_{r_-}^{r_+}\frac{dr}{r\varepsilon}\left\{\left(r\frac{\partial}{\partial r}(rE_\varphi)\right)\right|_{r=r_-}\\&\quad-mr\sum_\alpha\frac{\Omega^2_\alpha}{w_\alpha\omega_{m\alpha}}\left(\omega_{c\alpha}+2\frac{\mathcal{V}_\alpha}{r}\right)E_\varphi\Bigg\},\end{aligned} \tag{12}$$

$$\begin{aligned}&\left(r\frac{\partial}{\partial r}(rE_\varphi)\right)\Bigg|_{r_+}-\left(r\frac{\partial}{\partial r}(rE_\varphi)\right)\Bigg|_{r_-}\\&\quad=m\int_{r_-}^{r_+}dr\left\{\sum_\alpha\frac{\Omega^2_\alpha}{w_\alpha\omega_{m\alpha}}\left(\omega_{c\alpha}+2\frac{\overline{\mathcal{V}}_\alpha}{r}\right)\frac{1}{\varepsilon r}\right.\\&\quad\times\left[\left(r\frac{\partial}{\partial r}(rE_\varphi)\right)_{r_-}-mr\sum_\beta\frac{\Omega^2_\beta}{w_\beta\omega_{m\beta}}\left(\omega_{c\beta}+2\frac{\mathcal{V}_\beta}{r}\right)E_\varphi\right]\\&\quad\left.+m\left[\varepsilon-\sum_\alpha\frac{\Omega^2_\alpha}{w_\alpha\omega^2_{m\alpha}}\left(\frac{\mathcal{V}_\alpha}{r}-\frac{\partial\mathcal{V}_\alpha}{dr}\right)\left(\omega_{c\alpha}+2\frac{\mathcal{V}_\alpha}{r}\right)\right]E_\varphi\right\}.\end{aligned} \tag{13}$$

With the help of Eq. (9) the boundary conditions (12) and (13) reduce to the form

$$H_z(r=r_+)-H_z(r=r_-)=\lambda\frac{\partial H_z}{\partial r}\Bigg|_{r_-}+\overline{\beta}H_z(r=r_-), \tag{14}$$

$$\frac{\partial H_z}{\partial r}\Bigg|_{r_+}-\frac{\partial H_z}{\partial r}\Bigg|_{r_-}=\overline{\alpha}\frac{\partial H_z}{\partial r}\Bigg|_{r_-}+\varkappa H_z(r=r_-), \tag{15}$$

where

$$\overline{\alpha}=-\frac{\delta r}{r_-}-\frac{m}{r_-}\int_{r_-}^{r_+}\frac{dr}{\varepsilon}\sum_\alpha\frac{\Omega^2_\alpha}{w_\alpha\omega_{m\alpha}}\left(\omega_{c\alpha}+2\frac{\mathcal{V}_\alpha}{r}\right), \tag{16}$$

$$\overline{\beta}=m\int_{r_-}^{r_+}\frac{dr}{r\varepsilon}\sum_\alpha\frac{\Omega^2_\alpha}{w_\alpha\omega_{m\alpha}}\left(\omega_{c\alpha}+2\frac{\overline{\mathcal{V}}_\alpha}{r}\right), \tag{17}$$

$$\begin{aligned}\lambda=\int_{r_-}^{r_+}dr\left\{\varepsilon-\frac{1}{\varepsilon}\sum_{\alpha,\beta}\frac{\Omega^2_\alpha\Omega^2_\beta}{w_\alpha w_\beta\omega_{m\alpha}\omega_{m\beta}}\right.\\\times\left(\omega_{c\alpha}+2\frac{\overline{\mathcal{V}}_\alpha}{r}\right)\left(\omega_{c\beta}+2\frac{\mathcal{V}_\beta}{r}\right)\\\left.-\sum_\alpha\frac{\Omega^2_\alpha}{w_\alpha\omega^2_{m\alpha}}\left(\omega_{c\alpha}+2\frac{\mathcal{V}_\alpha}{r}\right)\left(\frac{\mathcal{V}_\alpha}{r}-\frac{\partial\mathcal{V}_\alpha}{\partial r}\right)\right\},\end{aligned} \tag{18}$$

$$\varkappa=\frac{m^2}{r_-}\int_{r_-}^{r_+}\frac{dr}{r\varepsilon},\quad |\omega|\ll\frac{|m|c}{r_-}. \tag{19}$$

Substituting expressions (8) and (9) into the boundary conditions (14) and (15) and taking into account that the electric field component E_φ is equal to zero at the boundary with the metal walls of the cavity ($r=a$, $r=b$), it is possible to eliminate the integration constants $A_\mp$ and $B_\mp$ and obtain the dispersion relation

$$\begin{aligned}
&N'(x_2)J'(x_1)-N'(x_1)J'(x_2)+\frac{\pi}{2}xN'(x_2)J'(x_1)\\
&\quad\times\Big\{k\delta r(2N'(x)J'(x)-J(x)N''(x)-N(x)J''(x))\\
&\quad+(\overline{\alpha}-\overline{\beta})(J(x)N'(x)+N(x)J'(x))\\
&\quad-2k\lambda N'(x)J'(x)+2\frac{\varkappa}{k}N(x)J(x)\Big\}\\
&\quad+\frac{\pi}{2}xJ'(x_1)J'(x_2)\Big\{k\delta r(N(x)N''(x)-N'^2(x))\\
&\quad-(\overline{\alpha}-\overline{\beta})N(x)N'(x)+k\lambda N'^2(x)-\frac{\varkappa}{k}N^2(x)\Big\}\\
&\quad+\frac{\pi}{2}xN'(x_1)N'(x_2)\Big\{k\delta r(J(x)J''(x)-J'^2(x))\\
&\quad-(\overline{\alpha}-\overline{\beta})J(x)J'(x)+k\lambda J'^2(x)-\frac{\varkappa}{k}J^2(x)\Big\}=0,
\end{aligned} \tag{20}$$

where $f'(x)=\partial f/\partial x$, $f''(x)=\partial^2 f/\partial x^2$, $x=kr_-$, $x_1=ka$, and $x=kb$.

Obviously, the first two terms in Eq. (20) are large in comparison with the remaining terms. It would be hard to analyze the dispersion relation (20) without making any assumptions about the arguments of the Bessel functions. Therefore we restrict the discussion to the case of practical importance in which the conditions

$$|x|\ll 1,\quad |x_2|\gg m^2/2 \tag{21}$$

are fulfilled.

Then the dispersion relation reduces to the form

$$\begin{aligned}
&\omega^{(1)}+i\nu-\Delta_\nu-\Delta_{\delta r}+\frac{\pi x_1^{|m|+1}\omega^{(0)}}{2^{2|m|+1}|m|!\,(|m|-1)!\;\eta^{3|m|-1}x_2}\\
&\quad\times\Big\{|m|k\lambda x^{|m|-2}(\eta^{2|m|}-1)^2-\frac{\varkappa x^{|m|}}{|m|k}(\eta^{2|m|}+1)^2\\
&\quad-(\overline{\alpha}-\overline{\beta})x^{|m|-1}(\eta^{4|m|}-1)\Big\}=0,
\end{aligned} \tag{22}$$

where

$$\begin{aligned}
\Delta_{\delta r}=&-\frac{\pi\omega^{(0)}x_1^{2|m|-1}k\delta r}{2^{2|m|+1}(|m|-1)!\,|m|!\;\eta^{2|m|+1}x_2}\\
&\times(4|m|\,\eta^{2|m|}+1-\eta^{4|m|}),
\end{aligned}$$

$\eta=r_-/a>1$, $\omega^{(1)}=\omega-\omega^{(0)}$, $|\omega^{(1)}|\ll\omega^{(0)}$, $\nu>0$, and $\omega^{(0)}$ is the natural frequency of the resonator with the rod in the absence of the plasma shell and in neglect of losses to radiation from the resonator and dissipation of the electromagnetic field in the walls of the resonator.

If conditions (21) are met, the natural frequency of the resonator satisfies the equation

$$\begin{aligned}
&\frac{\pi(\omega^{(0)}a/c)^{2|m|}}{2^{2|m|}|m|!\,(|m|-1)!}+\tan\left(\frac{\omega^{(0)}}{c}b-\chi_m\right)=0,\\
&\chi_m=\frac{\pi}{4}+\frac{\pi}{2}|m|,
\end{aligned} \tag{23}$$

which yields

$$\omega^{(0)}\simeq\frac{c}{b}(n\pi+\chi_m), \tag{24}$$

where n is an integer; according to the second of conditions (21) $n\gg m^2/2\pi$.

In Eq. (22) we have introduced the terms $i\nu$ and $-\Delta_\nu$. The term $i\nu$ phenomenologically allows for losses to radiation from the resonator and absorption of the energy of the waves by the resonator walls, and the term $-\Delta_\nu$ allows for the frequency shift associated with these losses. The contribution of the plasma shell to the dispersion relation is taken into account by the coefficients $\overline{\alpha}$, $\overline{\beta}$, λ, $\varkappa$. These coefficients grow dramatically when the denominators of expressions (16)–(19) are close to zero. The plasma then interacts most efficiently with the electromagnetic field. The zeros of the denominators of expressions (16)–(19) are expressed by the relations

$$w_\alpha=0,\quad \omega_{m\alpha}=0,\quad \varepsilon=0. \tag{25}$$

The first of Eqs. (25) corresponds to the cyclotron resonance in a rotating plasma[9] for particles of species α, and the second — to the Cerenkov resonance for particles of species α. In this case, the angular velocity of rotation of the particles of species α coincides with the angular phase velocity of the wave. Finally, the third of Eqs. (25) is the condition of a plasma resonance at which the frequency of the wave is equal to the frequency of the local natural oscillations of the plasma in the laboratory reference frame.

CYCLOTRON RESONANCE

In our consideration of the cyclotron resonance we will assume that the condition

$$\left|\sum_\alpha\frac{\Omega_\alpha^2\overline{\omega}_{m\alpha}}{w_\alpha\omega_{m\alpha}}\right|\ll 1,\quad \varepsilon\simeq 1 \tag{26}$$

is satisfied, since only in this case does the cyclotron resonance lead to enhancement of the interaction of the waves with the particles.

Condition (26) implies that the plasma should not be dense, and the collision frequency ν_α should be sufficiently large. Taking into account the relation

$$w_\alpha\simeq 0, \tag{27}$$

we obtain from the dispersion relation (22)

$$\mathrm{Im}(\omega)=-\nu-\frac{\pi c x_1^{2|m|}}{2^{2|m|}((|m|-1)!)^2\eta^{2|m|}br_-}\times\int_{r_-}^{r_+}dr\left[\frac{\omega_{m\alpha}\pm\omega_{c\alpha}\pm 2\mathcal{V}_\alpha/r}{\omega_{m\alpha}}+\eta^{2|m|}\frac{\omega_{m\alpha}\mp\omega_{c\alpha}\mp 2\mathcal{V}_\alpha/r}{\omega_{m\alpha}}\right]^2\times\frac{\Omega_\alpha^2\omega_{m\alpha}\nu_\alpha}{(\mathrm{Re}\,w_\alpha)^2+4\omega_{m\alpha}^2\nu_\alpha^2}. \tag{28}$$

The upper sign inside the brackets of expression (28) corresponds to positive values of m, and the lower sign to negative values. It follows from relation (28) that an instability occurs ($\mathrm{Im}\omega>0$) when $\omega_{m\alpha}<0$ and ν is not too large. Consequently, for generation of electromagnetic waves under conditions of a gyroresonance it is necessary that the angular velocity of the charged particles exceed the angular phase velocity of the wave. If condition (27) is satisfied in a narrow region of the plasma shell, expression (28) for the growth (damping) rate of the wave reduces to

$$\mathrm{Im}(\omega)=-\nu-\frac{\pi^2 c x_1^{2|m|}\mathrm{sign}\,(\omega_{m\alpha})}{2^{2|m|+1}((|m|-1)!)^2\eta^{2|m|}br_-}\times\left[\frac{\Omega_\alpha^2}{\omega_{m\alpha}^2|\partial(\mathrm{Re}\,\omega_\alpha)/\partial r|}\right]\Bigg|_{r=r_{c\alpha}}\left[\omega_{m\alpha}\pm\omega_{c\alpha}\pm 2\frac{\mathcal{V}_\alpha}{r}+\eta^{2|m|}\left(\omega_{m\alpha}\mp\omega_{c\alpha}\mp 2\frac{\mathcal{V}_\alpha}{r}\right)\right]^2\Bigg|_{r=r_{c\alpha}}, \tag{29}$$

where the point $r=r_{c\alpha}$ satisfies the equation

$$\mathrm{Re}(w_\alpha(r=r_{c\alpha}))=0. \tag{30}$$

The growth rate defined by relation (29) does not depend on the collision frequency ν_α.

ČERENKOV RESONANCE

Under conditions of Čerenkov resonance and plasma resonance, dissipative effects in the plasma, in particular collisions of charged particles, do not have as substantial an effect on the interaction of waves with the plasma as in the case of a cyclotron resonance. Therefore in what follows we set

$$\nu_\alpha=0,\quad \omega_\alpha=\omega,\quad \overline{\omega}_{m\alpha}=\omega_{m\alpha},\quad \overline{\mathcal{V}}_\alpha=\mathcal{V}_\alpha. \tag{31}$$

When the angular phase velocity of the wave is near the angular velocity of the particles of species α ($\omega_{m\alpha}\simeq 0$), the dispersion relation (22) can be written as

$$\omega_{m\alpha}^3+(i\nu-\Delta)\omega_{m\alpha}^2-\Delta_2^2\omega_{m\alpha}-\Delta_3^3=0, \tag{32}$$

where

$$\Delta\simeq\Delta_\nu+\omega^{(0)}-\frac{m\mathcal{V}_\alpha}{r_-}, \tag{33}$$

$$\Delta_2^2=-\frac{m}{|m|}\,\frac{\pi x_1^{2|m|}(\eta^{4|m|}-1)c}{2^{2|m|}((|m|-1)!)^2\eta^{2|m|}br_-}\times\int_{r_-}^{r_+}\frac{dr}{\varepsilon}\,\frac{\Omega_\alpha^2}{w_\alpha}\left(\omega_{c\alpha}+2\frac{\mathcal{V}_\alpha}{r}\right), \tag{34}$$

$$\Delta_3^3=\frac{\pi x_1^{2|m|-1}(\eta^{2|m|}-1)^2\omega^{(0)}}{2^{2|m|+1}((|m|-1)!)^2\eta^{2|m|+1}b}\times\int_{r_-}^{r_+}dr\left\{\frac{1}{\varepsilon}\left[\frac{\Omega_\alpha^2}{w_\alpha}\left(\omega_{c\alpha}+2\frac{\mathcal{V}_\alpha}{r}\right)\right]^2+\frac{\Omega_\alpha^2}{w_\alpha}\left(\omega_{c\alpha}+2\frac{\mathcal{V}_\alpha}{r}\right)\left(\frac{\mathcal{V}_\alpha}{r}-\frac{\partial\mathcal{V}_\alpha}{\partial r}\right)\right\}. \tag{35}$$

In the last three relations and in what follows, we assume that the quantities r, $\mathcal{V}_\alpha(r)$, and $\partial\mathcal{V}_\alpha/\partial r$ vary only slightly in the plasma shell ($r_-<r<r_+$).

Equation (32) is an equation of third degree in $\omega_{m\alpha}$. The imaginary part of $\omega_{m\alpha}$ coincides with the imaginary part of ω and, consequently, is the growth (damping) rate of the wave.

If $|i\nu-\Delta|\ll|\Delta_3|$, oscillations growing in time arise if the condition

$$|\Delta_3^3/\Delta_2^3|>2/3^{3/2} \tag{36}$$

is satisfied.

For $\Delta_3^3\neq 0$ the more stringent condition (36)

$$|\Delta_3^3|\gg|\Delta_2^3| \tag{37}$$

is easily satisfied.

Then the dispersion relation takes the form

$$\omega_{m\alpha}^3\simeq\Delta_3^3. \tag{38}$$

One of the three roots of Eq. (38) always corresponds to oscillations increasing in time. The growth rate in this case is maximum (proportional to the cube root of the small parameter $\delta r/b$).

For large losses or detuning of the resonance, when the conditions

$$|\Delta_2^2|\ll|\Delta_3^{3/2}(i\nu-\Delta)^{1/2}|,\quad |\Delta_3|\ll|i\nu-\Delta| \tag{39}$$

are satisfied, the solution of Eq. (32) has the form

$$\omega_{m\alpha}\simeq\pm\left(\frac{\Delta_3^3}{i\nu-\Delta}\right)^{1/2}. \tag{40}$$

One of the roots of Eq. (40) corresponds to oscillations growing in time.

It follows from what has been said that a Čerenkov resonance, i.e., efficient exchange of energy between the wave and a component of the plasma, is also possible when the velocities of the charged particles and the phase velocity of the wave are transverse to the constant magnetic field, provided the velocity of this component is close to the phase velocity of the wave.

PLASMA RESONANCE IN A UNIFORM SHELL

According to Eqs. (25), a plasma resonance occurs in the region where the condition

$$\varepsilon(\omega,r)=0 \tag{41}$$

is fulfilled.

If the plasma density grows abruptly from zero to its maximum value near $r=r_-$, remains practically constant ($\partial\Omega_\alpha/\partial r\simeq 0$) in the region $r_-<r<r_+$, and then falls abruptly to zero near $r=r_+$, the plasma resonance condition (41) can be approximately satisfied over the entire thickness of the narrow plasma shell. The dispersion relation (22) then reduces to a quadratic equation in $\delta\omega=\omega-\omega_p$, where ω_p is a root of Eq. (41). The solution of this quadratic equation has the form

$$\delta\omega=\frac{1}{2}\{\Delta_p-i\nu\pm((\Delta_p-i\nu)^2-4q)^{1/2}\}, \tag{42}$$

where

$$\Delta_p\simeq\Delta_\nu+\omega^{(0)}-\omega_p,$$

$$q=-\frac{\pi x_1^{2|m|}c\,\delta r}{2^{2|m|+1}((|m|-1)!)^{2|m|}br_-\tau}\left[\eta^{2|m|}+1-\frac{m}{|m|}(\eta^{2|m|}-1)\sum_\alpha\frac{\Omega_\alpha^2}{w_\alpha\omega_{m\alpha}}\left(\omega_{c\alpha}+2\frac{\mathcal{V}_\alpha}{r_-}\right)\right]^2, \tag{43}$$

$$\tau=\left.\frac{\partial\varepsilon}{\partial\omega}\right|_{\omega=\omega_p}=2\sum_\alpha\frac{\Omega_\alpha^2}{w_\alpha^2}\omega_{m\alpha}. \tag{44}$$

The imaginary part of $\delta\omega$ is the growth (damping) rate of the wave. As follows from Eq. (42), an instability occurs when $q>0$, and, consequently, according to Eqs. (43), $\tau<0$. Under ordinary conditions, the velocities of rotation of the various plasma components differ by an amount significantly less than the velocities themselves. Therefore, in the case under consideration, when the conditions of Čerenkov resonance are not fulfilled ($\omega_{m\alpha}\neq 0$), the values of $\omega_{m\alpha}$ have the same sign for all of the particles. Taking this into account together with Eq. (44), we arrive at the conclusion that under plasma resonance conditions, oscillations can grow in time whose angular phase velocity is less than the angular velocity of rotation of the plasma.

For a large detuning Δ_p or large losses to radiation from the resonator or to dissipation of energy in the walls, the wave growth rate according to Eq. (42) is given by

$$\mathrm{Im}(\omega)\simeq\frac{q\nu}{\Delta_p^2+\nu^2}, \tag{45}$$

from which it follows that an increase in the detuning or in the losses leads to a decrease of the growth rate. However, for $\Delta_p^2>4q$ it is the losses ($\nu\neq 0$) that are responsible for wave generation.

PLASMA RESONANCE IN A NONUNIFORM SHELL

Obviously, under experimental conditions it is very difficult to get the plasma density in the shell to depend weakly on r [$\partial(\Omega_\alpha^2)/\partial r\simeq 0$]. Therefore, it is advisable to examine the possibility of generating electromagnetic waves under conditions of plasma resonance in a nonuniform plasma.

Let the plasma density grow smoothly from zero at the point $r=r_-$ to some maximum value and then fall smoothly to zero at the point $r=r_+$. A plasma resonance will occur in the vicinity of the points $r=r_1$ and $r=r_2$ ($r_-<r_1<r_2<r_+$) satisfying Eq. (41) $\omega_p(r_1)=\omega_p(r_2)\simeq\omega$. It should be noted that in the case of a plasma resonance in a nonuniform plasma shell the method we have used, which assumes that the time dependence of all the perturbations and fields near the points $r=r_1$ and $r=r_2$ is expressed by the complex exponential factor $\exp(-i\omega t)$, with $\partial\omega/\partial r=0$, is inapplicable and we must resort to the Laplace transform in time.[8] However, it is also possible to obtain a valid result using our method if in the calculation of the integrals on the right-hand sides of Eqs. (16)–(19) the contour is taken around the zeros in the denominator as if the imaginary part of the frequency ω were positive. Thus the dispersion relation (22) reduces to an equation of first degree in $\omega^{(1)}$, which yields the following expression for the growth (damping) rate $\mathrm{Im}(\omega)$:

$$\mathrm{Im}(\omega)=-\nu-\frac{\pi^2x_1^{2|m|}ch}{2^{2|m|+1}((|m|-1)!)^2\eta^{2|m|}b\,r_-}\times\left\{\left[\eta^{2|m|}+1-\frac{m}{|m|}(\eta^{2|m|}-1)\times\sum_\alpha\frac{\Omega_\alpha^2}{w_\alpha\omega_{m\alpha}}\left(\omega_{c\alpha}+2\frac{\mathcal{V}_\alpha}{r}\right)\right]^2\times\mathrm{sign}\left(\sum_\alpha\frac{\Omega_\alpha^2\omega_{m\alpha}}{w_\alpha^2}\right)\right\}\Bigg|_{r=r_1\text{ or }r_2}, \tag{46}$$

where $h=|\partial\varepsilon/\partial r|^{-1}_{r=r_1}+|\partial\varepsilon/\partial r|^{-1}_{r=r_2}$.

It follows from Eq. (46) that as in the case of a uniform plasma shell, growth in time of the electromagnetic wave occurs when the angular frequency of rotation of the plasma is greater than the angular phase velocity of the wave. If the velocities of rotation of the various plasma components differ substantially, the condition of instability, according to Eq. (46), is satisfaction of the inequality

$$\left\{\sum_\alpha\frac{\Omega_\alpha^2\omega_{m\alpha}}{w_\alpha^2}\right\}\Bigg|_{r=r_1}\simeq\left\{\sum_\alpha\frac{\Omega_\alpha^2\omega_{m\alpha}}{w_\alpha^2}\right\}\Bigg|_{r=r_2}<0.$$

The second condition of growth of the electromagnetic wave is that losses to radiation from the resonator and dissipation of energy in the walls of the resonator be insignificant, in other words, the second term on the right-hand side of Eq. (46) should be greater than the first in magnitude.

Note that wave generation by a nonuniform plasma shell under conditions of plasma resonance does not require satisfaction of exact resonance conditions as in the case of a cyclotron resonance or a Čerenkov resonance or a plasma resonance in a uniform shell. It is sufficient that there should be a region in the plasma shell where $\varepsilon(\omega,r)<0$.

Since under conditions of a plasma resonance in a nonuniform shell the wave energy grows due to a resonant interaction not with the entire plasma but only with the plasma that is found in the vicinity of the points $r=r_1$ and $r=r_2$, the growth rates here are smaller than for a plasma resonance in a uniform shell.

CONCLUSION

It follows from the foregoing discussion that wave generation in the system under discussion is possible due to cyclotron resonance, Čerenkov resonance, or plasma resonance.

Cyclotron resonance is efficient when dissipative effects in the plasma are large, but the plasma density is small. Čerenkov resonance (coincidence of the velocity of rotation of a plasma component with the phase velocity of the wave) in this case leads to an efficient interaction of the wave with the plasma when the plasma velocity and the phase velocity of the wave are perpendicular to the constant magnetic field. Under conditions of Čerenkov resonance the wave growth rate can reach its maximum value when, in accordance with relations (35) and (38), it is proportional to the cube root of the small parameter $\delta r/b$. In the case of a plasma resonance in a uniform shell, according to Eqs. (42) and (43), the maximum value of the growth rate is proportional to the square root of $\delta r/b$.

Under conditions of a plasma resonance in a nonuniform shell, the growth rate, according to Eq. (46), for small losses to radiation from the resonator and energy dissipation in the walls, is proportional to the first power of the small parameter h/b. However, wave generation due to a plasma resonance in a nonuniform shell possesses a number of advantages. By transferring energy to the wave, the plasma component changes its velocity and radius. This leads to a violation of the conditions of Čerenkov resonance and plasma resonance in a uniform shell. The conditions of plasma resonance in a nonuniform shell in this case are not violated as long as there exists a region in the shell where $\varepsilon<0$.

In the cases of Čerenkov resonance and plasma resonance in a uniform shell, the frequencies of the growing and decaying waves are similar. Therefore, weak nonlinear effects can transform the wave from a growing wave into a decaying wave. Under conditions of plasma resonance in a nonuniform shell, the dispersion relation (22) for ω_1 has one solution. Therefore, in this case weak nonlinear effects probably cannot hinder the amplification of waves. Also note that as a result of a plasma resonance in a nonuniform shell, many waves can be amplified simultaneously.

[1] V. V. Dolgopolov, V. L. Sizonenko, and K. N. Stepanov, Ukr. Fiz. Zh. **18**(1), 18 (1973).
[2] V. G. Dem'yanov, Yu. N. Eliseev, Yu. A. Kirochkin, *et al.*, Fiz. Plazmy **14**, 840 (1988) [Plasma Phys. Rep. **14**, 494 (1988)].
[3] Yu. N. Eliseev, Yu. A. Kirochkin, and K. N. Stepanov, Fiz. Plazmy **17**, 1072 (1991) [Sov. J. Plasma Phys. **17**, 622 (1991)].
[4] Yu. N. Eliseev, Yu. A. Kirochkin, and K. N. Stepanov, Fiz. Plazmy **18**, 1575 (1992) [Sov. J. Plasma Phys. **18**, 816 (1992)].
[5] I. Alexeff and F. Dyer, Phys. Rev. Lett. **45**, 351 (1980).
[6] K. N. Stepanov, Zh. Tekh. Fiz. **35**, 1002 (1965) [Sov. Phys. Tech. Phys. **10**, 773 (1965)].
[7] K. N. Stepanov, Zh. Tekh. Fiz. **35**, 1349 (1965) [Sov. Phys. Tech. Phys. **10**, 1048 (1966)].
[8] V. V. Dolgopolov and A. Ya. Omel'chenko, Zh. Éksp. Teor. Fiz. **5**, 1384 (1970) [JETP **31**, 747 (1970)].
[9] V. V. Dolgopolov, Zh. Tekh. Fiz. **37**, No. 1, 23 (1967) [Sov. Phys. Tech. Phys. **12**, 16 (1967)].

Translated by Paul F. Schippnick

Experimental and computational study of the passage of an electron beam through the curvilinear element of the Drakon stellarator system in a tenuous plasma

V. V. Kondakov, S. F. Perelygin, and V. M. Smirnov

Moscow State Engineering Physics Institute (Technical University), Moscow, Russia
(Submitted July 23, 1997)
Zh. Tekh. Fiz. **69**, 22–26 (February 1999)

Results are presented from the first stage of studies on the passage of an electron beam with energy 100–500 eV in a magnetic field of 300–700 Oe through the curvilinear solenoid of the KRÉL unit, the latter being a prototype of the closing segment of the Drakon stellarator system, in the plasma–beam discharge regime. The ion density at the end of the curvilinear part of the chamber, $n_i \approx 8\times10^8 - 10^{10}$ cm^{-3}, the electron temperature $T_e \approx 4-15$ eV, and the positions at which the beam hits the target for different distances from it to the electron source are determined experimentally. The motion of the electron beam is computationally modeled with allowance for the space charge created by the beam and the secondary plasma. From a comparison of the experimentally measured trajectories and trajectories calculated for different values of the space charge, we have obtained an estimate for the unneutralized ion density of the order of 5×10^7 cm^{-3}.
[S1063-7842(99)00502-4]

INTRODUCTION

Recent years have witnessed an active search for alternative schemes of magnetic confinement of plasma for the purposes of controlled nuclear fusion, including the Drakon stellarator system proposed in Russia in 1981.[1] The Drakon plasma trap is a tandem of ''probkotron'' mirrors interconnected by curvilinear elements (KRÉL) in the form of solenoids with a three-dimensional axis. Theoretical and experimental studies[2,3] have demonstrated the potential of such a system. Further study of this magnetic trap requires the creation of a full-scale setup. One faces the problem of filling this complicated element (the closing segment) of the Drakon system with plasma.

PLASMA EXPERIMENTS IN THE KRÉL MAGNETIC FIELD

As the closing element of the Drakon system we used the KRÉL unit, which consists of two periods of a five-period helical torus whose axis is a geodesic line on a reference torus with major radius 40 cm and minor radius 12 cm. The geometrical axis of the three-dimensional solenoid in the form of a geodesic line affords very smooth modulation of the curvature and twist coefficients of the axis.[2] Figure 1 gives an overall view of the KRÉL unit. The coil of the three-dimensional solenoid was assembled by laying flexible copper wire in six layers on the bellows (vacuum) chamber, with outer diameter 100 mm. The solenoid of the magnet system of the device, of length 1830 mm, consists of three parts: the main, curvilinear part ($L_c = 1480$ mm), and two rectilinear parts: left ($L_l = 250$ mm) and right ($L_r = 154$ mm). The source of the electron beam is located in the left part at a distance of 80 mm from the start of that part. A diagram of the arrangement of these segments of the magnetic system and the main elements of the device is shown in Fig. 2. A current of 100, 150, and 200 A was sent through the coil, which produced a magnetic field with field strengths $P = 320$, 480, and 640 Oe.

In our experiments, to obtain plasma we used a gas dis-

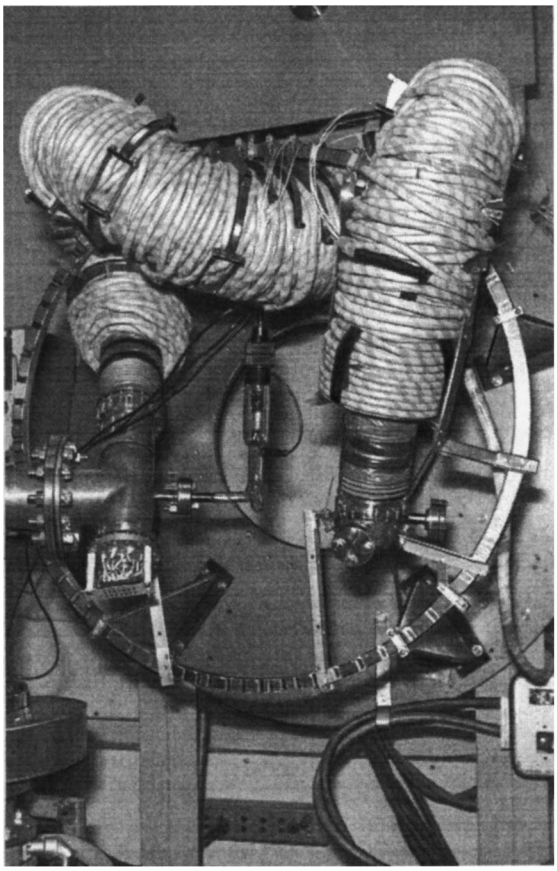

FIG. 1. Overall view of the KRÉL unit.

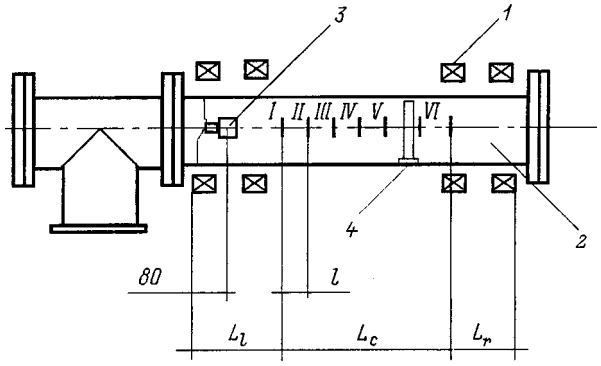

FIG. 2. Diagram showing the arrangement of the main components of the device and the measurement region of the plasma parameters: *1* — coil of the magnetic system; *2* — bellows-type vacuum chamber; *3* — electron beam source; *4* — movable carriage with diagnostic instrumentation; *I* $-VI$ — numbers of the stations at which measurements are made.

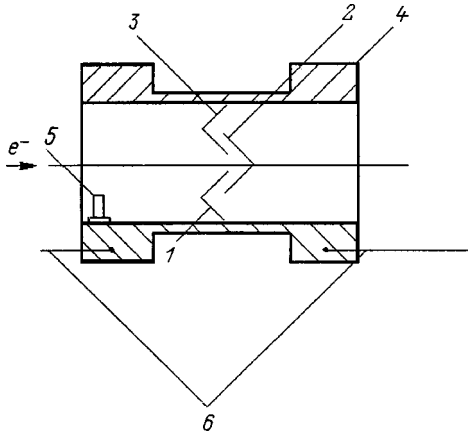

FIG. 3. Carriage with diagnostic instrumentation: *1–3* — collector segments; *4* — framework of the carriage; *5* — single probe; *6* — guide bars guiding movement of the carriage; the arrow at left indicates the direction of the electron flux.

charge in a longitudinal magnetic field. The source of the electron beam was a tungsten cathode (a ring of diameter 10 mm), which was heated by a current of 17–18 A. The heating power reached 50–60 W. An accelerating voltage U of from 100 to 500 V was applied between the chamber and the cathode. The electrons interacted with the neutral residual gas (pressure $2\times10^{-4}-4\times10^{-4}$ Torr). Thus, in the experiment we maintained the conditions of a stationary discharge regime.

Plasma diagnostics were performed by means of probe measurements. A diagram of the diagnostic system (carriage with diagnostic apparatus) is shown in Fig. 3. The single probe consisted of a tungsten rod 2 mm in diameter and 15 mm in length. It was located in that part of the carriage that faced the electron source, in the direction of the local center of curvature of the geometrical axis of the chamber. Beyond the probe was located an electron collector which was divided into three segments to facilitate vacuum pumping. The segments on the carriage were arranged so as to preclude direct transit of the particles and to prevent reflected electrons from falling onto the probe. The current on the probe and collector was measured with a resistance of 10 Ω. The device for moving the carriage along the chamber, whose design in described in detail in Ref. 3, ensured reliable orientation of the probes relative to the principal normal to the geometrical axis of the device.

The position of the charged particle beam was determined at six stations along the curvilinear part of the solenoid, spaced at a distance of $l=18$ cm (Fig. 2). The plasma formed in the beam-plasma discharge was investigated with the help of the current–voltage characteristics (CVC) at the last two stations, namely the fifth and sixth, at a separation from the electron source of 107 and 125 cm, respectively, for $U=100$, 200, 300, 400, and 500 V and $H=320$ and 640 Oe.

According to estimates for $H=320$ Oe, based on measurements of the electron temperature T_e and electron density n_e, in the region of the fifth and sixth stations, the Debye radius of the plasma was $1.5\times10^{-2}-1.0\times10^{-1}$ cm, and the electron Larmor radius was $2.1\times10^{-2}-4.1\times10^{-2}$ cm, i.e., i.e., the electrons in the system were magnetized. Since the inequality $T_i\ll T_e$ is always satisfied in a gas-discharge plasma, the ion saturation current was calculated according to the Bohm formula. Graphs of the CVCs had pronounced branches of the electron and ion saturation currents. At all boundaries of the measurements for various values of the magnetic field and accelerating voltage the rectilinear part of the transitional segment of the CVC was indicative of a Maxwellian electron velocity distribution.

The floating potential for various values of U for $H=320$ Oe at the fifth station varied from -40 to -50 V, and the plasma potential varied from $+15$ to $+25$ V. A twofold increase in the magnetic field lifted their values by roughly 10%. On passing to the sixth station the floating potential dropped by roughly 15% and the plasma potential by 10–15%. The electron temperature T_e at both stations varied weakly with variation of U: $T_e\approx4-15$ eV. The ion density n_i at these stations was $8\times10^8-10^{10}$ cm^{-3}.

From the ratio of the collector current I_k to the emission current $I_{\rm em}$ at all six measurement stations for various U and H we estimated the scattering of the electron beam in the device (Fig. 4). Between the first and third stations the decrease in the ratio $I_k/I_{\rm em}$ was not large, and after the third station we even noticed an increase. This paradox has a very simple explanation. Position 3 is located in the middle of the curvilinear segment of the KRÉL magnetic field. One peculiarity of our spatial configuration is that it compensates to-

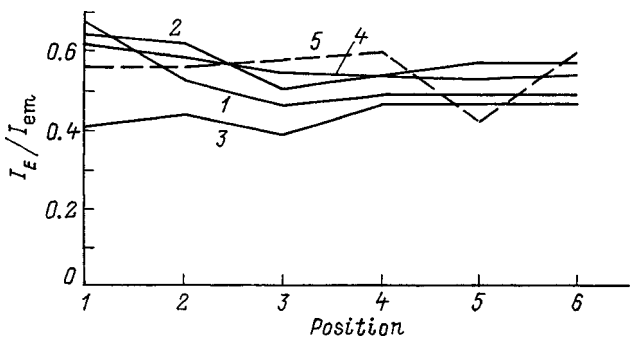

FIG. 4. Electron scattering along chamber as a function of H, Oe: *1, 2* — 320; *3* — 480; *4, 5* — 640; and of U, eV: *1* — 100, *2–5* — 200.

roidal drift of the charged particles. A physical picture of this process can be formed as follows. At the start of the KRÉL unit, an electron moving along the axis of the solenoid experiences toroidal drift and, consequently, moves away from the axis. In the middle of the KRÉL unit this drift reaches its largest value. As a consequence of the rotational transformation of the magnetic field lines, the particle drift changes its direction and the electrons start to approach the axis of the solenoid.[4] Such a particle drift effect is ensured by special design of the magnetic system. The electron beam in the region of station 3 approaches very close to the chamber wall. Near this station the curvature of the geometrical axis takes its maximum value, and the electron collector separates slightly from the wall. A portion of the beam falls into the gap thus formed and misses the collector. As the carriage moves further into the chamber, the axis of the device slopes more gently, the gap closes, and the fullest beam capture is regained. One peculiarity of curves *4* and *5* is that the direction of the current in the solenoid is different under the same conditions. This is the cause of the opposite direction of electron drift in the KRÉL.

It should be noted that the electron beam is shifted toward the local center of curvature of the geometrical axis of the system over the entire length of the chamber. This is clearly visible from the trace left by the beam in the collector: its larger part is found at electrode *1*, a small part at electrode *2*, and at electrode *3* no trace is seen at all (Fig. 3). This phenomenon illustrates the ability of a curvilinear magnetic field to shift the magnetic axis toward the local center of curvature of the geometrical axis.

COMPUTATIONAL STUDY OF THE PASSAGE OF AN ELECTRON BEAM THROUGH KRÉL

Under the conditions of our experiment, a monoenergetic electron beam propagates in a neutral gas at a pressure $p_0 = 1\times10^{-4} - 5\times10^{-4}$ Torr along a magnetic field $H = 350-700$ Oe in the equipotential space between metal walls; the entrance parameters of the beam are as follows: electron energy $U = 100-500$ eV, beam radius $R_0 = 0.4$ cm, and beam current $J = 0.1-1.0$ mA. The beam length $L = 34-148$ cm. As was shown in Ref. 5, when an electron beam with density

$$n_0 < n^* = \frac{v_i}{2L\sigma_i(u)u}, \tag{1}$$

propagates through a gas, where v_i is the mean velocity of the ions formed in the ionization of the gas by the beam electrons; u is the velocity of the beam electrons (in our case $u = 5.9\times10^8 - 1.3\times10^9$ cm/s); $\sigma_i(u)$ is the ionization cross section of the gas by the beam electrons, and the gas contains only fast electrons and the neutralizing ions.

The beam potential φ relative to the chamber walls, to which we assign the potential $\varphi = 0$, is negative. For $n_0 \geqslant n^*$ the beam will have positive potential relative to the walls and consist of three components: fast beam electrons with density n_1 (in our case $n_1 = 9.6\times10^5 - 2.1\times10^7$ cm^{-3}), ions with density n_i and temperature T_i, and slow (secondary) plasma electrons with density n_e and temperature T_e. Here, depending on the density and energy of the latter, two fundamentally different regimes of propagation of the beam in the gas are distinguished.

The first regime is observed when the density of the secondary electrons n_e is small in comparison with n_1. Here the main ionization channel of the gas is ionization by beam electrons.

The second regime is observed when the density of the secondary electrons is greater than or comparable to the density of beam electrons. When the beam interacts with such a plasma, a beam instability develops, and in the electromagnetic fields of the oscillations excited by the instability the plasma electrons heat up to ionization energies. As a result, collisions of the plasma electrons with the atoms of the neutral gas give rise to an avalanche breakdown process. This is the regime that is realized in our experiment.

Nezlin[5] gives a simplified treatment of the case when the rate of ion formation is greater than or equal to the rate of escape of ions through the end faces of the system for free spreading and the contribution to ionization of the gas by the secondary electrons is substantial (assuming that the electrons have a Maxwellian velocity distribution, and ignoring the energy removed by radiation and also the energy removed by plasma particles transverse to the magnetic field). He obtained

$$\frac{e\varphi}{T_e} = \frac{1}{2}\ln\left(\frac{e}{8\pi}\frac{m_i}{m_e}\right), \tag{2}$$

$$\gamma n_1 u \frac{m_e u^2}{2} = 2T_e n_e \ln\left(\frac{e}{8\pi}\frac{m_i}{m_e}\right)\sqrt{\frac{1}{e}\frac{T_e}{m_i}}, \tag{3}$$

where $e = 2.7\ldots$, e is the charge of the electron, m_e is its mass, m_i is the ion mass, and γ is the transformation coefficient of the beam energy into oscillations of the electromagnetic fields.

We determine n_e from the condition of electron balance in the beam

$$\frac{dn_e}{dt} = n_i(n_0 - n_e)\sigma_i(u)u + n_e(n_0 - n_e)\sigma_m \overline{v}_e e^{\frac{\varepsilon_i}{T_e}} - \alpha n_e^2 - 2n_e\sqrt{\frac{1}{e}\frac{T_e}{m_i}}\frac{1}{L}. \tag{4}$$

Here the first term on the right-hand side is the contribution to ionization of the gas by the electron beam, the second term is the contribution to ionization of the gas by secondary electrons (σ_m is the maximum ionization cross section of the gas, ε_i is the ionization energy, and

$$\overline{v}_e = \sqrt{\frac{8}{\pi}\frac{T_e}{m_e}}$$

is the mean velocity of the plasma electrons). The third term defines the loss of plasma electrons due to recombination (α is the recombination coefficient), and the fourth term defines the loss of electrons through the beam end face opposite to its entrance. In equilibrium $dn_e/dt = 0$. Thus, assuming that $n_e \ll n_0$ and ignoring recombination, we obtain

$$\frac{T_e}{\frac{m_e u^2}{2}} = \frac{\gamma}{\ln\left(\frac{e}{8\pi}\frac{m_i}{m_e}\right)}\left(\frac{1}{n_0\sigma_i(u)L} - \frac{1}{2}\frac{\sigma_m}{\sigma_i(u)}\sqrt{\frac{8e}{\pi}\frac{m_i}{m_e}}e^{\frac{\varepsilon_i}{T_e}}\right), \tag{5}$$

$$\frac{n_e}{n_i} = \frac{\gamma}{2\ln\left(\frac{e}{8\pi}\frac{m_i}{m_e}\right)}\frac{m_e u^2/2}{T_e}\frac{u}{\sqrt{\frac{1}{e}\frac{T_e}{m_i}}}. \tag{6}$$

Introducing the dimensionless quantities $x=\varepsilon_i/T_e$,

$$\xi=\frac{m_e u^2/2}{\varepsilon_i}, \quad a_0=\frac{\ln\left(\frac{e}{8\pi}\frac{m_i}{m_e}\right)}{\gamma},$$

$$b_0=\frac{1}{n_0\sigma_i(u)L}, \quad c_0=\frac{1}{2}\frac{\sigma_m}{\sigma_i(u)}\sqrt{\frac{8e}{\pi}\frac{m_i}{m_e}},$$

we can rewrite Eq. (5) in the form

$$\frac{a_0/\xi}{x}=b_0-c_0e^{-x}, \tag{7}$$

where b_0 and c_0 depend weakly on u.

It can be shown that if $a_0/\xi>0$, $b_0>0$, and $c_0>0$, Eq. (7) will always have a unique solution for $x>0$. In our case $(m_e u^2)/2=100-500$ eV, $L=100$ cm, $n_0=3.2\times10^{12}-1.6\times10^{13}$ cm^{-3}, $\sigma_i(u)\approx\sigma_m\approx10^{-16}$ cm^2, $\varepsilon_i\approx20$ eV, for air $m_i/m_e\approx5.32\times10^4$,

$$\ln\left(\frac{e}{8\pi}\frac{m_i}{m_e}\right)\approx8.65, \quad \sqrt{\frac{8e}{\pi}\frac{m_i}{m_e}}\approx6.05\times10^2.$$

According to Ref. 5, the fraction of energy transferred by the beam lies within the limits 1/3 to 3/4 (depending on the geometry of the problem), and is equally distributed between the thermal energy of the plasma electrons and the electrostatic energy of the oscillations. Following Ref. 5, we set $\gamma=1/4$. Then $\xi=5-25$, $a_0=34.6$, $b_0=6.25-31.25$, $c_0=302.5$. Solving Eq. (7), we obtain $x_0\approx2.29-4.18$. Thus, in the steady-state regime $T_e\approx4.8-8.7$ eV; hence from formulas (2) and (6) we find that $n_e\approx7.0\times10^8$ cm^{-3} and $e\varphi\approx21-38$ eV. The calculated values of T_e and n_e agree with the corresponding experimentally measured values, which makes it possible to use this simple model in further calculations.

The theory we use here[5] ignores the influence of the radial electric field on the motion of the electron beam. We assume that to first order it is similar to the field of a straight, uniformly charged (with density ρ) cylinder of radius R_0, i.e.,

$$\mathbf{E}=E_r(r)\mathbf{e}_r=2\pi\rho\mathbf{e}_r\begin{cases} r\to0\leqslant r<R_0, \\ \dfrac{R_0^2}{r}\to r\geqslant R_0, \end{cases} \tag{8}$$

where r is the distance from the axis of the cylinder.

On the basis of a program which calculates the motion of an electron in the KRÉL magnetic field by a third-order Runge–Kutta method, where the KRÉL unit is modeled by a field of 40 thin current rings of radius $a=3.75$ cm, uniformly spaced along the KRÉL axis of length 178 cm, we created a program which calculates the trajectory of the center of the beam from the trajectories of four electrons starting from the points $(n=R_0,\ b=0)$, $(n=-R_0,\ b=0)$, $(n=0,\ b=R_0)$, and $(n=0,\ b=-R_0)$ in the cross section of the fourth loop (start of the equilibrium segment) and moving in the space-charge field of the beam. Here **n** is the normal and **b** is the binormal to the geometrical axis of the system. The beam potential has the form [recall that the potential of the walls is taken to be equal to zero, $\varphi(a)=0$]

$$\varphi(r)=\pi\rho R_0^2\begin{cases} 1+2\ln\left(\dfrac{a}{R_0}\right)-\dfrac{r^2}{R_0^2}\to0\leqslant r<R_0, \\ 2\ln\left(\dfrac{a}{r}\right)\to R_0\leqslant r\leqslant a. \end{cases} \tag{9}$$

Thus, the potential on the beam axis relative to the chamber

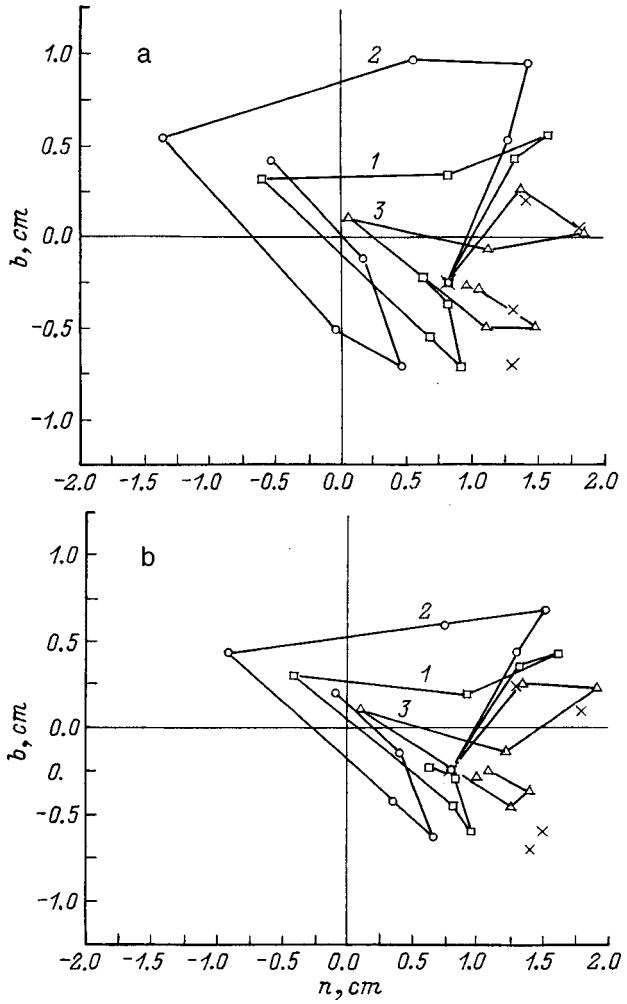

FIG. 5. Electron beam trajectories in (**nb**) coordinates for $\rho=0$ (*1*), $-5\times10^7|e|$ (*2*), $+5\times10^7|e|$ (*3*), and experimentally determined beam traces (denoted by crosses) for beam current $J=0.3$ mA, beam radius $R_0=0.4$ cm, for $U=300$ eV and $H=350$ (a), 525 (b).

$$\delta\varphi = \pi\rho R_0^2\left(1 + 2\ln\left(\frac{a}{R_0}\right)\right). \quad (10)$$

Figure 5a and b displays typical electron beam trajectories, calculated in (nb) coordinates for $\rho = 0$ (curve *1*), $-5\times10^7|e|$ (curve *2*), $+5\times10^7|e|$ (curve *3*), and also experimentally determined beam traces (denoted in the figures by crosses) at four measurement stations ($L_1 = 34$ cm, $L_2 = 52$ cm, $L_3 = 106$ cm, $L_4 = 124$ cm, where L is the distance along the KRÉL axis, reckoned from the entrance to the electron beam system). From a comparison of the experimental data with the calculated trajectories, it is possible to conclude that a plasma–beam discharge is observed in the experiments having positive equilibrium potential $\varphi \approx 20$ V. Hence, from formulas (2) and (6) we find that $T_e \approx 4.6$ eV and $n_e \approx 1.5\times10^{10}$ cm^{-3}, which agree with the values of T_e and n_e measured experimentally by the probe technique.

CONCLUSION

The experimental studies reported here of a plasma–beam discharge in the magnetic field of the three-dimensional solenoid of the KRÉL unit show that a Maxwellian electron velocity distribution is observed in the plasma formed in this device. Using the method of probe measurements, we have determined the ion density at the end of the curvilinear part of the chamber $n_i \approx 8\times10^8 - 10^{10}$ cm^{-3} and the electron temperature $T_e \approx 4 - 15$ eV. The plasma has a positive equilibrium potential $\varphi \approx +(15 - 25)$ eV relative to the walls.

The simplified model of propagation of an electron beam in a gas in the stationary regime proposed in Ref. 5 is applicable to the conditions of our experiment. It gives good agreement, which justifies its use in further calculations.

We have computationally modeled the motion of an electron beam with allowance for the space charge created by the beam and the secondary plasma for various values of the electron energy U, magnetic field H, and equilibrium potential φ. From a comparison of experimentally measured trajectories with the calculated ones for different values of the space charge we have obtained an estimate for the unneutralized ion density of 5×10^7 cm^{-3}, which corresponds to a secondary electron temperature of around 5 eV and a secondary electron density of 10^{10} cm^{-3}.

This work was supported by the Russian Fund for Fundamental Research (Project No. 94-02-05596a).

[1] V. M. Glagolev, B. B. Kadomtsev, V. D. Shafranov, and B. A. Trubnikov, *Tenth European Conference on Continuous Fusion and Plasma Physics*, Moscow, 1982, p. E-8.
[2] A. V. Dobryakov, S. F. Perelygin, and B. A. Trubnikov, Inventor's Certificate No. 1071137 (USSR); pub. Byull. Izobret., No. 23 (1988).
[3] S. F. Perelygin, Prib. Tekh. Eksp., No. 6, 165 (1992).
[4] S. F. Perelygin and V. M. Smirnov, Fiz. Plazmy **17**, 945 (1991) [Sov. J. Plasma Phys. **17**, 551 (1991)].
[5] V. M. Nezlin, *Dynamics of Beams in Plasma* [in Russian], Énergoizdat, Moscow, 1982, pp. 75–80.

Translated by Paul F. Schippnick

Phase transformations induced by mechanical stresses in powders of oxide solid solutions

V. M. Timchenko, G. Ya. Akimov, and N. G. Labinskaya

Donetsk Physicotechnical Institute, Ukrainian National Academy of Sciences, 340114 Donetsk, Ukraine
(Submitted April 29, 1997; resubmitted March 20, 1998)
Zh. Tekh. Fiz. **69**, 27–31 (February 1999)

The influence of cold isostatic pressing to 2.0 GPa on the phase transformations in powders of ZrO_2-Y_2O_3 solid solutions and γ-Al_2O_3 is investigated. The cold isostatic pressing of ZrO_2-Y_2O_3 is shown to lead to conversion of the tetragonal modification into a monoclinic phase. The extent of conversion decreases as the Y_2O_3 content and the particle size increase. In the case of γ-Al_2O_3 powders, cold isostatic pressing at 1.5 GPa leads to lowering of the temperature at which the α phase appears by 100 K in comparison to a γ-Al_2O_3 powder subjected to cold isostatic pressing at 0.1 GPa. A quantitative model, which accounts for the experimental results discovered, is proposed.
[S1063-7842(99)00602-9]

1. INTRODUCTION

It is known that phase transformations can be initiated in crystals by mechanical action.[1,2] One standard method for applying mechanical action to crystal particles is treatment in mills of various kinds.[3] An alternative method is cold isostatic pressing, during which self-deformation of the particles takes place according to scribing, self-indentation, compression, twisting, bending, and other mechanisms. These self-deformation processes are accompanied by a temperature increase in the contact zone. Cold isostatic pressing is the most effective method of mechanical treatment, since the pressure can reach many gigapascals and acts on the system being pressed uniformly in all directions.[4]

The present work is devoted to an investigation of the influence of cold isostatic pressing on phase transformations in powders of ZrO_2-Y_2O_3 solid solutions and γ-Al_2O_3.

2. STARTING MATERIALS AND EXPERIMENTAL METHOD

The starting materials used were powders of ZrO_2-Y_2O_3 solid solutions containing 3 or 6 wt% Y_2O_3, which were obtained by coprecipitation of the hydroxides from aqueous solutions of the salts followed by annealing for 1 h at 1000 °C, by the sol-gel method with annealing for 1 h at 800 °C, and by plasma-chemical synthesis followed by annealing for 1 h at 1000 °C. The γ-Al_2O_3 powders were obtained by annealing aluminum hydroxide at 1000 °C.

The cold isostatic pressing was carried out in a UVD-1 laboratory press. The residence time of the powders under high-pressure conditions was 1−3 min. Pressing pressures from 0.1 to 2.0 GPa were used. After cold isostatic pressing, the powdered compacts were removed from the latex shells used to eliminate contact between the powder and the liquid conveying the pressure and ground by a diamond disk. The samples of the ZrO_2-Y_2O_3 solid solutions were not processed further. Some of the γ-Al_2O_3 samples were annealed for 20 min at temperatures from 900 to 1600 °C (V. V. Storozh and I. V. Gorelik participated in some of the experiments with γ-Al_2O_3). The samples were placed in a preheated oven.[5]

The phase transformations were investigated by x-ray powder diffraction analysis of compacts after cold isostatic pressing and, in the case of Al_2O_3, after annealing. The powder diffraction investigations were performed on a DRON-3M diffractometer using Cu K_α radiation. A quantitative powder diffraction analysis of the ZrO_2-Y_2O_3 solid solutions was performed according to the method described in Ref. 6.

3. RESULTS AND DISCUSSION

Figure 1 presents the dependence of the content of the monoclinic phase of the ZrO_2-Y_2O_3 solid solutions on pressing pressure. Raising the pressing pressure leads to an increase in the extent of conversion. In addition, the extent of conversion increases as the Y_2O_3 content and the annealing temperature are lowered.

Figure 2 presents the dependence of the areas of the x-ray peaks of α-Al_2O_3 samples treated by cold isostatic pressing at 0.1 and 1.5 GPa on annealing temperature. It is seen that the temperature at which the α phase appears decreases by 100 K when the pressing pressure is increased.

At normal pressure the monoclinic phase of pure ZrO_2 is stable up to 1170−1200 °C, and the tetragonal phase is stable from 1200 to 2300 °C.[7,8] The tetragonal phase can become stable at room temperature when the crystal size is diminished,[9] solid solutions are formed,[7,8] and the external pressure is raised to a high level (in the range 4.0 −12.0 GPa, according to different data[7]).

Since two factors which raise the stability of the tetragonal phase, viz., a small crystal size, which is equal to 300 −1000 Å (Ref. 10), and the formation of a solid solution, act simultaneously in the present case, the tetragonal phase of the ZrO_2-Y_2O_3 solid solutions should be considered thermodynamically stable. Then, to effect the tetragonal-

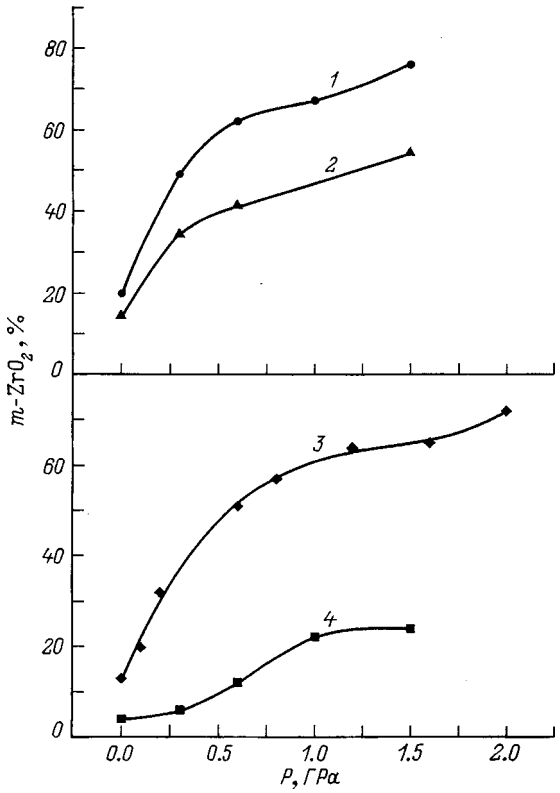

FIG. 1. Dependence of the content of the monoclinic phase (m-ZrO_2) in compacts of powders of ZrO_2-Y_2O_3 solid solutions on preliminary cold isostatic pressing pressure: *1* — ZrO_2-3 wt % Y_2O_3, coprecipitation, annealing for 1 h at 1000 °C; *2* — ZrO_2-3 wt % Y_2O_3, plasma-chemical synthesis followed by annealing for 1 h at 1000 °C; *3* — ZrO_2-6 wt % Y_2O_3, sol-gel method, annealing for 1 h at 800 °C; *4* — ZrO_2-6 wt % Y_2O_3, coprecipitation, annealing for 1 h at 1000 °C.

monoclinic transformation it is first necessary to bring each crystal into a metastable state, for example, by removing the oxide stabilizer from the bulk of the crystal (an increase in crystal size during cold isostatic pressing is a virtually impossible process).

The alternative, i.e., the assumption that the tetragonal phase of the solid solution is metastable, is incorrect, since it precludes explaining the increase in the extent of conversion

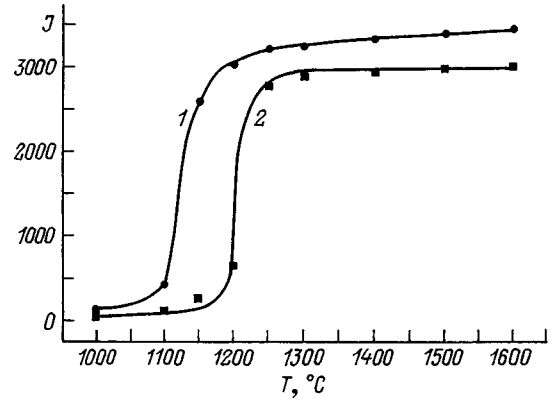

FIG. 2. Dependence of the integrated intensity of x-ray reflections of α-Al_2O_3 on the annealing temperature of the γ-Al_2O_3 powders: *1* — preliminarily cold isostatic pressing at 1.5 GPa, *2* — 0.1 GPa.

with decreasing annealing temperature, i.e., decreasing crystal size, since a smaller crystal size corresponds to greater stability of the tetragonal phase.

A decrease in the amount of Y_2O_3 in the bulk of a crystal can occur during the cold isostatic pressing of a powder of a ZrO_2-Y_2O_3 solid solution as a result of the diffusion of Y^{3+} ions from the bulk of the crystal to the surface or the redistribution of Y^{3+} ions in the bulk of the crystal under the action of a mechanical stress. Such a process is similar to some extent to the Gorsky effect discovered in 1934.[11]

Let us estimate the probability of the diffusion Y^{3+} ions in a crystal of a ZrO_2-Y_2O_3 solution during elastic deformation. For this purpose we must solve the Wagner equation,[12] which expresses the flux of diffusing particles in the field of an electrochemical potential

$$J_k = -\frac{K_k}{q_k^2}(\nabla \mu_k + q_k \nabla \varphi), \tag{1}$$

where J_k is the flux of particles of species k, K_k is the partial specific conductance, q_k is the charge carrier density, and μ_k and φ are, respectively, the chemical and electric potentials.

The quantity K_k, in turn, can be expressed in the following manner:

$$K_k = \gamma\left(\frac{N_k \cdot q_k^2}{kT}\right) \cdot c_k(1-c) z_k a^2 \nu_0 \exp\left(\frac{\Delta S}{k}\right) \times \exp\left(-\frac{E_m}{kT}\right)(\nabla \mu_k + q_k \nabla \varphi), \tag{2}$$

where γ is the geometric correlation coefficient, N_k is the number of particles of species k per unit volume, k is the Boltzmann constant, T is the temperature, c_k is the atomic fraction of particles of species k in the intrinsic sublattice, $(1-c)z_k$ corresponds to the number of free sites, i.e., z_k is the coordination number of the particles of species k in the intrinsic sublattice, $(1-c)$ corresponds to the relative concentration of vacancies in sublattice k, a is the jump length, ν_0 is the vibrational frequency of the particles in lattice sites, ΔS is the entropy change upon diffusion, and E_m is the activation energy for diffusion (the activation energy for vacancy migration).

With consideration of (2), the Wagner equation (1) can be written in the following manner:

$$J_k = -\gamma \frac{N_k}{kT} c_k c_v z_k a^2 \nu_0 \exp\left(\frac{\Delta S}{k}\right) \times \exp\left(-\frac{E_m}{kT}\right)(\nabla \mu_k + q_k \nabla \varphi), \tag{3}$$

where c_v is the relative concentration of vacancies in sublattice k.

Let the crystal be deformed by bending. Then a compressive stress $+\sigma_0$ acts on one of the surfaces of the crystal, and a tensile stress $-\sigma_0$ acts on the opposite surface. If we apply the linear approximation of the theory of elasticity and assume that the stress varies linearly across the thickness of the crystal, we obtain

$$\nabla \mu_k = \frac{kT}{N_k}\frac{\partial N_k}{\partial x} + \frac{2V\sigma_0^2}{Er}\left(\frac{2x}{r} - 1\right), \tag{4}$$

where V is the volume, E is Young's modulus, r is the linear dimension of the crystal, and x is the coordinate, which varies from 0 to r.

We assume that

$$\frac{kT}{N_k}\frac{\partial N_k}{\partial x} \ll \frac{2V\sigma_0^2}{Er}\left(\frac{2x}{r} - 1\right)$$

(we presume that the components are distributed uniformly in the original crystal). Then (3) is written as

$$J_k = -\gamma\frac{N_k}{kT}c_k c_v z_k a^2 \nu_0 \exp\left(\frac{\Delta S}{k}\right) \times \exp\left(-\frac{E_m}{kT}\right)\frac{2V\sigma_0^2}{Er}\left(\frac{2x}{r} - 1\right). \tag{5}$$

Plugging the values[13] of the quantities appearing in Eq. (5) into this equation and performing the calculations, we find that sufficient values for the fluxes of the intrinsic cations appear only at temperatures exceeding 500 °C.

Now, let us consider to what extent the values of the fluxes vary in response to the diffusion of Y^{3+} impurity ions. On the basis of (5), c_k and E_m should vary. The value of c_k is uniquely specified by the composition of the solid solution. To calculate the values of E_m, we examine the crystal structure and determine how elementary acts of diffusion occur for Y^{4+} and Y^{3+} ions in ZrO_2. For simplicity, we assume that ZrO_2 has a cubic crystal lattice [the tetragonality equals 1.016 (Refs. 7)] with a structure of the sphalerite (CaF_2) type[8] and a unit-cell parameter equal to 5.08 Å.[7] The ionic radii of oxygen, zirconium, and yttrium, according to Belov and Bokiĭ[14] with the corrections given by Zachariasen and Pauling[15] for the coordination number and valence are $r_{O^{2-}} = 1.286$ Å, $r_{Zr^{4+}} = 0.844$ Å, and $r_{Y^{3+}} = 0.998$ Å. On the basis of the structure of ZrO_2, migration of a Zr^{4+} cation first into an interstitial position of the intrinsic sublattice followed by passage into a regular vacant lattice site should be regarded as the most likely mechanism for the diffusion of these ions (Fig. 3).

The activation energy for diffusion is most probably the sum of two components, viz., a mechanical component, which is associated with deformation of the local environment of the diffusing ion upon formation of the activated state, and an electrostatic component, which is associated with the alteration of the electrostatic interaction of the diffusing ion with its environment in the activated state in comparison to the original state.

The minimum length of the diagonal of an oxygen square deformed by a Zr^{4+} ion upon the formation of the activated state is 4.26 Å. The length of the diagonal of an oxygen square in the absence of such deformation is 3.59 Å. Therefore, the strain of the oxygen square accompanying the formation of the activated state is $\varepsilon = 0.1866295$ Å. For simplicity, we shall assume that the deformed volume is a square prism with a height equal to the diameter of an oxygen ion and with a length of a side of the base equal to $2.54\cdot(1+\varepsilon)$ Å, where ε is the strain, which varies from 0 to 0.1866295. Performing the necessary calculations, we find that the value of the mechanical component of the activation energy for the diffusion of cations in ZrO_2 is at least 46.3 kJ/mol.

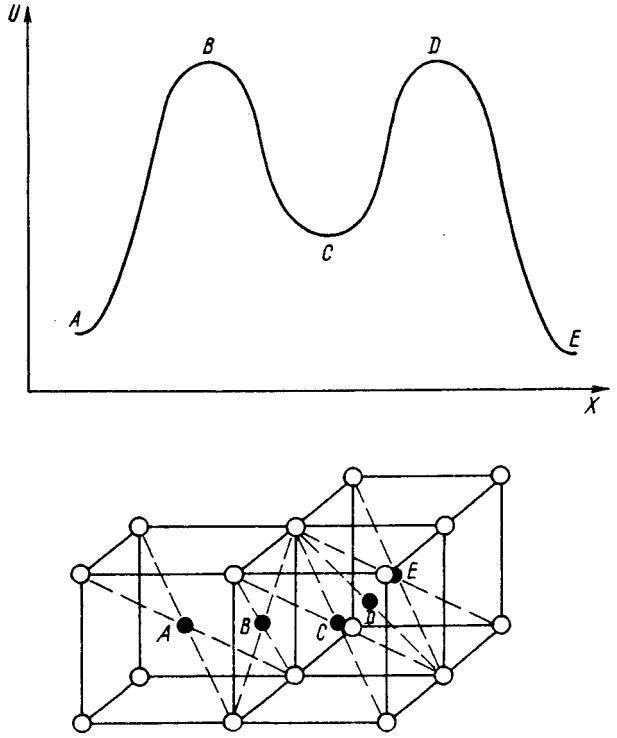

FIG. 3. Proposed dependence of the energy of the system on reaction coordinate for the diffusion of an intrinsic ion (Zr^{4+}) and positions of the diffusing ion corresponding to extremum energy values in the ZrO_2 crystal lattice.

When Zr^{4+} ions are replaced by Y^{3+} ions in ZrO_2, one oxygen vacancy appears for every two Y^{3+} ions to conserve the electroneutrality of the crystal.[11] It follows from the requirement for electroneutrality of any microvolume in the crystal that the vacancies must be located near the Y^{3+} ions. In the limit, the oxygen vacancy is located in the first coordination sphere of one of the two Y^{3+} ions.[16]

As a result of such formation of Y^{3+}–oxygen-vacancy clusters, the activated state for the diffusion of Y^{3+} will most probably correspond to the positioning of a Y^{3+} ion in an intrinsic first coordination sphere (the Y^{3+} ion occupies the site of the missing oxygen ion; see Fig. 4). Since the radius of Y^{3+} is smaller than the radius of O^{2-}, the mechanical component of the activation energy is equal to zero, and, therefore, the value of the activation energy will be reduced by 46 kJ/mol in comparison to the activation energy for self-diffusion. As a result, the values of the Y^{3+} fluxes are 2 $-$ 3 orders of magnitude greater than the values of the fluxes of the intrinsic Zr^{4+} ions (at 500 $-$ 700 °C).

Significant ion fluxes can be expected only at temperatures exceeding 500 °C. The temperature of the ZrO_2-Y_2O_3 powders can rise for several reasons. First, the cold isostatic pressing of powders is accompanied by friction processes, which can raise the temperature by many hundreds of degrees.[3,17] Second, the phase transformation to the monoclinic phase occurs with a high rate; therefore, conversion of

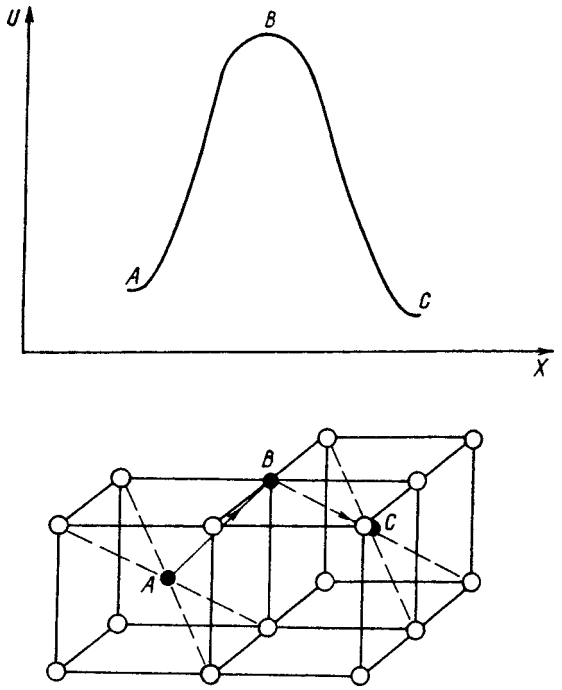

FIG. 4. Proposed dependence of the energy of the system on reaction coordinate for the diffusion of an impurity ion (Y^{3+}) and positions of the diffusing ion corresponding to extremum energy values in the ZrO_2 crystal lattice.

the enthalpy of the phase transformation into thermal energy should cause a large increase in the temperature of the material. The corresponding temperature increase for ZrO_2 amounts to 250 K,[13] i.e., when ZrO_2-Y_2O_3 powders are subjected to cold isostatic pressing, the temperature can easily reach 500 °C or more, especially on the contacts.[3,17]

The estimates given (the necessity of heating to 500 °C) are valid provided only elastic deformation of the crystals occurs during cold isostatic pressing. If dislocation multiplication and motion also take place during cold isostatic pressing, they can only facilitate the phase transformation. Taking into account the high value of the temperature and the mechanical stress, as well as the plastic properties of the tetragonal phase of ZrO_2,[18] we can expect a high mobility for dislocations in the crystals. A moving dislocation will be stopped when it encounters a Y^{3+} ion along its path. Being in the region of a dislocation core, the Y^{3+} ion can diffuse along the dislocation tube to the surface of the crystal. If, on the other hand, the Y^{3+} ion remains in the region of the dislocation core in the bulk of the crystal, its mechanical effect on the crystal structure, i.e., its stabilization of the tetragonal phase of ZrO_2, can decrease significantly or vanish entirely. Therefore, when dislocation motion and multiplication occur, the phase transformation becomes possible even at considerably smaller cation fluxes (for example, a small increase in the temperature of the crystal is sufficient for the transformation).

Under the proposed mechanism for the phase transformation, the step limiting the entire process is the diffusive removal of Y^{3+} ions from the bulk of the crystal, which leads to the transition of the tetragonal phase of the solid solution into a metastable state. According to (5), the diffusion of Y^{3+} ions becomes more efficient as the size of the crystals decreases, as is manifested by the increase in the extent of conversion as the annealing temperature is lowered (Fig. 1). On the other hand, such diffusive removal of these ions is most probably efficient when their content is $\sim$5 at. % (compare the extent of conversion in Fig. 1 for ZrO_2-Y_2O_3 solid solutions containing 3 and 6 wt % Y_2O_3).

With respect to the phase transformations of Al_2O_3, γ-Al_2O_3 has a spinel structural type (in which the Al^{3+} ions have coordination numbers equal to 4 and 6), while in the α and θ modifications of Al_2O_3 the coordination number of Al^{3+} equals 6 (Ref. 5). Since, according to the available data,[5] there is still no certainty regarding the filling order of Al^{3+} ions in the structure of γ-Al_2O_3, i.e., for transformation of the γ modification of Al_2O_3 into the θ or α phase, from 25 to 37.5% of the Al^{3+} ions must change their coordination number. On the one hand, such a percentage is excessively high, and, on the other hand, the Al^{3+} ions are intrinsic ions, rather than heterovalent substitutional ions. As a result, only the formation of nuclei or even potential nuclei of the α phase of Al_2O_3 takes place upon the self-deformation of γ-Al_2O_3 during cold isostatic pressing.

4. CONCLUSION

It has been shown experimentally that the self-deformation occurring during the cold isostatic pressing of ultradispersed powders of ZrO_2-Y_2O_3 solid solutions leads to the tetragonal-monoclinic transformation. The extent of conversion decreases with increasing Y_2O_3 content and crystal size.

The cold isostatic pressing of γ-Al_2O_3 powders leads to lowering of the temperature of the $\gamma \rightarrow \alpha$ transformation by 100 K.

A quantitative model, which attributes the phase transformation to the diffusion of ions in a field of mechanical stresses, has been proposed. It has been shown that the diffusion of heterovalent substitutional ions proceeds more easily (with a smaller value of the activation energy) than that of the intrinsic ions.

We thank V. G. Vereshchak for the γ-Al_2O_3 powders supplied, which were obtained by the sol-gel method and plasma-chemical synthesis, A. G. Belous for the γ-Al_2O_3 powders obtained by coprecipitation, and I. M. Belov for Al_2O_3 powders, as well as I. Yu. Prokhorov for a constructive remark.

[1] F. P. Bowden and A. D. Yoffe, *Fast Reactions in Solids*, Academic Press, New York (1958); IL, Moscow (1962), 244 pp.
[2] V. B. Brik, *Diffusion and Phase Transformations in Metals and Alloys* [in Russian], Naukova Dumka, Kiev (1985), 232 pp.
[3] E. G. Avvakumov, *Mechanical Methods for Activating Chemical Processes* [in Russian], Novosibirsk, Nauka (1986), 305 pp.
[4] G. Ya. Akimov, Fiz. Tverd. Tela (St. Petersburg) **38**, 654 (1996) [Phys. Solid State **38**, 364 (1996)].
[5] V. V. Storozh, G. Ya. Akimov, I. V. Gorelik, and N. G. Labinskaya, Zh. Tekh. Fiz. **66**(9), 86 (1996) [Tech. Phys. **41**, 905 (1996)].
[6] H. K. Schmid, J. Am. Ceram. Soc. **70**, 367 (1987).
[7] V. N. Strekalovskiĭ, Yu. M. Polezhaev, and S. F. Pal'guev, *Oxides with Impurity Disorder: Composition, Structure, and Phase Transformations* [in Russian], Nauka, Moscow (1987), 160 pp.
[8] M. Rühle and A. G. Evans, Prog. Mater. Sci. **33**, 85 (1989).

[9] J. E. Bailey, D. Lewis, Z. M. Librant, and L. J. Porter, Trans. J. Br. Ceram. Soc. **71**, 25 (1972).
[10] E. Bernstein, M. G. Blanchin, R. Ravelle-Chapuis, and J. Rodrigues-Carvajal, J. Mater. Sci. **27**, 6519 (1992).
[11] L. A. Shuvalov, A. A. Urusovskaya, I. S. Zheludev *et al.*, *Modern Crystallography*, Vol. 4 [in Russian], Nauka, Moscow (1981), 495 pp.
[12] V. N. Chebotin, *Chemical Diffusion in Solids* [in Russian], Nauka, Moscow (1989), 208 pp.
[13] R. A. Andrievskiĭ and I. I. Spivak, *Strength of Refractory Compounds and Materials Based on Them* [in Russian], Metallurgiya, Chelyabinsk (1989), 368 pp.
[14] V. A. Rabinovich and Z. Ya. Khavin, *Concise Chemical Handbook* [in Russian], Khimiya, Leningrad (1978), 392 pp.
[15] *Handbook of X-Ray Structural Analysis* [in Russian], edited by A. I. Kitaĭgorodskiĭ, Gostekhizdat, Moscow–Leningrad (1940), 316 pp.
[16] N. B. Hannay, *Solid State Chemistry*, Prentice-Hall, Englewood Cliffs, N. J. (1967); Mir, Moscow (1971), 244 pp.
[17] O. V. Klyavin, *Physics of the Plasticity of Crystals at Helium Temperatures* [in Russian], Nauka, Moscow (1987), 256 pp.
[18] J. Lankford, J. Am. Ceram. Soc. **66**(11), C-212 (1983).

Translated by P. Shelnitz

Complete reorganization of the mode structure of the wave function of a channeled electron in a crystal with a superlattice

T. A. Bobrova and L. I. Ognev

Kurchatov Institute Russian Scientific Center, 123182 Moscow, Russia
(Submitted July 17, 1997)
Zh. Tekh. Fiz. **69**, 32–37 (February 1999)

The dynamics of relativistic electrons subjected to planar channeling in distorted crystals is investigated using step-by-step numerical integration of the Schrödinger equation. It is shown that periodic distortion of a planar channel (the formation of a ''superlattice'') can cause complete reorganization of the mode structure of the wave function. In the limit of weak perturbations of the crystal lattice, the simulation results are consistent with the analytical results from perturbation theory. The position of each line in the spontaneous emission spectrum in the case of resonant distortions depends on the length of the superlattice period. © *1999 American Institute of Physics.* [S1063-7842(99)00702-3]

1. INTRODUCTION

The channeling of relativistic charged particles in single crystals has been the subject of numerous theoretical and experimental studies, which were reviewed in Refs. 1–3, and continues to arouse the interest of investigators.[4–6] Some experimental results cannot be interpreted within the existing theories of the channeling of relativistic electrons and channeling radiation.[1–3] Such phenomena include the weak orientational dependence of the bremsstrahlung and induced radioactivity in single-crystal targets subjected to irradiation by a low-divergence beam of relativistic electrons.[7] Channeling should lead to an increase in the yield of nuclear reactions and bremsstrahlung, but no orientational dependence of these phenomena was detected in experiments on the axial channeling of 50-MeV electrons[7] and the planar channeling of electrons with energies of 28–104 MeV.[8] On the other hand, the generation of radiation has been detected during channeling,[8] indicating the occurrence of electron channeling. In experiments with a silicon single crystal doped with 1% chromium, the appearance of an unidentified strong line of x radiation was noted in the case of axial channeling, while the high-energy lines vanished.[4] These effects can be caused both by the instability of the motion of channeled electrons in real crystals and by the initial evolution of the electron beam in the near-surface region, where the mode structure of the electronic wave functions has not yet been shaped. As follows from the results of the investigation of the influence of defects in the form of crystal-plane displacements,[9] such defects can lead to significant distortion of the initial population of states for transverse electron motion. The treatment of channeling and the emission of radiation during channeling in crystals with periodic strains as in a strained-layer ''superlattice'' is noteworthy. The appearance of such strains is often observed during the fabrication of various multilayer semiconductor crystal structures by molecular epitaxy (see, for example, Ref. 10). The radiation of electrons during axial channeling in crystals with a ''superlattice'' was previously treated by theoretical methods in Ref. 11 for small perturbations of the crystal. The two-wave approximation was used in the theoretical treatment of electron channeling in Ref. 11, and it was shown that in the resonance case, in which the difference between the two energy levels of transverse motion is a multiple of $2\pi\hbar c/T$ (T is the superlattice period), splitting of the total electron energy spectrum occurs. The degeneracy with respect to the longitudinal electron momentum is then removed.

The main purpose of this work was to study the influence of periodic deformation of the channel, which simulates a strained-layer superlattice, on the dynamics of the bound states of 5-MeV electrons during planar channeling in a Si(110) crystal without the explicit use of the mode approximation for the wave functions and simplifications (which are unavoidably inherent to analytical methods), such as the two-wave approximation, neglect of variations in the form of the averaged potential, confinement of the range of parameters considered, etc.

2. THEORY

The motion of a relativistic particle in a potential $V(z,r)$ can be described by an equation resembling the Schrödinger equation.[12] For the amplitude $\psi(z,r)$ of the wave function

$$\Psi(z,r)=\psi(z,r)\exp(ik_z z),$$

of an electron moving at a small angle to the $0z$ axis such that $k_z \approx |k|$, this equation has the form

$$2ik_z \partial\psi/\partial z+\Delta_\perp \psi=k_z^2 V'(z,\mathbf{r})\psi(z,\mathbf{r}). \quad (1)$$

Here k is the wave vector of the electron; $V'(z,\mathbf{r})=V(z,\mathbf{r})2\gamma m_0/(\hbar^2 k_z^2)$, where $\mathbf{r}=(x,y)$ denotes the transverse coordinates; m_0 is the electron rest mass; and γ is the Lorentz factor.

It was assumed during the derivation of (1) that

$$|\partial^2\psi/\partial z^2| \ll k_z|\partial\psi/\partial z|.$$

We shall henceforth assume that the potential fluctuations δV have a Gaussian distribution and are δ-correlated

along the direction of motion of the electron. Then, after averaging (1) over the fluctuation statistics for the amplitude $\langle\psi\rangle$, we have the (Dyson) equation

$$2ik_z\partial\langle\psi\rangle/\partial z+\Delta_\perp\langle\psi\rangle-k_z^2\langle V'(z,\mathbf{r})\rangle\langle\psi\rangle-ik_z^2V''(\mathbf{r})\langle\psi\rangle=0,$$

$$\psi(r,z=0)=\psi_0(r), \tag{2}$$

where

$$V''(r)=\frac{k_z}{4}\int_{-\infty}^{+\infty}\langle\delta V'(0,\mathbf{r})\,\delta V'(z,\mathbf{r})\rangle\,dz.$$

Equation (2) describes the coherent component of the wave function without consideration of nuclear recoil. A detailed discussion of the physical aspects of the approximations made, as well as a calculation of the imaginary part of the potential $V''(\mathbf{r})$ can be found in Ref. 13.

Let an electron impinge on a single crystal at a small angle to several crystal planes. Then the complex potential $V'+iV''$ can be averaged along crystal planes. In this case the dependence on the transverse coordinate y in Eq. (2) vanishes, and its numerical solution is simplified significantly.

The numerical method for solving Eq. (2), which was previously employed to study the motion of channeled electrons in ideal single crystals[14,15] and the reflection of positrons from an oblique single-crystal cut,[16] calls for the step-by-step calculation of the transverse wave function $\psi(x,z)$ on the basis of its initial value at $z=0$.

When an electronic wave propagates along the z axis, the transverse wave function $\psi(x,z)$ undergoes oscillations at a fixed value of x:

$$\psi(x,z)\sim\exp(iE_nz/(\hbar c)),$$

where $\{E_n\}$ is the set of eigenvalues of the transverse energy of motion of the electron.

Hence it is seen that the spectrum of transverse energies can be obtained by taking the Fourier transform of $\psi(x,z)$ with respect to the coordinate z and then integrating the spectrum over the channel width.

3. CALCULATION RESULTS

A crystal superlattice was simulated by a series of crystal-plane displacements (each of which did not exceed 1/32 of the interplanar distance) in accordance with the formula $U(x,z)=U_0(x+a\sin(2\pi z/T))$. Here T is the superlattice period, and a is the displacement amplitude, the value of a being taken in the range from 1/32 to 5/32 of the interplanar distance. Thus, there were from 2 to 10 crystal-plane displacements per lattice period. The case of a nondivergent electronic plane wave with an energy of 4.5 MeV impinging on the crystal surface at a zero angle to the channeling plane was considered.

Channeled 4.5-MeV electrons in the planar potential of a Si(110) crystal have two bound states with the transverse energies $E_0=8.41$ eV and $E_1=19.2$ eV, and the third (above-barrier) level has the energy $E_2=21.6$ eV. The depth of the potential well $U_0=21.22$ eV. The value $z_0=2\pi\hbar c/(E_1-E_0)\simeq1160$ Å can be taken as the characteristic length of the phase fluctuations. The values of a and T were chosen so that the maximum angle of inclination of a bent channel relative to the Z axis would not exceed the Lindhard angle. Figures 1–3 present the spectra for three different values of T: in the first case $T\gg z_0$, in the second case $T\sim z_0$, and in the third case $T<z_0$. The deformation amplitude was taken equal to $a=3/32$. Figure 4 presents the wave eigenfunctions corresponding to Fig. 2. The depen-

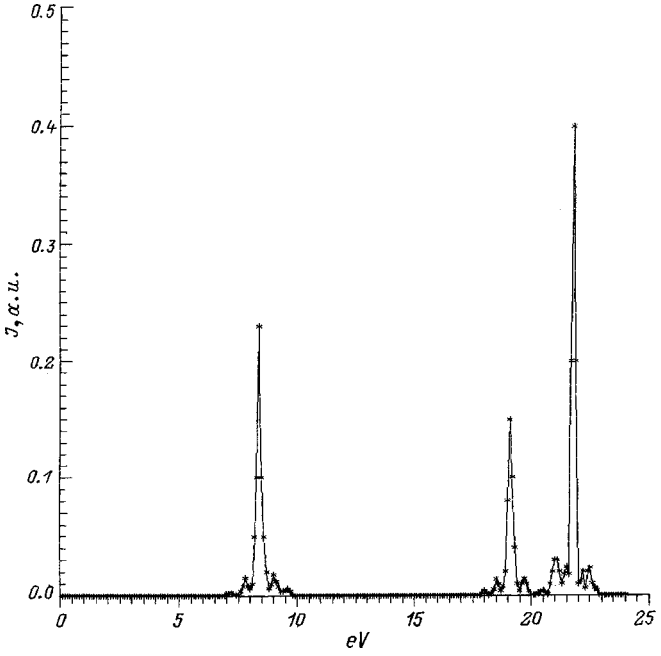

FIG. 1. Spectrum of transverse electron energies for a planar-channel distortion period $T=22\,000$ Å. The distortion amplitude $a=3/32d_0$, and the depth of the potential well of the undistorted channel $U_0=21.22$ eV.

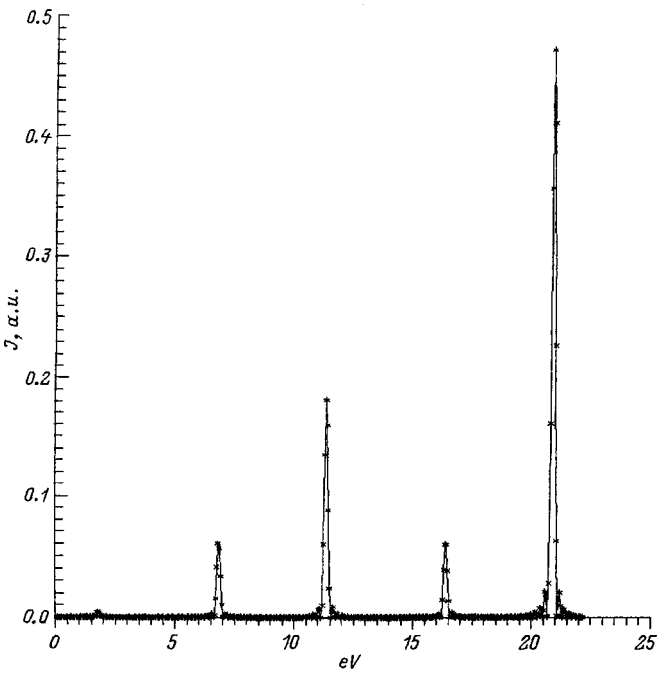

FIG. 2. Spectrum of transverse electron energies for a planar-channel distortion period $T=1300$ Å and $a=3/32d_0$.

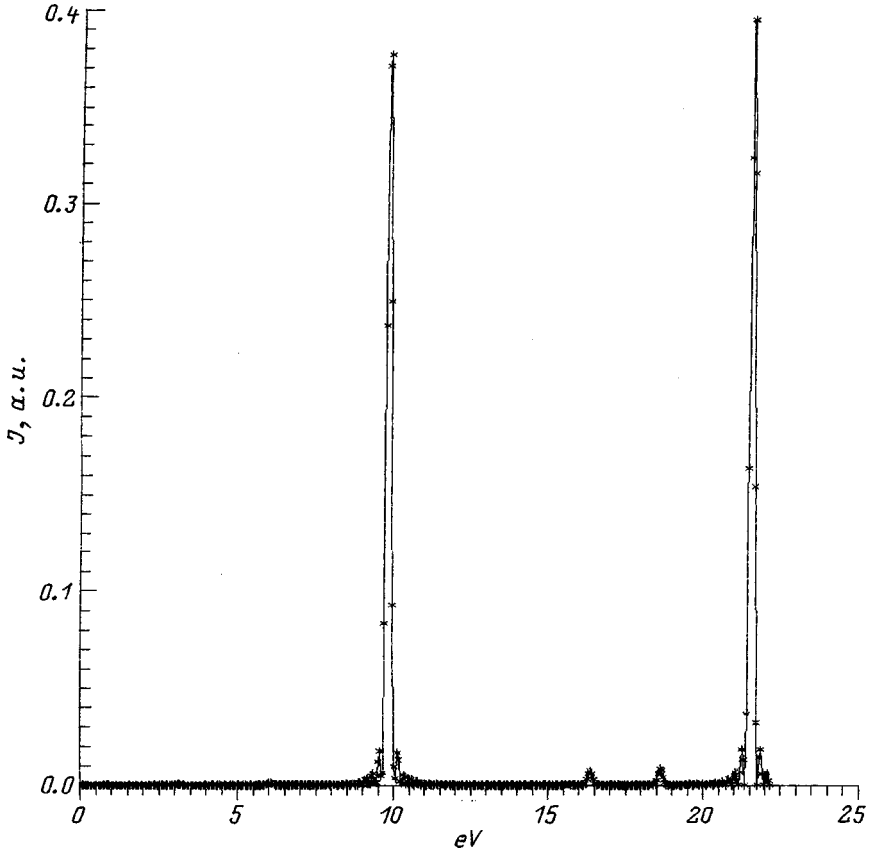

FIG. 3. Spectrum of transverse electron energies for a planar-channel distortion period $T = 800$ Å, $a = 3/32d_0$, and $U_0 = 21.22$ eV.

dence of the position of the spectral lines on superlattice period is presented in Fig. 5.

As was shown by the calculations in the range $T = 20\,000 - 30\,000$ Å, which corresponds to the case of $T \gg z_0$, the spectrum of transverse energies consists of two levels (the third is an above-barrier level), which correspond to the levels of an undistorted channel. Just as in the case of the results obtained using perturbation theory,[11] each level has two small satellites, the energy difference between the fundamental level and the satellite corresponding exactly to the channel distortion period

$$|E - E_s| = 2\pi\hbar c/T. \tag{3}$$

In the case of large periods ($T > 30\,000$ Å) the first fundamental level gradually vanishes (because of the parity of the wave function), and the satellites approach the fundamental lines and become smaller. Thus, the spectrum tends to the spectrum of an undistorted channel.

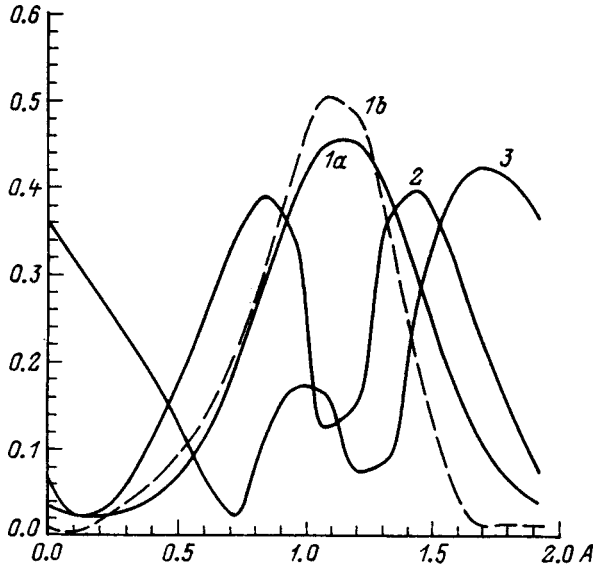

FIG. 4. Mode structure of the wave function corresponding to the spectrum shown in Fig. 2 (dependence of the probability density on transverse component): *1a*, *1b* — fundamental states at energies of 6.8 and 12.3 eV; *2*, *3* — at 16.3 and 20.8 eV.

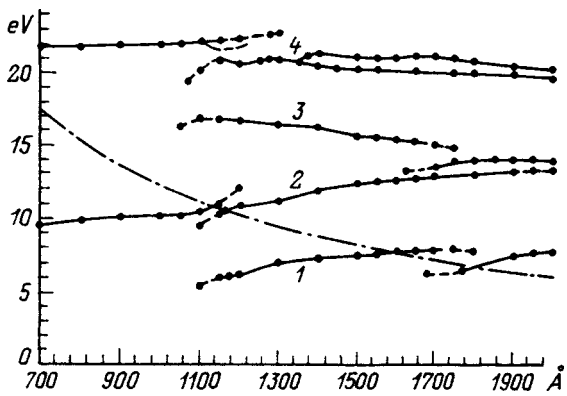

FIG. 5. Dependence of the transverse electron energy spectrum on the distortion period of the planar channel: $a = 3/32d_0$, $U_0 = 21.2$ eV; *1–4* — dependences for a distortion period equal to 1300 Å, which correspond to the modes represented in Fig. 4 by curves *1a*, *1b*, *2*, and *3*; dot-dashed curve — dependence for the equivalent channel distortion energy $2\pi\hbar c/T$; dashed curves — low-intensity states.

As the period is diminished ($T=2000-20\,000$ Å), the satellites move away from the fundamental lines in accordance with (3), and they become stronger. The approach of the satellites of the first and second fundamental levels leads to numerous splittings of both the fundamental lines and the satellites and to the appearance of new lines in the spectrum. As a result, for the lines near the potential barrier it is impossible to distinguish between the fundamental line and the satellites already when $T<5000$ Å. However, for each spectral line it is always possible to find a counterpart which is such that the relation (3) will be satisfied.

The range of periods $T=800-2000$ Å (Fig. 5) can be considered resonant, since $T\sim z_0$ here. In this case all the lines in the spectrum are comparable in strength. The dot-dashed line shows the dependence of $2\pi\hbar c/T$, which depicts the dependence of the effective energy corresponding to periodic distortions. Obviously, as the channel distortion amplitude decreases, the energy spectrum should approximate the spectrum of a straight channel. An analysis of the dependence of the transverse spectrum on a for $T=1160$ Å shows that as the distortion amplitude increases, levels 0, 1, and 2 descend into the potential well as a consequence of the lowering of the potential barrier as the potential of the bent channel is averaged along z (Ref. 17). For the averaged potential the presence of a bend in the channel is equivalent to an increase in the effective amplitude of the atomic vibrations, and it can be shown for $T\sim z_0$ that the lowering of the potential barrier

$$U_0-U\sim a^2 \quad \text{for} \quad T\sim z_0. \tag{4}$$

At the same time, an increase in the amplitude of the periodic disturbance of the superlattice leads to enhancement of the $0b$ level.[17] In the region $T<z_0$ (the superlattice period has a lower bound because of the channeling condition $T\geqslant 2\pi a/\alpha_l$) the spectrum shows only a single above-barrier level. This can be either because in this range of values of T the maximum angle of inclination of the channel $2\pi a/T\sim\alpha_l$ and the channeling effect is weakly expressed or because the depth of the potential is reduced. In general, if the distortion amplitude is not excessively small ($2\pi a/T\leqslant\alpha_l$) and the period $T\geqslant 2\pi\hbar c/U$, where U is the depth of the potential well, oscillatory motions of electrons with a large period cannot appear at all because of the constant dephasing.

Thus, the dependence of the spectrum on the superlattice period can be divided into three regions: A — the region of large values of T, where the spectral lines coincide with the lines of the undistorted crystal and have satellites; B — the resonance-interaction region, which is characterized by several bound states that differ significantly from the spectrum of the undistorted crystal; C — the region of small values of T, which is characterized by one above-barrier level. The boundaries of these regions are set by convention and depend, in particular, on the parameter a, which characterizes the amplitude of the channel distortions. For example, when $T=1160$ Å (Fig. 5), region B transforms into region A as the amplitude is increased.[17] This is associated with an increase in the angle of inclination of the channel up to α_l when $a=6/32$.

The transverse mode structure of the wave function of a channeled electron in a periodically distorted channel is shown in Fig. 4 for the case of $T\sim z_0$. In this case the fundamental level breaks up into two levels, viz., $0a$ and $0b$. For comparison, we note that there is only one 0 level of bound motion for $T<z_0$. It follows from the form of the eigenfunctions presented in Fig. 4 that the dipole moments for the $1\rightarrow 0a$ and $1\rightarrow 0b$ transitions are both nonzero, and, as can be seen from Fig. 5, the energy of the quantum of spontaneous radiation becomes dependent on the crystal deformation period.

A qualitative explanation for the results obtained can be given with consideration of the removal of the degeneracy with respect to the longitudinal momentum as a result of deformation of the channel. The appearance of distortions leads to the appearance of a longitudinal scale of the order of the distortion period, to which the oscillation period of an electron in the channel, which is rigorously related to the transverse energy, should be related. This is an analog of Bohr quantization. It can be seen in the example in Fig. 5, where the dot-dashed line is a plot of the equivalent energy corresponding to distortions with a period T, that at small distortion periods in the vicinity of $T=800$ Å level 1 corresponds to oscillations with a period significantly exceeding T. In this case the oscillation energy of the state is measured downward from the top of the channel. Therefore, the wave function does not complete a regular oscillation within the characteristic period, and the state does not form. When T increases and the equivalent energy $2\pi\hbar c/T$ decreases accordingly, decreases in the oscillation frequencies of the $0a$ and $0b$ states amounting roughly to the distortion frequency times 2 and 1, respectively, are observed.

The width of the spontaneous emission lines can be determined using the complex potential $V''(\mathbf{r})$ in Eq. (2) according to the method proposed in Ref. 18:

$$\Gamma_{ij}=\frac{1}{\hbar c}\sum_{n=i,j}\langle n|\int\langle\delta V(0,\mathbf{r}_\perp)\,\delta V(z',\mathbf{r}_\perp)\rangle\,dz'|n\rangle$$

or, with allowance for the averaging of the expression for Γ_{ij} over the channel distortion period

$$\overline{\Gamma}_{ij}=\frac{1}{T}\int\Gamma_{ij}\,dz.$$

Since the values of the scattering potential differ significantly from zero only near an atomic plane, a bending strain will lead only to a slight decrease in the width of the even eigenstates of the channeled particles and a slight increase in the width of the odd states and have little influence on the total value of $\overline{\Gamma}_{ij}$, which determines the width of the observed emission lines during channeling.

It follows from the investigations performed that complete reorganization of the wave function of a channeled electron in a crystal takes place with the superlattice parameters chosen. The weak influence of channel distortions on the broadening of a spectral line and the dependence of the radiation frequency on deformation period allow us to hope to experimentally detect the radiation from channeled relativistic electrons in single-crystal superlattices. Variation of

the orientation of a crystal with a ''superlattice'' relative to the electron beam with a fixed angle of incidence relative to the channeling planes, which is equivalent to variation of the superlattice period, will lead to transformation of the observed emission spectrum.

[1] R. Wedell, Phys. Status Solidi B **99**, 11 (1980).
[2] V. A. Bazylev and N. K. Zhevago, Usp. Fiz. Nauk. **160**(12), 47 (1990) [Sov. Phys. Usp. **33**, 1021 (1990)].
[3] L. V. Hau and J. U. Andersen, Phys. Rev. A **47**, 4007 (1993).
[4] A. Richter, Mater. Sci. Eng., B **11**, 139 (1992).
[5] A. P. Lazar', Zh. Tekh. Fiz. **66**(10), 102 (1996) [Tech. Phys. **41**, 1025 (1996)].
[6] J. Freundenberger, H. Genz, L. Groenig *et al.*, Nucl. Instrum. Methods Phys. Res. B **119**, 123 (1996).
[7] B. R. Meshcherov and V. I. Tumanov, JETP Lett. **51**, 572 (1990).
[8] M. Gouanere, D. Sillou, and M. Spighel, Phys. Rev. B **38**, 4352 (1988).
[9] T. A. Bobrova and L. I. Ognev, in *Abstracts of Reports to the 27th International Conference on the Physics of the Interaction of Charged Particles with Crystals* [in Russian], Moscow (1997), p. 77.
[10] M. Kriechbaum, K. E. Ambrosch, E. J. Fanter *et al.*, Phys. Rev. B **30**, 3394 (1984).
[11] V. N. Rud'ko, Zh. Éksp. Teor. Fiz. **89**, 1676 (1985) [Sov. Phys. JETP **62**, 967 (1985)].
[12] P. Lervig, J. Lindhard, and V. Nielsen, Nucl. Phys. A **96**, 489 (1967).
[13] L. I. Ognev, Radiat. Eff. Defects Solids **25**, 81 (1993).
[14] A. V. Andreev, S. A. Akhmanov, V. A. Vysloukh, and V. L. Kuznetsov, Zh. Éksp. Teor. Fiz. **84**, 1743 (1983) [Sov. Phys. JETP **57**, 1017 (1983)].
[15] T. A. Bobrova and L. I. Ognev, Radiat. Eff. Defects Solids **25**, 97 (1993).
[16] T. A. Bobrova and L. I. Ognev, Pis'ma Zh. Tekh. Fiz. **20**(19), 19 (1994) [Sov. Tech. Phys. Lett. **20**, 773 (1994)].
[17] T. A. Bobrova and L. I. Ognev, in *Abstracts of Reports to the 27th International Conference on the Physics of the Interaction of Charged Particles with Crystals* [in Russian], Moscow (1997), p. 78.
[18] L. I. Ognev, Zh. Tekh. Fiz. **64**(5), 78 (1994) [Tech. Phys. **39**, 499 (1994)].

Translated by P. Shelnitz

Development of shearing instability in metals

O. B. Drennov

All-Russian Scientific-Research Institute of Experimental Physics, 607190 Sarov, Russia
(Submitted 10 September 1997; resubmitted 13 January 1998)
Zh. Tekh. Fiz. **69**, 38–43 (February 1999)

The development of instability on a contact interface between steel objects is detected experimentally when it is loaded by an oblique shock wave. It is shown that disturbances form in the stage of shock-wave loading ($\Delta t<1\mu s$, $\Delta U>1$mm/μs) when the layers turn and the metals pass into a quasiliquid state. Then, at a relative slip velocity $\Delta\bar{U}\approx 0.1$ mm/μs the initial disturbances grow according to an exponential law and are ''frozen'' when the rarefaction wave reaches the contact interface (when the contact zone of the metal ''escapes'' from the plastic state). © *1999 American Institute of Physics.* [S1063-7842(99)00802-8]

The investigation of the hydrodynamic instability of an interface between two media is of great theoretical and practical interest. This is the reason for the increased attention which is being focused on the study of this process. Three types of instability of an interface have been distinguished traditionally: Rayleigh–Taylor instability, which appears when an interface between media of different density is subjected to acceleration with a vector that is perpendicular to it and is directed from the material of lower density into the material of higher density;[1] Richtmyer–Meshkov instability, which appears when a stationary shock wave, whose propagation direction is perpendicular to an interface between materials of different density, passes through that boundary (the boundary is abruptly accelerated on the shock-wave front and then moves without acceleration);[2] and Kelvin–Helmholtz instability (shearing instability), which appears when there is an offset in the tangential component of the velocity field.[3]

The laws governing the development of Rayleigh–Taylor and Richtmyer–Meshkov instability have been the subject of numerous analytical and experimental studies.[4–7] The studies in which attempts were made to take into account the effect of the strength of the media on the development of instability can be singled out.[8,9] Kelvin–Helmholtz instability has been studied quite thoroughly for the ideal case (analytically for an ideal incompressible fluid[10,11] and experimentally for liquids and gases[12]). Kelvin–Helmholtz instability can be described in its simplest form by the relations

$$U_y=U \text{ for } y<0; \quad \rho_y=\rho \text{ for } y<0;$$

$$U_y=U' \text{ for } y>0; \quad \rho_y=\rho' \text{ for } y>0. \tag{1}$$

More precisely, Kelvin–Helmholtz instability is the dynamic instability of the interface at $y=0$ toward the flow (1), including the cases of $\rho=\rho'$ (a homogeneous liquid) and $g=0$. The surface tension on the interface at $y=0$ weakens the instability, but does not eliminate it.

Without considering the long list of theoretical and experimental studies devoted to the development of disturbances on a contact interface between a pair of metals under high-speed oblique impact (explosive welding is realized in practice in this way), in which wave formation on the interface can be explained on the basis of the development of Kelvin–Helmholtz instability between a jet and a quasiliquid layer of a metallic plate,[13–16] only an extremely small number of studies of the development of shearing instability in metals can be noted. For example, in Ref. 17 shear flow appears for two tightly contacting metal plates (copper and steel) when they are loaded by a normally incident shock wave and the wedge-shaped gap below them is closed. The magnitude of the tangential velocity offset is estimated to be $\Delta U\approx 0.5$ mm/μs. It is noted that at least one of the metals must be in the plastic state.

This paper presents the results of experiments in which it was possible to observe the development of shearing instability on a contact interface between two metallic objects. In the first stage of the experimental investigations the object of observation was the contact interface between a disk and a ring (the material was grade 3 steel of thickness 14 mm, the outer diameter of the disk was 64 mm, the internal diameter of the ring was 64 mm, and the external diameter of the ring was 90 mm). The disk was placed in the ring with light-drive fit.

The dynamic pulse was received only by the disk. The slip velocity of the disk relative to the ring was $\Delta U \leqslant 0.5$ mm/μs. The relative slip time is estimated to be $\Delta t \leqslant 70$ μs. The pulsed pressure in the disk material with allowance for the damping of the amplitude of the shock wave is $P\approx 20$ GPa. This value exceeds the dynamic yield point of grade 3 steel and is sufficient for shifting the metal into the plastic deformation region. However, the disk-ring contact interface remained stable in all the experiments.

The results presented regarding the development of instability were obtained using the following loading scheme (Fig. 1). In order to protect the samples from the destructive effects of the rarefaction waves, disk *1* and ring *2* were placed in protective collar *3*, which has the form of a ring of external diameter $D=120$ mm, internal diameter $d=90$ mm, and thickness $h=14$ mm and were set on steel tray *4* with the dimensions 120×20 mm.

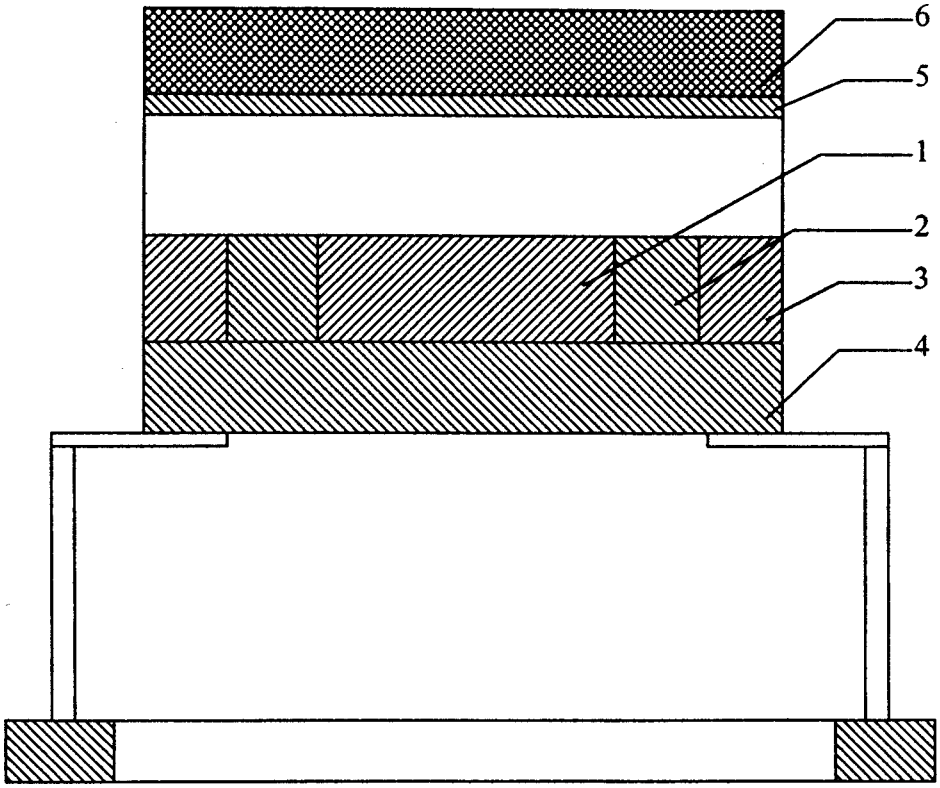

FIG. 1. Loading scheme.

The system was loaded by brass projectile pellet *5* with the dimensions $120\times(2\ldots3)$ mm, which was driven by the explosion products formed upon detonation of charge *6* of an explosive of the TG 50/50 type with the dimensions $120\times(20\ldots40)$ mm. A plane detonation wave was generated in the explosive charge. Thus, a shock wave with an amplitude in the range $40\leqslant P\leqslant55$ GPa was supplied to the input surface of the disk. With consideration of the damping, the shock-wave pressure at the point of exit from the sample was in the range $36\leqslant P\leqslant49$ GPa. The development of disturbances on the disk-ring contact interface was detected in the experiments described here. The development of disturbances was also noted on the ring-collar contact interface.

Figure 2 presents microsections of these contact interfaces ($20\times$ magnification): *a*, *b* — original contact interfaces of the disk and ring, respectively (smooth surface); *c* — disk-ring interface (fragment of the disk) (the wavelike disturbances of nearly sinusoidal form are characterized by an amplitude $\overline{a}\approx0.08$ mm and a wavelength $\overline{\lambda}\approx0.8$ mm, and a dramatic change in the structure of the steel is noted in a near-surface zone of width $\overline{\Delta}\approx0.03$ mm); *d* — ring–collar interface (fragment of the ring) (the disturbances are characterized by an amplitude $\overline{a}\approx0.06$ mm and a wavelength $\overline{\lambda}\approx0.7$ mm, and variation of the steel microstructure occurs in a near-surface zone of width $\overline{\Delta}\approx0.02$ mm).

To detail the mechanism with respect to displacement of the metal layers, the dynamic loading of the system (according to the scheme in Fig. 1) and the subsequent motion of its elements were examined by x-ray photography at different moments in time. A pulsed BIM-234 x-ray photography system with a gamma-quantum cutoff energy $E\approx2.5$ MeV (Ref. 18) was used in the experiments.

The individual phases of motion of the elements of the system can be distinguished after the shock wave meets the free surface of the tray (6 μs after the onset of loading). From the 7th to the 12th μs the mean rate of motion of the disk relative to the ring $\Delta\overline{U}\approx0.1$ mm/μs. From the 13th to 300th μs, $\Delta\overline{U}'\approx0.04$ mm/μs. Therefore, after separation of the disk and ring (under the action of the lateral rarefaction wave) in the 13th μs, inertial motion of the elements of the system takes place.

Figure 3 shows the experimental system in the stage of inertial motion (the 30th μs). Split-off fragments of collar *3* (lateral splitting) and tray *4* (lateral and posterior splitting), as well as separation of collar *3*, ring *2*, and disk *1* are seen.

The form of the shock-wave pulse entering the samples was investigated simultaneously in an independent series of experiments. The profile of the free surface of the projectile pellet at the time corresponding to impact on the disk-ring-collar system is recorded. An SFR-2M high-speed recording camera operating in the slit-scan regime (the so called flashing gap method[19]) was used for this purpose. The essence of the method is as follows. The optical receiver (two layers of Perspex separated by a thin gap) is mounted on a firm measurement base. After the projectile pellet strikes the receiver, the shock wave formed enters the gap, in which the luminescence of ionized air appears and mimics the profile of the free surface of the pellet. A typical photochronogram of the profile of the projectile pellet for the loading regime with $P\approx55$ GPa is shown in Fig. 4.

Next, the geometric center of the pellet is matched to the geometric center of the system with consideration of the enlargement factor in the coordinate plane. The angle of inclination of the pellet plane to the disk-ring and ring-collar

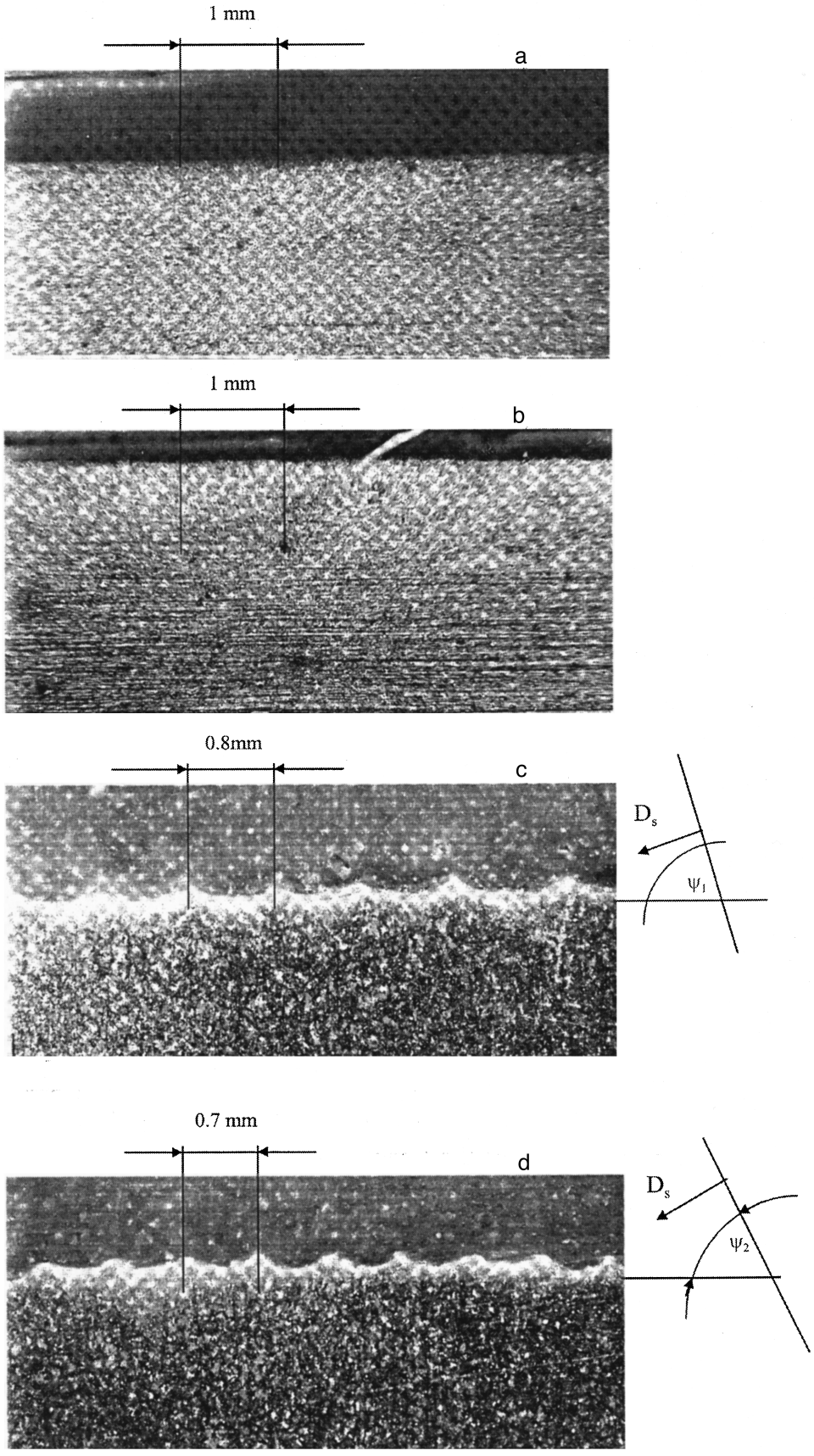

FIG. 2.

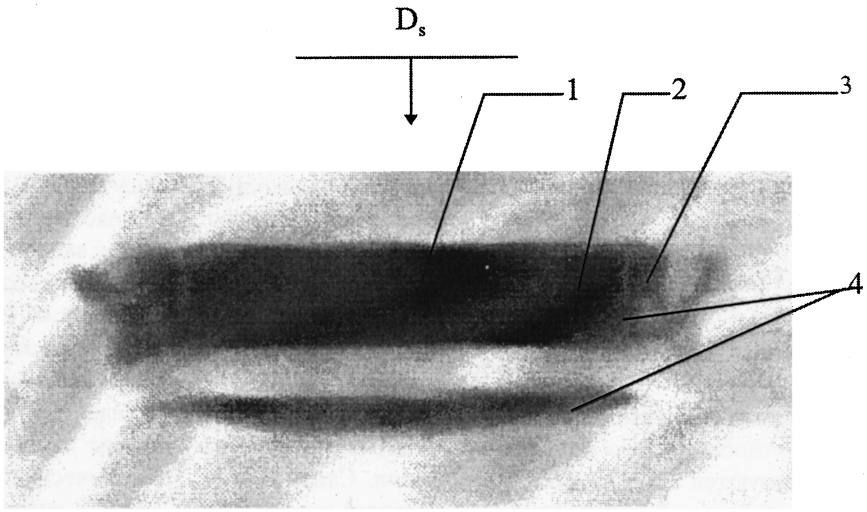

FIG. 3.

contact interfaces are found when these geometric centers are in tight contact. These angles of inclination determine the impact angles and, accordingly, the angles at which the shock waves load the respective contact interfaces (Ψ_1 and Ψ_2).

It follows from the photochronograms that the shock wave meets the disk-ring contact interface at an angle $\Psi_1 \approx 80°$ and the ring-collar interface at an angle $\Psi_2 \approx 70°$, i.e., the contact interface is loaded by an oblique shock wave. It follows from the conservation laws on the front of an oblique shock wave that the contacting metal layers turn through an angle ω behind the front.[20] A one-dimensional geometric treatment of a specific (for the loading parameters realized in the experiments) mechanism of ''inleakage'' of the flows on the front of an oblique shock wave followed by their turning through the angle ω does not permit unequivocal determination of the relative slip velocity of the elements of the system. However, the magnitude of the tangential velocity offset can be estimated by employing several successive simplifications: the metal layers are treated as flows only behind the shock-wave front, i.e., it can be assumed that at the moment when the disk-ring-collar system is loaded by the projectile pellet, a shock-wave state characterized by the pressure P and the mass velocity U is realized in the metal (in particular, in the case under consideration of $P \approx 55$ GPa, the disk material acquires a mass velocity $U \approx 1.1$ mm/μs); because of the asymmetry of the loading (actually, it follows from Fig. 4 that the disk reaches the plane of the system bent, i.e., the loading of the ring takes place after the loading of the disk) it can be assumed that movement of the mass of material (U) begins sooner in the disk than in the ring. A tangential velocity offset $\Delta U_1 \approx 1.1$ mm/μs is thereby created. Similarly, the velocity offset for the ring–collar interface is estimated to be $\Delta U_2 \approx 0.9$.

The turning of the ''flows'' behind the oblique shock front, as well as the high value of the relative slip velocity ΔU_1 (or ΔU_2), are characterized by short time intervals $\Delta t < 0.5$ μs. The disk-ring interface persists for a time $t_1 \approx 13$ μs (until the arrival of the lateral rarefaction wave). According to the results of the x-ray photographic experiments, a relative slip velocity $\Delta \bar{U} \approx 0.1$ mm/μs is maintained for all this time. Then the elements of the system separate. The ring–collar interface persists for a time $t_2 \approx 7$ μs and is characterized by similar processes.

The following mechanism for the development of shearing instability in metals can be proposed. An oblique shock wave crosses the contact interface. The temperature of the samples rises at the wave front. Their turning behind the

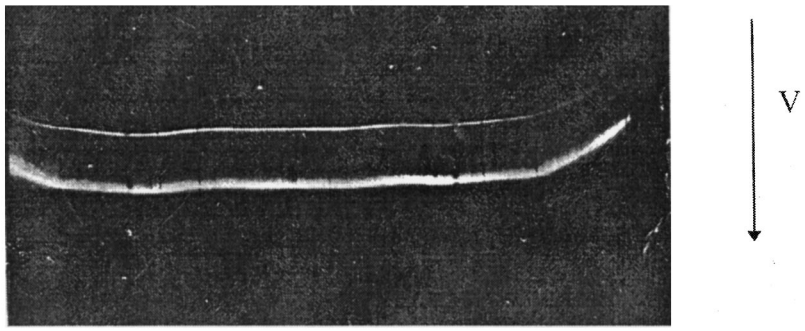

FIG. 4.

oblique shock wave front is accompanied by relative slip along the contact interface and the development of intense plastic shear strains. Thin near-surface layers of the metals pass into a quasiliquid state, and their partial melting is possible. These layers behave similarly to real viscous liquids. A tangential velocity offset ΔU appears in the stage of shock-wave-induced turning of the metal layers. This stage is completed quickly ($\Delta t < 0.5$ μs), but its duration is sufficient for the formation of the initial disturbance. The relative motion of the flows (the metal layers) subsequently continues with the tangential velocity offset $\Delta \overline{U}$. During this time, the initial disturbance takes on a sinusoidal form. Shearing instability (of the Kelvin–Helmholtz instability type) develops. The parameters of the disturbances grow according an exponential law. When the flows separate (when the near-surface zones of the metals escapes from the quasiliquid state) development of the instability and growth of the disturbances cease. The final form of the disturbances is ''frozen.''

As we have already noted,[1] for an interface between two liquids with the densities ρ and ρ' moving with the velocities U and U', respectively, a sinusoidal disturbance of the boundary surface with a wavelength $\lambda = 2\pi/k$ increases according to an exponential law $\exp[I(\lambda)t]$, where $[I(\lambda)]^2 = \rho\rho' k^2(\rho+\rho')^{-2}(U'-U)^2 - (\rho-\rho')(\rho+\rho')^{-1}gk - (\rho+\rho')^{-1}\gamma k^3$, γ is the surface tension on the boundary between the two media, and g is the acceleration of gravity.

In describing the development of disturbances on a contact interface between a pair of metals in the case of oblique impact (''explosive welding''), the metal in the impact zone is assumed to be a real liquid (high pressures, temperature increases, and large plastic strains are present), and the growth of the disturbances obeys an exponential law. Moreover, unrestricted growth of the disturbances is sustained by the surface tension.[15,16] In our opinion, the equations of motion and continuity must be supplemented by an equation of state with strength. In other words, at certain pressures $P_s > P^*$ the metals can be described in the quasiliquid approximation. The relationship between P_s^* and Y (the dynamic yield point of the metal) establishes the region for the existence of the regime under consideration and characterizes the size of the ''frozen'' waves. In addition, the dynamic parameters (the shock-wave velocity D_s and the rarefaction-wave velocity C), which influence the lifetime of the plastic state of the contact interface, are also taken into account by the relationship between P_s and Y ($P_s > Y$).

Summarizing the foregoing, we can state that the type of shearing instability described is characterized by the following definition: a straight (smooth) interface between two media is loaded (accelerated) by an oblique shock wave, whose amplitude must be sufficient for bringing the metals behind the front into the plastic quasiliquid state.

[1] *Hydrodynamic Instability*, American Mathematical Society, Providence (1962); Mir, Moscow (1964), 372 pp.
[2] E. E. Meshkov, Izv. Akad. Nauk SSSR, Mekh. Zhidk. Gaza No. 5, 151 (1969).
[3] G. Birkhoff, *Hydrodynamics: a Study in Logic, Fact, and Similitude*, 2nd ed., Princeton University Press, Princeton, NJ (1960); IL, Moscow (1964), 244 pp.
[4] J. W. Miles, General Atomics Rep. Gamo (1960), p. 7335.
[5] D. C. Drucker, *Introduction to Mechanics of Deformable Solids*, McGraw-Hill, New York (1967); Mir, Moscow (1983), 162 pp.
[6] V. A. Andronov, C. M. Bakhrakh, and V. V. Nikiforov, Izv. Akad. Nauk SSSR, Mekh. Zhidk. Gaza No. 6, 20 (1984).
[7] E. E. Meshkov, in *International Workshop of the Physics of Compressible Turbulent Mixing*, Princeton, NJ (1988).
[8] P. N. Nizovtsev and V. A. Raevskiĭ, Vopr. At. Nauki Tekh., Ser. Teor. Prikl. Fiz. No. 3, 11 (1991).
[9] S. M. Bakhrakh and N. P. Kovalev, in *Proceedings of the 5th All-Union Conference on Numerical Methods for Solving Problems in the Theory of Elasticity and Plasticity* [in Russian], Novosibirsk (1978), pp. 22–36.
[10] A. Amsden and F. N. Harlow, Phys. Fluids **7**, 327 (1964).
[11] G. Birkhoff and E. H. Zarantonello, *Jets, Wakes, and Cavities*, Academic Press, New York (1957); Mir, Moscow (1964), 466 pp.
[12] G. R. Cowan, O. R. Bergmann, and A. H. Holtzman, Metall. Trans. **2**, 3145 (1971).
[13] G. R. Cowan and A. H. Holtzman, J. Appl. Phys. **34**, 928 (1963).
[14] J. N. Hunt, Philos. Mag. **17**(148), 669 (1968).
[15] J. L. Robinson, Philos. Mag. **31**(3), 587 (1975).
[16] A. V. Utkin, A. N. Dremin, and A. N. Mikhaĭlov, Fiz. Goreniya Vzryva **16**(4), 126 (1980).
[17] A. L. Mikhaĭlov, Fiz. Goreniya Vzryva **15**(2), 158 (1979).
[18] A. I. Pavlovskiĭ, G. D. Kuleshov, and G. V. Sklizkov, Dokl. Akad. Nauk **160**, 68 (1965).
[19] A. Dubovik, *The Photographic Recording of High-Speed Processes*, John Wiley, New York (1981); 3rd. ed., Nauka, Moscow (1984), 320 pp.
[20] R. Courant and K. O. Friedrichs, *Supersonic Flow and Shock Waves*, Interscience, New York (1948); IL, Moscow (1950), 426 pp.

Translated by P. Shelnitz

High resolution x-ray diffractometry of the structural characteristics of a semiconducting (InGa)As/GaAs superlattice

Ya. I. Nesterets, V. I. Punegov, and K. M. Pavlov

Syktyvkar State University, 167001 Syktyvkar, Russia

N. N. Faleev

A. F. Ioffe Physicotechnical Institute, 194021 St. Petersburg, Russia
(Submitted October 6, 1997)
Zh. Tekh. Fiz. **69**, 44–53 (February 1999)

A statistical approach is used to construct a kinematic theory of x-ray diffraction on a semiconducting superlattice with a two layer period. This theory takes two types of structural deformations into account: crystal lattice defects caused by microdefects distributed chaotically over the thickness of the superlattice, and periodicity defects of an additional superlattice potential owing to random deviations in the thicknesses of the layers of its period from specified values. Numerical simulation is used to illustrate the effect of structural defects on the development of the diffraction reflection curve. The theory is used to analyze experimental x-ray diffraction spectra of semiconducting $In_xGa_{1-x}As/GaAs$ superlattices.
 [S1063-7842(99)00902-2]

INTRODUCTION

Semiconducting superlattices are a new and important class of modulated crystalline structures. Because of the additional periodic potential created by the alternation of two or more layers of a certain set of semiconductors, superlattices have a number of unique electrical and optical properties. Existing methods for epitaxial growth make it possible to create superlattices with a rather high structural perfection. Nevertheless, actual superlattices inevitably contain various kinds of defects. Because of its nondestructive character and relative simplicity, x-ray diffraction is the most effective method for determining the structural parameters of superlattices.

At present considerable attention is being devoted to describing the diffraction of x rays on superlattices with different structural defects. Studies have been made[1–3] of the effect of cluster microdefects on the formation of the two-crystal diffraction reflection curves from semiconducting superlattices.

The behavior of diffraction reflection curves from superlattices with irregularities of the heterointerfaces has been studied in number of papers.[4–7] A study has been made[8] of x-ray diffraction in the presence of macroscopic distortions of the modulated structure of a superlattice caused by fluctuations in the layer thicknesses and composition.

In reality, superlattices can contain microdefects (point defects and clusters of them, small-radius dislocation loops, etc.), as well as different kinds of macroscopic defects in the additional periodic structure which arise during the epitaxial growth process. In this paper we obtain expressions for the intensity of coherent and diffusely scattered waves taking fluctuations in the superlattice layer thicknesses and statistically distributed microdefects into account.

A MODEL OF DEFECTS

In order to describe microdefects we use a model of spherically symmetric amorphous Coulomb clusters. In this model, the chaotically distributed defects in the crystal give rise to the following random local atomic displacements:

$$\delta\mathbf{u}(\mathbf{r})=\begin{cases}\dfrac{A\mathbf{r}}{r^3}, & \text{if } |\mathbf{r}|>R_d\\ \text{a random quantity}, & \text{if } |\mathbf{r}|\leqslant R_d,\end{cases} \tag{1}$$

where R_d and A are the defect radius and power, respectively.

We introduce the following model of macroscopic defects in an N-period superlattice. We assume that there are random deviations $\delta l_p^{(n)}$ in the thickness of the pth layer in the nth period of the superlattice, $l_p^{(n)}$, from the specified value $\langle l_p\rangle$, so that $l_p^{(n)}=\langle l_p\rangle+\delta l_p^{(n)}$ $(n=1,2,\ldots,N;\ p=1,2)$. Since the superlattice is produced by successive deposition of layers, the fluctuations in the thicknesses of different layers can be regarded as independent. Thus, $\langle \delta l_p^{(n)}\cdot \delta l_s^{(m)}\rangle=0$, if $p\neq s$ or $n\neq m$.

COHERENT INTENSITY

In terms of the statistical approach to a kinematic theory of diffraction, the reflection amplitude coefficient for coherently scattered rays from a superlattice with a period of two layers is given by

$$\langle R^c\rangle=\sum_{n=1}^{N}\langle r^{(n)}\rangle\mu^{n-1}\prod_{m=1}^{n-1}\langle t^m\rangle, \tag{2}$$

where the brackets $\langle\ldots\rangle$ denote averaging the enclosed quantity over the fluctuations in the layer thicknesses. The solutions for the averaged reflection amplitude coefficient

$\langle r^{(n)}\rangle$ and the products of the transmission amplitude coefficients in the directions of the incident and reflected rays, $\langle t^{(n)}\rangle$, of the nth period of the superlattice are given by

$$\langle r^{(n)}\rangle=\langle r_1\rangle+\langle r_2\rangle\langle t_1\rangle\mu_1, \tag{3}$$

$$\langle t^{(n)}\rangle=\langle t_1\rangle\langle t_2\rangle, \tag{4}$$

where the corresponding quantities in the individual layers of the superlattice period, $\langle r_p\rangle$ and $\langle t_p\rangle$ have the following form ($p=1,2$):

$$\langle r_p\rangle=\sigma_p E_p\frac{\exp(i2A_p\langle l_p\rangle)D_p-1}{2A_p}, \tag{5}$$

$$\langle t_p\rangle=\exp(i2A_p^r\langle l_p\rangle)D_p. \tag{6}$$

Here

$$A_p=\tfrac{1}{2}\left(\eta_p+\frac{2\pi\Delta d_p}{d_0^2}\right);$$

$\Delta d_p/d_0$, l_p, and $\mu_p=\exp(-2A_p^i l_p)$ are, respectively, the relative deformation (strain), thickness, and a coefficient which accounts for photoabsorption in the pth layer of the superlattice period; d_0 is the interplane separation of the substrate; $\mu=\mu_1\cdot\mu_2$; the indices r and i denote, respectively, the real and imaginary part; the variable η_p is given in terms of the angular deviation $\Delta\vartheta=\vartheta-\vartheta_B$ of the diffraction angle ϑ from the exact Bragg angle ϑ_B of the substrate by

$$\eta_p=\frac{2\pi}{\lambda\gamma_0}(\chi_0^{(p)}+\Delta\vartheta\sin\vartheta_B), \tag{7}$$

where λ is the x-ray wavelength, $\chi_{0,g}^{(p)}$ are the Fourier components of the dielectric susceptibility in the directions of the incident and reflected beams, respectively, and $\gamma_{0,g}$ are the direction cosines of the incident and reflected rays; $\sigma_p=(\pi C\chi_g^{(p)})/(\lambda|\gamma_g|)$; C is the polarization factor; and E_p is the statistical Debye–Waller factor ($p=1,2$).

In Eqs. (5) and (6) we have introduced the quantity $D_p(\Delta\vartheta)=\langle\exp(i2A_p^r\delta l_p)\rangle$, which we define as the effective Debye–Waller factor of the pth layer of the period. The explicit expression for D_p depends on the particular form of the distribution of the fluctuations in the layer thickness. In particular, for a continuous Gaussian distribution, we can use

$$D_p(\Delta\vartheta)=\exp(-2(A_p^r\Omega_p)^2), \tag{8}$$

where Ω_p^2 is the dispersion of the distribution of the fluctuations in the thickness of the pth layer of the superlattice period.

In the case of symmetric Bragg diffraction, the solution for the coherently scattered intensity is expressed in terms of the reflection amplitude coefficient $\langle R^c\rangle$ as follows:

$$I^c=|\langle R^c\rangle|^2. \tag{9}$$

DIFFUSE INTENSITY

Defects cause incoherent (diffuse) scattering, whose angular distribution is found from the equation $I^d=I^t-I^c$, where I^t is the total scattering intensity.

For the diffuse intensity owing to fluctuations in the thicknesses of the superlattice layers, we obtain

$$I^d=\langle|R^c|^2\rangle-|\langle R^2\rangle|^2. \tag{10}$$

The expression for the total intensity averaged over the thickness fluctuations [the first term in Eq. (10)] is written in the form

$$\langle|R^c|^2\rangle=\sum_{n,n'=1}^{N}S_{n,n'}\mu^{n+n'-2}, \tag{11}$$

where

$$S_{n,n'}=\begin{cases}\langle|r^{(n)}|^2\rangle, & n=n';\\ \langle r^{(n)}\rangle\cdot\langle r^{*(n')}t^{(n')}\rangle\cdot\langle t\rangle^{n-n'-1}, & n>n';\\ \langle r^{(n)}t^{*(n)}\rangle\cdot\langle r^{*(n')}\rangle\cdot\langle t^{*}\rangle^{n'-n-1}, & n<n'.\end{cases} \tag{12}$$

The quantities $\langle|r|^2\rangle$ and $\langle r^*t\rangle$ in Eq. (12) are given by

$$\langle|r|^2\rangle=\langle|r_1|^2\rangle+\langle|r_2|^2\rangle\mu_1^2+2\,\mathrm{Re}(\langle r_1^*t_1\rangle\langle r_2\rangle)\mu_1, \tag{13}$$

$$\langle r^*t\rangle=\langle r_1^*t_1\rangle\langle t_2\rangle+\langle r_2^*t_2\rangle\mu_1. \tag{14}$$

The formulas for $\langle|r_p|^2\rangle$ and $\langle r_p^*t_p\rangle$ of the individual layers can be written as

$$\langle|r_p|^2\rangle=|\sigma_p|^2E_p^2\,\frac{1+\mu_p^2-2\mu_p\cos(2A_p^r\langle l_p\rangle)D_p}{4|A_p|^2}, \tag{15}$$

$$\langle r_p^*t_p\rangle=\sigma_pE_p\frac{\mu_p-\exp(i2A_p^r\langle l_p\rangle)D_p}{2A_p^*}. \tag{16}$$

Microdefects distributed in the superlattice layers also cause diffuse scattering whose angular profile is determined by the type, dimensions, and concentration of the defects. In the kinematic approximation, the solution for the diffusely scattered intensity can be written in the form[9]

$$I_d(\Delta\vartheta)=I_1^d(\Delta\vartheta)\mu^{n-1}\frac{\mu^N-\mu^{-N}}{\mu-\mu^{-1}}, \tag{17}$$

where

$$I_1^d(\Delta\vartheta)=2(|\sigma_1|^2(1-E_1^2)\tau_1l_1+|\sigma_2|^2(1-E_2^2)\tau_2l_2\mu_1) \tag{18}$$

is the angular distribution of the incoherently scattered intensity in the superlattice period.

An explicit expression for the correlation length τ_p corresponding to the microdefect model of Eq. (1) when the atomic fields of the displacements of the different clusters do not overlap has been obtained elsewhere:[10]

$$\tau_p(\Psi_p)=\frac{1}{1+\tilde{A}^2}\left\{\tau_0(\Psi_p)+\tilde{A}^2\tau_0(0)\left(\frac{\exp(ix_0)}{ix_0}\left(\frac{5}{3}-\gamma_0^2\right)+\frac{(\gamma_0^2+1)\gamma_0}{x_0^2}(1-\exp(ix_0))+\frac{8i}{3x_0}+2(1-\gamma_0^2)F+\frac{x_0^2(3\gamma_0^2-1)}{6}(F_0-F)\right)\right\}, \tag{19}$$

where $\tilde{A}=A|\mathbf{g}|/R_d^2$, $\mathbf{g}$ is the diffraction vector, $x_{0,1}=2R_{d,1}\Psi_p\gamma_0$, R_1 is the outer boundary of the field of elastic displacements, $\Psi_p=2A_p$ $(p=1,2)$,

$$F=\ln\left(\frac{x_1}{x_0}\right)+\int_{x_0}^{x_1}\frac{\exp(iz)-1}{z}dz, \tag{20}$$

$$F_0=\frac{\exp(ix_0)}{x_0^2}-\frac{\exp(ix_1)}{x_1^2}+\frac{i\exp(ix_0)}{x_0}-\frac{i\exp(ix_1)}{x_1}, \tag{21}$$

$$\tau_0(\Psi_p)=\tau_0^r(\Psi_p)+i\tau_0^i(\Psi_p), \tag{22}$$

$$\tau_0^r(\Psi_p)=\frac{3}{4}R_d\gamma_0\frac{8}{x_0^4}\left(\frac{x_0^2}{2}+1-\cos(x_0)-x_0\sin(x_0)\right), \tag{23}$$

$$\tau_0^i(\Psi_p)=\frac{R_d\gamma_0}{x_0^4}(2x_0^3-6\sin(x_0)+6x_0\cos(x_0)). \tag{24}$$

NUMERICAL SIMULATION

We shall analyze these equations using the example of a 10-period composite superlattice of 30 nm AlAs/30 nm GaAs grown on a massive (001)-oriented GaAs substrate. The layers in the period are enumerated from the substrate. Numerical calculations were done for the symmetric (004) reflection of σ-polarized CuK_{α_1} radiation. It is assumed that the superlattice is in a stressed state owing to coherent growth. Given the resulting tetragonal deformation of the crystal lattice, the strain of the pth layer of the superlattice period is given by

$$\frac{\Delta d_p}{d_0}=\frac{d_p-d_0}{d_0}K_p,$$

where d_p and d_0 are the easy-plane separations of the layer and substrate in the unstressed state and $K_p=(C_{11}^{(p)}+C_{12}^{(p)})/C_{11}^{(p)}$, where $C_{11}^{(p)}$ and $C_{12}^{(p)}$ are the elastic constants of the crystal lattice in the pth layer of the period $(p=1,2)$.

Figure 1 shows the angular distributions of the diffuse component and the total scattered intensity as functions of the cluster radius R_d. The static Debye–Waller factor of the layers in the period is $E_1=E_2=0.9$. It is clear from Fig. 1a that, for a constant degree of disruption of the crystalline lattice of the superlattice layers, a continuous reduction in the with of the angular distribution of the diffuse scattered intensity is observed with increasing defect radius. This in turn has a significant effect on the behavior of the angular profile of the total diffraction reflection curve. In Fig. 1b a rise in the profile of the total scattered intensity can be noticed in this angular region as the defect size increases.

There is some interest in an analysis of the formation of the diffraction reflection curve as the structural perfection of one of the layers in the superlattice period is varied. It has been shown[11] that for certain values of the static Debye–Waller factors, complete quenching of the coherent component of the scattered intensity of one or the other of the satellite peaks in the superlattice spectrum may occur. Figures 2 and 3 show the variations in the angular distributions of the coherent and total scattered intensities with the magnitude of the static factors E_1 and E_2, respectively, for a fixed defect radius $R_d=5$ nm. Dips are observed in the coherent intensity for the first satellite at $E_1=0.2$ and for the second, at $E_1=0.4$ (Fig. 2a). Here the second layer of the period is assumed perfect $(E_2=1)$. A similar pattern is observed in the graph for the total scattered intensity (Fig. 2b). In the case where the first layer of the superlattice period is perfect and the microdefects are concentrated in the second, the picture changes. Now dips in the coherent intensity are observed for the minus first and minus second satellites, respectively, at $E_2=0.35$ and $E_2=0.8$ (Fig. 3a). Note that, in general, the dips in the coherent intensity and the minima of the total intensity do not coincide (compare Figs. 3a and 3b for the minus second satellite). This is because even for a constant defect radius, as the static factor of one of the layers is reduced, the diffuse scattered intensity is found to rise.

We now turn to an analysis of the effect of fluctuations in the thickness of a superlattice layer on its x-ray diffraction spectra. Figure 4 shows the variations in the coherent, diffuse, and total scattered intensities with the magnitude of the relative fluctuations in the thicknesses of the superlattice layers (i.e., of the ratio of the root mean square deviation of the thickness of a layer to its mean value). It can be seen from Fig. 4a that, as the magnitude of the relative fluctuations in the layer thicknesses increases, a monotonic drop in the coherent intensity is observed, along with a broadening of the satellite peaks. This effect is stronger for higher satellite numbers. The existence of fluctuations in the layer thickness causes diffuse scattering (Fig. 4b) which is concentrated principally in the angular regions of the satellite peaks. As the magnitude of the fluctuations increases, a substantial enhancement is observed in the diffuse intensity. However, there is a limit to the rise in the diffuse intensity which, as can be seen from Fig. 4b, is more rapidly attained in the neighborhood of satellites with larger ordinal numbers. Regarding the total scattered intensity, we must note the following: as with the coherent intensity, when the magnitude of the fluctuations increases, a reduction in the total intensity of the satellites is observed, along with a broadening of the latter. Here, as the magnitude of the fluctuations increases, the fraction of the diffuse component in the total scattered intensity becomes larger, so that gradually the diffuse intensity begins to predominate. This is quite clear for the second and third satellites in Fig. 4c.

Therefore, microdefects statistically distributed over the superlattice volume and possible fluctuations in the layer thicknesses away from certain values do have a significant effect on the formation of the diffraction reflection curves. It is extremely important to take them into account in analyzing experimental x-ray diffraction spectra of superlattices.

X-RAY DIFFRACTION DIAGNOSTICS OF A SEMICONDUCTING (InGa)As/GaAs SUPERLATTICE

We shall use the formulas derived here to study a semiconducting $(In_xGa_{1-x})As/GaAs$ superlattice grown by molecular-beam epitaxy on an exactly (001)-oriented, perfect

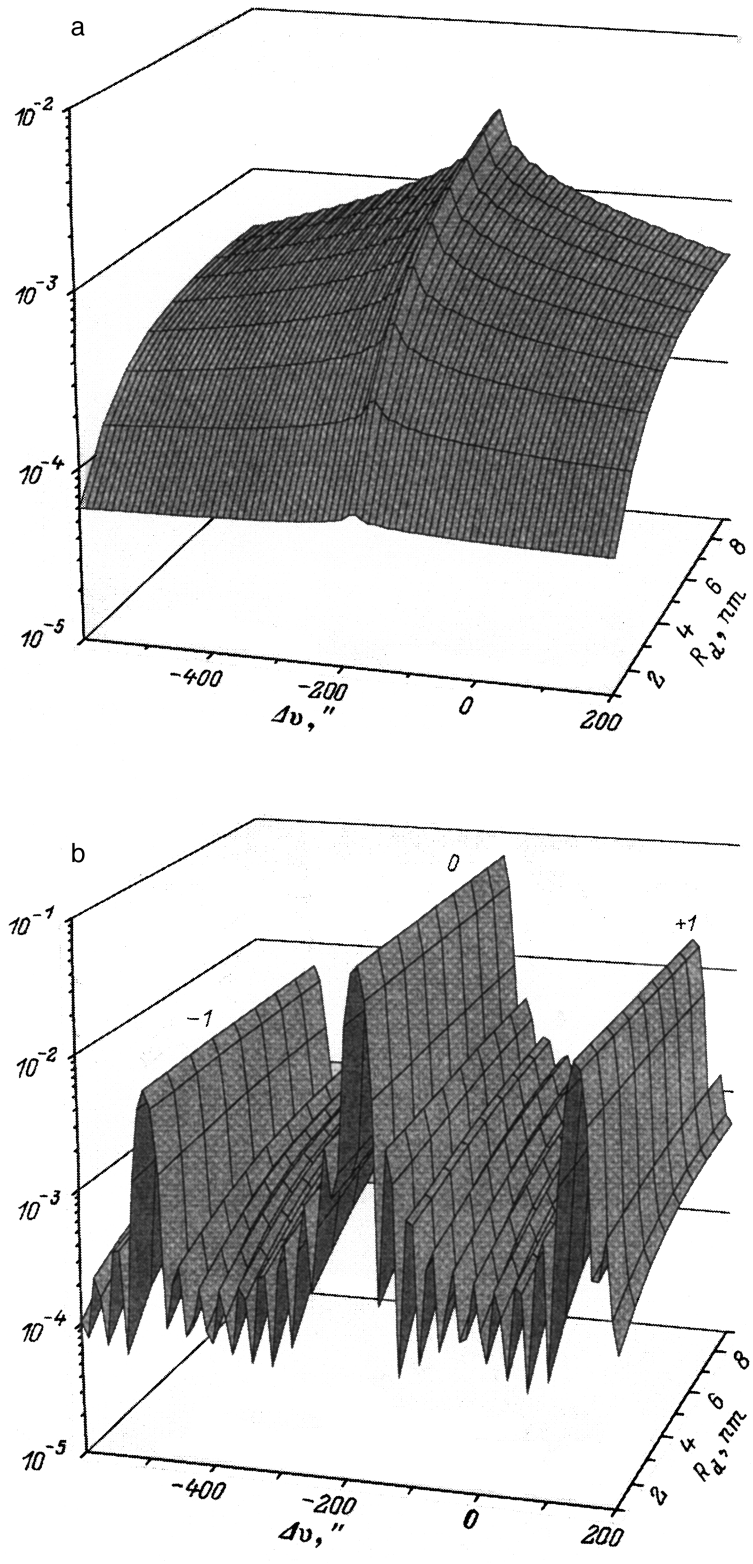

FIG. 1. Theoretical dependences of the angular distributions of the diffuse component (a) and the total scattered intensity (b) of a 10-period semiconducting 30 nm AlAs/30 nm GaAs superlattice on the cluster radius.

GaAs crystal. Two-crystal experimental diffraction reflection curves (Fig. 5a and b) of the superlattice were taken in the neighborhood of the (004) peak of the substrate. The (004) reflection from a perfect Ge crystal was used to monochromatize the x rays. The beam incident on the sample was stopped by horizontal and vertical slits of 0.1 and 2 mm widths, respectively. The experimental curve of Fig. 5b was obtained with a 0.1 mm slit placed between the sample and

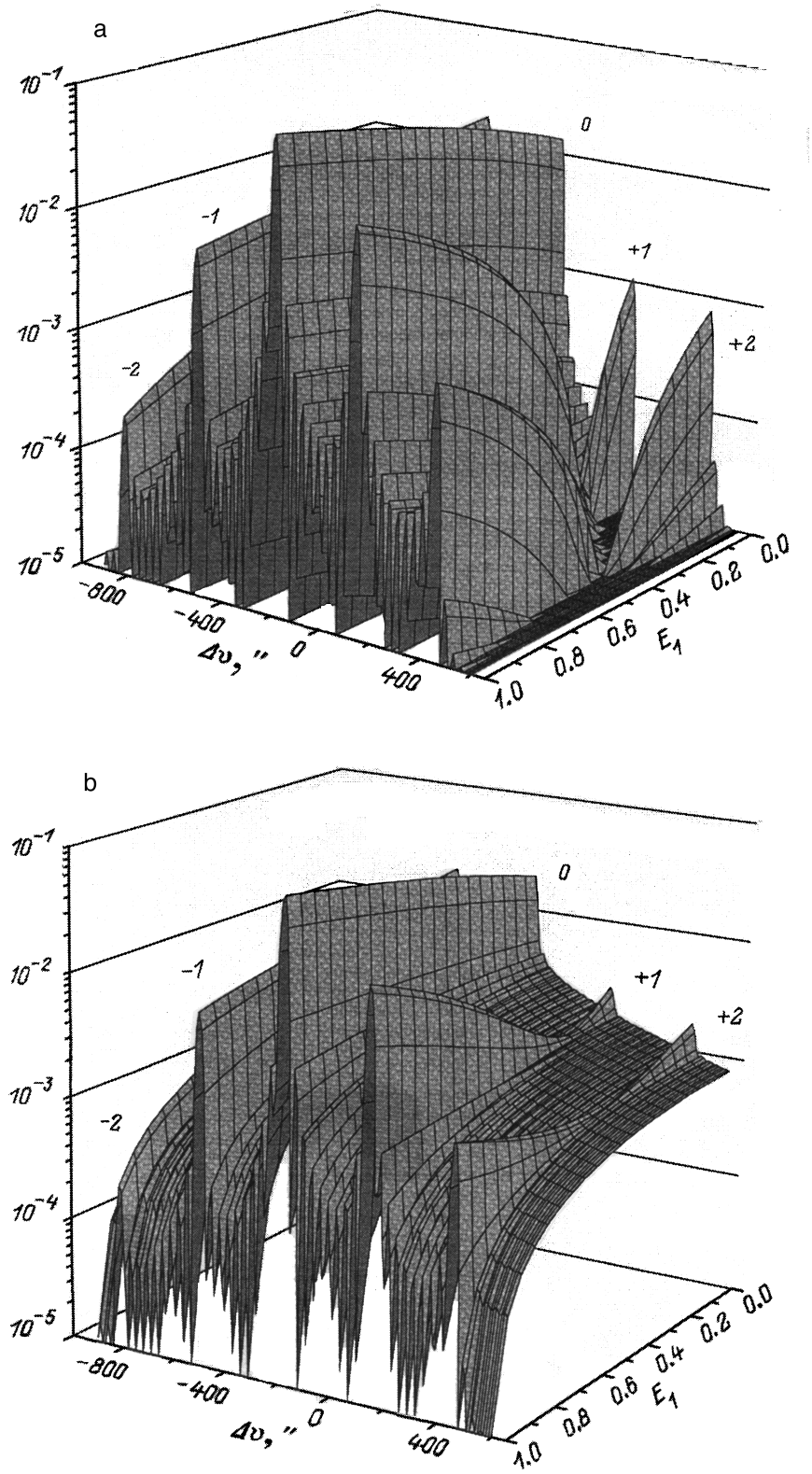

FIG. 2. Theoretical dependences of the angular distributions of the coherent component (a) and the total scattered intensity (b) on the static Debye–Waller factor E_1 of the first layer of a superlattice period. The superlattice is the same as in Fig. 1.

the detector (at a distance of 185 mm from the sample and 45 mm from the detector) in order to reduce the diffuse component of the scattered intensity. The curve of Fig. 5a was obtained without a slit.

During epitaxial growth, 20 pairs of 0.5-Å-thick InAs and roughly 300-Å-GaAs layers were deposited. An analysis of the experimental data, however, only revealed 19 periods. Using the relationship between the angular separation $\Delta\vartheta_l$ between satellites and the thickness l of a period,

$$\Delta\vartheta_l=\frac{\lambda|\gamma_g|}{l\sin 2\vartheta_B},$$

we obtain the following result: $l=261\pm 4$ Å. In addition, with the aid of the standard formula

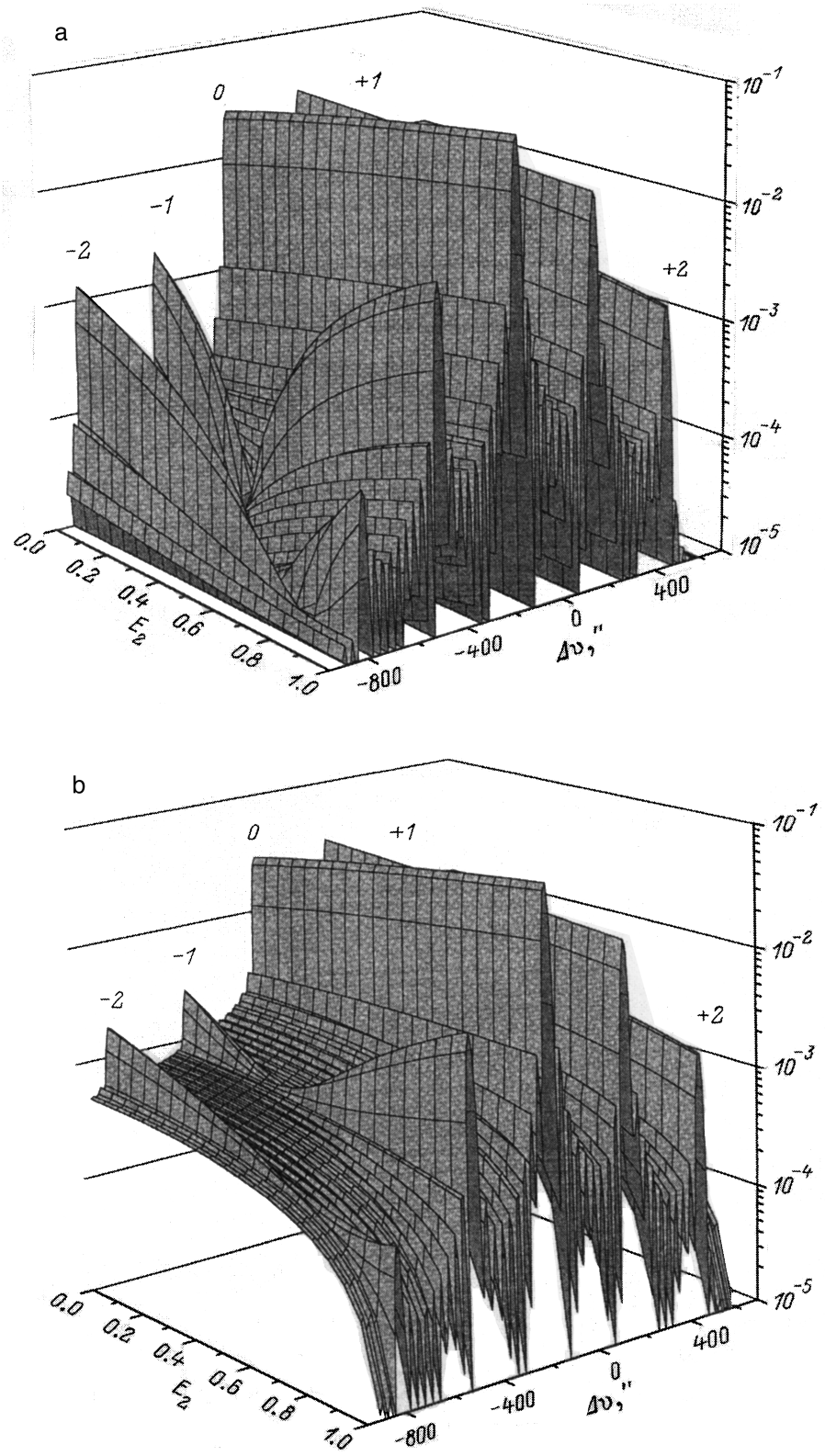

FIG. 3. Theoretical dependences of the angular distributions of the coherent component (a) and the total scattered intensity (b) on the statistical Debye–Waller factor E_2 for the second layer of a superlattice period. The superlattice is the same as in Fig. 1.

$$\Delta\vartheta_0 = -\frac{\Delta d}{d_0} K_1 \cdot x_{av} \tan\vartheta_B ,$$

where $\Delta d/d_0$ is the relative difference in the lattice parameters of the unstressed InAs and GaAs layers and K_1 is the Honstra coefficient for InAs, the magnitude of the angular deviation $\Delta\vartheta_0$ of the central superlattice peak from the substrate peak yielded an average (over the superlattice period) molar fraction of indium $x_{av} = (23 \pm 3) \times 10^{-4}$.

Since the thickness of the InAs layers during epitaxial growth was less than a monolayer, it was necessary to con-

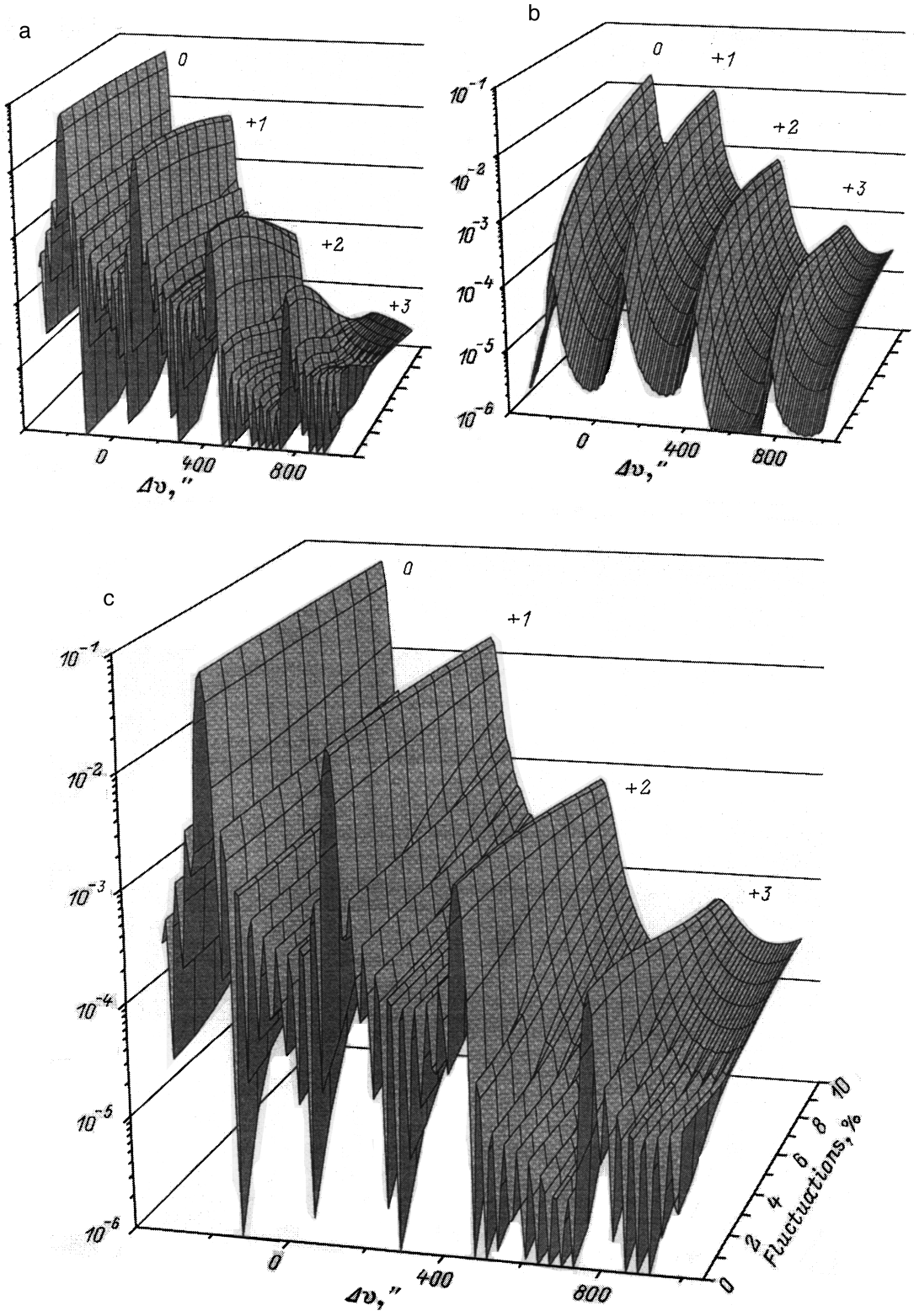

FIG. 4. Theoretical dependences of the angular distributions of the coherent (a) and diffuse components (b) and of the total scattered intensity (c) on the magnitude of the relative fluctuations in the thickness of the superlattice layers. The superlattice is the same as in Fig. 1.

sider a monolayer of $In_xGa_{1-x}As$, rather than a thin layer of InAs. This, in turn, allows us to find the thicknesses of the layers in the period, $l_{(InGa)As}$ and l_{GaAs}, and the molar fraction x of indium in the $In_xGa_{1-x}As$ layer ($l_{(InGa)As}=3.116 \pm 0.004$ Å, $l_{GaAs}=258\pm 4$ Å, and $x=0.19\pm 0.01$). The molar fraction estimate was refined to $x=0.22\pm 0.01$ during the course of numerically comparing the theoretical and experimental diffraction reflection curves.

Some theoretical diffraction reflection curves based on the superlattice parameters obtained from the numerical cal-

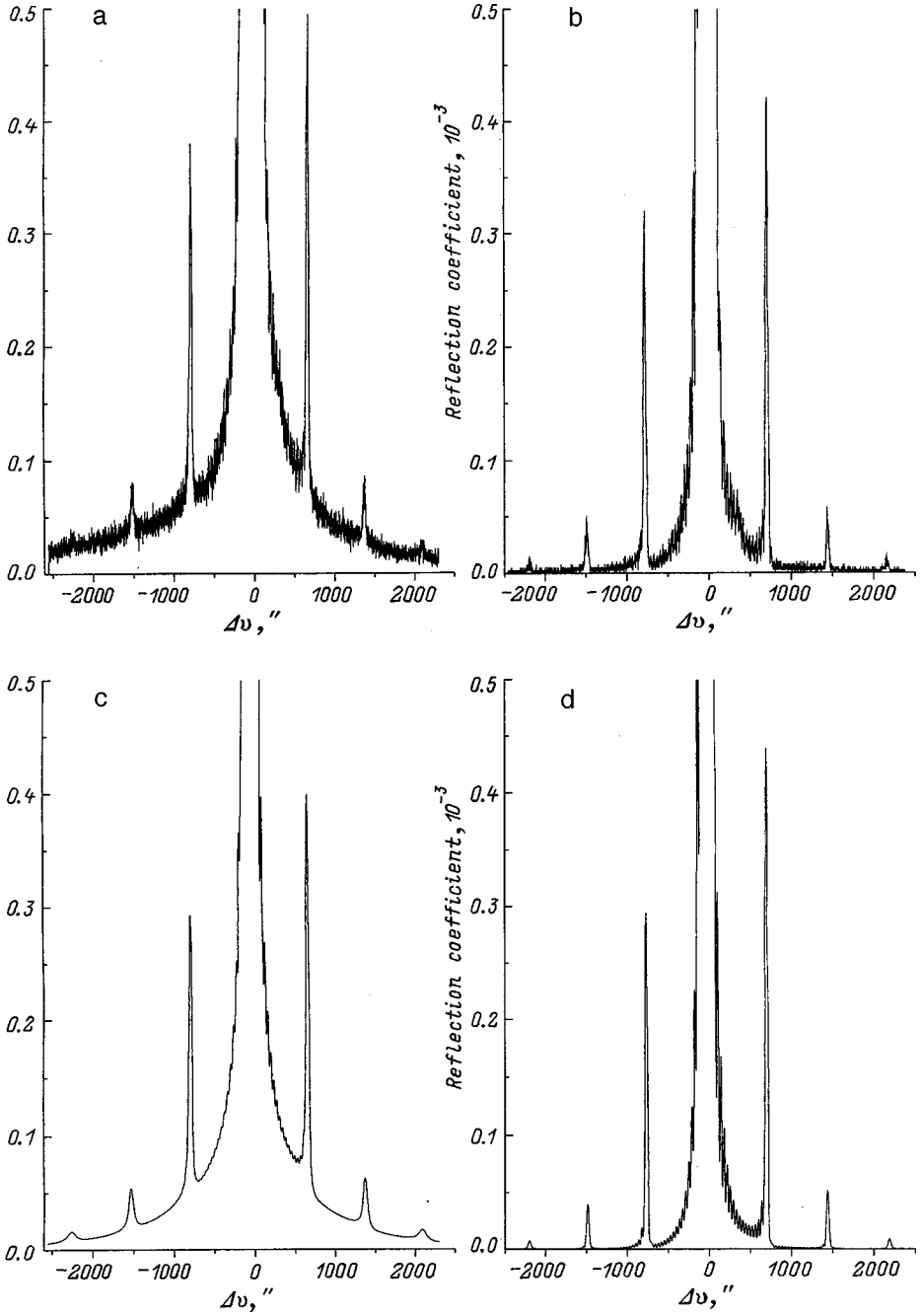

FIG. 5. Experimental (a, b) and the corresponding theoretical (c, d) diffraction reflection curves for a semiconducting (InGa)As/GaAs/ . . . /(001)GaAs superlattice.

culations are shown in Fig. 5c and d. These curves have been calculated using the formulas obtained in this paper for the corresponding experimental curves of Fig. 5a and b. In calculating the theoretical curves we have taken into account (1) the polarization and instrument function of the distribution of the radiation incident on the sample crystal (a Gaussian function was used for the latter), (2) fluctuations in the thicknesses of the superlattice layers, and (3) microdefects uniformly distributed over the superlattice thickness.

It was possible to obtain satisfactory agreement between the experimental and theoretical reflection curves for the following parameters: a width of 17 ± 2 for the instrument function distribution of the incident beam, $\Omega_1=8\pm1$ Å, $\Omega_2=0.09\pm0.01$ Å, a defect radius $R_d=8$ nm, and a static Debye–Waller factor $E=0.98$.

Using a narrow slit in front of the detector greatly reduces the diffuse component of the scattered intensity. Calculations showed that for the experimental geometry and microdefects having a radius of 10 nm, a 0.1-mm-wide slit in front of the detector allowed only a few percent of the diffusely scattered intensity to pass. For this reason only the coherent component of the scattered intensity is shown in Fig. 5d for comparison with the corresponding experimental curve (Fig. 5b).

[1] V. I. Punegov, Fiz. Tverd. Tela **32**, 2476 (1990) [Sov. Phys. Semicond. **32**, 1438 (1990)].
[2] V. I. Punegov, Pis'ma Zh. Tekh. Fiz. **18**(4), 66 (1992) [Tech. Phys. Lett. **18**, 120 (1992)].
[3] V. I. Punegov and K. M. Pavlov, Kristallografiya **38**(5), 34 (1993).
[4] V. Holý, J. Kuběna, and K. Ploog, Phys. Status Solidi B **162**, 347 (1990).
[5] V. Holý, J. Kuběna, I. Ohlidal, and K. Ploog, Superlattices Microstruct. **12**, 25 (1992).
[6] V. Holý, Appl. Phys. A: Solids Surf. **58**, 173 (1994).
[7] V. Holý, J. Kuběna, W. W. van den Hoogenhof, and I. Vávra, Appl. Phys. A: Solids Surf. **60**, 93 (1995).
[8] I. R. Prudnikov, Vest. Mosk. Univ. Ser. 3. Fiz. Astron **36**(4), 74 (1995).
[9] V. I. Punegov and Ya. I. Nesterets, Pis'ma Zh. Tekh. Fiz. **20**(16), 62 (1994) [Tech. Phys. Lett. **20**(8), 674 (1994)].
[10] K. M. Pavlov and V. I. Punegov, Kristallografiya **41**, 621 (1996).
[11] V. I. Punegov, Fiz. Tverd. Tela **37**, 1134 (1995) [Semiconductors **37**, 617 (1995)].

Translated by D. H. McNeill

Gas sensitivity of silicon carbide-based diode structures

V. I. Filippov, V. F. Sinyanskiĭ, A. A. Terent'ev, and S. S. Yakimov

Kurchatov Institute Russian Science Center, 123182 Moscow, Russia

P. A. Ivanov

A. F. Ioffe Physicotechnical Institute, Russian Academy of Sciences, 194021 St. Petersburg, Russia
(Submitted November 17, 1997)
Zh. Tekh. Fiz. **69**, 54–57 (February 1999)

Modification of the electrophysical characteristics of Pt/6H–SiC by hydrogen treatment is investigated. It is found that the change in the bias voltage of a Pt/6H–SiC structure for a fixed capacitance is related to the hydrogen concentration by the Nernst equation. The sensor response at 150 °C is 39 mV per decade of variation of the hydrogen concentration. The changes in the forward and reverse currents and the differential resistances of the diode structure in a hydrogen-containing atmosphere are calculated. The shift of the current–voltage characteristic toward negative voltages and the decrease in the differential resistance of the junction are caused by a decrease in the height of the potential barrier of the Schottky barrier as a result of dissociative adsorption of hydrogen with the formation of a double charged layer at the metal–semiconductor boundary. At a working temperature around 150 °C the characteristics of the structures are stable. We also investigated the effect of a temperature anneal (500 °C). The formation of platinum silicides at this temperature leads to degradation of the gas-sensitive properties of the metal–semiconductor junction.
[S1063-7842(99)01002-8]

INTRODUCTION

Semiconductor structures (MIS capacitors, field-effect transistors, Schottky diodes) with electrodes fabricated from catalytically active metals (metals of the platinum group) are used as primary converters in gas sensors — devices recording changes in the concentration of some gas. As a result of reactions taking place at the three-phase boundary (metal–gas–subgate layer), there occurs a change in the electrophysical characteristics of the structures: the flat-band voltage, the threshold voltage, and the forward and reverse currents.[1] A change in any of the above-enumerated characteristics, by virtue of being related to a change in the concentration of the investigated gas, can be considered as a sensor signal. Depending on the structure of the active electrode, the material of the subgate layer, and, finally, the working temperature, gas sensors have sensitivity to hydrogen, gases with polar molecules (carbon monoxide, ammonia, water vapor), saturated hydrocarbons, and fluorine.[2,3] In order to raise the working temperature of the sensor, which is very important in a number of practical applications (e.g., in diagnostics of engine exhaust gases), the wide-gap semiconductor silicon carbide is used instead of silicon. Devices based on 6H–SiC, which has a band gap of around 3 eV, can operate up to 600° (Ref. 4). The authors of Ref. 5 investigated the characteristics of a gas sensor based on the structure $Pt/SiO_2/SiO$ for diagnostics of hydrogen and hydrogen-containing gases. It was noted that an important aspect of the stable operation of the sensor is the quality of the SiO_2 layer grown on the silicon surface.

The presence of sodium ions in the SiO_2 layer leads to drift of the sensor signal[6] upon interaction with hydrogen. This phenomenon, which has come to be referred to as hydrogen-induced drift (HID), increases in intensity with increase of the temperature. In addition, as a result of the interaction of hydrogen with the insulator at elevated temperatures, the formation of unstable chemical bonds of the type Si–H and Si–OH, inducing complex physical phenomena during aging, is important.[7] This study noted a degradation of the $Pt/SiO_2/Si$ structure at temperatures around 150 °C associated with diffusion of platinum atoms in SiO_2 over oxygen vacancies and the formation of a Pt_2Si layer moving toward the Si/SiO_2 interface.

The absence of an oxide layer or, in other words, the use of a Schottky diode as the sensing element, allows us to eliminate the influence of an oxide layer on the operation of the structure. The authors of Ref. 8 considered the operation of a gas sensor based on the diode structure Pd/6H–SiC. They observed a sensitivity of the Pd/SiC Schottky diode to hydrogen and hydrocarbons.

The use of platinum as the gate material instead of palladium allows one to avoid structural changes in the electrode due to the cyclic action of hydrogen[9] and also to reduce the effect of oxygen on the sensor signal.[10] The aim of the present work is to examine the action of hydrogen on the electrophysical characteristics of Pt/SiC Schottky diodes and the effect of a temperature anneal on the stability of these characteristics.

METHODS OF STUDY, DEVICES, AND INSTRUMENTATION

As our experimental samples we used crystals of *n*-6H–SiC with dimensions 4×4 mm^2 with grown-on *n*-type

homoepitaxial films. An epitaxial layer of thickness around 5 μm was grown by vacuum sublimation epitaxy on the polar (0001) face of a 6H–SiC crystal. The electron concentration in the epitaxial layer was 3.2×10^{16} cm^{-3}. A high-temperature Ohmic contact was formed on the substrate: pressed-on nickel with tungsten deposited above it.

A platinum electrode of diameter 0.7 mm and thickness around 600 Å was deposited on the epitaxial film by magnetron sputtering in an argon atmosphere. To stabilize the morphology of the platinum electrode, the structures were annealed in air at 300 °C for 30 min.

The structures were placed in a gas cell, where they were mounted directly to the heating element. To avoid oxidation at high temperatures, the contacts to the gate and to the Ohmic contact were prepared from graphite. The cell (working volume 50 cm^3) with the investigated structure was connected to the dynamic-mixing gas stand. The RGD-9 automated control system for the gas-flow regulators enabled us to form gas fluxes with a hydrogen concentration from 10 to 1000 ppm with a steady total flow rate of 10 cm^3/s. As the carrier gas we used either helium or synthetic air.

We measured the high-frequency (10 kHz) capacitance–voltage and current–voltage characteristics of the diode structures. The measurement complex, based on standard devices (a 1250 frequency analyzer and an E7-12 *LCR* meter), allowed us not only to measure the characteristics of the structures, but also enables regimes of operation that are characteristic when testing the gas-sensitivity of MIS sensors, specifically measurement of the change in the bias voltage for fixed capacitance of the structure as the gas is let into the cell.

RESULTS AND DISCUSSION

A high-frequency capacitance–voltage characteristic of a Pt/6H–SiC diode structure at 150 °C is shown in Fig. 1a. From the dependence of $1/C^2$ on the applied bias voltage we have estimated the height of the potential barrier at the platinum–silicon carbide interface (Fig. 1b) as 1.3 ± 0.1 eV.

The action of hydrogen on the structure shifts the characteristics toward negative voltages. Figure 2 plots the kinetics of the change in the bias voltage (for a constant capacitance of 275 pF) for successive feed to the measurement chamber of pure synthetic air followed by an air mixture with a hydrogen concentration of 50, 400, and 800 ppm. The working temperature of the structure was 150 °C. At this temperature the response of the structure to the action of hydrogen had a stable and reproducible character, but the processes of interaction with hydrogen were quite rapid. The steady-state value of the change in the bias voltage upon hydrogen being fed to the cell was reached after a time on the order of an minute.

The dependence of the change in the bias voltage on the hydrogen concentration is described by the Nernst equation

$$\Delta U = E = E^0 - 2.3\frac{RT}{ZF}\log\left(\frac{C_{H_2}}{C_{H_+}^2}\right), \qquad (1)$$

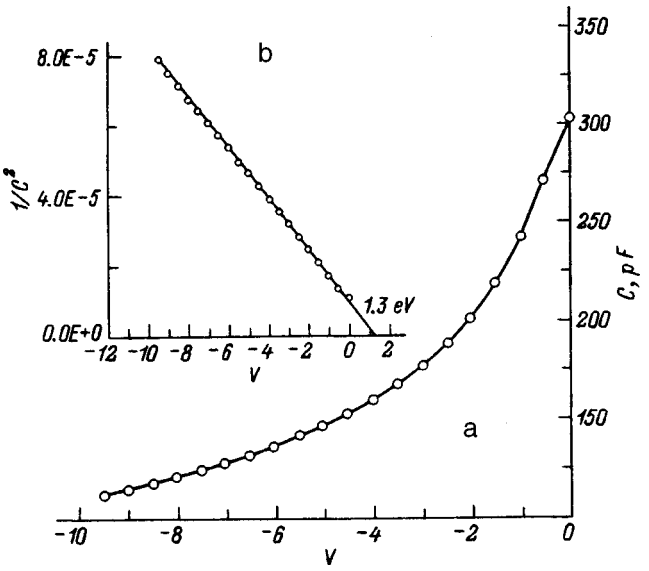

FIG. 1. a — High-frequency capacitance–voltage characteristic of the structure Pt/*n*-6H–SiC, b — dependence of the square of the reverse capacitance of the structure on the bias voltage. Height of the potential barrier at the metal–semiconductor interface 1.3 eV. Temperature of the structure 150 °C.

where R is the universal gas constant, T is the absolute temperature, F is the Faraday number, Z is the number of electrons participating in the reaction, C_{H_2} is the activity of gaseous hydrogen, C_{H_+} is the activity of protons at the metal–semiconductor interface (Fig. 3).

At 150 °C for $Z=2$ it follows from Eq. (1) that the response of the sensor should be 41.9 mV per decade of variation of the hydrogen partial pressure. This stands in good agreement with the value of 39 mV obtained from the experiment. This allows us to speak of dissociative adsorption of hydrogen at the metal–semiconductor interface with formation of a double charged layer and an absence of any

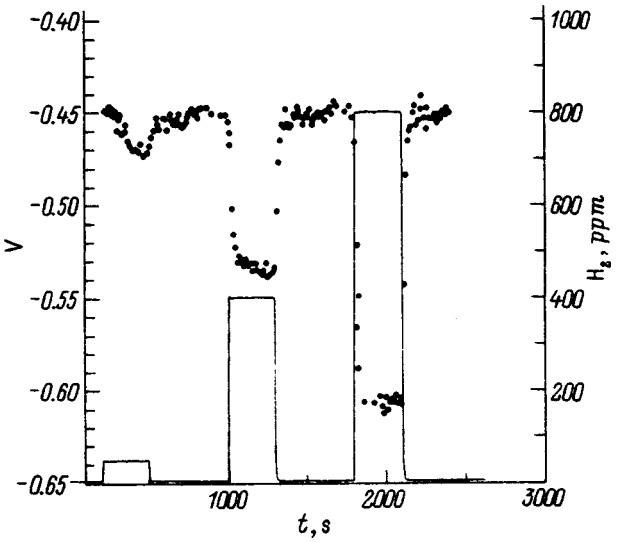

FIG. 2. Variation of the bias voltage for fixed capacitance of the structure (275 pF) for successive feed to the measurement chamber of air and an air mixture with a hydrogen concentration of 50, 400, and 800 ppm. Temperature of the structure 150 °C.

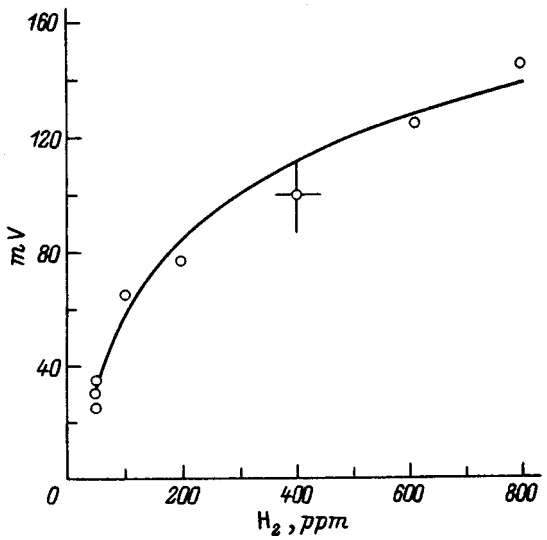

FIG. 3. Dependence of the change in the bias voltage of a Pt/6H–SiC structure on the hydrogen concentration of the hydrogen–air mixture: ○ — experimental data points, solid curve — theoretical dependence $\Delta U = 39 \log C_{H_2}$. Temperature of the structure 150 °C.

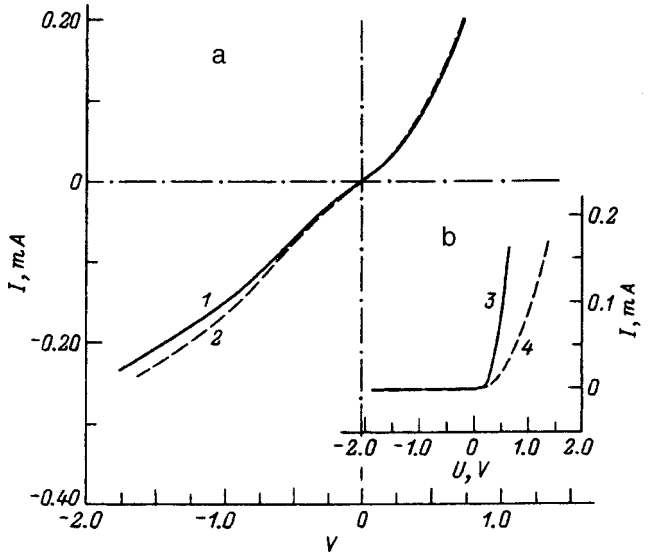

FIG. 5. a — CVC of the structure in a helium atmosphere (*1*) and for a hydrogen concentration of 100 ppm (*2*) (the Pt/6H–SiC structures were kept at a temperature of 500 °C for 100 h), temperature of the structure 150 °C; b — CVC of the structure at room temperature before (*3*) and after (*4*) temperature treatment.

interaction between the adsorbed hydrogen and the surface states of the semiconductor. Such an interaction was observed in a study of Schottky diodes (and structures a tunnel-thin insulator) based on silicon and led to an anomalously large (7 V) shift of the capacitance–voltage characteristic upon treatment with 3000 ppm hydrogen in argon.[11]

Formation of a double charged layer upon adsorption of hydrogen changes the height of the barrier of the Pt/SiC junction, which leads to changes in the current–voltage characteristics of the structure (Fig. 4a). Thus, the differential resistance of the structure at zero bias changes by 50% upon treatment with 100 ppm hydrogen in helium. The kinetics of the change in the current through the structure for a fixed reverse bias is plotted in Fig. 4b. As in the case of the change in the bias voltage for a fixed capacitance, the current reaches its steady-state value quite rapidly (after about a minute), and no long-term drift, which is characteristic of structures with a thick oxide layer, is observed.

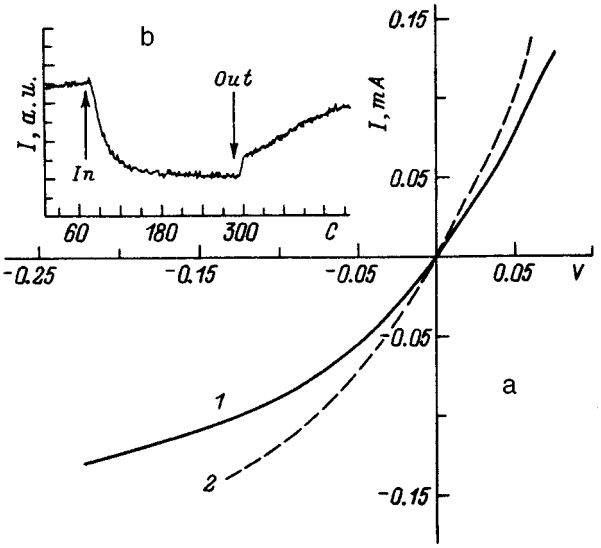

FIG. 4. a — CVC of a Pt/6H–SiC structure in an atmosphere of pure helium (*1*) and for hydrogen concentration in helium 100 ppm (*2*), temperature of the structure 150 °C; b — kinetics of the change in the reverse current through the structure (arbitrary units) in response to a change in the hydrogen concentration in the measurement chamber.

The saturation current density of a Schottky barrier is described by the expression

$$I_0 = \xi A^* T^2 \exp\left(-\frac{e\varphi_B}{kT}\right), \tag{2}$$

where e is the charge of the electron, k is Boltzmann's constant, T is the absolute temperature, ξ is the probability of an electron tunneling through the thin insulating layer (if it exists), A^* is the effective Richardson constant, and φ_B is the height of the Schottky barrier.[12]

However, the large currents on the reverse branch of the CVC associated with leakage due to inhomogeneity of the structures did not allow us to obtain the exponential growth of the current expected from expression (2) in response to the decrease in the height of the potential barrier caused by adsorption of hydrogen at the metal–semiconductor interface.

At working temperatures around 150 °C the structures exhibited a high stability in their current–voltage and capacitance–voltage characteristics. Heating to a temperature of 150 °C for 240 h in an atmosphere of synthetic air did not lead to a change in the maximum capacitance of the structure, as was observed in Ref. 7 for $Pt/SiO_2/Si$, or in the differential resistance of the structure at zero bias. When the annealing temperature was raised to 500 °C, a change in the current–voltage characteristics was observed after 100 h. A change in the reverse current through the structure in response to hydrogen treatment is observed in this case at large bias voltages (Fig. 5a). The change in the CVC (Fig. 5b) and, in particular, in the differential resistance of the junction are

apparently connected with the formation of platinum silicides. The formation of palladium silicides at the Pt–SiC interface at temperatures on the order of 500 °C was also observed experimentally in Ref. 8 by Auger spectroscopy.

CONCLUSIONS

We have shown that the action of hydrogen on a Pt/6H–SiC structure alters its electrophysical characteristics. Formation of a double charged layer of protons at the metal–semiconductor interface leads to a change in the height of the potential barrier and, as a consequence, to a shift of the capacitance–voltage characteristic and a decrease in the differential resistance of the structure.

It is possible to realize the high-temperature properties of the semiconductor material and stabilize the characteristics of a Pt/6H–SiC structure by decreasing the leakage currents by enhancing the homogeneity of the metal–semiconductor interface, and by introducing a buffer layer between the Pt and SiC to prevent the formation of silicides.

[1] J. Janata and R. J. Hubert (eds.), *Solid State Chemical Sensors*, Academic Press, New York, 1985.
[2] I. Lundström, A. Spetz, F. Winquist *et al.*, Sens. Actuators B **1**, 15 (1990).
[3] W. Moritz, V. Filippov, L. Bartolomäus *et al.*, in *Proceedings of the International Conference on Solid State and Actuators*, Chicago, 1997, pp. 1073–1076.
[4] P. A. Ivanov and V. E. Chelnokov, Fiz. Tekh. Poluprovodn. **29**, 1921 (1995) [Semiconductors **29**, 1003 (1995)].
[5] A. Spetz, A. Arbab, and I. Lundström, in *Proceedings of the Fifth SiC and Related Materials Conference*, Washington, 1993, pp. 629–632.
[6] C. Nylander, M. Armgarth, and C. Svensson, J. Appl. Phys. **56**, 1177 (1984).
[7] M. O. Duchenko and V. M. Kalygina, Poverkhnost', No. 1, 65 (1995).
[8] L.-Y. Chen, G. W. Hunter, P. G. Neudeck *et al.*, *Transactions of the Third International High Temperature Electronics Conference*, Albuquerque, New Mexico, 1996, pp. 17–22.
[9] L. I. Kikoin, A. A. Terent'ev, V. I. Filippov, and S. S. Yakimov, Zh. Tekh. Fiz. **64**(7), 131 (1994) [Tech. Phys. **39**, 703 (1994)].
[10] V. Filippov, A. Terentjev, and S. Yakimov, Sens. Actuators B **17**, 121 (1994).
[11] K. Ito, T. Nakazawa, and A. Tamagawa, in *Proceedings of the Third Sensor Symposium*, 1983, pp. 191–194.
[12] S. M. Sze, *Physics of Semiconductor Devices*, Wiley, New York, 1969; Énergiya, Moscow, 1973, 655 pp.

Translated by Paul F. Schippnick

Thin-film electroluminescent devices excited by a linearly rising voltage

N. T. Gurin and O. Yu. Sabitov

Ulyanovsk State University, 432700 Ulyanovsk, Russia
(Submitted July 30, 1997)
Zh. Tekh. Fiz. **69**, 58–63 (February 1999)

The average and instantaneous luminances of a thin-film electroluminescent device (TFELD) are determined as functions of the voltage rise time by solving kinetic equations for the concentration of excited emission centers in the electroluminescent layer of the device. It is shown theoretically and experimentally that the dependences of the average and peak luminances, the external and internal quantum yield, the energy yield, and the luminous efficacy as functions of the voltage rise time all have a maximum, and the position of that maximum depends on the frequency of the driving voltage. The calculated and experimental dependences make it possible to determine the main parameters of the electroluminescence process: the collisional excitation cross section for the emission centers, the concentration of emission centers, and the transition probability of the emission centers to an excited state, as well as the radiative and nonradiative recombination probabilities of these and other centers. [S1063-7842(99)01102-2]

Our earlier studies[1,2] indicate that the luminance (brightness) and luminous efficacy of thin-film electroluminescent devices (TFELDs) change significantly when the shape of the driving voltage pulse is varied, increasing for higher rates of rise of the voltage, the other conditions being the same.

In this paper we analyze the changes in the luminance and luminous efficacy during excitation of TFELDs by a symmetric, sign-changing trapezoidal voltage pulse with a linearly rising front[1] to determine the optimum excitation conditions in terms of maximum luminance and luminous efficacy, as well as to determine the physical parameters characterizing the electroluminescence process in these structures.

The theoretical analysis of the operation of TFELDs under these excitation conditions is predicated on the collisional excitation of emission centers by free charge carriers, a typical model for electroluminescent structures based on zinc sulfide phosphors. The kinetics of the concentration of excited emission centers is described by the following equation:[3]

$$\frac{dN^*(t)}{dt}=\alpha[N-N^*(t)]-\frac{N^*(t)}{\tau}-\beta N^*(t), \tag{1}$$

where N is the concentration of emission centers; $N^*(t)$ is the concentration of excited emission centers; $\alpha(t)=\sigma j(t)/e$ is the probability of a transition of an emission center from the ground to an excited state per unit time, where σ is the collision excitation cross section for an emission center, $j(t)$ is the conduction current density in the phosphor film which causes it to radiate, and e is the charge of the electron; τ is the relaxation time constant of the excited emission centers; and, β is the nonradiative transition probability for these centers per unit time.

As before,[4] in the analysis we have assumed that the insulators are homogeneous and that there are no dielectric losses. The electroluminescent structure is symmetric and the luminance waveforms are the same in the different half periods of the driving voltage.

We shall solve Eq. (1) assuming a low level of excitation, where σ is independent of the electric field strength, and include nonradiative processes. Introducing the notation

$$\tau^*=\left(\frac{1}{\tau}+\beta\right)^{-1} \tag{2}$$

and using the expression $j(t)=C_{d0}(dV/dt)=C_{d0}(V_m/t_m)$ for the active current density, where C_{d0} is the specific capacitance formed by the insulating layers of the electroluminescent structure and t_m is the time when the driving voltage reaches an amplitude of V_m,[1,4] we find, by analogy with Ref. 1, the variation in the concentration of excited centers during the time when the driving voltage is rising to its maximum V_m,

$$N_r^*(t)=C\exp\left[-\left(\alpha+\frac{1}{\tau^*}\right)t\right]+\frac{\alpha N}{\alpha+1/\tau^*}, \tag{3}$$

and during the time of the flat peak and fall of the voltage pulse,

$$N_{\rm dec}^*(t)=C\exp\left(-\frac{t}{\tau^*}\right), \tag{4}$$

where the C's are constants determined by the initial conditions.

Substituting the solutions (3) and (4), subject to the initial conditions, into the equation

$$L(t)=\eta_c d_{\rm lum}\frac{N^*(t)}{\tau^*}, \tag{5}$$

which relates the emission of the electroluminescent devices to the concentration of excited emission centers, where η_c is the luminous output efficiency (quantity of light), defined by

$$\eta_c = \eta_{\text{ext}} f_\lambda h\nu, \tag{6}$$

assuming monochromatic radiation, where η_{ext} is the external quantum yield, defined as the ratio of the number of photons emitted from the surface to the total number of photons produced in the volume of the luminescent layer, where f_λ is the coefficient of luminosity of the radiation, $h\nu$ is the energy of the emitted photons (h is Planck's constant), and d_{lum} is the thickness of the phosphor layer,[3] we obtain the time dependence of the instantaneous luminance as the driving voltage rises from its threshold V_{thr} at the time t_{thr} when the emission from the TFELD begins ($L_r(t_{\text{thr}})=0$) until the time t_m when the voltage reaches its peak V_m,

$$L_r(t) = \frac{\eta_c d_{\text{lum}} N}{\tau^*} \frac{\alpha}{\alpha + 1/\tau^*}\left[1-\exp\left[-\left(\alpha+\frac{1}{\tau^*}\right)(t-t_{\text{thr}})\right]\right]. \tag{7}$$

Equation (7), which is valid for low repetition rates of the driving voltage pulses, where luminance falls essentially to zero during a half period, i.e., for $(4-5)\tau \leqslant T/2$ (where T is the repetition period of the driving voltage pulses), can be used to determine the luminance rise time

$$\tau^{**} = \left(\alpha+\frac{1}{\tau^*}\right)^{-1}. \tag{8}$$

Similarly, taking the initial conditions to be equality of the peak luminance during its rise and fall, i.e., $L_r(t_m) = L_{\text{dec}}(t_m)$, we find an expression for the drop in luminance with time,

$$L_{\text{dec}}(t) = \frac{\eta_c d_{\text{lum}} N}{\tau^*} \frac{\alpha}{\alpha + 1/\tau^*}\left[1-\exp\left[-\left(\alpha+\frac{1}{\tau^*}\right)\times(t_m - t_{\text{thr}})\right]\right]\exp\left(-\frac{t-t_m}{\tau^*}\right), \tag{9}$$

which can be used to determine τ^*. In general, for an arbitrary voltage pulse repetition rate, at t_m, given that

$$\alpha = \frac{a}{t_m}, \tag{10}$$

where $a = \sigma C_{d0} V_m / e$, we obtain the peak luminance as a function of the voltage rise time,

$$L_m(t_m) = \eta_c d_{\text{lum}} N \frac{a}{a\tau^* + t_m}\left[1-(1-A)\times\exp\left[-\left(a+\frac{t_m}{\tau^*}\right)\left(1-\frac{1}{n}\right)\right]\right], \tag{11}$$

where

$$A = \left[1-\exp\left[-\left(\alpha+\frac{1}{\tau^*}\right)(t_m - t_{\text{thr}})\right]\right] \times \exp\left(-\frac{t_{\text{thr}} + T/2 - t_m}{\tau^*}\right),$$

$n = V_m / V_{\text{thr}}$, A characterizes the nonzero initial conditions which occur during the steady state at high pulse repetition rates ($(4-5)\tau > T/2$).

Equation (11) implies that $L_m(t_m)$ increases as the excitation pulse repetition period T decreases.

At low frequencies, for $t_m = \tau^*$ the peak luminance L_m is given by

$$L_m(\tau^*) = \frac{\eta_c d_{\text{lum}} N a}{\tau^*}\left[1-\exp\left[-\left(1-\frac{1}{n}\right)\right]\right]. \tag{12}$$

For $t_m = a\tau^*$, L_m is given by

$$L_m(a\tau^*) = \frac{\eta_c d_{\text{lum}} N}{2\tau^*}\left[1-\exp\left[-2\frac{\sigma C_{d0}}{e}(V_m - V_{\text{thr}})\right]\right]. \tag{13}$$

As the voltage rise time approaches zero, i.e., for excitation by rectangular voltage pulses, L_m approaches

$$L_m(t_m \to 0) = \frac{\eta_c d_{\text{lum}} N}{\tau^*}\left[1-\exp\left[-\frac{\sigma C_{d0}}{e}(V_m - V_{\text{thr}})\right]\right]. \tag{14}$$

The theoretical analysis of the function (11) is extremely cumbersome. However, Eq. (11) does imply that for $\alpha \ll 1/\tau^*$, which corresponds to the region of large t_m, the peak luminance $L_m \propto \alpha \propto 1/t_m$, i.e., it falls as the reciprocal of t_m. For $\alpha \gg 1/\tau^*$ we have $L_m \propto a(1-t/t_m)$, i.e., it increases as t_m. For $\alpha \approx 1/\tau^*$, L_m is given by Eq. (13) and is independent of t_m. Thus $L_m(t_m)$ has a maximum in the neighborhood of $\alpha \approx 1/\tau^*$, i.e., for $t_m \approx a\tau$. A numerical analysis of Eq. (11) confirms the existence of a maximum in the function $L_m(t_m)$ (Fig. 1), where the maximum shifts toward shorter voltage rise times as the frequency increases (Fig. 3a). The physical significance of the fact that the peak luminance L_m rises with decreasing voltage rise time for constant N, σ, τ, and β lies in a rise in the active current passing through the electroluminescent layer, i.e., in an increase in the rate of rise of the electron concentration within this layer, which leads to an increased excitation probability α per unit time for the emission centers. For short excitation voltage rise times, such that the condition $\alpha = (a/t_m) \gg 1/\tau^*$ is satisfied, the rate of excitation of emission centers exceeds the rate of radiative and nonradiative recombination, and L_m increases as t_m increases. For $a \sim 1/\tau^*$, the rates of excitation and recombination of the emission centers balance each other. Given the field dependence of σ,[5] according to Eq. (10) one should expect a more rapid rise in α with increasing t_m for short rise times t_m. This causes a shift in the peak of $L_m(t_m)$ to larger t_m.

Using the ratio of the peak luminances L_m at $t_m = a\tau^*$ and $t_m = \tau^*$ for the low-frequency region according to Eqs. (12) and (13), one can determine the cross section σ for elastic excitation of the emission centers,

$$\sigma = \frac{e}{C_{d0} n V_{\text{thr}}} \times \frac{(1-1/n) - [L_m(a\tau^*)/L_m(\tau^*)][1-\exp[-(1-1/n)]]}{2(1-1/n)^2}. \quad (15)$$

Taking preliminary values of a calculated for[8] $\sigma = 4 \times 10^{-16}\,\text{cm}^2$ and the ratio $L_m(a\tau^*)/L_m(\tau^*)$ determined from the experimental $L_m(t_m)$ curves, we find a value of σ which is then used to further refine the estimate of a, to further refine the value of the elastic excitation cross section, etc., until the discrepancy between the resulting values of σ is smaller than a given error. Here the systematic error in this technique is less than 1%.

Summing Eqs. (7) and (9) and taking the average of that sum over the half period of the excitation voltage, we obtain an average luminance for a linearly rising excitation voltage consistent with Talbott's law,

$$L_{\text{mid}} = \frac{2\eta_c d_{\text{lum}} \alpha N}{T\tau^*(\alpha + 1/\tau^*)} \left\{ (t_m - t_{\text{thr}}) - \frac{1-A}{(\alpha+1/\tau^*)} \times \left[1 - \exp\left[-\left(\alpha + \frac{1}{\tau^*} \right)(t_m - t_{\text{thr}}) \right] \right] + \tau^* \left[1 - (1-A)\exp\left[-\left(\alpha + \frac{1}{\tau^*} \right)(t_m - t_{\text{thr}}) \right] \times \left[1 - \exp\left(-\frac{t + T/2 - t_m}{\tau^*} \right) \right] \right] \right\}. \quad (16)$$

An analysis of Eq. (16) for the average luminance of an electroluminescent device as a function of the voltage rise time at low frequencies shows that for $t_m \gg a\tau^*$, the average luminance falls off monotonically with increasing voltage rise time.

For $t_m = a\tau^*$ at low frequencies, the average luminance is

$$L_{\text{mid}}(a\tau^*) = \frac{\eta_c d_{\text{lum}} N a}{T} \left\{ \left(1 - \frac{1}{n} \right) + \frac{1}{2a} \times \left[1 - \exp\left[-2a\left(1 - \frac{1}{n} \right) \right] \right] \right\}. \quad (17)$$

As $t_n \to 0$, i.e., for excitation by rectangular pulses, at low frequencies the average luminance approaches

$$L_{\text{mid}}(t_m \to 0) = C \left[1 - \exp\left[-a\left(1 - \frac{1}{n} \right) \right] \right] \times \left[1 - \exp\left(-\frac{T}{2\tau^*} \right) \right], \quad (18)$$

where $C = 2\eta_c d_{\text{lum}} N/T$.

For high frequencies we have

$$L_{\text{mid}}(t_m \to 0) = C \left[1 - \left(1 - \left[1 - \exp\left[-a\left(1 - \frac{1}{n} \right) \right] \right] \times \exp\left(-\frac{T}{2\tau^*} \right) \exp\left[-a\left(1 - \frac{1}{n} \right) \right] \right) \times \left[1 - \exp\left(-\frac{T}{2\tau^*} \right) \right] \right]. \quad (19)$$

Equations (16)–(19) provide a most complete description of the luminance–voltage characteristics of electroluminescent devices for different excitation voltage rise time, since these formulas relate both the physical and structural parameters of the devices (the quantities σ, V_{thr}, and C_{d0}) and parameters which characterize the excitation regime (the quantities t_m and V_m).

A numerical analysis of Eq. (15) shows that the function $L_{\text{mid}}(t_m)$, like $L_m(t_m)$, has a maximum (Fig. 2a and b) which shifts toward lower values of t_m as the frequency of the excitation voltage is raised (Fig. 3b).

A numerical simulation of Eqs. (10) and (15) with the choice of the parameters a and τ^* that yields the best agreement between the calculated and experimental curves makes it possible, using Eqs. (2), (6), (7), and (9), to determine the physical parameters that characterize the electroluminescence process: α, τ^*, σ (and, once τ is known, β as well). The value of τ is determined from the slope of an experimental plot of the decay of the luminance with time plotted in coordinates $\ln L_{\text{dec}} = f(t)$.

The other parameters characterizing the luminescence process according to Eqs. (5) and (6) are η_c and N and also the external η_{ext} and internal η_{int} quantum yields, the energy

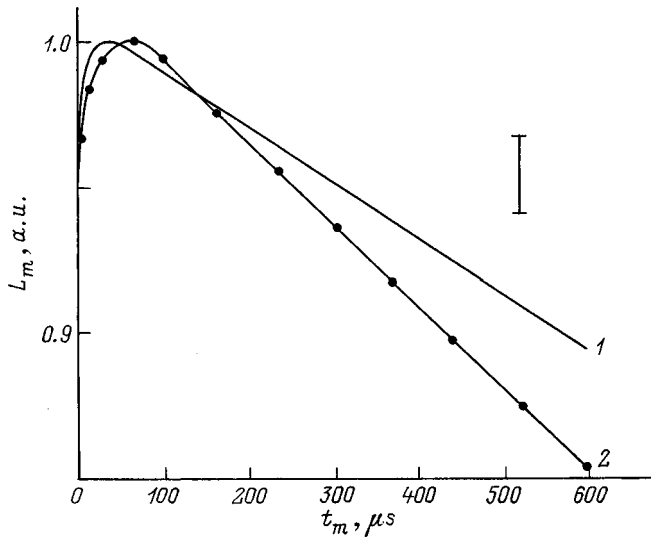

FIG. 1. The peak luminance of a TFELD as a function of the rise time of the driving voltage to V_m at a frequency of 250 Hz: *1* — calculated, *2* — experiment.

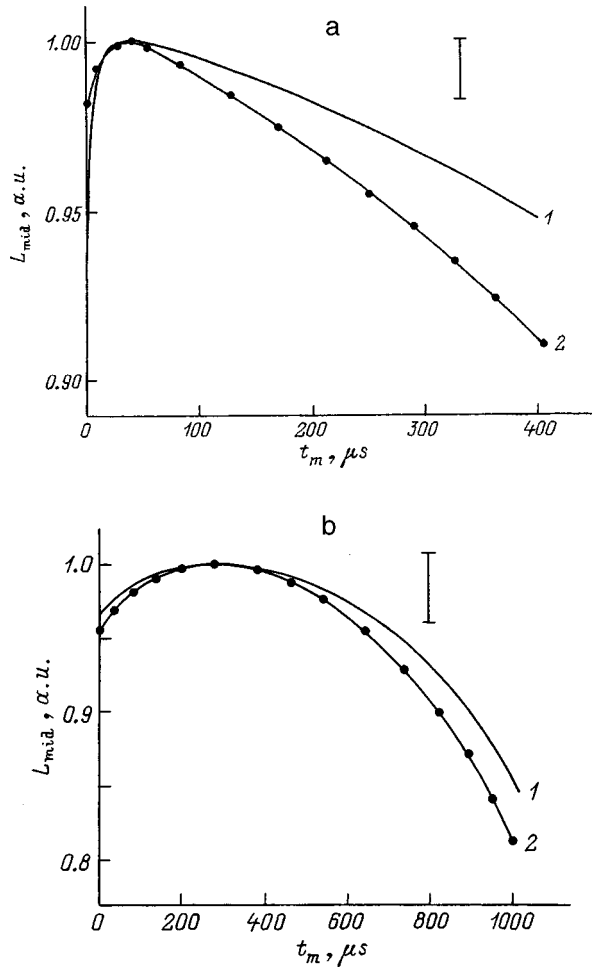

FIG. 2. The average luminance of a TFELD as a function of the rise time of the driving voltage to V_m at frequencies of 1 kHz (a) and 250 Hz (b): *1* — calculated, *2* — experiment.

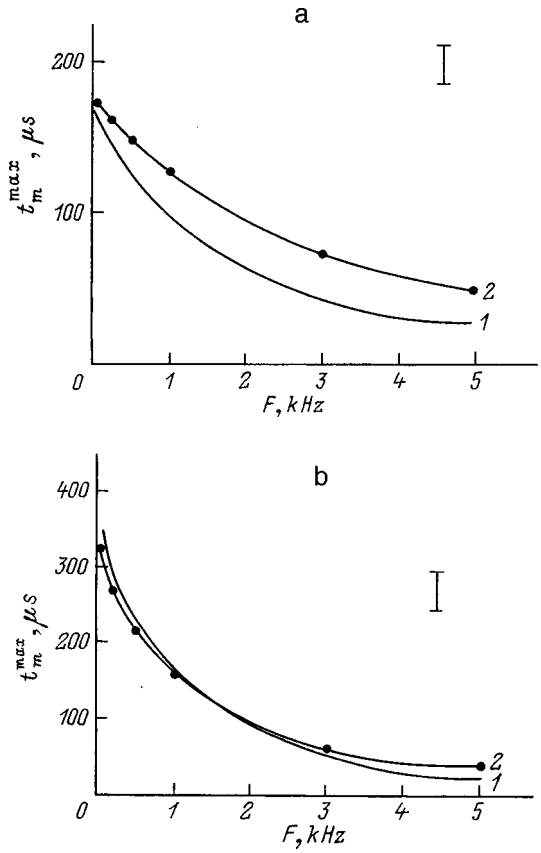

FIG. 3. The dependence of the position of the maximum of the $L_m(t_m)$ and $L_{mid}(t_m)$ luminance curves on the frequency of the driving voltage: $L_m(t_m)$ (a), $L_{mid}(t_m)$ (b); *1* — calculated, *2* — experiment.

efficiency η_w, the luminous efficacy η_L, and the number of emission centers N_1 excited by a single electron as it passes through the electroluminescent layer.[5] The external η_{ext} and internal η_{int} quantum yields are related as follows:

$$\eta_{ext} = \eta_{int} K_0, \tag{20}$$

where K_0 is a coefficient that accounts for the fraction of radiation escaping the electroluminescent device.[5]

According to Ref. 4, η_{ext} is given by

$$\eta_{ext} = \frac{\pi e L_{mid} T}{2 f_\lambda h \nu Q}, \tag{21}$$

where $Q = Q^s_{thr}(b+1)(n-1) = C_d(V_m - V_{thr})$; Q^s_{thr} is the threshold charge density in the electroluminescent layer; $Q^s_{thr} = C_{lum} V_{thr.lum}/S_{lum} = C_{lum0} V_{thr.lum}$, where S_{lum} is the area of the electroluminescent device, $V_{thr.lum}$ is the threshold voltage of the electroluminescent layer, and C_{lum0} is the specific capacitance formed by the phosphor layer; and, $b = C_{d0}/C_{lum0} = (\varepsilon_d/\varepsilon_{lum})/(d_d/d_{lum})$, where d_d, d_{lum}, and ε_{lum} are the dielectric constants of the materials and the thicknesses of the insulating and electroluminescent layers.

Using the expression (6) for η_c and the previously determined value of σ, we find N from Eq. (17) as

$$N = \frac{e L_{mid}(a\tau^*) T}{\eta_c d_{lum} \sigma C_{d0}}. \tag{22}$$

N_1 is defined by analogy with Ref. 5 as

$$N_1 = \frac{\eta_{int}}{P_{em}} = \frac{\eta_{ext}}{P_{em} K_0}, \tag{23}$$

where we find P_{em}, the radiative transition probability, by determining β and τ using Eq. (2) and proceeding from the probabilities of radiative $(1/\tau)$ and nonradiative (β) transitions per unit time to the absolute probabilities,

$$P_{em} = \frac{1/\tau}{1/\tau + \beta}. \tag{24}$$

Our previous calculations and experimental studies indicate that the charge passing through the electroluminescent layer and causing excitation of emission centers does not depend on the shape or the rise time of the driving voltage pulse.[1,4]

By analogy with the charge Q, the active power P_a expended in exciting the luminescence and caused by the conduction current is also independent of the rise time of the driving voltage when the other conditions are the same. This is confirmed by determinations of P_a from the charge–voltage characteristics and it is given by[1,4]

$$P_a = P^s_{thr}(b+1)(n-1) S_{lum}, \tag{25}$$

where $P^s_{\text{thr}}=2FQ^s_{\text{thr}}V_{\text{thr.lum}}=2FQ^s_{\text{thr}}E_{\text{thr.lum}}d_{\text{lum}}$ is the threshold power density, $E_{\text{thr.lum}}$ is the threshold field in the electroluminescent layer, and $F=1/T$ is the frequency of the driving voltage.

Then, the dependences of the energy efficiency η_w and luminous efficacy η_L on the voltage rise time t_m, which are proportional to the ratios of the average luminance of the electroluminescent device to the active power P_a (Ref. 4) will given by

$$\eta_w(t_m)=\frac{\pi}{f_\lambda P^s_{\text{thr}}(b+1)(n-1)}L_{\text{mid}}(t_m), \tag{26}$$

$$\eta_L(t_m)=\frac{\pi}{P^s_{\text{thr}}(b+1)(n-1)}L_{\text{mid}}(t_m). \tag{27}$$

Equations (20), (21), (26), and (27) show that the functions $\eta_{\text{ext}}(t_m)$, $\eta_{\text{int}}(t_m)$, $\eta_w(t_m)$ and $\eta_L(t_m)$ will qualitatively repeat the functional dependence $L_{\text{mid}}(t_m)$.

For the experimental studies we used samples of a TFELD consisting of MISIM (metal–insulator–semiconductor–insulator–metal) structures, where M denotes a first transparent electrode made of 0.15-μm-thick SnO_2 and a second opaque 0.15-μm-thick Al electrode, I denotes a 0.2–0.3-μm-thick insulating layer based on a solid solution of the oxides of zirconium and yttrium (ZnO_2/Y_2O_3), and S denotes an electroluminescent layer based on ZnS:Mn with a thickness $d_{\text{lum}}=0.8-0.9$ μm and an initial manganese content of 0.5 mass %. The transparent electrode was produced by hydrolysis of tin chloride, the insulating layers were deposited by electron-beam evaporation, and the phosphor, by vacuum thermal evaporation in a quasi-closed volume. The opaque aluminum electrode was also obtained by vacuum thermal evaporation. The threshold voltage for the test electroluminescence structure was 80 V.

The samples were excited using a G5-89 signal generator with an auxiliary amplifier. The amplitude of the voltage pulses was 120 V, the pulse repetition period was varied over 0.2–20 ms, and the pulse rise time, over 1–1000 μs. The average luminance of the emission from the samples was measured by a YaRM-3 luminance–luxmeter with a measurement error of 8%. The emitted pulses, as well as the peak amplitude of the emission in relative units, were recorded with an FÉU-75 photomultiplier whose output was fed into the first channel of an S1-114 dual-trace oscilloscope (10% error). The excitation voltage for the electroluminescent device was fed into the second channel of the oscilloscope. An S1-83 oscilloscope was used to estimate the current and charge flowing through the electroluminescent structure.

The experimental data confirm the theoretically predicted existence of a maximum in the peak luminance as a function of the voltage rise time (Fig. 1b). However, the location of the maximum in the experimental curve is shifted relative to the calculated peak toward larger values of t_m. The fall in the experimental curve after the maximum is steeper than in the theoretical curve. This shift and the steeper drop can be explained in terms of the above remarks by the neglect of the field dependence of σ in the calculations.

As opposed to this, the locations of the peaks in the calculated and experimental $L_{\text{mid}}(t_m)$ curves are the same at low and high frequencies. The $L_{\text{mid}}(t_m)$ curve at high frequencies, like the $L_{\text{mid}}(t_m)$ curves, has a steeper fall than the calculated curve.

The calculated and experimental dependences of the location of the maxima in the $L_m(t_m-t_m^{\max})$ and $L_{\text{mid}}(t_m)-t_m^{\max})$ curves as functions of the frequency of the driving voltage indicate that $t_m^{\max}$ decreases with rising frequency, and the $L_{\text{mid}}(t_m)$ curves agree, both qualitatively and quantitatively.

Thus, the experimental data indicate that the proposed model is valid.

The experimental $\ln L_m(t)=f(t)$ curve has only one linear segment with $\tau=0.6$ ms, which is close to the published values and is evidence of single-step collisional excitation of the emission centers.[6,7] The value of the collisional excitation cross section determined using Eq. (15) with $C_{d0}=32$ nF/cm^2, $V_n=80$ V, and $n=1.5$ was $\sigma\approx(2.0\pm0.5)\times10^{-15}$ cm^2, which is close to the published values.[5,8] The value of σ determined from the value of α using Eq. (9), which itself is determined by the kinetics of the rise in the luminance to $L_m(t_m)$, is $(2.52\pm0.3)\times10^{-15}$ cm^2. The agreement among the values of σ determined by the different methods is further evidence of the validity of the proposed model. The standard method of determining σ from the collision length characteristic of the collisional excitation process by measuring the luminous efficacy is rather tedious and gives $\sigma=4\times10^{-16}$ cm^2 according to the data of Max[8] and $\sigma=10^{-16}$ cm^2 according to the data in Vereschchagin.[5] This scatter in the values of the collisional excitation cross section according to different sources may be related to the different parameters of the sample electroluminescent devices, as well as to the existence of a field dependence for σ.

The value of the decay constant for the concentration of emission centers including nonradiative transitions, $\tau^*=0.8$ ms, determined from the closest possible matching of the theoretical and calculated $L_m(t_m)$ and $L_{\text{mid}}(t_m)$ curves can be used to determine the nonradiative transition probability per unit time, $\beta=417$ s^{-1}, using Eq. (2). Given that $\tau=0.6$ ms, the radiative transition probability per unit time is 1667 s^{-1}. Then the absolute magnitudes of the probabilities of radiative P_{em} and nonradiative $P_{\text{em.o}}$ transitions, according to Eq. (24), are $P_{\text{em}}=0.8$ and $P_{\text{em.o}}=0.2$.

After determining that $\tau^{**}=75\mu$s from the exponential dependence of $L_r(t)$ in its rising portion, we find from Eq. (8) that the probability per unit time of exciting the emission centers is $\alpha=1.2\times10^4$ s^{-1}.

According to Eq. (21) the external quantum yield at a frequency of $F=1$ kHz at the peak of the $L_{\text{mid}}(t_m)$ curve for the test sample, which was unoptimized in terms of structural and technological parameters, was $\eta_{\text{ext}}=1.3\%$ for $L_{\text{mid}}=123$ cd/m^2 and $C_{d0}=32$ nF/cm^2.

In Ref. 5, η_{ext} is estimated using a value of $K_0=0.2$. Our calculation of K_0 including Fresnel losses and the losses associated with the critical angle[9] for refractive indices of 2.35 for the zinc sulfide, 1.55 for the glass substrate, and 2.0 for the transparent electrode and insulator, yields $K_0=0.17$. Then Eq. (20) gives an internal quantum yield of η_{int}

$=7.8\%$ and Eq. (6) gives a light quantity of $\eta_c = 2.4 \times 10^{-18}$ lm·s. Then, with Eq. (22), the concentration of emitting centers is $N = 1.28 \times 10^{20}$ cm^{-3}. The number of emitting centers excited by a single electron passing through the electroluminescent layer [Eq. (23)] is $N_1 = 0.1$.

Using the values given above for f_λ, $h\nu$, C_{d0}, V_m/V_{thr}, and $L_{\text{mid}}(t_m)$ at a frequency of $F = 1$ kHz, we obtain an energy yield and a luminous efficacy of $\eta_w = 4.27 \times 10^{-4}$ and $\eta_L = 0.22$ lm/W.

The calculated and experimental dependences of the peak and average luminances, as well as of the external and internal quantum yields, energy yield, and luminous efficacy on the rise time of the driving voltage to its peak value, therefore, have maxima which are shifted toward shorter rise times for higher pulse repetition rates. This makes it possible to optimize the excitation conditions for TFELDs for improving their electrooptical characteristics.

The computational formulas derived here and the parameters found from the experimental dependences of the peak and average luminances on the rise time of the driving voltage make it possible to determine the main parameters characterizing the excitation of the emission and lasing spectra from TFELDs: the collisional excitation cross section, the concentration of emission centers, the excitation probabilities per unit time of the emission centers, the probabilities of radiative and nonradiative transitions, the number of emission centers excited by a single electron passing through the electroluminescent layer, the external and internal quantum yields, the energy yield, and the luminous efficacy.

[1] N. T. Gurin and O. Yu. Sabitov, Zh. Tekh. Fiz. **69**(2), 64 (1999) [Tech. Phys. **44**, 190 (1999)].
[2] N. T. Gurin and O. Yu. Sabitov, in *Proceedings of the International Scientific Conference on Deep Level Centers in Semiconductors and Semiconductor Structures* [in Russian], Ul'yanovsk (1997), pp. 122–123.
[3] M. K. Samokhvalov, Zh. Tekh. Fiz. **66**(10), 139 (1996) [Tech. Phys. **41**, 1045 (1996)].
[4] N. T. Gurin, Zh. Tekh. Fiz. **66** (5), 77 (1996) [Tech. Phys. **41**, 448 (1996)].
[5] I. K. Vereshchagin (ed.), *Electroluminescent Light Sources* [in Russian], Énergoatatomizdat, Moscow (1990), 168 pp.
[6] Yu. G. Sukharev, A. V. Andriyanov, and V. S. Mironov, Zh. Tekh. Fiz. **64**(8), 48 (1994) [Tech. Phys. **39**, 773 (1994)].
[7] A. A. Zhigal'skiĭ, E. B. Nefedtsev, and P. E. Troyan, Izv. Vyssh. Uchebn. Zaved. Fiz., No. 2, pp. 37–41 (1995).
[8] R. Max, in *Polycrystalline Semiconductors. Physical Properties and Applications*, edited by G. Harbeck, Mir, Moscow (1989), pp. 264–292.
[9] Yu. R. Nosov (Ed.), *Applications of Optoelectronic Devices* [in Russian], Radio i Svyaz', Moscow (1981), 344 pp.

Translated by D. H. McNeill

Effect of driving voltage pulse shape on the luminance of thin-film electroluminescent devices

N. T. Gurin and O. Yu. Sabitov

Ulyanovsk State University, 432700 Ulyanovsk, Russia
(Submitted July 18, 1996; resubmitted November 25, 1997)
Zh. Tekh. Fiz. **69**, 64–69 (February 1999)

The dependence of the average luminance on the parameters of the metal–insulator–semiconductor–insulator–metal structures in thin-film electroluminescent devices (TFELDs) and on the excitation conditions is found by solving kinetic equations for the variation in the concentration of excited emission centers in the phosphor layer of TFELDs for different driving voltage pulse shapes (triangular, trapezoidal, sinusoidal, and rectangular with an exponential leading edge). It is shown that for equal amplitudes and pulse repetition rates of a sign-changing symmetric voltage, the average luminance and luminous efficacy of TFELDs increase as the rate of rise of the voltage is increased for different driving voltage pulse shapes in the following sequence: triangular, sinusoidal, trapezoidal, rectangular. The calculations are confirmed by experiment. © *1999 American Institute of Physics.* [S1063-7842(99)01202-7]

Thin film electroluminescent devices with metal–insulator–semiconductor–insulator–metal layers based on zinc sulfide phosphors (Fig. 1) doped with manganese (yellow emission) or terbium fluoride (green) have high electrooptical and operational parameters (luminance, luminous efficacy, longevity, etc.), so that they are presently one of the most promising devices for creating flat displays. At the same time, the luminance (brightness) of thin-film electroluminescent devices (TFELDs) for red and, especially, blue light is not yet high enough for full-color flat display panels. Another shortcoming of TFELDs is the need to drive them with a sign-changing voltage of amplitude 60–300 V. In this regard, here, for the purpose of determining the feasibility of enhancing the luminance or of lowering the driving voltage of TFELDs, we conduct theoretical and experimental studies of the dependence of the luminance of TFELDs on the shape of the driving voltage pulse while other conditions are held fixed.

The calculation of the kinetics of the variation in the luminance of TFELDs with excitation conditions is based on the collisional excitation of the emission centers of a phosphor,[1–3] a model process typical of a manganese-doped zinc sulfide (ZnS:Mn) TFELD. The process of exciting the emission centers can be divided into the following stages: tunneling emission of electrons from interfacial states of the cathode surface of the insulator–phosphor interface, their acceleration in a high electric field, multiplication of charge carriers by collisional ionization, excitation of emission centers by high-energy electrons, radiative transitions to an unexcited state, and capture of carriers by interfacial states at the anode surface of the insulator–phosphor interface. Here the kinetics of the variation in the concentration of excited emission centers in the phosphor film obeys the equation[3]

$$\frac{dN^*(t)}{dt}=\alpha[N-N^*(t)]-\frac{N^*(t)}{\tau}, \tag{1}$$

where N is the concentration of emission centers, $N^*(t)$ is the concentration of excited emission centers, α is the probability per unit time of a transition of an emission center from the ground to an excited state, and τ is the relaxation time constant for the excited centers owing to radiative transitions to the ground state.

The quantity α characterizing the interaction of free charge carriers with emission centers is usually expressed in terms of the collisional excitation cross section σ by

$$\alpha(t)=\frac{1}{e}\sigma j(t), \tag{2}$$

where e is the charge of the electron and $j(t)$ is the conduction current density flowing through the phosphor layer.

The luminance of the electroluminescent structure depends on the rate at which emission centers under a transition from the excited to the ground state,[3]

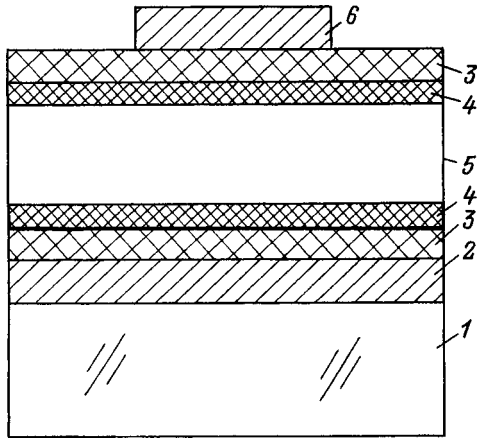

FIG. 1. Structure of an electroluminescent device: *1* — glass substrate, *2* — transparent electrode based on SnO_2, *3* — insulating layer based on SiO_2, *4* — insulating layer based on $ZrO_2\times Y_2O_3$, *5* — electroluminescent layer of ZnS:Mn, *6* — opaque electrode based on Al.

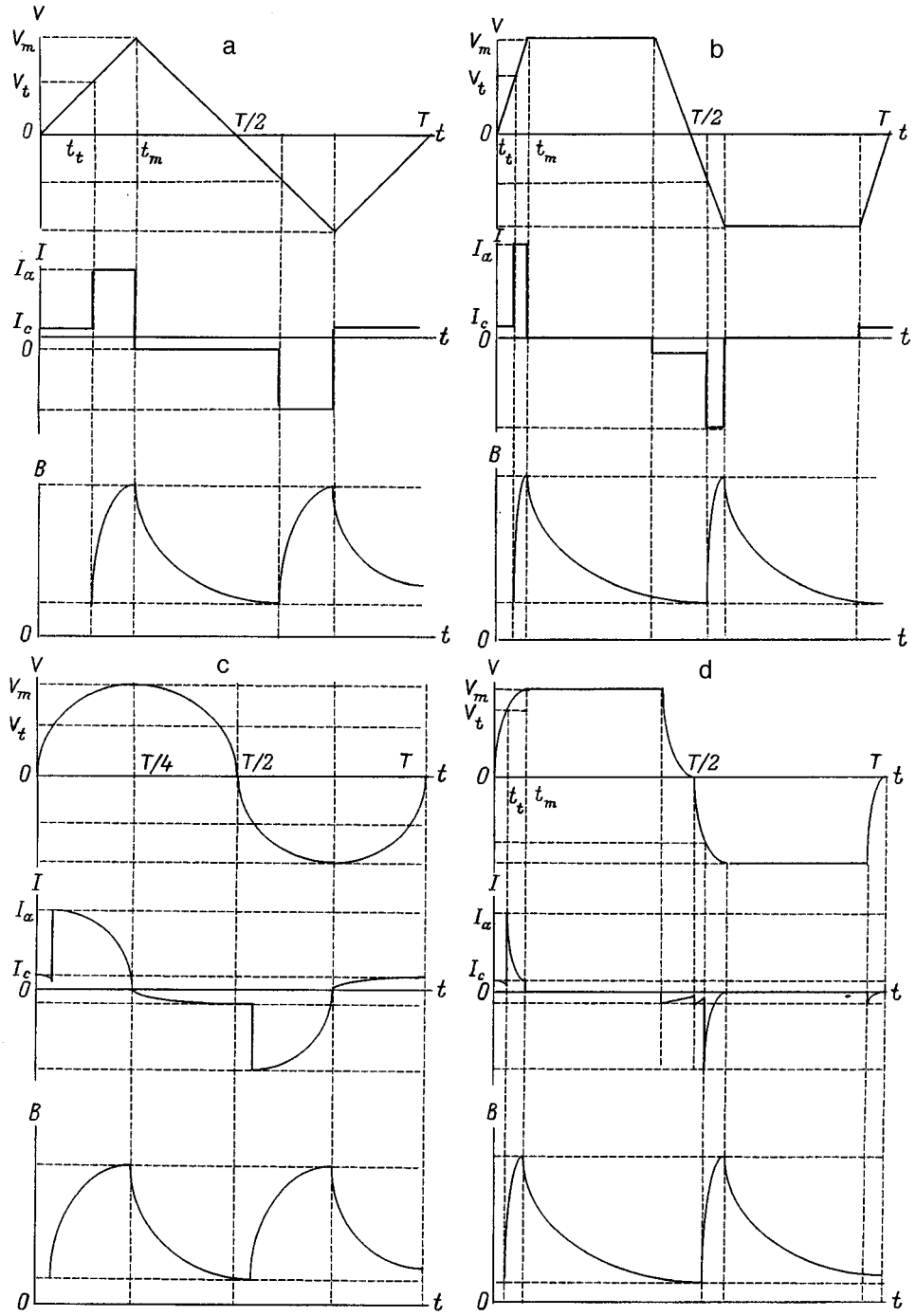

FIG. 2. Time variations in the voltage, current, and luminance of TFELDs for different shapes of the driving voltage pulse: triangular (a), trapezoidal (b), sinusoidal (c), and rectangular (d).

$$B(t)=\eta_e d_e \frac{N^*(t)}{\tau}, \tag{3}$$

where d_e is the thickness of the phosphor layer and η_e is luminous output efficiency, which is proportional to the number of photons emitted from the surface to the total number of photons produced in the volume of the luminescent layer.

Equation (3) was solved for driving voltage pulses with triangular, trapezoidal, sinusoidal, and rectangular shapes. The rectangular pulse shape was assumed to have an exponential leading edge with a rise time τ_i much shorter than the luminance rise time of the TFELD, in accordance with the actual conditions for forming these pulses. In the calculations it was assumed, by analogy with Ref. 4, that: the electroluminescent device is driven by a periodically sign-changing symmetric voltage; the insulating layers of the structure are identical, homogeneous, and have no dielectric losses; the luminance waveform determined by Eq. (3) is the same in the different half periods of the driving voltage; and, η_e and τ are independent of the shape and amplitude of the driving voltage. In this case, the shapes of the current pulses passing through the electroluminescent layer and the shapes of the luminance waveforms from the electroluminescent device shown in Fig. 2 are close to the shape of the current pulses and luminance waveforms observed in real TFELDs by ourselves and others.[5,6] Over a time $t<t_t$ during which the driv-

ing voltage reaches the threshold voltage V_b of the electroluminescent structure, which corresponds to the onset of emission from the electroluminescent device, there is no conduction current through the electroluminescent layer, and only a capacitive current flows through the electroluminescent device.[4] When $V \geqslant V_t$, the voltage drop across the electroluminescent layer is determined by charge carrier generation owing to collisional ionization and remains roughly constant and equal to the peak value of the threshold voltage V_{te} of the electroluminescent layer itself.[7] Until the external voltage reaches its peak V_m at $t = t_m$, a conduction current

$$j(t) = C_{d0} \frac{dV(t)}{dt} \tag{4}$$

flows through the electroluminescent layer, where C_{d0} is the specific capacitance of the insulating layers of the electroluminescent device and $V(t)$ is the time variation of the driving voltage.

Let us now consider the solution of Eq. (1) for various shape of the driving voltage. For triangular and trapezoidal voltage pulse shapes, in the rising portion of the voltage ($CV(t) = bt$, where $b = V_m/t_m$) the conduction current density is given by

$$j(t) = C_{d0} \frac{V_m}{t_m}. \tag{5}$$

Then, with Eq. (5), the value of α for a linearly rising voltage is

$$\alpha = \frac{\sigma}{e} C_{d0} \frac{V_m}{t_m} = \frac{a}{t_m}, \tag{6}$$

where $a = \sigma C_{d0} V_m / e$.

When Eq. (6) is taken into account, Eq. (1) becomes

$$\frac{dN^*(t)}{dt} = \frac{a}{t_m}[N - N^*(t)] - \frac{N^*(t)}{\tau}. \tag{7}$$

The solution of this equation is the sum of the general solution of the homogeneous equation and the particular solution of the inhomogeneous equation. The general solution of the homogeneous equation has the form

$$N^*(t) = D \exp\left[-\left(\alpha + \frac{1}{\tau} \right) t \right], \tag{8}$$

where α is given by Eq. (6), and D is a constant of integration.

The particular solution of the inhomogeneous equation is

$$N^*(t) = \frac{\alpha N}{\alpha + 1/\tau}. \tag{9}$$

Summing Eqs. (8) and (9), we obtain the general solution of Eq. (7),

$$N_i^*(t) = D \exp\left[-\left(\alpha + \frac{1}{\tau} \right) t \right] + \frac{\alpha N}{\alpha + 1/\tau}, \tag{10}$$

where D is determined by the initial conditions.

For $t > t_m$, when the amplitude of the driving voltage becomes less than V_m (for a triangular voltage pulse) or does not vary (for a trapezoidal voltage pulse), the voltage across the electroluminescent layer falls below V_{te} on account of the charge on the capacitances of the insulating layers; then carrier generation by collisional ionization ceases, the conduction current through the electroluminescent layer approaches zero, and a drop in the luminous intensity of the TFELD begins which continues until the next time the applied voltage reaches $|V_t|$. Here $j(t) = 0$, and Eq. (1) takes the form

$$\frac{dN^*(t)}{dt} + \frac{N^*(t)}{\tau} = 0. \tag{11}$$

The solution of this equation is

$$N_d^*(t) = D \exp\left(-\frac{t}{\tau} \right), \tag{12}$$

where D is a constant determined from the condition $N_i^*(t_m) = N_d^*(t_m)$.

Solving Eqs. (7) and (11) for a steady-state excitation regime where the concentration $N_d^*(t)$ does not reach zero during the drop (i.e., the high-frequency regime, for which the criterion is $\tau > T/2$ [Eqs. (4) and (5)], where T is the period of the driving voltage) and substituting the results in Eq. (3), we obtain a formula that describes the kinetics of the variation in the luminance of a TFELD, $B(t)$, when it is driven by a linearly rising voltage. In accordance with Talbott's law, the observed average luminance is

$$B_{\text{mid}} = \frac{2}{T} \int_{t_t}^{t_t + T/2} B(t)\, dt. \tag{13}$$

Then the average luminance of a TFELD driven by a triangular voltage pulse will be given by

$$\begin{aligned} B_{\text{mid}} = \frac{2 \eta_e d_e \alpha N}{T \tau (\alpha + 1/\tau)} \Bigg\{ & (t_m - t_t) - \frac{1 - A}{\alpha + 1/\tau} \\ & \times \left[1 - \exp\left[-\left(\alpha + \frac{1}{\tau} \right)(t_m - t_t) \right] \right] \\ & + \tau \left[1 - (1 - A) \left(\exp\left[-\left(\alpha + \frac{1}{\tau} \right)(t_m - t_t) \right] \right. \right. \\ & \left. \left. \times \left[1 - \exp\left(-\frac{t_t + T/2 - t_m}{\tau} \right) \right] \right] \right\}, \end{aligned} \tag{14}$$

where

$$A = \left[1 - \exp\left[-\left(\alpha + \frac{1}{\tau} \right)(t_m - t_t) \right] \right] \exp\left(-\frac{t_t + T/2 - t_m}{\tau} \right).$$

For a trapezoidal driver voltage pulse, the solution of Eq. (1) is described by Eqs. (10) and (12), analogously to the case of a triangular voltage pulse. For a trapezoidal voltage pulse, however, at the time t_m the total current through the electroluminescent structure goes to zero (Fig. 1).

For a sinusoidal driving voltage of the form $V = V_m \sin \omega t$, where $\omega = 2\pi/T$ is the angular frequency, with Eqs. (2) and (4) we find α to be given by

$$\alpha = \frac{\sigma}{e} C_{d0} V_m \omega \cos \omega t = a \omega \cos \omega t. \tag{15}$$

Then, with Eq. (15) the general solution of the homogeneous equation (1) is

$$N^*(t)=D\exp\left[-\left(a\sin\omega t+\frac{t}{\tau}\right)\right]. \tag{16}$$

The initial Eq. (1) is not solved analytically, but for $\alpha \ll 1/\tau$ one can obtain an approximate general solution.

The drop in the concentration $N^*(t)$ for $\alpha=0$ is described by Eq. (12). Then, taking the initial conditions into account and averaging the resulting solution of Eq. (1) in accordance with Eq. (13) over the time interval $[t_t; t_t+T/2]$, we find an expression for the average luminance of an electroluminescent device driven by a sinusoidal voltage,

$$\begin{aligned}B_{\text{mid}}=\frac{2\eta_e d_e a N}{T\tau}\frac{\omega\tau}{1+\omega^2\tau^2}\Bigg\{&\tau\cos\omega t_t\exp\left(-\frac{2t_t}{\tau}\right)+3\frac{\exp(-2t_t/\tau)(\omega\tau\sin\omega t_t-2\cos\omega t_t)-\omega\tau\exp(-T/2\tau)}{\omega^2\tau[1+(2/\omega\tau)^2]}\\&+\left[\left[\frac{1+\omega^2\tau^2}{\omega\tau}A\exp\left[a\sin\omega t_t+\frac{t_t}{\tau}\right]\right]+\tau\exp\left(-\frac{t_t}{\tau}\right)(\omega\tau\sin\omega t_t-\cos\omega t_t)\right]\left(\exp\left(-\frac{T}{4\tau}\right)-\exp\left(-\frac{t_t}{\tau}\right)\right)\\&+\tau\exp\left[-\left(a+\frac{T}{4\tau}\right)\right]\left[\omega\tau\exp\left(-\frac{T}{4\tau}\right)-\exp\left(-\frac{t_t}{\tau}\right)(\omega\tau\sin\omega t_t-\cos\omega t_t)+\frac{1+\omega^2\tau^2}{\omega\tau}A\exp\left[a\sin\omega t_t+\frac{t_t}{\tau}\right]\right]\\&\times\left[1-\exp\left(-\frac{t_t+T/2-t_m}{\tau}\right)\right]\Bigg\},\end{aligned} \tag{17}$$

where

$$\begin{aligned}A=&\frac{\omega\tau}{1+\omega^2\tau^2}\exp\left[-\left(a+\frac{T}{4\tau}\right)\right]\cdot\left[\omega\tau\exp\left(-\frac{T}{4\tau}\right)\right.\\&\left.-\exp\left(\frac{t_t}{\tau}\right)(\omega\tau\sin t_t-\cos\omega t_t)\right]\\&\times\exp\left(-\frac{t_t+T/2-t_m}{\tau}\right).\end{aligned}$$

For a real driving voltage of rectangular form with an exponential leading edge that varies as $V(t)=V_m\times[1-\exp(-t/\tau_i)]$, where τ_i is the rise time of the leading edge of the pulse, $\tau \gg \tau_t$, with the aid of Eqs. (2) and (4), we find α to be

$$\alpha=\frac{\sigma}{e}C_{d0}\frac{V_m}{\tau_i}\exp\left(-\frac{t}{\tau_i}\right)=\frac{a}{\tau_i}\exp\left(-\frac{t}{\tau_i}\right). \tag{18}$$

Then, with Eq. (18), the general solution of the homogeneous equation (1) will be

$$N^*(t)=D\exp\left[-\left(\frac{t}{\tau}-a\exp\left(-\frac{t}{\tau_i}\right)\right)\right]. \tag{19}$$

Equation (1) is not solved analytically, but in the specific case of $\tau \gg \tau_i$ and $\alpha \ll 1/\tau$, on neglecting α we can obtain an approximate general solution of the inhomogeneous equation.

The drop in concentration $N^*(t)$ is also determined by Eq. (12). Then, on averaging the results over the time interval $[t_t; t_t+T/2]$, we obtain an expression for the average luminance of an electroluminescent device driven by a rectangular voltage pulse,

$$\begin{aligned}B_{\text{mid}}=\frac{2\eta_e d_e a N}{T\tau}\Bigg\{&\left[A\exp\left[\frac{t_t}{\tau}-a\exp\left(-\frac{t_t}{\tau_i}\right)\right]\right.\\&\left.+\exp\left(-\frac{t_t}{\tau_i}\right)\right]\tau\left(\exp\left(-\frac{t_t}{\tau}\right)-\exp\left(-\frac{t_m}{\tau}\right)\right)\\&-\tau_i\left(\exp\left(-\frac{t_t}{\tau_i}\right)-\exp\left(-\frac{t_m}{\tau_i}\right)\right)\\&+\tau\left[A\exp\left[\frac{t_t}{\tau}-a\exp\left(-\frac{t_t}{\tau_i}\right)\right]+\exp\left(-\frac{t_t}{\tau_i}\right)\right.\\&\left.-\exp\left(-\frac{t_m}{\tau_i}\right)\right]\exp\left[-\frac{t_m}{\tau}-a\exp\left(-\frac{t_m}{\tau_i}\right)\right]\Bigg\}\\&\times\left[1-\exp\left(-\frac{t_t+T/2-t_m}{\tau}\right)\right],\end{aligned} \tag{20}$$

where

$$\begin{aligned}A=&\left[\exp\left(-\frac{t_t}{\tau_i}\right)-\exp\left(-\frac{t_m}{\tau_i}\right)\right]\\&\times\exp\left[-\left(\frac{t_m}{\tau}-a\exp\left(-\frac{t_m}{\tau_i}\right)\right)\right]\\&\times\left[1-\exp\left(-\frac{t_t+T/2-t_m}{\tau}\right)\right].\end{aligned}$$

Based on Eqs. (14), (17), and (20) we have calculated the average luminance of TFELDs for different shapes of the sign-changing symmetric driving voltage compared to the average luminance of a TFELD driven by a triangular voltage pulse for the same peak voltages and repetition rates of the pulses. For determining the calculated average luminance, the specific capacitance of the insulating layers of the TFELD was taken to be $C_{d0}\approx 10^{-8}$ F/cm^2 and the values of

TABLE I. Calculated and experimental values of the average luminance for different driving voltage pulse shapes.

Voltage waveform	Calculated	Experiment
Triangular	1	1
Sinusoidal	1.22	1.26
Trapezoidal	1.70	2.02
Rectangular	2.06	2.33

σ and τ were taken from data[8] for ZnS:Mn, at $\sigma \approx 4 \times 10^{-16}\,\mathrm{cm}^2$ and $\tau \approx 2$ ms. As Table I shows, the calculated values of the average luminance of the electroluminescent device increase with the rate of rise of the voltage, in accordance with Eq. (4).

In order to verify the analytic results, we have studied thin-film electroluminescent metal–insulator–semiconductor–insulator–metal structures based on ZnS:Mn (Fig. 1). Glass slabs with a continuous 0.2-μm-thick transparent SnO_2 electrode deposited on them were used as substrates. Two insulating layers were deposited over the transparent electrode: silicon dioxide (SiO_2) to a thickness of 0.2 μm and a solid solution of the oxides of zirconium and yttrium ($ZrO_2 \times Y_2O_3$ (13 mass %)) to a thickness of 0.05 μm. The thickness of the electroluminescent layer was 0.7 μm. Layers of SiO_2 with a thickness of 0.2 μm and $ZrO_2 \times Y_2O_3$ (13 mass %) with a thickness of 0.05 μm were also used as a second insulator for the structure. The second opaque electrode was a 0.25-μm-thick aluminum film.

The samples were excited using a special version of a G6-37 signal generator with an additional amplifier. The luminance of the electroluminescent structures was measured using a YaRM-3 luminance–luxmeter with a measurement error of 8%. The voltage acruss the electroluminescent device was measured with a V7-40/3 digital voltmeter. The amplitude of the voltage pulses was 300 V and their repetition rate was 500 Hz. For the trapezoidal voltage pulse the rise and fall times were 80 μs. The rise time of the voltage in the rectangular pulse was $\tau_i = 1$ μs.

The experimental results (see Table I) confirm the effect of the shape of the driving voltage on the average luminance of the TFELDs, while the rise in the average luminance as the rate of voltage rise is increased was greater than in the calculations. This quantitative discrepancy between the theoretical and experimental results can be explained by the approximate solutions of Eq. (1) for sinusoidal and rectangular voltages, differences between the initial parameters in the calculations (C_{d0}, σ, τ) from the actual values, and experimental error, as well as the failure to include the dependences of η_e, σ, and τ on the shape of the driving voltage pulse.

The rise in the luminance of the emission can then be attributed to a different charge flowing through the electroluminescent layer during the time when carriers are generated in it, which leads to different values of the active power expended in generating the radiation.

However, the charge flowing through the electroluminescent layer during the time when carriers are generated there is[4]

$$Q = \int_{t_t}^{t_m} C_d \frac{dV(t)}{dt} dt = mC_eV_1(m-1) = Q_t(m+1)(n-1), \tag{21}$$

where Q_t is the threshold charge in the electroluminescent layer corresponding to the onset of emission and is independent of the driving voltage pulse shape, $a = C_d/C_e = (\varepsilon_d/\varepsilon_e)/(d_d/d_e)$, ε_d and ε_e are the dielectric constants of the materials in the insulating and electroluminescent layers, and $n = V_m/V_t$.

According to Eq. (4), the active power released in the electroluminescent device and caused by the flow of the active current through the electroluminescent layer is nonzero for $t_t \leqslant t < t_m$, i.e., when the voltage on the electroluminescent device $V \geqslant V_t$. Then the instantaneous active power is determined in the form

$$P_a(t) = V_{te} \cdot I_a(t), \tag{22}$$

and, taking the sameness of the half waves into account, the active power P_a is given by

$$P_a = \frac{2}{T} \int_0^{T/2} P_a(t)dt. \tag{23}$$

Given Eqs. (22) and (4), we have

$$P_a(t) = C_dV_{te} \frac{dV(t)}{dt}. \tag{24}$$

With Eqs. (21) and (24), the expression for P_a takes the form

$$P_a = \frac{2}{T} \int_{t_t}^{t_m} C_dV_{te} \frac{dV(t)}{dt} dt = \frac{2}{T} C_dV_{te} \int_{V_t}^{V_m} dV = \frac{2}{T} V_{te}Q. \tag{25}$$

Equation (25) implies that the active power produced in the electroluminescent device is independent of the shape of the driving voltage pulse and, by analogy with Ref. 4, is given by

$$P_a = P_t^s(m+1)(n-1)S_e, \tag{26}$$

where $P_t^s = 2FQ_t^sV_{te} = 2FQ_t^sE_{te}d_e$ is the threshold power density, V_{te} and E_{te} are the threshold voltage and field strength in the electroluminescent layer, Q_t^s is the threshold charge density in the electroluminescent layer, $Q_t^s = C_eV_{te}/S_e$, and S_e is the area of the electroluminescent device.

Our experimental studies of the charge–voltage characteristics of the TFELDs using an S1-83 oscilloscope following a method described by Herman[9] for the different driving voltage pulse shapes indicate that the areas of the hysteresis loops in these characteristics when radiation is generated by the TFELDs are proportional to the active power P_a and are, to within the measurement error, the same for equal amplitude and frequency of the driving voltages. This confirms that the active power dissipated in the electroluminescent devices is independent of the shape of the driving voltage pulse.

For a TFELD that radiates uniformly in all directions at its surface, the luminous efficacy, defined as the ratio of the emitted luminous flux to the active power, is then, by analogy with Ref. 4, given by

$$\eta_B = \frac{\pi B_{\text{mid}}}{P_t^s (m+1)(n-1)} \tag{27}$$

and increases similarly to the rise in luminance when the rate of rise of the voltage is increased (when the shape of the driving voltage pulse is changed).

The mechanism for the rise in luminance when the shape of the driving voltage pulse is changed is that, when the rate of rise of the voltage is increased, then according to Eqs. (2) and (4) the amplitude of the conduction current pulse $I_a(t)$ increases (Fig. 2) and the probability per unit time of an emitting center's undergoing a transition from the ground to an excited state becomes greater, which, in turn, leads to higher concentrations of the excited centers and, therefore, higher instantaneous luminancees at time $t = t_m$. For equal relaxation times τ of the excited centers, this leads to a rise in the observed average luminance of TFELDs.

These theoretical and experimental studies have shown, therefore, that as the shape of the driving voltage pulse is changed with an increase in its rate of rise there is a substantial rise in the average luminance and luminous efficacy of TFELDs. These data can be used both to increase the luminance of electroluminescent devices of this type and to reduce the amplitude of the driving voltage pulse for a given luminance.

[1] I. K. Vershchagin (Ed.), *Electroluminescent Light Sources* [in Russian], Énergoatomizdat, Moscow (1990), 168 pp.
[2] N. A. Vlasenko, *Physical Foundations of Semiconductor Electronics* [in Russian], Kiev (1985).
[3] M. K. Samokhvalov, Zh. Prikl. Spektrosk. **62**(3), 182 (1995).
[4] N. T. Gurin, Zh. Tekh. Fiz. **66**(5), 77 (1996) [Tech. Phys. **41**, 448 (1996)].
[5] V. P. Singh, S. Krishna, and D. Morton, J. Appl. Phys. **70**, 1811 (1991).
[6] Y. S. Chenh and D. C. Krupka, J. Appl. Phys. **43**, 4089 (1972).
[7] N. T. Gurin, Élektron. Tekh. Ser. 3. Mikroélektronika, No. 1 (135), pp. 88–90 (1990).
[8] R. Max, in *Polycrystalline Semiconductors. Physical Properties and Applications*, edited by G. Harbeck, Mir, Moscow (1989), pp. 264–292.
[9] M. Herman, Electron Technol. **19**, No. 1/2, pp. 23–58 (1986).

Translated by D. H. McNeill

Propagation of magnetostatic backward surface waves in ferrite–insulator–metal structures magnetized by linearly nonuniform magnetic fields

V. I. Zubkov and V. I. Shcheglov

Institute of Radio Technology and Electronics, Russian Academy of Sciences, 141120 Fryazino, Moscow Region, Russia

(Submitted May 19, 1997; resubmitted December 15, 1997)
Zh. Tekh. Fiz. **69**, 70–77 (February 1999)

A theoretical study is made of the trajectories and of the changes in magnitude and direction of the wave vectors of magnetostatic backward surface waves with different frequencies propagating in ferrite–insulator–metal structures with different insulating layer thicknesses and magnetized by a linearly nonuniform static field. It is shown that both forward and backward magnetostatic surface waves (MSSWs) propagate in a waveguide channel, on one side of which MSSWs undergo mirror reflection and on the other side of which their propagation direction is rotated, independently of the thickness of the insulator in the structure. It is shown that when MSSWs propagate in a nonuniform field, the forward wave is converted into a backward wave and, under certain conditions, the backward wave is converted into a forward wave. Some features of the propagation characteristics of magnetostatic backward surface waves are determined. © *1999 American Institute of Physics.* [S1063-7842(99)01302-1]

The possibility of using different types of magnetostatic waves for creating solid state analog signal processing systems[1] adds to the urgency of studying the dispersion of the forward and backward magnetostatic surface waves (MSSWs) which exist in ferrite–insulator–metal (FIM) structures. The dispersion of magnetostatic waves depends greatly on the thickness of the insulating layer[1–6] and can be controlled, in particular, by creating a nonuniform magnetic field H_g (referred to below simply as the field H_g) along the propagation path of the MSSWs.[7–12] Studies[13] have been made of the propagation of magnetostatic forward surface waves (MSFSWs) in FIM structures magnetized by a one-dimensional, linearly nonuniform, static field H_g. Here we present results from a study of the trajectories and of the changes in magnitude and direction of the wave vector $\mathbf{k}$ of magnetostatic backward surface waves (MSBSWs) propagating in this type of structure.

Let us consider an FIM structure that is infinite in the yz plane and consists of a ferrite film of thickness d, magnetized to saturation, an ideally conducting metal layer, and an insulating layer of thickness s between them. Let the $x=0$ plane be the surface of the ferrite film, which is located in a weak nonuniform field $\mathbf{H}_g=\mathbf{H}_0+\mathbf{H}_n$, where H_0 is a uniform field (referred to below as the field H_0) and H_n is a nonuniform supplement to it which is much lower than H_0 and varies slowly along the length of a MSSW. Then the field $\mathbf{H}_0$ can be regarded as one-dimensional[8–14] and, for concreteness, as directed along the z axis, and, in the case of a linear nonuniformity, can be written in the form[13]

$$H_g=H_z(z)=H_0+4\pi M_0 z a^{-1}=4\pi M_0(\Omega_H+z a^{-1}), \tag{1}$$

where $\Omega_H=H_0(4\pi M_0)^{-1}$, and $4\pi M_0$ is the saturation magnetization of the ferrite film.

The contours of the field H_g in the plane of the ferrite film form a family of straight lines parallel to the y axis.

Let a magnetostatic surface wave with frequency $\omega_i=2\pi f_i$ propagate in the FIM structure with its wave vector $\mathbf{k}$ and group velocity $\mathbf{v}_g$ directed at angles φ and ψ to the y axis. Since $H_n \ll H_0$, the dispersion relation for MSSWs in the FIM structure has the same form as for MSSWs in the field H_0,[2,5] and it can be written as the sum of two terms, of which the first is the dispersion relation for MSSWs in the ferrite layer and the second is an increment to it owing to the presence of the insulator and metal layers,[13]

$$[\beta-2\mu\alpha\coth(\alpha k d)]+(\beta+2-2p\nu\cos\varphi)\exp(-2ks)=0, \tag{2}$$

where $\alpha=[\mu^{-1}\sin^2\varphi+\cos^2\varphi]^{1/2}$, $\beta=(\nu^2-\mu^2+\mu)\cos^2\varphi-\mu-1$, $\mu=1+\Omega_g(\Omega_g^2-\Omega_i^2)^{-1}$, $\nu=\Omega_i(\Omega_g^2-\Omega_i^2)^{-1}$, $\Omega_i=\omega_i(4\pi|\gamma|M_0)^{-1}$, $\Omega_g=H_g(4\pi M_0)^{-1}$, γ is the electron gyromagnetic ratio, $p=1$ for propagation of MSSWs in the plane $x=0$, $p=-1$ for propagation of MSSWs in the plane $x=-d$, and the nonuniformity of the field H_g in Eq. (2) has been taken into account by substituting the required value from Eq. (1) into the components μ and ν of the magnetic permeability tensor.

Since for $p=-1$, MSBSWs do not exist,[4] we shall consider the case $p=1$, where both forward (with a positive projection of the group velocity $\mathbf{v}_g$ on the direction of the phase velocity $\mathbf{v}_{ph}$) and backward (with a negative projection of the group velocity $\mathbf{v}_g$ on the direction of the phase velocity $\mathbf{v}_{\rm ph}$) magnetostatic surface waves exist. Equation (2) was obtained in the magnetostatic approximation, so the dielectric permittivity does not appear in it, and this layer is identical to a vacuum gap. For $s\to\infty$, Eq. (2) becomes the dispersion relation for MSSWs in a ferrite film and for $s=0$, the dispersion relation for MSSWs in ferrite–metal structures. In

the following we assign the index s to those functions which depend on s, replacing it by ∞ for ferrite films and by 0 for ferrite–metal structures.

The problem of the propagation of MSSWs in ferrite films and FIM structures magnetized by a field H_g of arbitrary form is solved by a Hamilton method[11,12] and reduces to solving a system of three differential equations:

$$\frac{dk}{dy}=-k\left(\frac{\partial k}{\partial y}\cos\varphi+\frac{\partial k}{\partial z}\sin\varphi\right)\left(k\cos\varphi+\frac{\partial k}{\partial\varphi}\sin\varphi\right)^{-1},$$

$$\frac{d\varphi}{dy}=\left(\frac{\partial k}{\partial y}\sin\varphi-\frac{\partial k}{\partial z}\cos\varphi\right)\left(k\cos\varphi+\frac{\partial k}{\partial\varphi}\sin\varphi\right)^{-1},$$

$$\frac{dz}{dy}=\left(k\sin\varphi-\frac{\partial k}{\partial z}\cos\varphi\right)\left(k\cos\varphi+\frac{\partial k}{\partial\varphi}\sin\varphi\right)^{-1}, \quad (3)$$

where the partial derivatives $\partial k/\partial y$, $\partial k/\partial z$, and $\partial k/\partial\varphi$ are calculated from Eq. (2).

The initial conditions for solving Eq. (3) are given at the point $y=z=0$ and for a MSSW with frequency Ω_i have the form

$$\Omega=\Omega_i, \quad \varphi=\varphi_0, \quad H_g=H_0, \quad k=k_{0,i}, \quad (4)$$

where $k_{0,i}$ is found from Eq. (2) when the first three conditions of Eq. (4) are satisfied.

The knowledge of the MSSW trajectories $z(y)$ and of the dependences of the wave number $k(y)$ and the angle $\varphi(y)$ on the coordinate y obtained from Eq. (3) can be used to obtain a complete picture of the propagation of MSSWs. However, this solution, which is valid for both forward and backward MSSWs, does not distinguish the type of wave. Therefore, in studying the propagation of MSSWs we shall also examine the change in the propagation direction of the energy of a MSSW (in the direction of the group velocity $\mathbf{v}_g$), i.e., the function $\psi(y)$, which is determined from the trajectories $z(y)$ of the MSSWs using the fact that the tangents to $z(y)$ at each point of the ferrite film coincide with the direction of group velocity $\mathbf{v}_g$. A simultaneous analysis of the $\varphi(y)$ and $\psi(y)$ curves allows us to judge the type of MSSW.

When broadband converters are used, it is primarily the MSFSWs with the smallest value of $k_{y,i}$ which are excited.[13] Exciting both forward and backward waves requires separate narrowband converters, each of which excites MSSWs with their own value of $k_{y,i}$ ($k_{yf,i}$ for forward and $k_{yb,i}$ for backward waves).

When MSSWs with a given frequency Ω_i propagate in the field H_g, the projection of the wave vector $\mathbf{k}$ on a level line of the field H_g remains constant ($k_{y,i}=C_{f(b),i}(s)$) and this causes the angle φ to vary over the range $-\varphi_{c,s}\leqslant\varphi<\varphi_{c,s}$ and the wave vector k to increase as the absolute value of φ increases.[8–13]

Let us recall the properties of a MSSW in the field H_g which follow from Eq. (2) and the condition $k_{y,i}=C_{f(b),i}(s)$.[13] The lower bound frequency Ω_l is independent of φ, the gap s, and $k_{y,i}$ and is given by

$$\Omega_l=\sqrt{\Omega_g(\Omega_g+1)}. \quad (5)$$

The upper frequency boundary $\Omega_{u,s}(k_y,\varphi)$ depends on the angle φ, the gap s, and $k_{y,i}$ and has a maximum at $\varphi=0$ and $k_{y,i}=C_{f(b),i}(s)$; its smallest value $\Omega_{u,\infty}(k_y,0)$ for a gap $s\to\infty$ and its largest value $\Omega_{u,0}(k_y,0)$ for $s=0$ are equal to[13]

$$\Omega_{u,\infty}(k_y,0)=\sqrt{(\Omega_g+0.5)^2-0.25\exp(-2k_{u,i}d)}, \quad (6)$$

$$\Omega_{u,0}(k_y,0)=\{1+\sqrt{(3+4\Omega_g)^2+4\varkappa_{-1}(1+\Omega_g)[(1+4\Omega_g)+\varkappa_{-1}\Omega_g]}\}(2\varkappa_{+1})^{-1}, \quad (7)$$

where $\varkappa_{-1}=\coth k_{y,i}d-1$ and $\varkappa_{+1}=\coth k_{y,i}d+1$.

For $k_{y,i}\to\infty$, Eqs. (6) and (7) transform to the known equations

$$\Omega_{u,\infty}(\infty,0)=\Omega_g+0.5, \quad (6a)$$

$$\Omega_{u,0}(\infty,0)=\Omega_g+1. \quad (7a)$$

Magnetostatic surface waves exist within the range of angles $\varphi=\pm\varphi_{c,s}$, where $\varphi_{c,s}$ are the ''cutoff'' angles bounded by the limits $\varphi_{c,\infty}\leqslant\varphi_{c,s}\leqslant\varphi_{c,0}$, with

$$\varphi_{c,\infty}=\arccos\{[\Omega_i+\sqrt{\Omega_i^2-\Omega_g(\Omega_g+1)}](\Omega_g+1)^{-1}\}, \quad (8)$$

$$\varphi_{c,0}=\arccos\sqrt{[\Omega_i^2-\Omega_g(\Omega_g+1)](\Omega_g+1)^{-1}}. \quad (9)$$

The positions of the upper z_u and lower $z_{l,s}(k_y)$ bounds of the MSSW trajectories $z(y)$ in the yz plane are determined from the following considerations. A MSSW with a given frequency Ω_i and angle φ_0 in the field H_g can propagate only as the field H_f varies from $H_{gl,s}(k_y)$ to H_{gu}; $H_{gl,s}(k_y)$ and H_{gu} are found from the dispersion relation (2) for $\Omega_i=\text{const}$. Substituting them in Eq. (1), one calculates the bounds z_u and $z_{l,s}(k_y)$, which lie within the limits $z_{l,\infty}(k_y)\leqslant z_{l,s}(k_y)\leqslant z_{l,0}(k_y)$, where z_u, $z_{l,\infty}(k_y)$, and $z_{l,0}(k_y)$ are given by[13]

$$z_u=0.5a(\sqrt{4\Omega_i^2+1}-1-2\Omega_d), \quad (10)$$

$$z_{l,\infty}(k_y)=0.5a(\sqrt{4\Omega_i^2+\exp(-2k_{y,i}d)}-1-2\Omega_g), \quad (11)$$

$$z_{l,0}(k_y)=0.5a\{[-1+\sqrt{(2\varkappa_{+1}\Omega_i-1)^2+\varkappa_{+1}\varkappa_{-1}}](\varkappa_{+1})^{-1}-1-2\Omega_g\}. \quad (12)$$

The lower bounds $z_{l,s}(k_y)$ for MSFSWs and MSBSWs are different, since $k_{yf,i}$ for a forward wave differs from $k_{yb,i}$ for a backward wave.

Since solving the MSSW propagation problem in FIM structures by the Hamilton method[11,12] does not distinguish between MSFSWs and MSBSWs, it is necessary to analyze

the dispersion relation for MSSWs in FIM structures (2) directly. The dispersion relation (2) describes a dispersion surface $\Omega_s(k,\varphi)$ or $\Omega_s(k_y,k_z)$, where $k_y=k\cos\varphi$ and $k_z=k\sin\varphi$.[2,6] The shape of the $\Omega_s(k_y,k_z)$ surface is deformed as the gap s changes. MSBSWs can exist if the convexities of the $\Omega_s(k_y,k_z)$ surface are intersected by the plane $\varphi=\varphi_0$, where the angle φ_0 is specified by the propagation direction of the MSSWs (excited by a MSSW antenna). The complicated shape of the surface $\Omega_s(k_y,k_z)$ makes it necessary to analyze it using different cross sections.[6,10,14] A complete picture of it can be obtained using the cross sections in the $k_z=0$ plane [the dispersion curve $\Omega_s(k_y,0)$] and in a set of planes $\Omega_i=$const [the curves $k_z(k_y)$] in the plane of the MSSW wave numbers). MSBSWs exist, in principle, if the $\Omega_s(k_y,0)$ has a maximum and the curves k_z and k_y have at least one tangent passing through the point $k_y=k_z=0$. The conditions for excitation in the k_y,k_z plane are described by the intersection of a line starting from the coordinate origin at a given angle φ_0, with the curve $k_z(k_y)$ corresponding to the field H_g at the point of excitation. An intersection of this sort can occur at two or three points. The perpendiculars to the k_y axis from the intersection points determine the projections of the wave vector $k_{yf(b),i}$ for the forward and backward waves, while the perpendiculars to the tangents to the $k_z(k_y)$ curves at these points determine the direction in which the energy of the MSSW is transported (the angles $\psi_{0f(b)}$). From the relationship of the angles φ_0 and ψ_0 it can be stated that the first and third points of intersection, counting outward from the coordinate origin, correspond to forward waves, while the second corresponds to a backward wave.

We now examine the dispersion surface $\Omega_s(k_y,k_z)$ in FIM structures in a field H_g. For possible comparison with experiment, we choose specifically the generalized variables Ω_i, Ω_H, φ, kd, and ks in Eq. (2) and provide a calculation of the dispersion surfaces and propagation characteristics of MSSWs in FIM structures with ferrite films of yttrium iron garnet having a saturation magnetization $4\pi M_0=1750$ G and thickness $d=15\mu$m in a field H_g with $\Omega_H=0.25$ and $a=32$. Recall that in a field H_0 the dispersion surfaces $\Omega_s(k_y,k_z)$ are different for MSSWs in FIM structures with small ($s\leqslant s_b(\Omega_H)$) and large ($s>s_b(\Omega_H)$) gaps.[6] In a field H_g, the form of the dispersion curves $\Omega_s(k_y,0)$ is qualitatively the same as in a field H_0. In FIM structures with a small gap s, the dispersion curve $\Omega_s(k_y,0)$ begins at the frequency Ω_l, has a maximum at $\Omega_{u,s}(k_y,0)$, and as $k\to\infty$ approaches $\Omega_{u,\infty}(\infty,0)$. In FIM structures with a large gap s, the dispersion curve $\Omega_s(k_y,0)$ begins at the frequency Ω_l, has a maximum at $\Omega_{u,s}(k_y,0)$, a minimum at $\Omega_{\min,s}(k_y,0)$, and as $k\to\infty$ approaches the frequency $\Omega_{u,\infty}(\infty,0)$.[6]

Figure 1 shows plots of $k_z(k_y)$ for MSSWs with a frequency of 3600 MHz in an FIM structure with a small gap $s=d/3$ (Fig. 1a) and with a frequency of 3650 MHz in an FIM structure with a large gap $s=(5/3)d$ (Fig. 1b) in different fields H_g. (In a field $\Omega_H=0.25$, the gap $s_b(\Omega_H)\approx(4/3)d$.) The choice of the fields H_g is related to the characteristic points of the MSSW trajectories $z(y)$ (the upper z_u and lower $z_{l,s}(k_y)$ bounds according to Eqs. (10)–(12) and others explained in Figs. 2 and 5). The curve $k_z(k_y)$ for a

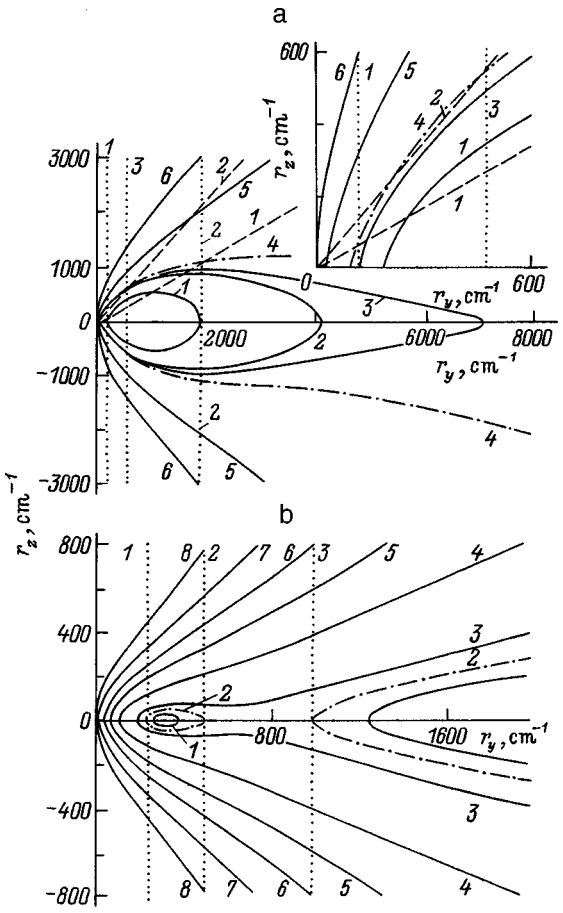

FIG. 1. $k_z(k_y)$ curves for MSSWs in FIM structures: (a) $f_i=3600$ MHz, $s=d/3$, solid curves for H_g (Oe): 278.4 (*1*), 395 (*2*), 410 (*3*), 437.5 (*4*), 611 (*5*), and 680 (*6*); (b) $f_i=3650$ MHz, $s=5d/3$, solid curves for H_g (Oe): 433.8 (*1*), 437.5 (*2*), 445 (*3*), 492.2 (*4*), 546.9 (*5*), 601.6 (*6*), 656.2 (*7*), and 694 (*8*). The inset to Fig. 1a shows a square with sides $(0–600)k_z$ and $(0–600)k_y$.

MSSW excited in a field $\Omega_H=0.25$ is indicated for clarity by a dot-and-dash curve.

It is clear that the $k_z(k_y)$ curves for MSSWs in FIM structures with a small gap s are either similar to ellipses of a noncanonical form [curves *1–3*, as has been found to occur in a field H_0 for MSSWs with frequencies $\Omega_i>\Omega_{u,\infty}(\infty,0)$][6] or are unclosed circles lying between two curves similar to hyperbolas and corresponding to gaps $s=0$ and $s\to\infty$ [curves *4–6*, as has been found to occur in a field H_0 for MSSWs with frequencies $\Omega_i<\Omega_{u,\infty}(\infty,0)$].[6] This means that the dispersion surface $\Omega_s(k_y,k_z)$ in a field H_g is spread out compared to that in a field H_0. The change in the form of the $k_z(k_y)$ curves as the field H_g is reduced is qualitatively the same as in a field H_0 as the frequency of the MSSW is raised. The form of the $k_z(k_y)$ curve and the frequency range and range of angles φ in which MSSWs exist are no longer connected by the relation that is characteristic for the field H_0.[6] It follows from the form of the $\Omega_s(k_y,0)$ and $k_z(k_y)$ curves that in these FIM structures there is one forward and one backward MSSW; here MSSWs with the same frequency Ω_i exist in low fields H_g within the range of angles $-\varphi_{c,0}<\varphi<\varphi_{c,0}$ and in high fields H_g within the range of angles $-\varphi_{c,0}<\varphi<-\varphi_{c,\infty}$ and $\varphi_{c,\infty}<\varphi<\varphi_{c,0}$.

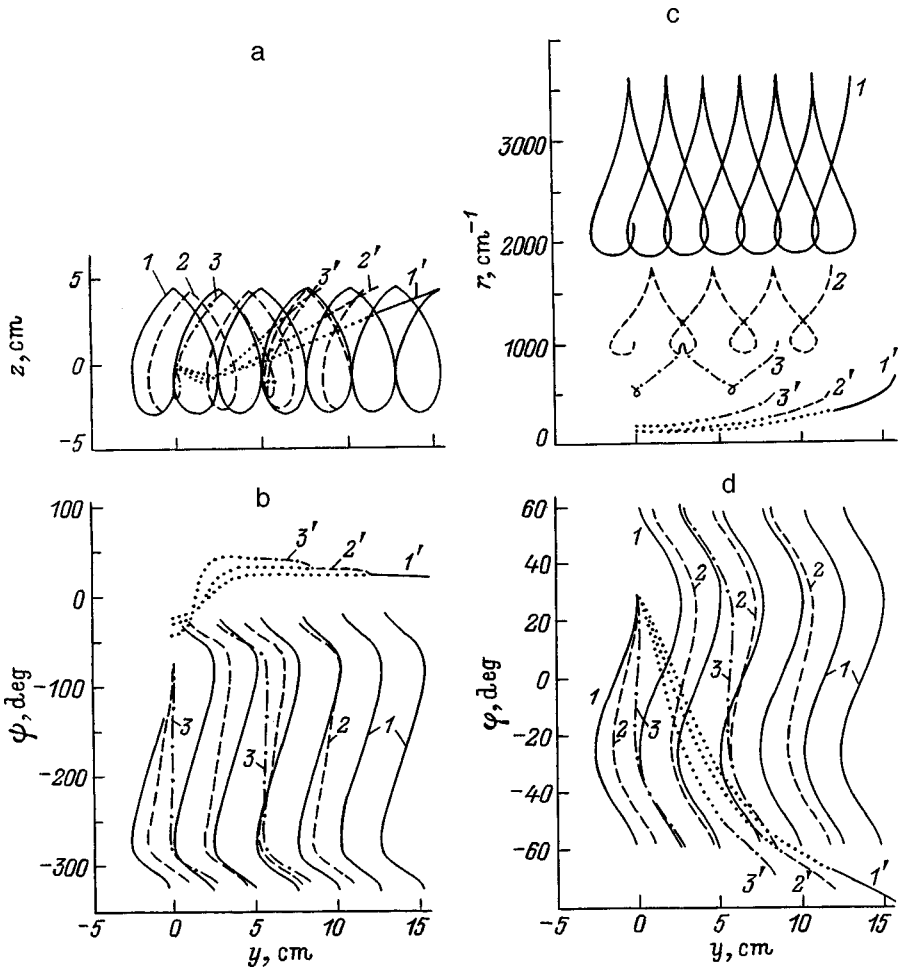

FIG. 2. Trajectories $z(y)$ ($1'$–$3'$) (a) and plots of $\psi(y)$ (b), $k(y)$ (c), and $\varphi(y)$ (d) for MSSWs with frequency $f_i=3600$ MHz in FIM structures: $s=d/3$ (solid curve *1*), $2d/3$ (dashed curve *2*), and d (dot-and-dash curve *3*).

The $k_z(k_y)$ curves for MSSWs in FIM structures with a large gap s are either a combination of a figure similar to a noncanonical ellipse and a curve similar to a hyperbola and corresponding to a gap $s\to\infty$ (curves *1* and *2*, as happened in a field H_0 for a MSSW with a frequency $\Omega_i\approx\Omega_{u,\infty}(\infty,0)$)[6] or unclosed curves lying between two curves similar to the hyperbolas corresponding to gaps $s=0$ and $s\to\infty$, with a convexity and a concavity which, as the gap s decreases, shift along a curve similar to a hyperbola corresponding to a gap $s\to\infty$ toward smaller values of k_y (curves *3–8*, as has been found to occur in a field H_0 for MSSWs with frequencies $\Omega_i<\Omega_{u,\infty}(\infty,0)$).[6] The form of the $\Omega_s(k_y,0)$ and $k_z(k_y)$ curves implies that in these FIM structures there are two forward and one backward wave; here MSSWs with one and the same frequency Ω_i exist for low fields H_g within the range of angles $-\varphi_{c,\infty}<\varphi<\varphi_{c,\infty}$ and for high fields H_g within the ranges of angles $-\varphi_{c,\infty}-\delta\varphi_s<\varphi<-\varphi_{c,\infty}$ and $\varphi_{c,\infty}<\varphi<\varphi_{c,\infty}+\delta\varphi_s$, where $\delta\varphi_s>0$ and $\delta\varphi_s\to 0$.

The $k_z(k_y)$ curves can be used to study the propagation of MSSWs. The excitation of MSSWs begins at the points of intersection of a straight line extending from the coordinate origin at a specified angle φ_0 (dashed curves in Fig. 1), with the $k_z(k_y)$ curve corresponding to a field H_g at the point where the MSSW is excited. The lines $k_{y,i}=k_{yf,i}$ and $k_{y,i}=k_{yb,i}$ are drawn from the points of intersection, and the end of the wave vector **k** moves along these as the MSSW propagates in the field H_g. Here the end of the wave vector **k** lies on the $k_z(k_y)$ curves for different fields H_g, thereby determining the points of the trajectory [according to Eq. (1)], the full magnitude of the wave vector k, and the angles φ and $\psi_{f(b)}$ at each point of the MSSW trajectory.[10,14]

In Fig. 1a one can see two previously unknown effects. The first is that the MSFSW in FIM structures with a small gap s is transformed into a backward wave in some field H_g. This follows from the change in the $k_z(k_y)$ curves [from curves *1–4* ($H_g<H_{gfb}$) to curves *5* and *6* ($H_g>H_{gfb}$)], intersected by the dotted line *1* ($k_y=k_{yf}$) passing through the point of intersection of the dashed line *1* which goes from the coordinate origin at an angle $\varphi_0=30°$ with the dot-and-dash curve $k_z(k_y)$ (Fig. 1a and the inset in it). This effect occurs for MSSWs with arbitrary frequencies. In the second effect, a MSBSW directed at an angle $|\varphi_0|=|\varphi_{c,s}|-|\delta\varphi_s|$, where $\delta\varphi_s\approx 0$, in FIM structures with a small gap s undergoes a transformation into a MSFSW in some field H_{gbf}. This follows from a change in the curves $k_z(k_y)$ [from curves *2–6* ($H_g>H_{gbf}$) to curve *1* ($H_g<H_{gbf}$)], in which are intersected by the dotted line *3* ($k_y=k_{yb}$) passing through the point of intersection of the dashed line *2* going from the coordinate origin at an angle $\varphi_0=50°$ with the dot-and-dash curve $k_z(k_y)$ (Fig. 1a and the inset in it). This effect also occurs for MSSWs with arbitrary frequencies. For $|\varphi_0|<|\varphi_{c,s}|$ a MSBSW always remains a backward wave (see the variation in the $k_z(k_y)$ curves intersected by the dotted line *2*, $k_y=k_{yb}$). It follows from Fig. 1b that these effects

also occur for MSSWs in FIM structures with a large gap s. The first effect is more marked for smaller angles $|\varphi_0|$. (In Fig. 1b, $\varphi_0=0$ and the dashed lines coincide with the k_y axis.) Evidently, the first MSFSW transforms into a MSBSW at lower fields H_g than does the second MSFSW (cf. the intersection of the dotted lines *1* and *3* with the $k_z(k_y)$ curves). The second effect shows up only when the $k_z(k_y)$ curve for the field H_g in which a MSSW is excited is continuous, and it does not occur in the example shown in Fig. 1b.

Magnetostatic surface waves in FIM structures magnetized by a linearly nonuniform field H_g are known[12,13,15] to propagate in a waveguide channel of the first kind, which is characterized by the fact that MSSWs reach both boundaries, $z_{l,s}(k_y)$ and z_u. At the $z_{l,s}(k_y)$ boundary, the propagation direction of the MSSW rotates and at the z_u boundary, the MSSW undergoes mirror reflection. This is valid for both forward and backward MSSWs. The behavior of a MSSW at the boundaries determines the shape of the trajectory $z(y)$ and the functions $\psi(y)$, $k(y)$, and $\varphi(y)$. The arguments of Refs. 12–15 imply that when a MSSW propagates in a waveguide channel of the first kind the trajectories $z(y)$ and the functions $\psi(y)$, $k(y)$, and $\varphi(y)$ are periodic functions with the same period L_y, which is different for the forward (L_{yf}) and backward waves (L_{yb}). The form of the singular points at the edges of the period L_y is determined by the mirror reflection law at the z_u boundary: these are kinks in the MSSW trajectories $z(y)$ and in the functions $k(y)$ and points of discontinuity in the functions $\psi(y)$ and $\varphi(y)$,[12,13] the coordinates of which, $y=y_{sp,n}$ (where n is the number of the singularity), are all the same. The periods L_{yf} and L_{yb} are most easily determined from the trajectories of the MSSWs, $z(y)$, as the distance along the y axis between two reflections of a MSSW from the z_u boundary. The rotation in the propagation direction of a MSSW at the boundary $z_{l,s}(k_y)$ causes minima to appear in the functions $z(y)$ and $k(y)$ at $y=y_{e,n}$ (n in the ordinal number of the minimum points) and the points $y_{\varphi n}$ and $y_{\psi n}$, at which $\varphi(y)=0$ and $\psi(y)=0$ for MSFSWs and $\varphi(y)=180°$ for MSBSWs ($y=y_{e,n}=y_{\varphi n}=y_{\psi n}$). The functions $z(y)$ and $k(y)$ are symmetric with respect to straight lines parallel to the ordinate and passing through the points $y=y_{e,n}$. The functions $\varphi(y)$ and $\psi(y)$ are symmetric with respect to a 180° rotation about the points $y=y_{e,n}$, $\varphi=0$ and $y=y_{e,n}$, $\psi=0$ for MSFSWs and $\psi(y)=180°$ for MSBSWs. For $0\leqslant\varphi_0\leqslant\varphi_{c,s}$ the beginning of the first period of the functions is shifted relative to the coordinate origin by $y_0<0$.

The propagation characteristics of MSSWs are shown in Figs. 2–5. Since MSFSWs are converted into MSBSWs and vice versa, in Figs. 2–5 the segments of the characteristics corresponding to MSFSWs are distinguished by dotted curves, while those corresponding to MSBSWs in Figs. 3–5 are indicates by continuous curves. The characteristics of the forward (at the point of excitation) MSSWs are the same as those in Ref. 13.

Figure 2 shows the trajectories $z(y)$ (a) and the functions $\psi(y)$ (b), $k(y)$ (c), and $\varphi(y)$ (d) for MSSWs with a frequency $f_i=3600$ MHz propagating in FIM structures with different gaps s ($s\leqslant s_b$) for $\varphi_0=30°$. The MSSW trajectories

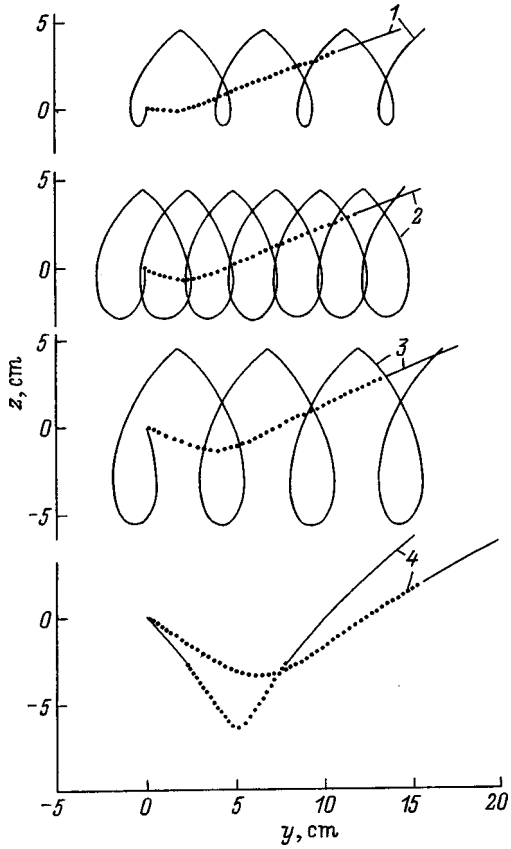

FIG. 3. Trajectories $z(y)$ of MSSWs in an FIM structure for different angles φ_0: 20 (*1*), 30 (*2*), 40 (*3*), 50 (*4*); $s=d/3$.

begin at the point $y=0$, $z=0$. The trajectories of the MSBSWs are similar to a stretched cycloid, with the difference that the peaks are kinks. As the gap s is increased, the area of each of the loops of the stretched cycloid and the extent of the loop within a period L_{yb} decrease. There is a correlation between the form of the MSSW trajectory $z(y)$ and the form of the curves $k_z(k_y)$ in Fig. 1a. In Fig. 1a the $k_z(k_y)$ curves have been plotted for fields H_g corresponding to the following characteristic points on the MSSW trajectory: the coordinate origin (curve *4*), the points at which $\psi=90$ and $-270°$ (curve *2*), the minimum point on the trajectory (curve *1*), the point where the trajectory intersects itself (curve *5*), and a point close to the kink (curve *6*). It is seen that the presence of loops in the trajectory is caused by the intersection of the straight line $k_{y,i}=k_{yb,i}$ (the dotted line *2* in Fig. 1a) with $k_z(k_y)$ curves similar to ellipses of a noncanonical form. The minimum of the trajectory corresponds to tangency of the straight line $k_{y,i}=k_{yb,i}$ with a curve $k_z(k_y)$ (curve *1*) similar to a noncanonical ellipse. At the points of the trajectory where $\psi=-90$ and $-270°$ the straight line $k_{y,i}=k_{yb,i}$ intersects a curve $k_z(k_y)$ that is similar to a noncanonical ellipse (curve *2*) at the points where $k_z(k_y)$ has horizontal tangents. The straight line $k_{y,i}=k_{yb,i}$ intersects the unclosed curve $k_z(k_y)$ (curve *6*) at the point where the straight line drawn to this point from the coordinate origin is inclined to the k_y axis at an angle $\varphi_{c,\infty}$, which corresponds to a kink on the trajectory. The function $k(y)$ within the limits of the period L_{yb} is similar to a catenary with loops

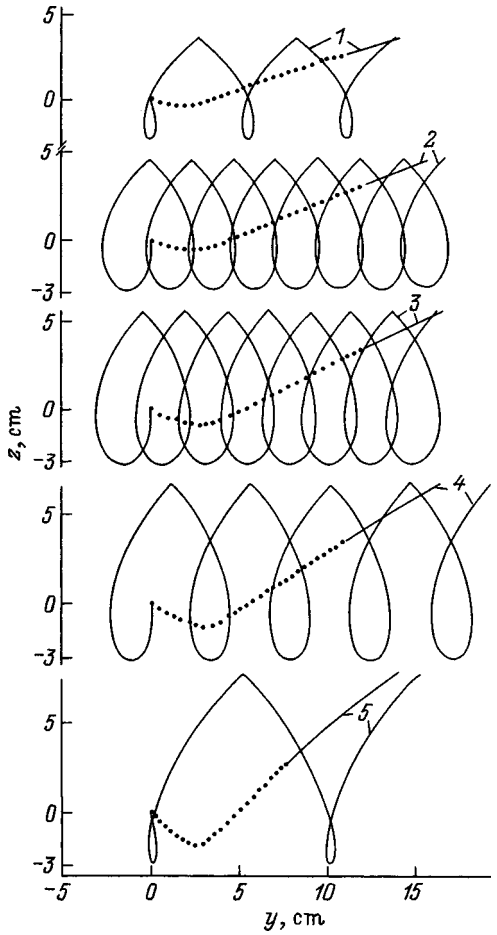

FIG. 4. Trajectories $z(y)$ of MSBSWs with different frequencies in an FIM structure with $s=d/3$ and $f=3400$ (*1*), 3600 (*2*), 3800 (*3*), 4000 (*4*), and 4200 MHz (*5*).

attached to its peak; as the gap s is increased the area of the loops becomes smaller. Within a period L_{yb} the functions $\varphi(y)$ and $\psi(y)$ have two vertical tangents each; as the gap s is increased, the distance along y between the vertical tangents decreases. The period L_{yb} for MSBSWs is always less than that of the MSFSWs, L_{yf}, and the ratio $L_{yb}L_{yf}^{-1}$ is smaller when the gap s is smaller. The characteristics of the MSFSWs and the MSBSWs excited by them are qualitatively similar to those for MSFSWs in ferrite films.[12]

Figure 3 shows trajectories $z(y)$ for MSSWs with a frequency $f_i=3600$ MHz propagating in an FIM structure with a gap $s=d/3$ for angles φ_0 in the interval from $|\varphi_{c,\infty}|=14.3°$ to $|\varphi_{c,s}|=52°$, where MSFSWs and MSBSWs exist (as is easily confirmed from Fig. 1a). Qualitatively the trajectories $z(y)$ have the same shape as in Fig. 2. The form of the functions $\psi(y)$, $k(y)$, and $\varphi(y)$ is uniquely related to the form of the MSSW trajectory $z(y)$. If the form of the trajectories is the same for any sets of parameters f, s, and φ, then the form of the functions $\psi(y)$, $k(y)$, and $\varphi(y)$ will also be the same. Thus, we can qualitatively judge the shapes of the functions $\psi(y)$, $k(y)$, and $\varphi(y)$ as the angle φ varies from Fig. 2, so they are not shown here. The trajectories $z(y)$ have a loop and at some angle φ_0 the width of the loop relative to the period L_{yb} is greatest (compare curves *1* and *3* with curve *2*). Depending on the width of the loop in $z(y)$, the functions

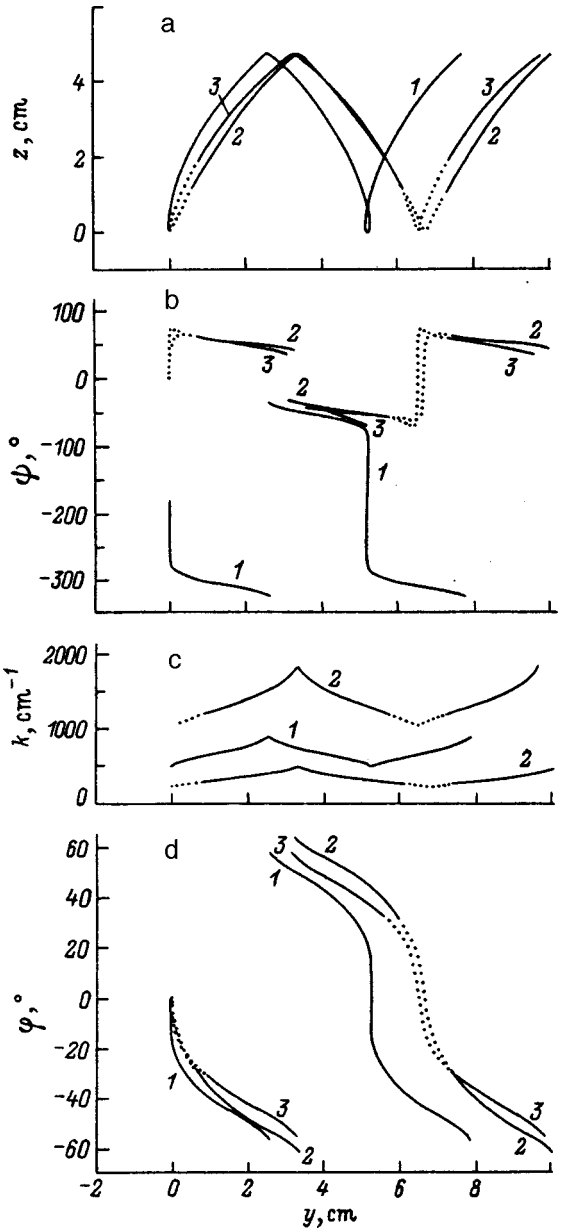

FIG. 5. Trajectories $z(y)$ (a) and $\psi(y)$ (b), $k(y)$ (c), and $\varphi(y)$ (d) curves for MSSWs in an FIM structure with $s=(5d/3)$: (*1*) backward wave, (*2*) first ''forward'' wave, and (*3*) second ''forward'' wave.

$\psi(y)$, $k(y)$, and $\varphi(y)$ also behave as in Fig. 2. An exception is the MSSW characteristics for $\varphi_0\approx 50°$. This is because for $\varphi_0\approx\varphi_{c,s}$, as they propagate toward lower values of the field H_g the MSBSWs are converted into MSFSWs over small distances y (curve *4*), which is apparent from the inset to Fig. 1a from the change in the $k_z(k_y)$ curves intersected by the dotted line *3*. The trajectories of the MSBSWs and the MSFSWs excited by them are qualitatively similar to those for MSSWs in ferrite films.[12]

Figure 4 shows trajectories $z(y)$ for MSSWs with different frequencies propagating in an FIM structure with a gap $s=d/3$ for $\varphi_0=30°$. (The correspondence between the form of the functions $\psi(y)$, $k(y)$, and $\varphi(y)$ and the MSSW trajectories is the same as in Fig. 2.) Evidently, the period L_{yb} has a minimum for a MSBSW whose frequency is

$\Omega_{u,\infty}(\infty,0)$. For this MSSW the loops in the trajectory and the function $k(y)$ have the greatest extent, while the distance between the vertical tangents of the $\psi(y)$ and $k(y)$ curves are maximal. As for the possibility of converting forward into backward MSSWs, it is easy to confirm by comparing with Ref. 13 that the focusing effect described there[13] actually only occurs for MSFSWs. This effect does not exist for MSBSWs. Formally this is because for MSFSWs the period L_{yf} has a maximum at a frequency $\Omega_{u,\infty}(\infty,0)$,[12,13] while it has a minimum for MSBSWs.

Figure 5 shows the trajectories $z(y)$ (a) and the functions $\psi(y)$, $k(y)$, and $\varphi(y)$ (b–d) for MSSWs with a frequency $f_i=3650$ MHz propagating in an FIM structure with a gap $s=(5/3)d$ at an angle $\varphi_0=0$. A comparison with Fig. 1b shows that the field H_0 corresponds to the following points on the MSSW trajectory: the coordinate origin (curve *2*); the minimum point on the trajectory (curve *1*); the points where $\psi=-90$ and $-270°$ (curve *3*); the points where $z=1-4$ (curves *4–7*); and, a point close to the kink (curve *8*). On the $z(y)$ and $k(y)$ curves for the MSSW wave which is always backward, there are loops which are poorly visible on the scale of Fig. 5. For the MSBSWs excited by the MSFSWs, there are no loops of this sort. The periods of the $z(y)$, $\psi(y)$, $k(y)$, and $\varphi(y)$ curves for all the types of MSSWs differ little.

We have examined the propagation of MSBSWs in FIM structures with different insulating layer thicknesses in which a waveguide channel of the first kind develops, on one boundary of which the MSSW undergoes mirror reflection, while on the other boundary the propagation direction of the MSSW is altered. For MSBSWs the shape of the trajectory $z(y)$ and the variation in the wave number $k(y)$ differ from those for MSFSWs in having loops, and the angle of inclination of the group velocity $\psi(y)$ differs in having two vertical tangents. It was found that during propagation of MSSWs, conversion of MSFSWs into MSBSWs always occurs and, under certain conditions, MSBSWs are converted into MSFSWs. There is no spatial focusing effect for MSBSWs.

These results make it possible to set up experiments on FIM structures in an informed way through direct observation of magnetostatic backward surface waves and their conversion into forward waves and back, and to design various devices based on MSSWs.

We thank A. V. Vashkovsky for discussing the results of this work and for advice.

These studies were funded by the Russian Fund for Fundamental Research (Grant No. 96-02-17283-a).

[1] W. S. Ishak, Proc. IEEE **76**, 171 (1984).
[2] A. V. Vashkovsky, V. S. Stalmakhov, and Yu. P. Sharaevsky, *Magnetostatic Waves in Microwave Electronics* [in Russian], Izd. SGU, Saratov (1993), 312 pp.
[3] G. A. Vugal'ter and I. A. Gilinsky, Izv. Vyssh. Uchebn. Zaved. Radiofiz. **32**, 1187 (1989).
[4] Yu. I. Bespyatykh, A. V. Vashkovsky, and R. I. Zubkov, Radiotekh. Elektron. **20**, 1003 (1975).
[5] A. B. Valyavsky, A. V. Vashkovsky, A. I. Stalmakhov, and V. A. Tyulyukin, Radiotekh. Elektron. **33**, 1820 (1988).
[6] R. I. Zubkov and V. I. Shcheglov, Radiotekh. Elektron. **42**, 1114 (1997).
[7] D. D. Stancil and F. R. Morgenthaler, J. Appl. Phys. **54**, 1613 (1983).
[8] A. V. Vashkovskii, V. I. Zubkov, É. G. Lokk, and V. I. Shcheglov, Pis'ma Zh. Tekh. Fiz. **15**(4), 5 (1989) [Sov. Tech. Phys. Lett. **15**(2), 121 (1989)].
[9] G. N. Burlk, V. V. Grimalsky, and N. Ya. Kotsarenko, Zh. Tekh. Fiz. **59**(8), 32 (1989) [Sov. Phys. Tech. Phys. **34**, 860 (1989)].
[10] V. I. Zubkov, E. H. Lock, and V. I. Shcheglov, Radiotekh. Elektron. **35**(8), 1627 (1990); J. Commun. Technol. Electron. Journal of Communications Technology and Electronics **35**(13), 66 (1990).
[11] A. V. Vashkovskii, V. I. Zubkov, É. H. Lokk, and V. I. Shcheglov, Zh. Tekh. Fiz. **60**(7), 138 (1990) [Sov. Phys. Tech. Phys. **35**, 833 (1990)].
[12] A. V. Vashkovsky, V. I. Zubkov, E. H. Lock, and V. I. Shcheglov, Radiotekh. Elektron. **36**(1), 18 (1991); J. Commun. Technol. Electron. **36**(9), 53 (1991).
[13] A. V. Vashkovskii, V. I. Zubkov, É. G. Lokk, and V. I. Shcheglov, Zh. Tekh. Fiz. **65**(8), 78 (1995) [Tech. Phys. **40**, 790 (1995)].
[14] A. V. Vashkovsky, V. I. Zubkov, E. H. Lock, and V. I. Shcheglov, Radiotekh. Elektron. **40**(6), 950 (1995); J. Commun. Technol. Electron. **40**(9), 84 (1995).
[15] A. V. Vashkovsky, V. I. Zubkov, E. H. Lock, and V. I. Shcheglov, Radiotekh. Elektron. **39**, 217 (1994).

Translated by D. H. McNeill

Theory of group synchronism in free-electron waveguide lasers fed a sequence of short electron pulses

N. S. Ginzburg, E. R. Kocharovskaya, and A. S. Sergeev

Institute of Applied Physics, Russian Academy of Sciences, 603600 Nizhniĭ Novgorod, Russia
(Submitted September 16, 1997)
Zh. Tekh. Fiz. **69**, 78–83 (February 1999)

A theory of free-electron lasers fed a sequence of short electron pulses is developed. It is assumed that the group velocity of the electromagnetic pulse that develops in the cavity is the same as the translational velocity of the particles, and the repetition period of the electron pulses equals the transit time of the electromagnetic radiation in the cavity. Under these conditions of group synchronism, the principal factors governing the feasibility of establishing a stationary pulsed lasing regime are found to be the dispersive spread of the electromagnetic pulse and the channeling properties of an electron bunch. The conditions for self-excitation are found, and the characteristics of the stationary lasing regimes are determined assuming that the cavity has a high Q and using a parabolic equation for the evolution of the electromagnetic pulse shape. [S1063-7842(99)01402-6]

INTRODUCTION

In experiments on millimeter and submillimeter free electron lasers (FELs) conducted at ENEA-Frascati[1,2] a microtron which produces electron bunches of duration 15 ps with a repetition rate of 3 GHz was used as an injector. The electrodynamic system of the laser consisted of a segment of regular waveguide bounded by reflectors in the form of metal grids which are transparent to the electrons with the distance between them chosen so that the transit time of the electromagnetic pulse developing in the cavity corresponded to or was a multiple of the repetition period of the electron pulses. In a large number of similar experiments in the IR and optical ranges,[3–5] the group velocity of the radiation exceeded the translational velocity of the bunches, so that, in order to ensure stationary lasing, it was necessary to introduce a certain detuning between the repetition period of the electron pulses and the transit time of the field along the resonator. Using waveguide dispersion has made possible a group synchronism regime in which the group velocity of the electromagnetic pulse propagating in the waveguide tract is the same as the velocity of the electron bunches. Under these conditions, a stationary lasing regime can be attained when the repetition period T_i of the electron pulses and the round-trip transit time $T_R = 2l_0/v_{gr}$ of the electromagnetic pulse are equal, where l_0 is the distance between the mirrors and v_{gr} is the wave group velocity. In the stationary regime the electromagnetic pulse is amplified as it travels along with the electron pulse. Subsequently the electron pulse leaves the interaction region, while the electromagnetic pulse is reflected from the mirror located on the collector side and reaches the cathode mirror at the moment the next electron pulse arrives. For mutual synchronization of the radiation in the volume of the electron pulse it is of fundamental importance to take into account the dispersive spreading of the electromagnetic pulse, which causes different parts of the electron beam to have an effect. Another important factor is the localization of the field near the electron pulse owing to the reactive part of the electron susceptibility. Because of this effect, there is an exponential decay of the fields with distance from the bunch.

In this paper a theoretical model of the interaction of a sequence of short electron bunches with an electromagnetic pulse under group synchronism conditions is developed assuming that the cavity has a high Q and that the amplitude of the field of the electromagnetic pulse changes little during a single pass. A parabolic equation is used to describe the evolution of the shape of the electromagnetic pulse. The conditions for self-excitation of the laser and the stationary lasing parameters are found. The analogy with radiation channeling by transversely bounded electron streams is pursued.

MODEL AND BASIC EQUATIONS

Let the laser radiation propagating inside a waveguide tract be trapped between two mirrors with reflectivities $R_{1,2}$ separated by a distance l_0. Electrons oscillating in the undulator field and moving longitudinally with a translational velocity $v_\parallel$ equal to the group velocity v_{gr} of the wave are injected into the cavity in the form of a sequence of short pulses of duration τ_p with a repetition rate T_i equal to the transit time T_R of the field across the cavity.

The field in a single pass in such a cavity can be written in the form

$$\mathbf{A} = \mathrm{Re}[\mathbf{E_s}(\mathbf{r}_\perp) A_n(z,t) \exp(i(\omega_0 t - h_0 z))],$$

where $A_n(z,t)$ is a function describing the evolution of the field amplitude along the longitudinal coordinate, $\mathbf{E_s}$ is a function specifying a fixed transverse distribution of the field of the working waveguide mode, ω_0 is the carrier frequency which is chosen to be the frequency of exact tangency of the dispersion curves, and $h_0 = h(\omega_0)$.

The interaction takes place under conditions of synchronism, $\omega - hv_{\parallel} \simeq \Omega_{\perp}$, where $\Omega_{\perp} = h_u v_{\parallel}$ is the frequency of the oscillations of the electrons in the undulator field, $h_u = 2\pi/\lambda_u$, and λ_u is the undulator period.

We shall investigate the process of exciting the cavity by a sequence of short electron pulses under the following conditions: (a) the moduli of the reflectivities of the mirrors are close to unity, i.e., $R_{1,2} \simeq 1$, so the change in the amplitude of the envelope of the signal in a single pass through the cavity is small, and (b) the dispersive spreading of the wave beam in a single pass through the cavity is small.

Under these assumptions, after transforming from the discrete variable n, the number of the pass, to the slow time τ, for which the unit is T_R, the evolution of the field inside the cavity can be described by the equation[6–8]

$$\frac{\partial \alpha}{\partial \tau} + \frac{\omega_0}{2Q}\alpha + \frac{\nu v_{\mathrm{gr}}}{2}\frac{\partial^2 \alpha}{\partial \xi^2} = \frac{i2\pi I_0 e \kappa v_{\mathrm{gr}}}{mc^3 \gamma d b N_s h_0 l_0} \int_0^{l_0} I_{\omega} dz f(\xi), \tag{1}$$

where

$$I_{\omega} = \frac{1}{\pi}\int_0^{2\pi} e^{-\Theta} d\Theta_0$$

is the amplitude of the fundamental mode of the rf current, $\xi = t - z/v_{\mathrm{gr}}$ is the time variable, $v_{\mathrm{gr}} = \partial\omega/\partial h$ is the wave group velocity, $\nu = \partial^2 h/\partial\omega^2$ is the dispersive spreading parameter, $Q = \omega_0 l_0/(v_{\mathrm{gr}}(1 - R_1 R_2))$ is the Q of the cavity, I_0 is the peak current, $\gamma = 1/\sqrt{1-\beta^2}$ is the mass factor, $N_s = [(n/b)^2 + (m/d)^2]d^2/m^2$ is the form factor for the working TE_{nm} mode (for TE_{01} with electron injection along the waveguide axis, $N_s = 1$), d and b are the transverse dimensions of the waveguide, κ is a coupling parameter proportional to the oscillatory velocity of the particles in the undulator field, $f(\xi)$ is a function describing the shape of the electron pulse, and $\alpha = eA_n/(mc\omega_0\gamma_0)$ is the dimensionless field amplitude.

The above assumptions permit the periodic boundary conditions $\alpha(\tau, \xi) = \alpha(\tau, \xi + T_R)$, so the field can be represented as the Fourier series

$$\alpha(\tau, \xi) = \sum_{m=-\chi}^{\chi} a_q \exp(-i2\pi q \xi/T_R).$$

The amplitude of each of the harmonics can be regarded as the amplitude of a cavity mode with a given longitudinal index q.

Assuming that the change in the energy of the electrons is small and neglecting the near Coulomb interaction of the particles, we can write the averaged equations of motion for the electrons in the form

$$\frac{\partial^2 \Theta}{\partial z^2} = \left(\frac{\omega_0}{c}\right)^2 \mu\kappa \mathrm{Im}(\alpha e^{i\Theta}) \tag{2}$$

with the boundary conditions

$$\left.\frac{d\Theta}{dz}\right|_{z=0} = \Delta, \quad \Theta_{z=0} = \Theta_0 \in [0, 2\pi],$$

where $\Delta = (\omega_0 - hv_{\parallel} - \Omega_{\perp})/\omega_0$ is the detuning from synchronism at the carrier frequency and μ is the inertial bunching parameter ($\mu \simeq \gamma_0^{-2}$).

Switching to the normalized variables

$$\zeta = \xi\sqrt{\frac{1 - R_1 R_2}{\nu l_0}}, \quad \hat{\tau} = \omega_0 \tau/2Q,$$

$$Z = z\frac{\omega_0}{c}P,$$

$$P = \left(\frac{eI_0}{mc^3}\frac{4\pi c \mu \kappa^2}{\gamma d b h \omega_0^2 N_s \sqrt{\nu l_0 (1 - R_1 R_2)}}\right)^{1/3},$$

we transform the system of Eqs. (1) and (2) to the form

$$\frac{\partial a}{\partial \hat{\tau}} + a + i\frac{\partial^2 a}{\partial \zeta^2} = iF(\zeta)\int_0^L I_{\omega} dZ, \tag{3}$$

$$\frac{\partial^2 \Theta}{\partial Z^2} = \mathrm{Im}(a e^{i\Theta}), \tag{4}$$

$$a(\hat{\tau}, \zeta) = a(\hat{\tau}, \zeta + \hat{T}_R),$$

$$\Theta|_{z=0} = \Theta_0 \in [0, 2\pi], \quad \left.\frac{d\Theta_0}{dZ}\right|_{Z=0} = \hat{\Delta},$$

where

$$a = \alpha P^{-2}\kappa\mu, \quad \hat{T}_R = T_R\sqrt{\frac{1 - R_1 R_2}{\nu l_0}};$$

$L = l_0 P \omega_0/c$ is the normalized interaction length of the electrons with the electromagnetic field; and, the function $F(\zeta)$, which describes the shape of the electron pulse, is normalized as follows: $\int_{R0}^{\hat{T}} F d\zeta = 1$ (after this we will omit the hat $\hat{}$ from symbols).

LINEAR THEORY

Linearizing the equation of motion of the electrons (4), we obtain an equation for field excitation in a high-Q cavity by a sequence of electron bunches,

$$\frac{\partial a}{\partial \tau} + i\frac{\partial^2 a}{\partial \zeta^2} = iaL^3 \Psi(\Phi) F(\zeta), \tag{5}$$

where

$$\Psi(\Phi) = 2i\frac{1 - e^{i\Phi}}{\Phi^3} - \frac{1 + e^{-i\Phi}}{\Phi^2}$$

is a function which specifies the complex electronic susceptibility introduced in the cavity by the beam (Fig. 1).

We shall find the eigenmodes of the system, writing the solution of the equation in the form $a = e^{i\Omega t}\tilde{\alpha}(\zeta)$, where Ω is the complex eigenfrequency. These modes are referred to as supermodes, since they represent a definite set of modes of a cold two-mirror cavity.

Let us assume for simplicity that the electron pulse has a rectangular shape

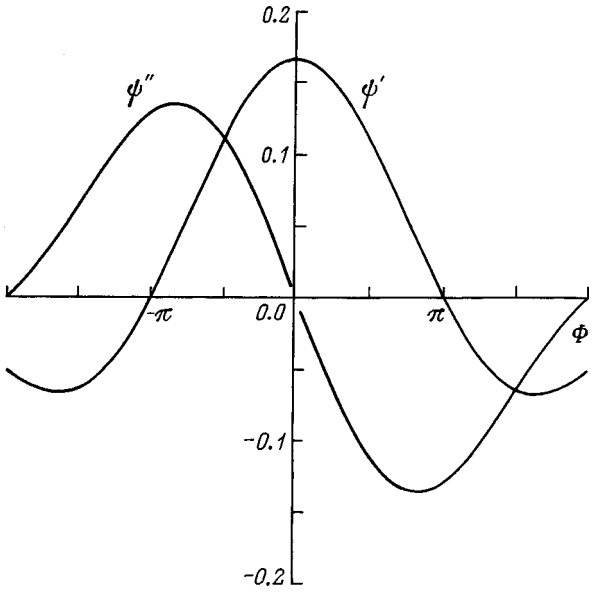

FIG. 1. The active Ψ'' and reactive Ψ' parts of the effective susceptibility introduced in the cavity by the electron beam as a function of the transit angle Φ of the electrons.

$$F(\zeta)=\begin{cases}1/T_P, & \text{for } |\zeta|\leqslant T_P/2\\ 0, & \text{for } |\zeta|>T_P/2,\end{cases}$$

where $T_P=\tau_p\sqrt{(1-R_1R_2)/\nu l_0}$ is the normalized duration of an electron bunch.

We write the field inside an electron pulse, $|\zeta|\leqslant T_P/2$ as the sum of two oppositely directed waves,

$$a=e^{i\Omega\tau}\cdot(A_1e^{i\chi\zeta}+A_2e^{-\chi\zeta}),$$

where the wave number χ obeys a dispersion relation that includes the electronic susceptibility,

$$i\Omega+1-i\chi^2=-iL^3\Psi(\Phi)/T_P.$$

We write the field in the region outside the bunch ($|\zeta|>T_P/2$) in the form

$$a=e^{i\Omega\tau}\cdot\begin{cases}C_1e^{ig\zeta}+C_2e^{-ig\zeta}, & \text{for } \zeta>T_P/2,\\ C_3e^{ig\zeta}+C_4e^{-ig\zeta}, & \text{for } \zeta<T_P/2,\end{cases}$$

where the wave number q outside the electron bunch is determined from the equation

$$i\Omega+1-iq^2=0.$$

Using the periodic conditions

$$a(\tau,\zeta=-T_R/2)=a(\tau,\zeta=T_R/2),$$

$$\left.\frac{\partial a}{\partial\zeta}\right|_{\tau,\zeta=T_R/2}=\left.\frac{\partial a}{\partial\zeta}\right|_{\tau,\zeta=-T_R/2}$$

and the continuity condition for the electric field and its derivative (the magnetic field) at the boundary between the active medium and the vacuum, we obtain the following characteristic equations:

$$\tan\left(\frac{q(T_P-T_R)}{2}\right)=\frac{\chi}{q}\tan\left(\frac{\chi T_P}{2}\right)\quad\text{for symmetric modes,}\tag{6}$$

and

$$\cot\left(\frac{q(T_P-T_R)}{2}\right)=\frac{\chi}{q}\cot\left(\frac{\chi T_P}{2}\right)\quad\text{for antisymmetric modes.}\tag{7}$$

First we shall find the condition for self-excitation of FELs fed a sequence of short pulses. We assume initially that the electron pulse is very short on the scale of the length of the electromagnetic pulse and also as compared to the transit period T_R of the wave. In this approximation, which actually neglects the interference of the fields emitted by the bunch in the positive and negative z directions over an interval $T_R/2$, we can use a model of an infinitely thin electron bunch $[F(\zeta)=\delta(\zeta)]$ in an infinite space ($T_R\to\infty$). Letting T_p approach zero and T_R increase without bound, we reduce the characteristic equation (6) for the symmetric modes to the form

$$q=-iL^3\Psi(\Phi)/2.\tag{8}$$

According to Eq. (8), the imaginary part q'' of the wave number is proportional to the real part of the susceptibility, Ψ', while the real part q' of the wave number is determined by the imaginary part of the susceptibility, Ψ''. Thus Ψ' is responsible for the exponential drop in the field with distance from the electron bunch, while Ψ'' determines the flux of electromagnetic energy leaving the bunch. This solution is analogous to one obtained[9,10] for describing the channeling of radiation as a thin layer by a ribbon electron beam moving through a high-circulation cavity.

In this limit there is a single symmetric mode, for which the growth rate $G=-\operatorname{Im}\Omega$ and frequency shift $\operatorname{Re}\Omega$ are

$$G=-1-\operatorname{Im}(q^2)=-1+L^6\Psi'\Psi''/2$$

$$\operatorname{Re}\Omega=\operatorname{Re}(q^2)=L^6[(\Psi'')^2-(\Psi')^2]/4.\tag{9}$$

Accordingly, the starting condition ($G=0$) can be reduced to the form

$$L_{\text{st}}=\sqrt{\frac{2}{\Psi'\Psi''}},$$

$$I_{\text{st}}=\frac{mc^3}{e}\cdot\sqrt{\frac{2}{\Psi'\Psi''}}\cdot\left(\frac{c}{l_0\omega_0}\right)^3\frac{\gamma dbn_s h\omega_0^2\sqrt{(1-R_1R_2)\nu l_0}}{4\pi c\mu\kappa^2}.\tag{10}$$

It is clear from Eq. (10) that, unlike in the case where the electron stream entirely fills the cavity, the growth rate and starting current include both the imaginary and real parts of the electronic susceptibility. This is because, whereas the imaginary part of the susceptibility is responsible for amplifying the radiation, it is the real part which determines the channeling properties of the electron bunch. (See the form of the electromagnetic pulse shown as curve *3* of Fig. 2.) The greater Ψ'' is, the more the electromagnetic pulse is localized, the smaller the volume occupied by the electromagnetic field is, and the larger the time growth rate is for a given charge in the bunch. In this regard, for a model of delta-function bunches, the optimum transit angle Φ for lasing is about $-\pi/2$ (Fig. 3).[9,10]

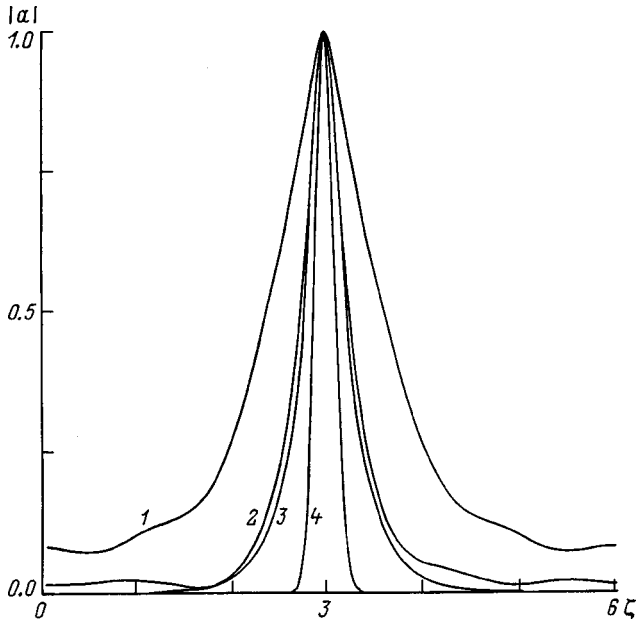

FIG. 2. The structure of an electromagnetic pulse ($\sigma=0.37$, $T_R=6$): (*1*) solution of the evolution equations (3) and (4) for stationary lasing; (*2*) solution of the evolution equations (3) and (4) in the linear stage; (*3*) solution of the characteristic equation (6) ($T_P=0.26$, $T_R=6$); (*4*) a profile of an electron bunch.

Assuming, as before, that the electron bunch is infinitely short, let us consider a resonator of finite length, i.e., consider that the tails of the electromagnetic pulse, although they fall off exponentially, nevertheless do interfere over a distance $T_R/2$ from the site of the electron bunch. Evidently, in this case an infinite discrete spectrum of modes develops with different spatial structure and different temporal growth/decay rates. Evidently, in this case there are two families of modes. The first is the modes of a cold cavity, only slightly modified under the influence of the electron bunches. These modes can be referred to as volume modes, i.e., they fill the entire space of the growth rates for the second family of modes, localized near the electron bunch. Given the finiteness of T_R the characteristic equation for the symmetric modes takes the form

$$q\tan\left(\frac{qT_R}{2}\right)=-\frac{L^3\Psi(\Phi)}{2}. \tag{11}$$

Here we restrict ourselves to including the effect of the finiteness of T_R on the starting conditions and the structure of the fundamental symmetric mode. For the modes that are strongly compressed toward the beam ($\Phi\simeq-\pi/2$), in the expression for the complex wave number which follows from Eq. (11), there is only a small correction associated with the finiteness of T_R [cf. Eq. (8)],

$$q\simeq -i\frac{L^3\Psi(\Phi)}{2}\left[1+2\exp\left(-\frac{T_RL^3\Psi(\Phi)}{2}\right)\right]. \tag{12}$$

According to Eq. (12), for $T_RL^3\Psi(\Phi)/2\geqslant 2$ the correction to the wave number q is exponentially small. The expression for the growth rate

$$G=-1+\frac{2rs}{T_R^2}(1+4e^{-r}\cos s+4e^{-2r}\cos 2s)$$
$$+\frac{4(s^2-r^2)}{T_R^2}(e^{-r}\sin s+e^{-2r}\sin 2s), \tag{13}$$

where

$$r=\frac{L^3T_R\Psi'}{2}$$

and

$$s=\frac{L^3T_R\Psi''}{2},$$

also remains substantially unchanged from Eq. (9).

A comparison of the expressions for the starting length as a function of the transit angle obtained in terms of the above models shows that the results are essentially completely in agreement for $T_R>6$. The exact solution of the characteristic equation (11) shows that for $\Phi\simeq-\pi/2$ the starting interaction length for these two models are essentially the same (Fig. 3).

As an estimate of the correction associated with the finite thickness of the electron layer, let us consider a model of an electron layer of finite thickness, neglecting the finiteness of T_R for simplicity. In this case, the characteristic equation (6) for symmetric modes takes the form

$$q=-i\chi\tan\left(\frac{\chi T_P}{2}\right). \tag{14}$$

In the case $|\chi T_P|\ll 1$, its solution can be written approximately in the form

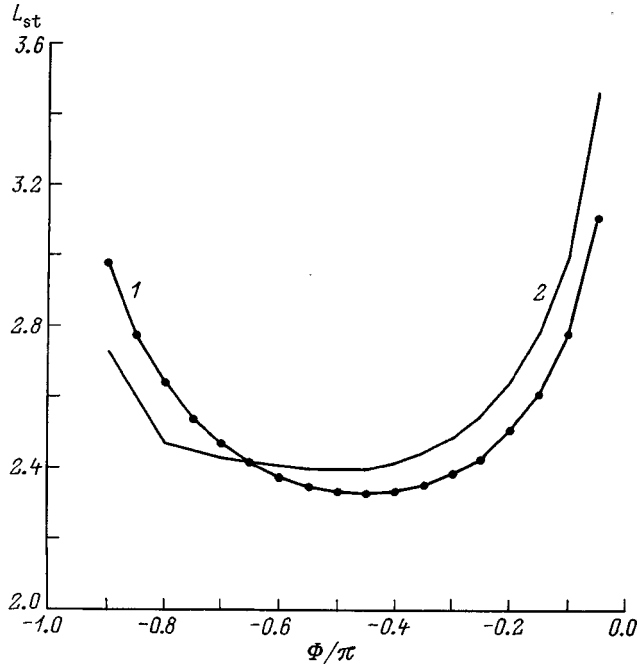

FIG. 3. The normalized starting length L_{st} on the transit angle Φ of the electrons: (*1*) model of a delta-function bunch of electrons for $T_R\to\infty$ (the points denote the solution for $T_R=6$), (*2*) model of an electron bunch of finite thickness $T_P=0.26$ for a transit period $T_R=6$.

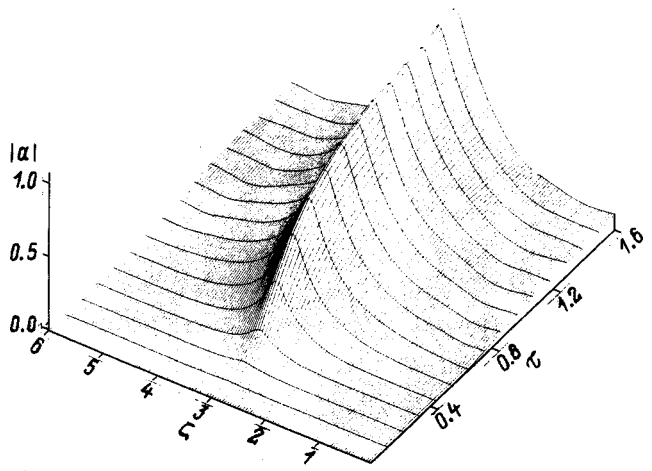

FIG. 4. Time evolution of the shape of an electromagnetic pulse.

$$q \simeq -i\frac{L^3\Psi}{2}\sqrt{1-\frac{T_P L^3\Psi}{16}}.$$

When $T_P L^3|\Psi|/16 \ll 1$ the structure of the fundamental mode for the delta-layer model is essentially identical to the field structure for a model with a layer of finite width. Naturally, this assertion is correct as long as the electron layer remains thin on the scale of the electromagnetic pulse length. The growth rate including the finiteness of T_P can be written in the form

$$G=\frac{L^6\Psi'\Psi''}{2}-1-\frac{L^9 T_P\Psi''}{64}((\Psi')^2-\Psi'').$$

It is clear that when the above condition is satisfied, the growth rate does not change significantly compared to the growth rate for the delta-layer model.

Thus, accounting for the finiteness of the field transit time T_R across the cavity and the finite duration of the electron beam does not have much effect on the starting conditions and growth rates, or on the spatial structure of the fundamental symmetric mode. Thus, it possible to use the fairly simple model of a delta-function bunch in an infinite space for practical estimates of the parameters of the system. For comparison with the analytical results, Fig. 3 shows exact numerical solutions of the characteristic equation (6) for finite values of T_P and T_R. This solution was also used for comparison with a numerical simulation of the nonlinear system of equations (3) and (4).

NUMERICAL SIMULATION

The nonlinear stage of the interaction was analyzed with the aid of a numerical simulation of Eqs. (3) and (4). For convenience of modeling, the shape of the electron pulse was approximated by the Gaussian function

$$F(\zeta)=\exp(-\zeta^2/\sigma^2)/\sqrt{2\pi}\sigma.$$

The results of the numerical simulation are shown in Figs. 3–5. The time evolution of the electromagnetic pulse leading to a stationary pulse shape is shown in Fig. 4. This figure shows that in both the linear stage and during stationary lasing, the radiation is strongly pressed to the electron bunch, so we can speak of a channeling effect in this system. For comparison, Fig. 2 contrasts the electromagnetic pulse profiles found using the characteristic equation (6) (curve *3*) and the solution of the evolution equations (3) and (4) which develops in the linear stage (curve *2*). These curves are in good agreement. In the nonlinear stage there is some broadening of the electromagnetic pulse (curve *1*) compared to the linear stage. The numerical calculation was done for a dimensionless pulse duration $\sigma=0.37$ ($T_P=0.26$), repetition period $T_R=6$ of the electron pulses, and interaction length $L=4$. These parameters were calculated from the results of an experiment[1] in which electron bunches of duration 15 ps and with a maximum current $I_p=6$ A and particle energy $\varepsilon=2.3$ MeV were repeated at a rate of 3 GHz. A rectangular waveguide ($d=1$, $b=0.4$ cm) was located in an undulator with a period $\lambda_u=2.5$ cm, length 22.5 cm, and maximum field 6 kOe, which corresponds to $k\simeq\gamma_0^{-1}$. Mirrors with reflectivities $R_{1,2}\geqslant 0.99$ were placed at the ends of the waveguide, separated by a distance $l_0=29$ cm. Lasing was observed at a wavelength $\lambda=0.24$ cm. The spectrum of the pulse in the stationary lasing regime is shown in Fig. 5. The individual components in this figure correspond to the amplitudes of cavity modes with a different number of longitudinal variations in the field. It is clear that the spectrum of this signal includes roughly 5 longitudinal modes, consistent the with spectral measurements.[1] The 80 ps duration of the microwave pulses is in good agreement with the measured 100 ps.

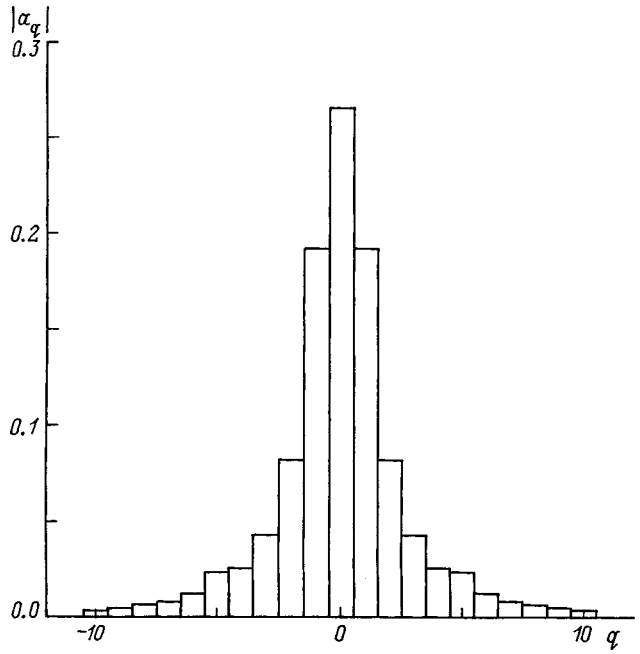

FIG. 5. The spectrum of an electromagnetic pulse in the stationary lasing regime.

[1] F. Ciocci, R. Bartolini, A. Doria *et al.*, Phys. Rev. Lett. **70**, 928 (1993).
[2] A. Doria, R. Bartolini, J. Feinstein *et al.*, IEEE J. Quantum Electron. **29**, 1428 (1993).
[3] D. A. G. Deacon D.A.G., L. P. Elias, J. M. J. Madey *et al.*, Phys. Lett. **38**, 892 (1977).
[4] H. Boehmer, M. A. Gapony, J. Edighoffer *et al.*, Phys. Rev. Lett. **48**, 141 (1982).
[5] V. Billardon, P. Elleaum, J. M. Ortega *et al.*, Phys. Rev. Lett. **51**, 1652 (1983).
[6] N. S. Ginzburg and M. I. Petelin, Izv. vyssh. Uchebn. Zaved. Prikl. Nelineĭn. Dinamika **2**(6), 3 (1994).
[7] Ya. L. Bogomolov, N. S. Ginzburg, V. L. Bratman *et al.*, Opt. Commun. **36**, 209 (1985).
[8] N. S. Ginzburg and M. I. Petelin, Int. J. Electron. **59**, 291 (1985).
[9] N. S. Ginzburg, N. F. Kovalev, and N. Yu. Rusov, Opt. Commun. **46**, 300 (1983).
[10] N. S. Ginzburg, Radiotekh. Elektron. **34**, 1935 (1989).

Translated by D. H. McNeill

Effect of intermode coupling on the compression of radio pulses in an oversize cavity with an interference switch

S. N. Artemenko and V. A. Avgustinovich

Scientific-Research Institute of Nuclear Physics, Tomsk Polytechnical University, 634050 Tomsk, Russia
(Submitted September 12, 1997; resubmitted April 20, 1998)
Zh. Tekh. Fiz. **69**, 84–86 (February 1999)

The results of an experimental investigation of the effect of intermode coupling at the exit window of a cavity on the compression of radio pulses in an oversize cylindrical cavity with an interference switch, operating on $H_{01(n)}$ modes, are reported. The effect of the intermode coupling at the exit window of a cavity on the energy extraction process is analyzed in a simple model in which the interacting modes are represented in the form of a system of two coupled cavities. The results of the analysis are compared with the experimental data. © *1999 American Institute of Physics.* [S1063-7842(99)01502-0]

1. One promising method of rapid extraction of microwave energy from oversize cavities with a large store of energy for the purpose of obtaining powerful nanosecond radio pulses is a method based on extraction through an interference switch.[1–4] This method is promising on account of its simplicity and potentially good performance. However, at present its potential capabilities cannot be realized: The experimental results are substantially below expectations. This is most likely due to the demonstrational nature of the experiments which have been performed. These experiments do not touch upon the fundamental problems that must be solved in order for the promise of the method to be fulfilled. One such problem is maintaining high working characteristics in oversize axisymmetric cavities, which are most suitable for accumulating energy in axisymmetric H modes. Our experience in working with such cavities shows that the real accumulation and extraction processes in them are substantially different from the picture developed in Refs. 1–4. The reason for this is that the modes interact with one another at the cavity–switch coupling window.

In the present paper we investigate the effect of intermode coupling on the operation of a microwave compressor with an interference switch in the presence of accumulation and extraction of energy at $H_{01(n)}$ modes of an oversize cylindrical cavity.

2. Working at a low power level, the Q of the working mode, which characterizes its degree of purity, was investigated first. The investigations consisted in determining the dependence of Q and the frequency of the cavity on the length of the input arm of the switch and the magnitude of its coupling with the cavity. The experiments were performed on a 3-cm range copper cavity with a diameter of 90 mm and a length that could be varied from 50 to 250 mm with the aid of a contact-free piston. A diagram of the system is displayed in Fig. 1: *1* — Cavity; *2* — piston; *3,4* — windows for coupling with the high-frequency section *5* and the switch *6*, made in the form of an H-tee with an entrance arm *6a*, switching arm *6b*, and exit arm *6c*; *7* — commutator. At low power the switch was replaced by a waveguide stub with a shorting plunger, which made it possible to regulate the length of the stub from 0 to $5\lambda w/2$ (λ is the wavelength in the waveguide). The stub simulated the entrance arm of the switch in the accumulation mode. The cavity operated in the frequency range 9.1–9.6 GHz, corresponding to the band of the magnetron used in experiments at high power. The number n is the variant of the working field mode on the cavity axis and could be varied from 3 to 14 with the aid of the piston. The working frequency was chosen so as to reduce to a minimum the effect of other modes on the working mode. The computed value of Q for the working modes with $n=3-14$ was $0.8-1.3\times10^5$.

Figure 2 shows the Q for $H_{10(n)}$ modes versus the diameter d of the exit window for the characteristic stub lengths — the high-frequency half-wave ($\lambda^+/2$ curves), for which the amplitude of the signal from the stub is maximum and the frequency of the system is higher than the frequency of the cavity with the switch open; low-frequency half-wave ($\lambda^-/2$), for which the amplitude of the signal from the stub is also maximum but the frequency is lower than the frequency of the cavity with the switch open; quarter-wave ($\lambda/4$), for which the amplitude of the wave in the stub is minimum and the frequency equals the frequency of the cavity with the switch open; and, finally, optimal (λ^0), corresponding to maximum Q and the frequency of the cavity

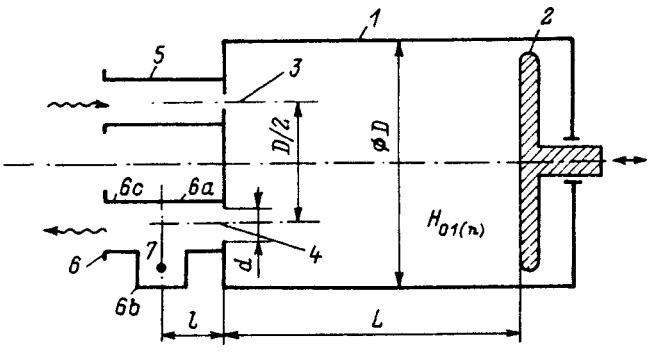

FIG. 1. Diagram of the experimental oversize cavity with an interference switch.

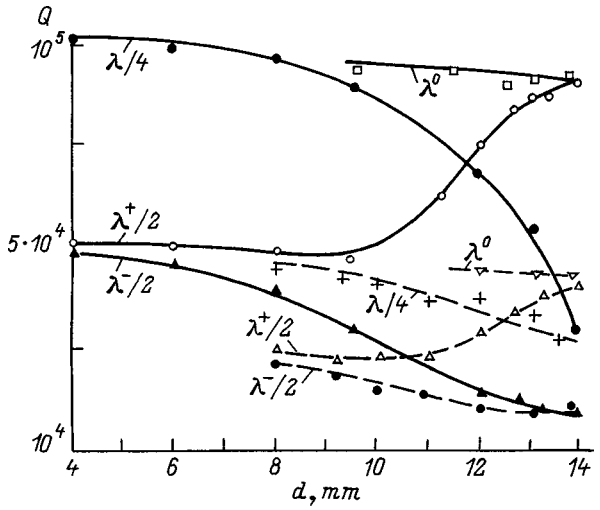

FIG. 2. Curves of Q versus the diameter of the cavity–switch coupling window for various lengths of the input arm of the switch and various values of the entrance coupling.

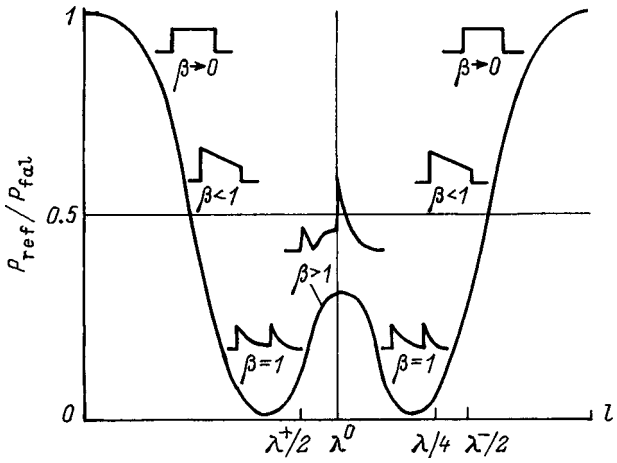

FIG. 3. High-frequency power reflected from the system versus the length of the entrance arm of the switch in the frequency rocking mode (1) and pictures of the reflected signals with pulsed excitation of the system.

with no exit window. The dependences hold for any n, but for each n only in definite frequency ''windows.'' There are frequency ranges where it is impossible to isolate the working mode. The solid curves were obtained with a weak entrance coupling β ($\beta\rightarrow 0$), and the dashed curves were obtained with the critical value of β ($\beta\rightarrow 1$).

It is evident from Fig. 2 that for d small but already giving a strong cavity–stub coupling, the maximum Q is achieved with a quarter-wave stub and this stub length is optimal, while a half-wave stub operates as a low-Q resonant load. This situation corresponds to Ref. 3. At the same time the character of the behavior of Q changes as d increases. For a low-frequency half-wave stub, Q decreases strongly; for a quarter-wave stub it also decreases but not as strongly; and, for high-frequency half-wave stub, after decreasing by a small amount, Q starts to grow. Moreover, the length at which Q is almost constant and close to the value for a cavity with no switch and to which the Q of a system with a high-frequency half-wave stub evolves as d increases can be indicated. The character of the dependences is identical for both weak and critical entrance coupling.

This behavior of Q is evidently due to the appearance of a coupling between modes at the exit window. For weak cavity–stub coupling the stub operates as a low-Q resonant or antiresonant load in the main volume and intermode coupling is weak. As the window increases in size, the character of the loading changes. The stub changes from a low-Q resonant load into a weak perturbation of the main volume of the cavity essentially without changing its characteristics. However, the intermode coupling starts to predominate and leads to a lower Q for a quarter-wave stub and a low-frequency half-wave stub. In the opposite case, an increase in Q with increasing d would be observed both with high- and low-frequency half-wave stubs and the optimum length would be quarter-wave. The different strength of the intermode coupling at the exit window is due to the different degree of distortion of the field near the window with different stub lengths. This is also confirmed by the evolution of the entrance coupling constant as a function of the stub length, shown in Fig. 3 by the pictures of the reflected signal in the frequency rocking mode and in the pulsed mode, where the optimal length corresponds to maximum $\beta>1$ (on the ''hump'') with the loaded Q not less than Q for $\beta=1$ (to the left and right of the ''hump'').

3. The intermode coupling also affects the characteristics of the exit signals from the compressor. This was established in experiments at high power, which were performed by powering the system with a magnetron with $\sim$60 kW pulsed power and pulse duration $\sim 1\,\mu$s. A gas-discharge commutator, operating at atmospheric pressure in air or in a mixture of air with argon, was used in the switch.

Figure 4 shows the characteristic form of the envelopes of the output pulses obtained when the exit window can serve as a strong intermode coupling element ($d>9$ mm). For a smaller window diameter, extraction is inefficient because of weak cavity–load coupling. The curve in Fig. 4a corresponds to extraction with a low-frequency half-wave length, Fig. 4b corresponds to a quarter-wave length, Fig. 4c to high-frequency half-wave length with the optimal value

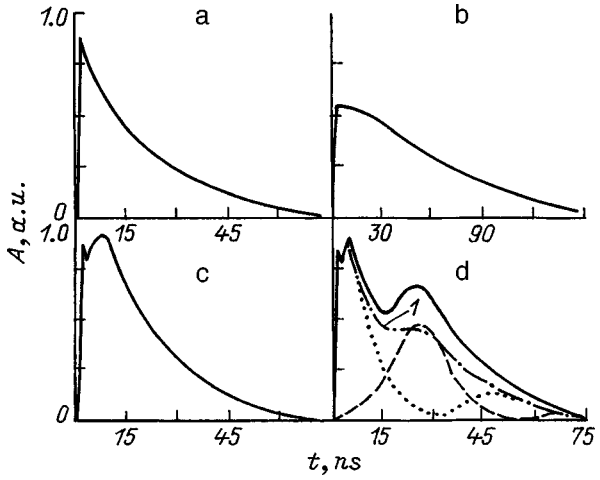

FIG. 4. Characteristic envelopes of the exit radio pulses.

with no or suppressed intermode coupling, and Fig. 4d to high-frequency half-wave length and the optimal value with strong intermode coupling.

The characteristic features of the envelopes are due to the change in the structure of the field near the exit window at the moment of extraction. This change is uniquely related with the change in the frequency of the system accompanying extraction. As energy accumulates in the system with the quarter-wave length or low-frequency half-wave arm, accumulation occurs on a hybrid form with the same energy distribution between the coupled modes. If the system operates with a low-frequency half-wave arm, then an adiabatic increase of the frequency of the system occurs at the moment of extraction. At the same time the coupling at the window decreases and the working mode becomes ''favored.'' The mutual transfer of energy in this case does not occur or it does occur but more slowly than the oscillations decay as a result of radiation into the load. For this reason, just as with a quarter-wave arm, where the frequency of the system and the coupling between modes in the accumulation and extraction mode are unchanged and the extraction occurs from each mode of oscillations independently, in the case of the low-frequency half-wave length signals are observed with virtually pure exponential decay. The process is completely different in the case of high-frequency half-wave and optimal lengths, in which case accumulation proceeds on a quite pure working form with a weak intermode coupling but at the moment of extraction, when the frequency of the system drifts, strong intermode coupling kicks in and, together with extraction at the working mode, energy transfer also occurs to a parasitic mode, which results in the appearance of a ''hump'' on the trailing edge of the exit signal. Adiabatic frequency drift was noticed in Ref. 3, and we confirmed it by measuring the frequency of the signal by the method of displacement with a reference signal with known frequency.

4. The extraction process in the system can be described in a model in which the interacting modes are represented in the form of coupled cavities.[5] In so doing, the intermode coupling parameter m can be estimated by using the fact that the intermode coupling coefficient γ_{12} (Ref. 6) and the drift of the frequency of the system are proportiona to the effective volume of the coupling window and the relation $m \approx 100\gamma_{12}$ (Ref. 7). Figure 5 shows m as a function of the stub length l for various window diameters. One can see that for any d there always exists a length λ^0 for which $m=0$, and as

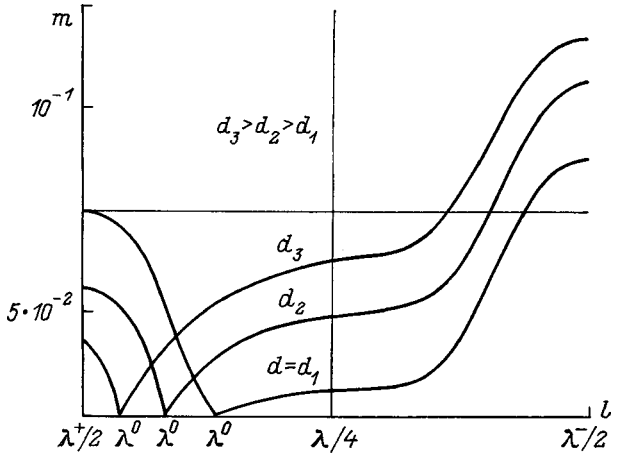

FIG. 5. Curve of the intermode coupling parameter versus the length of the entrance arm of the switch.

d increases, this length evolves in the direction of the high-frequency half-wave length. Curve *1* in Fig. 4d shows the computed envelope of the exit signal with intermode energy transfer on extraction. This envelope agrees qualitatively well with the experimental envelope.

In summary, the results of the present investigation explain the anomalies in the process of compression of radio pulses in an oversize cylindrical cavity working in $H_{01(n)}$ modes, and they indicate methods for eliminating these anomalies. A positive aspect of intermode energy transfer during extraction could be its application for correcting the exit signal envelope.

We thank Yu. G. Yushkov for encouragement in the course of this work.

[1] A. N. Didenko and Yu. G. Yushkov, *High-Power Nanosecond Microwave Pulses* [in Russian], Énergoatomizdat, Moscow, 1984, 112 pp.
[2] D. Birx, G. L. Dick, W. A. Little *et al.*, Appl. Phys. Lett. **33**, 466 (1978).
[3] R. A. Alvarez, D. Birx, D. Byrne *et al.*, IEEE Trans. Magn. **MAG-17**, 935 (1981).
[4] V. A. Avgustinovich, L. Ya. Avgustinovich, S. N. Artemenko, and Yu. G. Yushkov, Izv. Vyssh. Uchebn. Zaved. Radioélektron. **30**, 90 (1987).
[5] S. N. Artemenko, Izv. Vyssh. Uchebn. Zaved. Radiofiz. **30**(10), 1289 (1987).
[6] V. B. Shteĭnshleĭger, *Wave Interaction Phenomena in Electromagnetic Cavities* [in Russian], Oborongiz, Moscow, 1955, 112 pp.
[7] S. N. Artemenko, Radiotekh. Elektron. **40**, 1184 (1955).

Translated by M. E. Alferieff

Calculation of the characteristics of the radiation from a generator with a virtual cathode

S. L. Ginzburg, V. F. D'yachenko, V. V. Paleĭchik, and K. V. Khodataev

M. V. Keldysh Institute of Applied Mathematics, Russian Academy of Sciences, 125047 Moscow, Russia; Moscow Radio Engineering Institute, Russian Academy of Sciences, 113519 Moscow, Russia
(Submitted November 11, 1997)
Zh. Tekh. Fiz. **69**, 87–92 (February 1999)

A three-dimensional computer model, described by a system of Maxwell–Vlasov equations, for the interaction of a plasma with the electromagnetic field was used to calculate the excitation of a field by a relativistic electron beam with a virtual cathode oscillating in a resonance chamber. The characteristics of the generator radiation are investigated. © *1999 American Institute of Physics.* [S1063-7842(99)01602-5]

INTRODUCTION

The present investigation is a continuation of Ref. 1 on the simulation of the generation of electromagnetic oscillations in a device, which, in the terminology used in Ref. 2, is called a reflex diode. In this device an electron beam penetrates through a thin anode foil into a resonant cavity where it produces a virtual cathode. The virtual cathode is an unstable formation and fluctuates at a frequency close to the plasma frequency of the beam.[3] The oscillations of the virtual cathode excite the characteristic modes of the resonant cavity. The energy of the excited electromagnetic oscillations is extracted through a coupling element into a load. The reflex diode is a type of vircator — an electronic device with a virtual cathode.

In Ref. 1, the processes occurring were described assuming azimuthal symmetry. At the same time, for real structures large deviations from symmetry are to be expected because of the need to extract the generated microwave power into a waveguide section. Here a 3D model is used. It made it possible to introduce into the simulated structure of a reflex diode a rectangular branch waveguide, at whose distant end the nonreflective boundary conditions simulate a nonselective equivalent load. The information obtained in Ref. 1 on the characteristics of the electron flux which depend on the geometric parameters and the applied voltage were used to choose typical beam regimes for the purpose of maximizing the microwave generation efficiency.

It is well known that the formation of a virtual cathode in a reflex diode is accompanied by the accumulation of electrons in a potential well formed by the electrostatic field of the self-charge of the beam and the applied potential. The trapped electrons oscillate with respect to the anodic foil. In the presence of oscillations, the electron trapping time is limited to several periods. The energy spectrum and, correspondingly, the frequency spectrum of the oscillations of the trapped particles are quite wide. Depending on the specific conditions, the trapped particles can or cannot participate in the general oscillatory process of the virtual cathode. In the first case they increase the generation efficiency, but in the second case their role reduces to increasing the nonproductive losses.

To increase the generation efficiency, either the trapped electrons must be made to participate in the collective oscillatory process or the presence of the trapped electrons must be reduced to a minimum. The 3D model developed makes it possible to investigate the basic features of the generation process and the degree to which the geometry of the apparatus and the applied voltage influence the generation parameters.

STATEMENT OF THE PROBLEM

The interaction of a relativistic electron beam with an electromagnetic field is described by the system of Maxwell–Vlasov equations. For the appropriate (indicated below) choice of measurement units, the system has the form

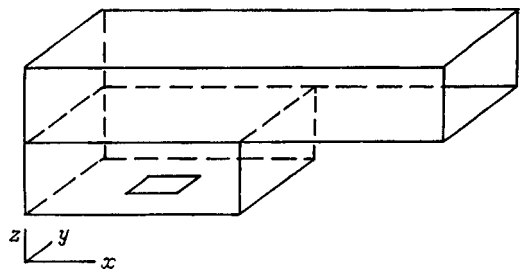

FIG. 1. Diagram of the structure.

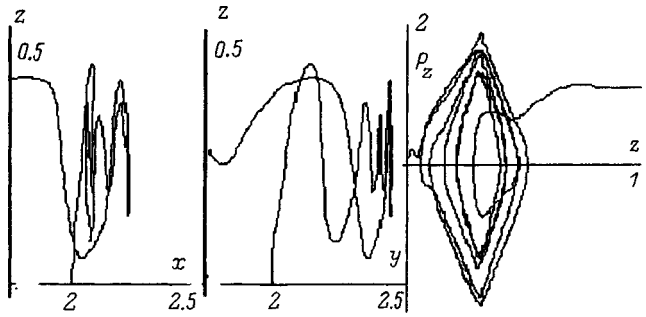

FIG. 2. Projections of the particle trajectory.

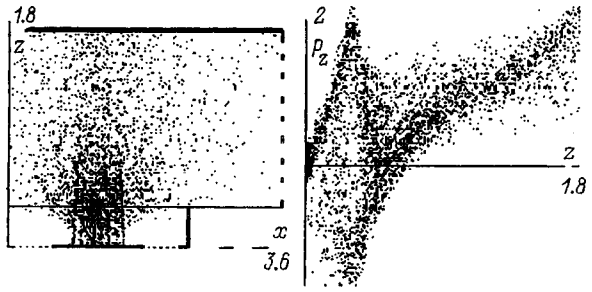

FIG. 3. Form of the flux and its phase portrait.

$$\frac{\partial \mathbf{E}}{\partial t}-\nabla\times\mathbf{H}+\mathbf{j}=0, \quad \nabla\cdot\mathbf{E}=\rho,$$

$$\frac{\partial \mathbf{H}}{\partial t}-\nabla\times\mathbf{E}=0, \quad \nabla\cdot\mathbf{H}=0,$$

$$\frac{\partial f}{\partial t}+\mathbf{v}\cdot\frac{\partial f}{\partial \mathbf{x}}-(\mathbf{E}+\mathbf{v}\times\mathbf{H})\cdot\frac{\partial f}{\partial \mathbf{p}}=0,$$

where $\mathbf{E}(t,\mathbf{x})$ and $\mathbf{H}(t,\mathbf{x})$ is the electromagnetic field, $f(t,\mathbf{x},\mathbf{p})$ is the electron distribution function, $\mathbf{p}$ and $\mathbf{v}$ are, respectively, the electron momentum and velocity, and

$$\rho=-\int f d^3p, \quad \mathbf{j}=-\int \mathbf{v} f d^3p$$

are the charge and current density, respectively.

A general view of the structure being calculated is shown schematically in Fig. 1. It consists of two rectangular chambers: large (top) and small (bottom). The top chamber consists of a waveguide with a square cross section, short-circuited on the left and open on the right, where the relations $E_y-H_z=0$ and $E_z+H_y=0$ are used as the ''nonreflective'' boundary condition. In addition, to simulate the free extraction of the radiation flux into a small layer adjoining this boundary, the medium is assumed to be conducting, i.e., in Maxwell's equations $\mathbf{j}$ is replaced by $\mathbf{j}+\sigma\mathbf{E}$, where σ is the conductivity.

A square cathode, insulated from the chamber walls and the waveguide, is centered at the bottom of the lower chamber. The waveguide is the anode. An electric field, which produces the cathode–anode potential difference applied to the system, is prescribed on the surface of the ''insulator.'' The emissivity of the cathode is realized by a boundary condition on the distribution function $f=-j_{z0}\delta(\gamma-\gamma_0)$ and $j_{z0}=(\nabla\times\mathbf{H})_z$, with, of course, $p_z>0$ and $j_{z0}<0$. Here γ_0 is the prescribed total initial electron energy.

The chambers are separated by a metal foil, which is transparent to electrons (the stopping and scattering of electrons by the foil are neglected at this stage of the investigation). The tangential component of the electric field on the foil and all other walls of the chambers (conducting or with a high permittivity, as in the case of the insulator) is zero. Particles reaching the chamber walls are absorbed there.

The computational results are described using the following measurement units: L — length (characteristic size); c — speed of light in vacuum; L/c — time; c/L — frequency; $c/4\pi L$ — conductivity; mc — electron momentum, where m is the electron rest mass; mc^2 — electron energy; mc^2/eL — field, where e is the elementary charge; mc^2/e — potential; $mc^3/4\pi e$ — current; $m^2c^4L/4\pi e^2$ — energy of the system; $m^2c^5/4\pi e^2$ — power. The problem was solved by a numerical method whose basic principles are presented in Ref. 4.

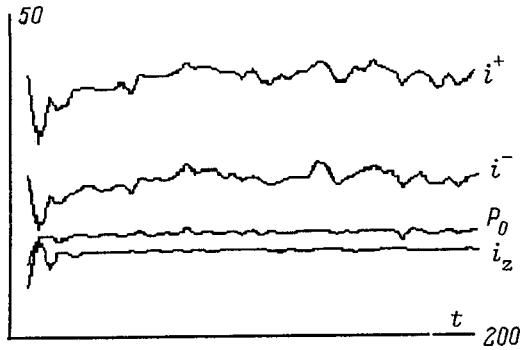

FIG. 5. Current distribution.

BASIC COMPUTATIONAL VARIANT

We take as the basic computational variant the following set of computational parameters: lower chamber — 5×5

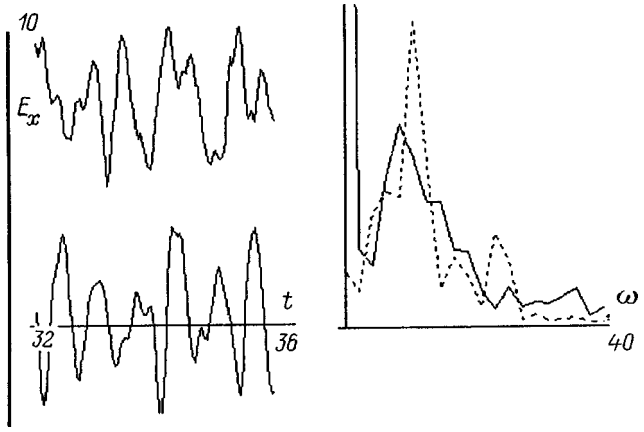

FIG. 4. Field and its frequency spectrum.

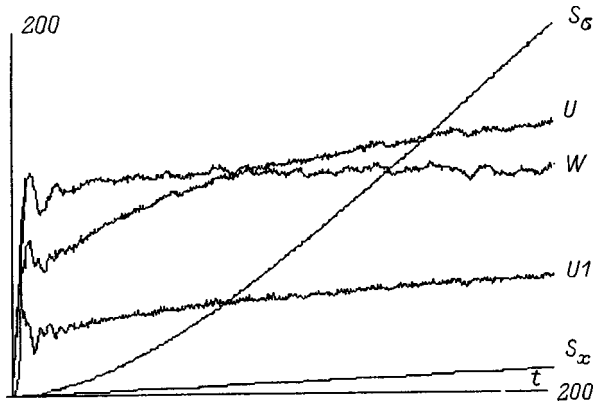

FIG. 6. Energy distribution.

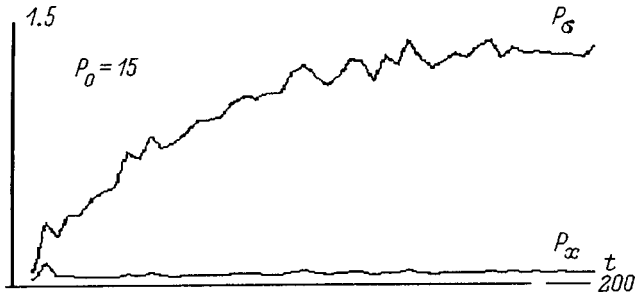

FIG. 7. Useful power.

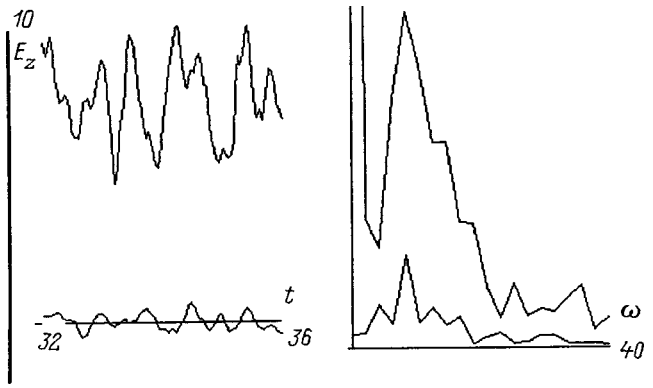

FIG. 8. Field and its spectrum.

square base, height 0.3; upper chamber — 7.6×5 rectangle, height 1.5; cathode — 1.6×1.6 square; voltage $\varphi=1$; kinetic energy of emitted electrons $\gamma_0-1=0.001$; conductivity grows linearly in the layer $6.6<x<7.6$, and its average value $\sigma=1$.

The electromagnetic field arising in the lower chamber when the voltage φ is switched on results in electron emission from the cathode. Accelerated by this field up to energy $\gamma_1\sim1+\varphi$, the electrons penetrate through the anode grid and excite an electromagnetic field in the upper chamber. If the electron beam current is sufficiently high, then, as is well known, a virtual cathode — a surface that reflects some electrons backward — arises inside the beam. Returning to the lower chamber, the electrons once again are turned by the field in the forward direction and can oscillate near the anodic grid. Figure 2 shows the trajectories of one particle (in projections on the x,z and y,z planes) and the corresponding phase portrait (z,p_z). Of course, not all electrons survive this long.

Figure 3 shows the overall arrangement of the ensemble of particles at a certain moment in time (in the projection onto the (x,z) plane) and the general phase portrait (z,p_z) of the ensemble. Aside from the already mentioned oscillations near the anodic grid and the virtual cathode, which filters the electron beam, one other filter is observed in the figure — adjacent to the cathode. It is formed as a result of the low energy of the emitted particles in the presence of the same high current. Actually, only electrons starting in intervals where and when $E_z<0$ pass through.

Figure 4 shows the functions $E_z(t)$ at one point of the near-cathode layer (bottom curve) and behind the foil (top curve), as well as the frequency spectrum (right side) of these oscillations (dotted curve for the first case), obtained by Fourier analysis of these curves. It is obvious that oscillations at the frequency $\omega\sim10$ predominate.

Figure 5 shows the currents arriving through the anode grid in the forward i^+ and backward i^- directions, as well as the currents i_z escaping through the top surface of the transanode cavity. In addition, the power consumption P_0 of the system is also presented here.

Figure 6 demonstrates the energy dynamics of the process. Here W is the total energy of the particles present in the system; U is the electromagnetic energy of the system; $U1$ is the part of the energy confined in the lower chamber; S_σ is the electromagnetic energy absorbed by the conducting layer; and, S_x is the energy escaping from the system through the open right-hand boundary.

Figure 7 shows the time dependence of the power $P_\sigma=dS_\sigma/dt$ absorbed in the conducting layer and the power $P_x=dS_x/dt$ absorbed by the system through the open boundary. The power consumption P_0, which is practically constant, is also shown.

Table I shows how the electromagnetic energy $S0$ absorbed by the system is distributed among the kinetic energy V of the particles, the energy $U1$ of the lower chamber, the energy $U2$ of the upper chamber, and the energy S $(=S_\sigma+S_x)$ going to the load; also shown are the currents i^+ and i^- passing through the foil, the power consumption P_0, and the generated power P, at four different times.

The external conditions are stationary, and many characteristics of the process reach an essentially steady state comparatively quickly. If the small high-frequency oscillations are neglected, then the effective transmitted current $i=i^+-i^-$, the power consumption P_0 (in addition, as should be, $P_0=i*\varphi$), and the energy W of particles present in the system are found to be constant. At the same time, the energy stored in the electromagnetic field in the bottom and top chambers, $U1$ and $U2$, respectively, and also the useful power P reach steady state values much later, at $t=100-200$.

TABLE I. Energy distribution.

t	$S0$	V	$U1$	$U2$	S	i^+	i^-	P_0	P	eff., %
50	760	638	42	55	25	37	22	15	0.8	5
100	1515	1320	50	69	76	38	23	15	1.2	8
150	2270	2005	56	77	139	39	24	15	1.3	9
200	3024	2675	60	82	205	39	24	15	1.3	9

TABLE II. Variation of the voltage.

φ	$S0$	$U1$	$U2$	S	i^+	i^-	P_0	P	eff., %
0.5	15.5	9.3	8.9	4.1	13.7	7.5	3.1	0.11	3.5
1.0	760	43	55	25	37	22	15	0.81	5.4
1.5	1923	108	180	70	71	46	38	2.6	7

TABLE III. Variation of the cathode size.

Q	$S0$	$U1$	$U2$	S	i^+	i^-	P_0	P	eff., %
1.44	1049	42	48	52	21	10.5	10.5	0.87	8.3
2.56	1515	50	69	76	38.5	23.5	15.1	1.22	8.1
4.00	1990	57	92	99	60	40	20	1.51	7.6

The frequency characteristic of the radiation is demonstrated in Fig. 8, which shows $E_z(t)$ near the conducting layer (bottom curve) and at the foil (top curve — the same as in Fig. 4). Fourier analysis of these curves gives the spectral density, shown on the right-hand side, of the radiation as a function of frequency.

VARIATION OF THE PARAMETERS

Everything described above also refers to the basic variant, whose parameters are enumerated at the beginning of the preceding section. To determine the effect of a particular parameter on the characteristics of the process, a series of calculations, in each of which one of the parameters of the basic set was varied, was performed. Since the overall picture of the process does not change much, we present only individual results, mainly in the form of tables of values of the basic characteristics — the energy $S0$ absorbed by the system; the energy $U1$ and $U2$ stored in the bottom and top chambers, respectively; the energy dissipated in the load, $S=S_\sigma+S_x$; the forward i^+ and backward i^- currents through the foil; and, the power consumption P_0, the delivered power $P=P_\sigma+P_x$, and their ratio — the efficiency.

Table II gives (at the time $t=50$) the results of varying the applied voltage φ while keeping all other parameters of the basic variant (which is presented in the middle row) constant.

A voltage change affects the frequency of the oscillations of the field in the lower chamber. Figure 9 shows (left side) the component E_z of the electric field near the cathode for variants with $\varphi=0.5$ and 1.5 (dotted curves) and behind the foil (right side). The frequency of the latter remains essentially unchanged.

The effect of the cathode size is demonstrated in Table III, which gives the results obtained at time $t=100$ for three variants differing only by the area Q of the cathode (the central row corresponds to the basic set of parameters). As the area increases, the power consumption and the released power increase but the efficiency decreases.

Changing the height h of the lower chamber gives the results (obtained at time $t=50$) shown in Table IV.

TABLE IV. Variation of the height of the lower chamber.

h	$S0$	$U1$	$U2$	S	i^+	i^-	P_0	P	eff., %
0.2	1235	70	139	59	106	82	24	2.25	9.4
0.3	760	43	55	25	57	22	15	0.81	5.4
0.4	520	27	31	16	18	8	10	0.45	4.5

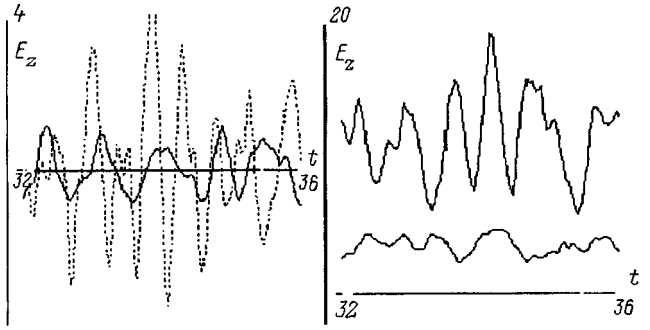

FIG. 9. Field at the cathode and behind the foil.

Analysis of the data in this table leads to dependences of the type $i^+\sim h^{-2.5}$ or $P_0\sim h^{-1.3}$, which should not be extended to small values of h. The latter require a special investigation.

Changing the size of the lower chamber also changes the frequency of the oscillations of the field. Figure 10 shows the electric field for two variants — with $h=0.4$ and 0.2 (dotted curve) at the cathode, behind the foil, and at the exit from the top chamber, respectively. Variation of the vertical size H of the top chamber gives the results (obtained at time $t=100$) presented in Table V. An appreciable change in the frequency of the emitted field is not observed in this case as well.

Doubling the horizontal size of the upper chamber — the length D of the waveguide — has virtually no effect on the values of the basic characteristics. Only a natural redistribution of energy occurs. Figure 11 shows the field energy U contained in the system and the energy S_σ, S_x dissipated in the load for the basic variant and for the variant with an increased horizontal size of the upper chamber (shown by the dotted line). The sum $U+S_\sigma+S_x$ is clearly the same. The time shift in the power output and the energy fluxes through the section $x=$ const for these two variants are shown by the second and third plots in Fig. 11. All this justifies indirectly the method of simulating energy extraction by inserting a conducting layer.

Several variants were also devoted to clarifying the quality of this simulation. Table VI shows the computational results (obtained at time $t=50$) with different average values of the conductivity σ.

Evidently, the optimal value is $\sigma\sim 1$.

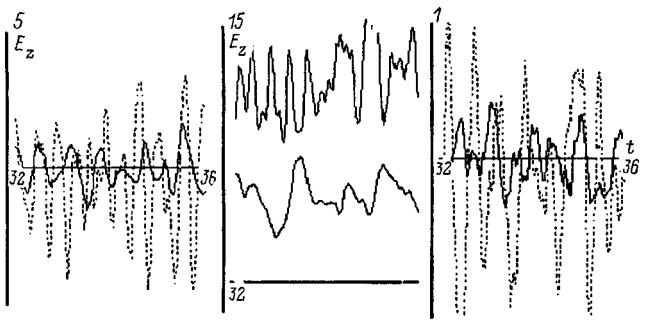

FIG. 10. Field at the cathode, behind the foil, and at the exit.

TABLE V. Variation of the height of the upper chamber.

H	$S0$	$U1$	$U2$	S	i^+	i^-	P_0	P	eff., %
0.75	1718	49	57	62	33	16	17	0.85	5
1.5	1515	50	69	76	38.5	23.5	15	1.22	8
2.25	1458	50	57	89	40	25	15	1.47	10

TABLE VII.

i^+	i^-	i	$W2$	$U2$	S	P	eff., %
10	2.4	7.6	35.5	17.4	3.8	0.06	0.8
16	6	10	57	32	13.2	0.36	3.6
40	29.6	10.4	80	65	35	1.0	9

ONE-CHAMBER VARIANT

The role of the lower chamber reduces to forming the electron flux penetrating through the anodic foil into the upper chamber. For methodological purposes, it makes sense to examine a simplified formulation of the problem with only one chamber in which electrons with energy γ_+, which produce a current i^+, are injected from an area q.

For low values of i^+ the entire current $i=i^+$ passes and there is virtually no radiation. When the injected current reaches a critical (for the given construction) value, a virtual cathode is formed, some electrons turn backward and radiation appears. As the calculations show, for a further increase in i^+ the transmitted current i increases very little, and the growth in the radiation power likewise slows down. Table VII gives the computational results for variants differing only by the current i^+ with $\gamma_+=2$ and injection area $q=2$. The previous notation is used: $W2$ and $U2$ are the energy of the particles and the field, respectively, of one (top) chamber, and the efficiency is defined as the ratio of the useful power P to the quantity $i^*(\gamma_+-1)$ — the equivalent of $i^*\varphi$.

Most quantities reach stationary values quite rapidly, already for $t<10$. The establishment of steady values of the field energy in the volume, especially in high-current cases, is delayed. This is demonstrated in Fig. 12.

In summary, on the whole, one- and two-chamber calculations are in good agreement with one another. The frequency range of the radiation $\omega<20$ with $\omega\sim10$ predominating also does not change. Specifically, this is evident in Fig. 13, which shows the field at the exit and its spectral composition (right side) for the variant $i^+=16.2$.

CONCLUSIONS

The model developed made it possible to clarify for the example of a vircator with a very simple geometry (reflex diode with no magnetic field) the basic features of the process leading to the generation of electromagnetic oscillations in devices of this type.

The generation mechanism is based on the instability of the virtual cathode, which at the nonlinear stage reaches a limit cycle. The height of the virtual cathode is close to the cathode–anode gap width. The maximum spectral density of the oscillations corresponds to the frequency determined by the average frequency of the oscillations of the trapped electrons near the anode. The fundamental frequency of the spectrum can be estimated as the ratio of the velocity of the accelerated electrons to the cathode–anode gap width. Radiation appears when a virtual cathode is formed.

The numerical experiment showed that the fundamental frequency generated is sensitive only to the gap width, and for sufficiently relativistic voltage ($\varphi\geqslant1$) it is not sensitive to the applied voltage. Charge density oscillations above the anode foil are accompanied by radiation, whose frequency spectrum is virtually identical to that of the electric field in the virtual cathode, which is essentially of an electrostatic nature.

Hence it can be concluded that the main generation mechanism is dipole emission from an oscillating virtual cathode. Comparing the computational results for the two-chamber and (methodological) one-chamber variants confirmed this supposition.

Attempts to stimulate oscillations of the virtual cathode and narrow the generation spectrum by producing resonance conditions in the upper chamber were unsuccessful. Variation of the vertical size H of the upper chamber does not give an appreciable change in the frequency of the emitted field. The range of radiation frequencies $\omega<20$ with $\omega\sim10$ predominating also does not change. This result is not surprising, since the wavelength of the generated oscillations is several times shorter than the dimensions of the above-anode (top) cavity. Decreasing its dimensions destroys the dynamics of the virtual cathode and cuts off the oscillations.

The relations obtained show that the process can be optimized. In the main variants, an efficiency of 0.09 was consistently observed (the ratio of the power of the electromagnetic oscillations in the dead load integrated over the spectrum to the power fed into the beam). This is the same as the typical values obtained in real experiments. As the cathode area increases, the consumed and released power increase, but the efficiency decreases. This is natural, since the

TABLE VI. Variation of the conductivity.

σ	$S0$	$U1$	$U2$	S	i^+	i^-	P_0	P	eff., %
0.0	762	44	60	18	38	23	15	0.6	4
1.0	760	43	55	25	37	22	15	0.81	5.4
10.0	763	44	58	21	37	22	15	0.7	4.7

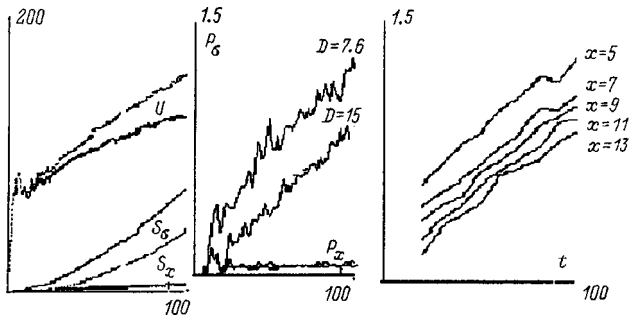

FIG. 11. Energy, output power, and energy fluxes.

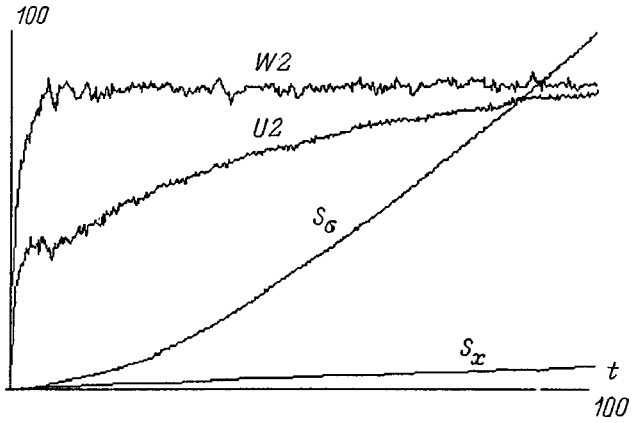

FIG. 12. Energy distribution.

peripheral part of the virtual cathode forms dipole radiation as a result of the edge effect. The efficiency increases as the voltage becomes increasingly more relativistic.

In superpowerful generation devices, such as the vircator investigated here, a substantial complicating and limiting element is the appearance of plasma in the volume. The model developed above permits taking account of this factor, just as

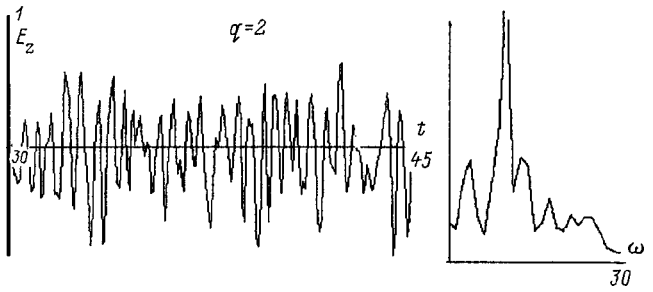

FIG. 13. Emitted field and its spectrum.

the scattering of electrons by the anode foil and vaporization of the foil.

[1] S. L. Ginzburg, V. F. D'yachenko, V. V. Paleĭchik, and K. V. Khodataev, Preprint No. 38 [in Russian], M. V. Keldysh Institute of Applied Mathematics, Russian Academy of Sciences, Moscow, 1995.
[2] A. A. Rukhadze, S. D. Stolbtsev, and V. P. Tarakanov, Radiotekh. Elektron. **37**(3), 385 (1992).
[3] S. L. Ginzburg, V. F. Dyachenko, V. S. Imshennik *et al.*, in *Proceedings of the III International Conference on High-Power Electron and Ion Beam Research and Technology*, Novosibirsk, 1979, Vol. 2, p. 670.
[4] V. F. D'yachenko, Zh. Vychisl. Mat. Mat. Fiz. No. 4, 622 (1985).

Translated by M. E. Alferieff

Ranges of low- and medium-energy heavy ions in an amorphous material

E. G. Sheĭkin

Scientific-Research Enterprise for Hypersonic Systems, 196066 St. Petersburg, Russia
(Submitted July 28, 1997; resubmitted December 25, 1997)
Zh. Tekh. Fiz. **69**, 93–97 (February 1999)

A theory of the passage of ions in an amorphous material is developed with elastic and inelastic stopping processes taken into account. Inelastic stopping of ions is studied in the continuous deceleration approximation. Elastic stopping is studied with allowance for the discrete character of the change in energy and direction of motion of the ions in elastic scattering by the target atoms. Integral equations are obtained for the total and projected ion ranges. Expressions are obtained for the probability of a change in ion energy in elastic and inelastic stopping. Calculations of the projected ranges of Cu and Ga ions in Si and C targets are performed. The computational results agree well with experiment. © *1999 American Institute of Physics.* [S1063-7842(99)01702-X]

A theory of the passage of heavy ions in an amorphous material was developed in Refs. 1–3. The low-energy range, where the main process in the motion of ions in the material is elastic scattering by target atoms, was investigated, and inelastic processes were neglected. The results obtained in Refs. 1–3 agree satisfactorily with experiment in the energy range $\varepsilon \leqslant 0.1$. Here ε is the reduced energy in the Lindhard approximation, where ε is related with the ion energy E by the relation $\varepsilon = Em_2a/(Z_1Z_2e^2(m_1+m_2))$, where Z_1, Z_2 and m_1, m_2 are, respectively, the charge and mass of the nucleus of an ion and a target atom, e is the electron charge, $a = 0.8853a_0(Z_1^{2/3}+Z_2^{2/3})^{1/2}$, and a_0 is the Bohr radius.

As the ion energy increases, inelastic processes become more important,[4] and to give an adequate description of the propagation of ions in matter the inelastic stopping processes must be taken into account. In the present work, elastic and inelastic stopping of ions are taken into account. The approach developed in Refs. 1–3 is extended to the case of low and medium ion energies. The following model formulation of the problem is considered. An ion with initial energy E_0 is incident on an amorphous body in a direction orthogonal to the body's surface, located at $x=0$. An ion moving in the material loses energy, undergoing elastic and inelastic collisions. The energy losses in inelastic collisions are studied in the continuous moderation approximation. The elastic scattering is described in the modified hard-sphere model approximation.[1] In the elastic scattering, the energy and direction of motion of an ion change discretely. During the motion of an ion between successive elastic scattering events, the energy of the ion decreases continuously in the process of inelastic stopping; the direction of motion of the ion does not change. An ion stops in the material when its energy drops below a certain threshold value E_{th}. By analogy with Refs. 1 and 5, we introduce the following concepts: R — the total range of an ion — is the distance traversed by the ion in the material before stopping, and R_p is the projected range of an ion — the projection of the distance traversed by an ion in the material in a distinguished direction of motion. For the ion energy $\varepsilon > 0.1$, according to Ref. 3, the threshold energy E_{th} can be set approximately to zero, $E_{\text{th}}=0$, when calculating the ranges. For $\varepsilon < 0.1$, in Ref. 3 simple equations were obtained for converting the ion ranges calculated in the approximation $E_{\text{th}}=0$ to the case of nonzero values of the threshold energy E_{th}. As will be shown below, such a conversion is also applicable in an approximation that takes inelastic stopping of an ion into account. In what follows, we set $E_{\text{th}}=0$ and make the appropriate correction of the results at low ion energies. In this case, according to Ref. 3, the expressions for calculating the total and projected ion ranges have the form

$$R = \sum_{k=0}^{\infty} \lambda_k, \quad R_p = \sum_{k=0}^{\infty} \lambda_k \mu_k, \tag{1), (2}$$

where λ_k is the average range of an ion between the kth and $(k+1)$th elastic collisions and μ_k is the average value of the cosine of the angle between the direction of motion of an ion after the kth collision and the x axis.

Expressions for calculating λ_k in an approximation that takes only elastic scattering of the ions account are obtained in Ref. 2. We shall obtain expressions for calculating λ_k in a more general form which takes into account the inelastic ion energy losses. Since the elastic scattering cross section of an ion in general depends on the energy of the ion, the average mean free path of an ion also depends on energy. The dependence of λ_k on the number of elastic collisions undergone by an ion is due to the corresponding change in the ion energy distribution function. We introduce the following concepts: $\lambda_0(\varepsilon)$ — the average travel distance of an ion with initial energy ε up to the first elastic collision with a target atom and $F_k(\varepsilon)$ — the energy distribution function of ions which have undergone k elastic collisions. The formation of the distribution function $F_k(\varepsilon)$ is determined by discrete energy losses of ions in elastic stopping and continuous energy losses in inelastic stopping. We assume that a monoenergetic flux of ions with energy $\varepsilon = \varepsilon_0$, i.e., $F_0(\varepsilon) = \delta(\varepsilon - \varepsilon_0)$, is incident on the surface of the target. The average travel dis-

tance of ions with initial energy ε_0 which have undergone k collisions in the material is determined by the expression

$$\lambda_k(\varepsilon_0)=\int_0^{\varepsilon_0}\lambda_0(\varepsilon)F_k(\varepsilon)d\varepsilon. \tag{3}$$

To determine $\lambda_k(\varepsilon_0)$ with a known function $\lambda_0(\varepsilon)$, it is necessary to know the distribution function $F_k(\varepsilon)$. The transformation of the distribution function as the number of ions which have undergone collisions increases is described by the following recurrence relation:

$$F_k(\varepsilon)=\int_{\varepsilon}^{\varepsilon_0}F_{k-1}(\varepsilon')p_{\text{en}}(\varepsilon'\to\varepsilon)d\varepsilon'. \tag{4}$$

where $p_{\text{en}}(\varepsilon'\to\varepsilon)$ is the probability density of a change in the energy of an ion with elastic (index n) and inelastic (index e) energy losses,

$$\int_0^{\varepsilon'}p_{\text{en}}(\varepsilon'\to\varepsilon)d\varepsilon=1.$$

Substituting expression (4) in Eq. (3) and changing the order of integration, we obtain

$$\lambda_k(\varepsilon_0)=\int_0^{\varepsilon_0}F_{k-1}(\varepsilon')\int_0^{\varepsilon'}\lambda_0(\varepsilon)p_{\text{en}}(\varepsilon'\to\varepsilon)d\varepsilon d\varepsilon'. \tag{5}$$

Let us rewrite Eq. (5) in the form

$$\lambda_k(\varepsilon_0)=\int_0^{\varepsilon_0}F_{k-1}(\varepsilon')\tilde{\lambda}_1(\varepsilon')d\varepsilon',$$

$$\tilde{\lambda}_1(\varepsilon')=\int_0^{\varepsilon'}\lambda_0(\varepsilon)p_{\text{en}}(\varepsilon'\to\varepsilon)d\varepsilon.$$

Repeating the operation performed, we obtain in a general form

$$\lambda_k(\varepsilon_0)=\int_0^{\varepsilon_0}F_{k-i}(\varepsilon')\tilde{\lambda}_i(\varepsilon')d\varepsilon',$$

$$\tilde{\lambda}_i(\varepsilon')=\int_0^{\varepsilon'}\tilde{\lambda}_{i-1}(\varepsilon)p_{\text{en}}(\varepsilon'\to\varepsilon)d\varepsilon. \tag{6}$$

For $i=k$ we obtain from Eq. (6)

$$\lambda_k(\varepsilon_0)=\int_0^{\varepsilon_0}F_0(\varepsilon')\tilde{\lambda}_k(\varepsilon')d\varepsilon'\equiv\tilde{\lambda}_k(\varepsilon_0).$$

Since the index k is arbitrary, $\tilde{\lambda}_k=\lambda_k$ for all k. Thus, we obtain from Eq. (6) the following recurrence relation for calculating $\lambda_k(\varepsilon)$:

$$\lambda_k(\varepsilon)=\int_0^{\varepsilon}\lambda_{k-1}(\varepsilon')p_{\text{en}}(\varepsilon\to\varepsilon')d\varepsilon' \quad \text{for} \quad k\geqslant 1. \tag{7}$$

It is remarkable that expression (7) makes it possible to calculate the average travel distance of an ion after k collisions without finding the ion distribution function $F_k(\varepsilon)$. Using Eqs. (1) and (7), we shall find an expression for the total range of ions in the material. Summing expression (7) over k from 1 to ∞, we obtain

$$\sum_{k=1}^{\infty}\lambda_k(\varepsilon)=\sum_{k=1}^{\infty}\int_0^{\varepsilon}\lambda_{k-1}(\varepsilon')p_{\text{en}}(\varepsilon\to\varepsilon')d\varepsilon'.$$

Transferring the summation sign in this expression into the integrand and using the definition (1) for $R(\varepsilon)$, we obtain the following integral equation for the total range of ions in the material:

$$R(\varepsilon)=\lambda_0(\varepsilon)+\int_0^{\varepsilon}R(\varepsilon')p_{\text{en}}(\varepsilon\to\varepsilon')d\varepsilon'. \tag{8}$$

The equation obtained has a clear physical meaning. Indeed, the total range of an ion includes the distance traversed by the ion up to the first elastic collision, and the total range, averaged with the corresponding probability, of an ion whose energy which changes as a result of inelastic and elastic losses.

We shall now obtain a similar equation for the projected range of ions in a material. In this case, it is necessary to determine an expression for the average cosine of the direction angle of motion of an ion after the kth collision. Acording to Ref. 1, $\mu_k=\mu_s^k$, where μ_s is the average cosine of the scattering angle of an ion in a collision with a target atom and is given by

$$\mu_s=\begin{cases}1-\dfrac{1}{3}\left(\dfrac{m_2}{m_1}\right)^2, & m_1>m_2,\\[2ex] \dfrac{2}{3}\dfrac{m_1}{m_2}, & m_1\leqslant m_2.\end{cases}$$

We premultiply expression (7) by μ_s^k and repeat the sequence of operations in the derivation of Eq. (8). As a result, we obtain the following integral equation for the projected ion range:

$$R_p(\varepsilon)=\lambda_0(\varepsilon)+\mu_s\int_0^{\varepsilon}R_p(\varepsilon')p_{\text{en}}(\varepsilon\to\varepsilon')d\varepsilon'. \tag{9}$$

The integral equations (8) and (9) for the total and projected ion ranges in a material were obtained under quite general assumptions about the mechanism of energy loss during the motion of an ion in the material. These are Volterra integral equations of the second kind. The mathematical formalism for solving such equations has been developed in detail (see, for example, Ref. 6). One possible method of solution is the method of iterations. It is easy to show that expressions (1) and (2), together with the recurrence relation (7), are solutions of the integral equations (8) and (9) by the method of iterations using the function $\lambda_0(\varepsilon)$ as the zeroth approximation. In the present paper we shall confine ourselves to investigating this solution.

To calculate the ranges, it is necessary to know the functions $p_{\text{en}}(\varepsilon\to\varepsilon')$ and $\lambda_0(\varepsilon)$. These functions are determined in terms of the density $p(x)$ of the probability that an ion undergoes an elastic collision after traversing a distance x. The probability density $p(x)$ is introduced by the following obvious relation:

$$p(x)=n\sigma(x)\exp\left(-\int_0^x n\sigma(x')dx'\right), \tag{10}$$

where n is the density of target atoms and σ is the cross section for elastic scattering of an ion by the target atoms.

The dependence of the cross section σ on the coordinate x is due to the continuous decrease in the ion energy during the inelastic stopping between two successive elastic scattering events, i.e., in reality $\sigma(x)=\sigma(\varepsilon(x))$. Following Refs. 1 and 2, we shall determine the energy dependence of the elastic scattering cross section in terms of the dimensionless stopping power of ions for elastic energy losses $s_n(\varepsilon)$ (the notation is conventional) by the relation

$$\sigma(\varepsilon)=2\pi a^2 s_n(\varepsilon)/\varepsilon. \tag{11a}$$

According to Ref. 7, the change in the ion energy due to inelastic losses in the continuous stopping approximation can be determined in terms of the dimensionless stopping power for inelastic energy losses $s_e(\varepsilon)$ by the relation

$$\frac{d\varepsilon}{dx}=-As_e(\varepsilon),$$

$$A=\pi a^2 n\,\frac{4m_1m_2}{(m_1+m_2)^2}. \tag{11b}$$

The equations (10) and (11) make it possible to obtain an expression for the probability that the energy of an ion changes due to inelastic losses as the ion moves between two successive events of elastic scattering by target atoms. We denote the corresponding probability density as $p_e(\varepsilon_b\to\varepsilon)$, where ε_b is the energy with which the ion ''commences'' its energy, having undergone a successive elastic collision; ε is the energy with which an ion ''terminates'' its motion and undergoes the next elastic collision. Using the law of transformation of random variables,[8] according to which $p(\varepsilon)d\varepsilon=p(x)dx$, after simple transformations of the Eqs. (10) and (11), we obtain

$$p_e(\varepsilon_b\to\varepsilon)=Q\,\frac{s_n(\varepsilon)}{\varepsilon s_e(\varepsilon)}\exp\left[-\int_\varepsilon^{\varepsilon_b} Q\,\frac{s_n(\varepsilon')}{\varepsilon' s_e(\varepsilon')}d\varepsilon'\right], \tag{12}$$

where

$$Q=\frac{(m_1+m_2)^2}{2m_1m_2}.$$

The density of the probability that the energy of an ion changes from ε to ε' as a result of elastic scattering by target atoms is determined, according to Ref. 2, by the relation

$$p_n(\varepsilon_b\to\varepsilon')=\frac{Q}{2\varepsilon}\begin{cases}1 & \text{for } \alpha\varepsilon\leqslant\varepsilon'\leqslant\varepsilon,\\ 0 & \text{for } \varepsilon'>\varepsilon,\ \varepsilon'<\alpha\varepsilon,\end{cases} \tag{13}$$

where

$$\alpha=\left(\frac{m_1-m_2}{m_1+m_2}\right)^2.$$

The function $p_{en}(\varepsilon\to\varepsilon')$, determining the density of the probability that the energy of an ion changes in inelastic and elastic stopping processes, can be expressed in terms of the functions p_e and p_n, given by expressions (12) and (13), as follows:

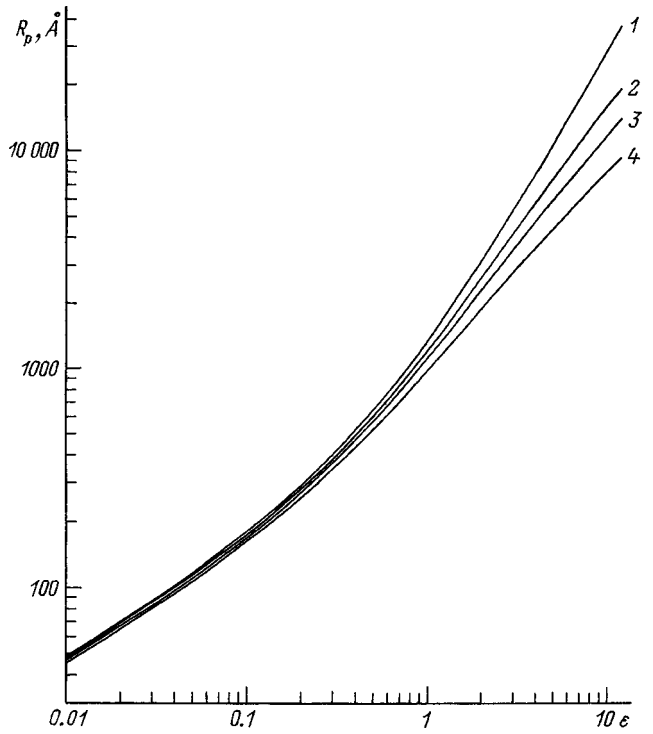

FIG. 1. Projected range of Cu ions in a Si target as a function of energy: $g=0.45$, $b=0.3$, k: *1* — 0, *2* — 0.05, *3* — 0.1, *4* — 0.2.

$$p_{en}(\varepsilon_b\to\varepsilon')=\int_{\varepsilon'}^{\varepsilon} p_e(\varepsilon\to\varepsilon'')p_n(\varepsilon''\to\varepsilon')d\varepsilon''. \tag{14}$$

We shall now determine the average range of an ion with energy ε_b, taking into account the change in the energy of an ion due to inelastic stopping. For this, we employ the relations (11b) and (12), which describe the energy losses of an ion in inelastic collisions. Integrating expression (11b), we obtain an expression for the distance $x(\varepsilon_b,\varepsilon)$ over which the energy of an ion decreases as a result of inelastic stopping from ε_b to ε,

$$x(\varepsilon_b,\varepsilon)=\frac{1}{A}\int_\varepsilon^{\varepsilon_b}\frac{d\varepsilon'}{s_e(\varepsilon')}.$$

We obtain an expression for $\lambda_0(\varepsilon_b)$ by averaging $x(\varepsilon_b,\varepsilon)$ with the probability density determined in Eq. (12):

$$\lambda_0(\varepsilon_b)=\int_0^{\varepsilon_b} x(\varepsilon_b,\varepsilon)p_e(\varepsilon_b\to\varepsilon)d\varepsilon.$$

Simple transformations yield

$$\lambda_0(\varepsilon_b)=\frac{1}{A}\int_0^{\varepsilon_b}\frac{1}{s_e(\varepsilon)}\exp\left(-\int_\varepsilon^{\varepsilon_2} Q\,\frac{s_n(\varepsilon')}{\varepsilon' s_e(\varepsilon')}d\varepsilon'\right)d\varepsilon. \tag{15}$$

For prescribed functions $s_e(\varepsilon)$ and $s_n(\varepsilon)$, Eqs. (1), (2), (7), (14), and (15) together make it possible to calculate the total and projected ranges of ions in an amorphous material. In the calculations, we shall employ the following functions: $s_e(\varepsilon)=k\sqrt{\varepsilon}$, $s_n(\varepsilon)=g\sqrt{\varepsilon}/(b+\varepsilon)$. According to Ref. 7, the expression for $s_n(\varepsilon)$ for $g=0.45$ and $b=0.3$ is a good approximation for calculating the stopping power of ions, ob-

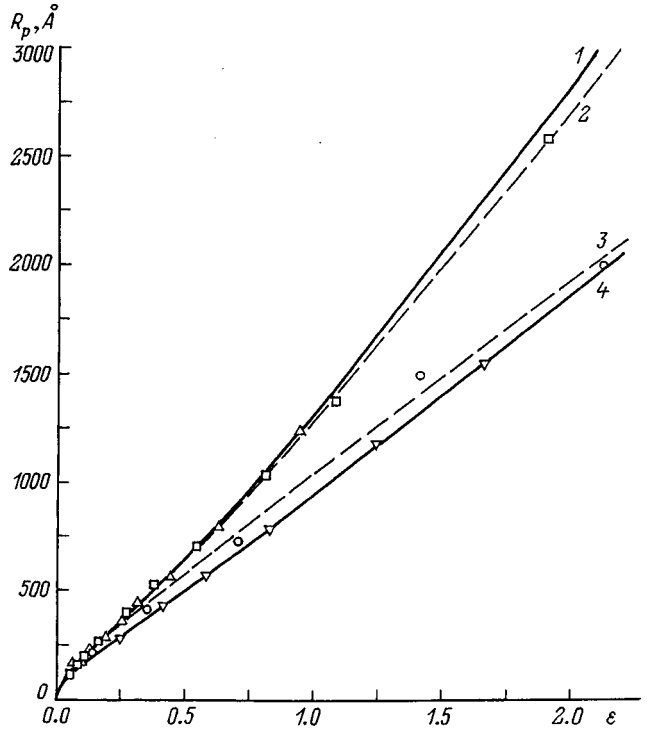

FIG. 2. Comparison of the experimental and theoretical projected ranges of ions: Curves — calculation according to Eqs. (2), (7), (14), and (15) for the following ion–target combinations: *1* — Cu–Si with $k=0.04$, $g=0.43$; *2* — Ca–Si, $k=0.06$, $g=0.46$; *3* — Ga–C, $k=0.17$, $g=0.30$; *4* — Cu–C, $k=0.09$, $g=0.34$; symbols — experiment of Ref. 10: △ — Cu–Si, □ — Ga–Si and experiment of Ref. 9: ▽ — Cu–C, ○ — Ga–C.

tained using the interaction potential in the Thomas–Fermi–Firsov model, in the energy range $0.001 \leqslant \varepsilon \leqslant 10$.

Let us investigate the effect of inelastic stopping on the projected range of ions in a material. Figure 1 shows the projected range of Cu ions in Si for various values of the coefficient k. It follows from Fig. 1 that the projected range decreases with increasing inelastic energy losses (with increasing k). For $\varepsilon=10$, taking inelastic energy losses into account substantially decreases the projected range of the ions. Specifically, for $k=0.1$ the projected range is approximately a factor of 2 shorter than the projected range for $k=0$. For $\varepsilon<0.1$, the effect of inelastic energy losses on the projected range is negligible. This makes it possible to use the method developed in Ref. 3 to calculate the ion ranges in the elastic stopping approximation, making a correction of the projected range of low-energy ions with allowance for the nonzero value of the threshold energy E_{th}.

Figure 2 compares the results of numerical calculations of the projected ranges of ions with the experimental results obtained in Refs. 9 and 10. The two parameters g and k characterizing the stopping powers of ions in a material were chosen by the least-squares method by comparing the experimental and theoretical values of the ion ranges. The parameter b was assumed to be constant for all ion–target pairs: $b=0.3$. It follows from Fig. 2 that the theory agrees well with experiment.

Let us conclude with a summary of the main results of this work. A theory of ion passage through a material was developed with elastic and inelastic energy losses taken into account. Integral equations were obtained for the total and projected range of the ions. Expressions for the probability that the ion energy changes in elastic and inelastic collisions were obtained. The calculations performed show good agreement between the theoretical and experimental results.

[1] E. G. Sheĭkin, Zh. Tekh. Fiz. **66**(10), 63 (1996) [Tech. Phys. **41**, 1005 (1996)].
[2] E. G. Sheĭkin, Zh. Tekh. Fiz. **67**(10), 16 (1997) [Tech. Phys. **42**, 1128 (1997)].
[3] E. G. Sheĭkin, Zh. Tekh. Fiz. **68**(9), 33 (1998) [Tech. Phys. **43**, 1039 (1998)].
[4] A. F. Akkerman, *Simulation of Charged-Particle Trajectories in Matter* [in Russian], Énergoatomizdat, Moscow, 1991, 200 pp.
[5] W. Eckstein, *Computer Simulation of Ion-Solid Interactions*, Springer-Verlag, New York, 1991 [Russian trans., Mir, Moscow, 1995, 320 pp.].
[6] A. F. Verlan' and V. S. Sizikov, *Handbook of Computer Methods for Solving Integral Equations* [in Russian], Naukova Dumka, Kiev, 1978, 292 pp.
[7] M. A. Kumakhov and F. F. Komarov, *Ion Energy Losses and Ranges in Solids* [in Russian], Minsk, 1979.
[8] D. Hudson, CERN report (unpublished), Geneva (1964) [Russian trans., Mir, Moscow, 1967, 244 pp.].
[9] M. Grande, F. C. Zawislak, D. Fink, and M. Behar, Nucl. Instrum. Methods Phys. Res. B **61**, 282 (1991).
[10] P. F. Fichter, M. Behar, C. A. Oliveri *et al.*, Nucl. Instrum. Methods Phys. Res. B **28**, 481 (1987).

Translated by M. E. Alferieff

Theoretical investigation of the bunching of an electron beam in relativistic power amplifiers

É. A. Perel'shteĭn, L. V. Bobyleva, A. V. Elzhov, and V. I. Kazacha

Joint Institute for Nuclear Research, 141980 Dubna, Moscow Region, Russia
(Submitted July 15, 1997)
Zh. Tekh. Fiz. **69**, 98–102 (February 1999)

The modern approach to designing an injector for the driver of a two-beam accelerator is based on the use of a bunched electron beam. The results of simulation and comparison of the processes leading to bunching of a relativistic electron beam in a free-electron laser and in a traveling-wave tube at low electron beam energies are discussed. The simulation and existing experimental results for bunching of an electron beam in a free-electron laser are compared. [S1063-7842(99)01802-4]

INTRODUCTION

Work on the next generation of electron–positron colliders for the TeV range is now going on all over the world. These machines will require large gradients of the accelerating electric fields (up to ~100 MeV/m) to conserve energy and so that the accelerators not be too long. Two schemes based on the concept of a two-beam accelerator are being investigated to solve this problem.[1,2] In the two-beam accelerator, the first accelerator produces a high-current electron beam that should be bunched over the entire length of the collider. The electron bunches generate rf electromagnetic power for the accelerating resonators in the second accelerator, which accelerates the main beam up to the TeV range.

Several schemes for obtaining such high-intensity driver electron bunches exist. One such scheme was implemented in Refs. 1 and 3, where the so-called ''Choppertron'' employed transverse modulation of the velocity of the 2.5 MeV main beam with a 1 kA current in a deflecting resonator with a collimator to obtain longitudinal bunching of the beam. The other idea for obtaining such bunches is to use the bunching of a beam that occurs in a free-electron laser (FEL). In Refs. 5 and 6, detailed numerical calculations were performed for the purpose of assessing the advantages of this method and determining the bunching efficiency as a function of the beam energy, the beam current, and the emittance. It was also shown in Refs. 5 and 6 that in FEL amplifiers a high degree of beam bunching can be obtained over quite short lengths. However, in this bunching method the sensitivity of the phase stability to a change in beam energy during a pulse and the rapid debunching of the beam with excitation of the FEL are serious problems.

The first results on the direct observation of bunching of a relativistic electron beam in a powerful FEL were reported in Refs. 7–9. The measurements, employing both electromagnetic and optical techniques, were performed at the wiggler exit and clearly demonstrated bunching of the beam.

The present work is devoted to a numerical simulation and comparison of bunching of a relativistic electron beam in a FEL and in a traveling-wave tube (TWT). The computational results for the bunching of an electron beam in a FEL are also compared with the experimental results obtained in Refs. 7 and 8.

EQUATIONS DESCRIBING BUNCHING OF A BEAM

The following equations describe the self-consistent spatial problem of the motion of a relativistic electron beam in a microwave electric field. They can be used both for a FEL in the Compton mode and for the TWT:

$$\frac{d\gamma_j}{dZ} = -\kappa a_s \sin\psi_j \quad (j=1,\ldots,M), \tag{1}$$

$$\frac{d\Theta_j}{dZ} = \frac{1}{\beta_{\parallel j}} - \frac{1}{\beta_{\rm ph}}, \tag{2}$$

$$\frac{da_s}{dZ} = \eta\langle \sin\psi_j \rangle, \tag{3}$$

$$\frac{d\varphi}{dZ} a_s = \eta\langle \cos\psi_j \rangle. \tag{4}$$

Here M is the number of electrons (macroparticles); γ_j is the energy of the jth electron ($E_j = m_0c^2\gamma_j$) in the units $E_0 = m_0c^2$; m_0 is the electron rest mass; c is the speed of light; $Z = z\omega_0/c$ is the dimensionless longitudinal coordinate; and, ω_0 is the microwave frequency. The quantity Θ_j is the phase of the jth electron relative to the electromagnetic field; φ is the phase of the complex amplitude ($\hat{a} = a_s \exp(i\varphi)$); and, $\psi_j = \varphi + \Theta_j$ is the total ponderomotive phase. The brackets in Eqs. (3) and (4) indicate averaging over a bunch. The quantity a_s is the dimensionless amplitude of the microwave electric field

$$a_s = \frac{eE_s}{m_0\omega_0 c}, \tag{5}$$

where e is the electron charge and E_s is the amplitude of the microwave electric field.

The parameter k is the coupling constant between the electrons and the microwave. Its value depends on the type of setup employed. The parameter η in Eqs. (3) and (4) is given by the expression[10]

$$\eta=\left(\frac{I_b}{I_A}\right)\frac{2\kappa}{N}. \tag{6}$$

The constant $I_A=m_0c^3/e\simeq 17$ kA, N is the norm of the electromagnetic wave, $\beta_{\parallel j}$ is the longitudinal electron velocity, and $\beta_{\rm ph}$ is the phase velocity of the microwave.

SIMULATION OF BUNCHING IN A FREE-ELECTRON LASER

To obtain a system of differential equations for simulating the bunching in a FEL with a helical wiggler, we took as a basis the corresponding equations from Refs. 10 and 11, taking account of the effective shift of the frequency ω_p due to the plasma wave in the beam. This corresponds to taking account of the plasma wave under the resonance conditions in Refs. 7 and 8. We have, finally,

$$\frac{d\omega_j}{dZ}=\kappa_{1j}a_s\sin\psi_j \quad (j=1,\ldots,M), \tag{7}$$

$$\frac{d\Theta_j}{dZ}=-\frac{(k_\omega+k_s)c}{\omega_0}+1+\frac{\omega_p}{\omega_0\beta_z}+\frac{1+a_\omega^2+a_\omega a_s\cos\psi_j}{2\gamma_0^2(1-\omega_j)^2}, \tag{8}$$

$$\frac{da_s}{dZ}=\eta_1\left\langle\frac{\sin\psi_j}{1-\omega_j}\right\rangle, \tag{9}$$

$$\frac{d\varphi}{dZ}a_s=\eta_1\left\langle\frac{\cos\psi_j}{1-\omega_j}\right\rangle, \tag{10}$$

where

$$\kappa_{1j}=\frac{a_\omega}{2\gamma_0\gamma_j}=\frac{\kappa_0}{1-\omega_j}. \tag{11}$$

Here $\omega_j=1-E_j/E_0$ is the relative change in the energy of the jth electron; $k_\omega=2\pi/\lambda_\omega$; λ_ω is the period of wiggler; k_s is the axial wave number of the resonant waveguide mode in the wiggler; $\gamma_0=1/\sqrt{1-\beta_0^2}$ is the initial energy of the electron beam; β_z is the longitudinal dimensionless velocity of the resonant particle, determined from the relations $\beta_z=\sqrt{\beta_0^2-\beta_\perp^2}$, $\beta_\perp/\beta_z=a_\omega/\gamma_0$; $\kappa_0=a_\omega/2\gamma_0^2$; ω_p is the relativistic plasma frequency

$$\omega_p=\sqrt{\frac{4\pi n_e e^2}{m_0}}\,\frac{1}{\gamma_z\gamma^{1/2}}. \tag{12}$$

Here n_e is the density of the electron beam, $\gamma_z=1/\sqrt{1-\beta_z^2}$, the parameter a_ω is given by the formula

$$a_\omega=\frac{eB_\omega\lambda_\omega}{2\pi m_0c^2}, \tag{13}$$

where B_ω is the amplitude of the magnetic field of the wiggler.

The coefficient η_1 is given by the expression

$$\eta_1=\left(\frac{I_b}{I_A}\right)\frac{2k_0\gamma_0}{N}. \tag{14}$$

For our simulation we employed the electron-beam and FEL parameters from Refs. 7 and 8: electron beam energy $\sim$2.2 MeV ($\gamma_0\simeq 5.31, \beta_0\simeq 0.982$); electronic current inside the wiggler $I_b\sim 500$ A; electron beam radius ~ 0.5 cm; wiggler period $\lambda_\omega=12$ cm; wiggler field $B_\omega=0.11$ T; and, microwave frequency $f_0=3.5\times10^{10}$ Hz (H_{11} mode).

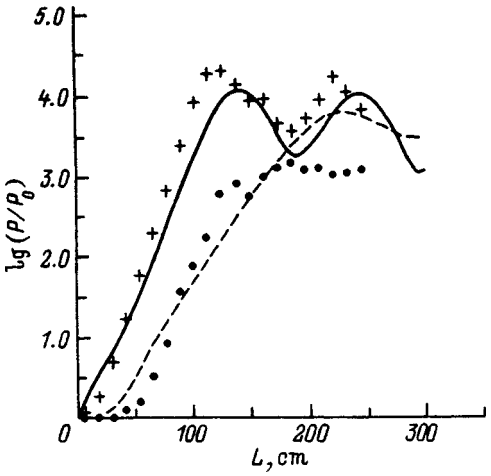

FIG. 1. Microwave power of a FEL as a function of the interaction length of the electron beam with the wiggler: $\sigma=0$ (solid curve), 5% (dashed curve); curves — calculation, + — theory of Ref. 7, ● — experiment of Ref. 7.

In Refs. 7 and 8 an initial microwave power of 10 kW was injected into a circular waveguide in the H_{11} mode. The corresponding amplitude of the microwave electric field is $a_s\simeq 4.4\times10^{-4}$ [see Eq. (5)]. Then we obtain the following values of the parameters from Eqs. (11), (13), and (14): $\kappa_0\simeq 0.022$ and $\eta_1\simeq 2.5\times10^{-4}$ (the norm of the wave in our case is $N=N_{11}\simeq 24.3$).

We determine the bunching parameter B just in Ref. 7: $B=|\langle\exp(i\psi)\rangle|$. We simulated the initial energy spread in the electron beam using 2000 electrons distributed over the phase at 40 points from $\Theta=0$ to 2π and at each point 50 electrons possessed a Gaussian relative-energy distribution with variance σ.

The system of differential equations (7)–(10) was solved by the Runge–Kutta method for the parameter values indicated above. Figure 1 shows the computational results for the microwave power of the FEL and compares these results with those obtained in Refs. 7 and 8. To take account of the adiabatic entrance of the wiggler in Refs. 7 and 8, we assume that exponential power growth commences 48 cm from the wiggler entrance. This point corresponds to the point $z=0$ in Fig. 1. As one can see, these results are in quite good agreement. Comparing the microwave power distribution along the wiggler, obtained experimentally in Refs. 7 and 8, it can be concluded that the observed difference of the maximum microwave power by a factor of ~ 10 relative to the computed value for a monoenergetic beam can be partially explained by the presence of an initial energy spread in the electron beam.

Figure 2 shows the computed dependences of the bunching parameter B on the distance L along the wiggler. The curves in Fig. 2 correspond to measurements of the time dependence of the bunching parameter along the beam.[7] The regular part of the wiggler terminates at L approximately equal to 170 cm. Our calculations beyond the regular part of the wiggler are not accurate enough. Thus, comparing the

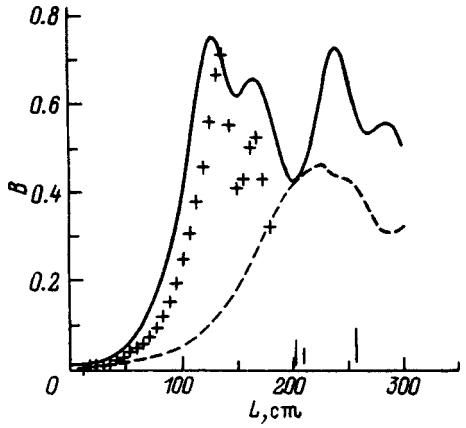

FIG. 2. Bunching parameter in a FEL versus the interaction length of an electron beam with the wiggler: $\sigma=0$ (solid curve), 5% — dashed, + — numerical simulation.[7]

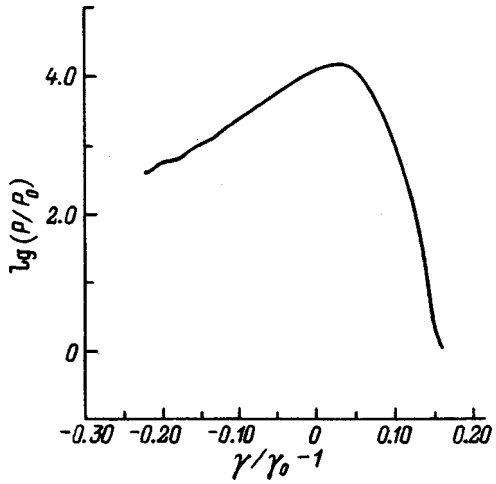

FIG. 4. Microwave power at the wiggler exit versus the initial beam energy.

computed curve corresponding to $\sigma=5\%$ with the experimental results, it can be inferred that the low experimental value of the bunching parameter in Ref. 7 ($B\sim0.1$) can be explained by the energy spread of the electrons in the beam. The distance at which the maximum bunching is attained lies in the maximum microwave power range.

The character of the electron distribution in phase space $\{\gamma,\psi\}$ for $B\simeq0.75$ in the case of a monoenergetic beam ($\sigma=0$) is shown in Fig. 3. The dependence of the computed microwave power at the wiggler exit on the initial beam energy ($\sigma=0$) is shown in Fig. 4. It is obvious that this resonance curve is asymmetric and its maximum value corresponds to $\gamma_0\simeq5.6$ for our parameter values.

SIMULATION OF BUNCHING IN A TRAVELING-WAVE TUBE

We employed the following system of differential equations to simulate the bunching of an electron beam in a FEL accelerator based on a corrugated waveguide:

$$\frac{d\omega_j}{dZ}=\kappa_2 a_s\sin\psi_j\quad(j=1,\ldots,M),\tag{15}$$

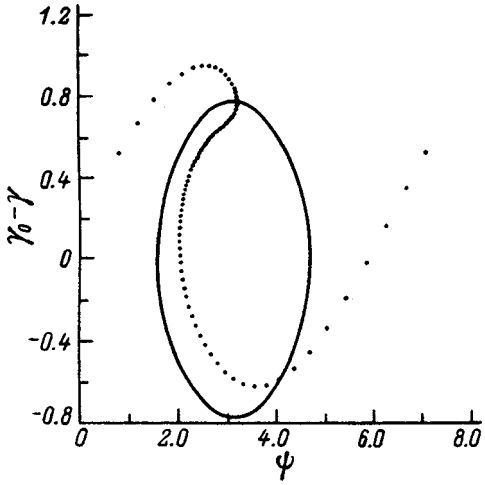

FIG. 3. Phase-space distribution of a bunched beam in a FEL at the point $z=129.5$ cm, corresponding to the maximum bunching parameter. The solid line shows the computed separatrix.

$$\frac{d\Theta_j}{dZ}=\frac{1-\omega_j}{\sqrt{(1-\omega_j)^2-1/\gamma_0^2}}-\frac{1}{\beta_{\rm ph}},\tag{16}$$

$$\frac{da_s}{dZ}=\eta_2\langle\sin\psi_j\rangle,\tag{17}$$

$$\frac{d\varphi}{dZ}a_s=\eta_2\langle\cos\psi_j\rangle,\tag{18}$$

where

$$\kappa_2=\frac{\pi l_0}{\gamma_0 d},\tag{19}$$

l_0 is the amplitude of the corrugation, and d is the spatial period of the corrugation.[12]

The parameter η_2 is defined as

$$\eta_2=\left(\frac{I_b}{I_A}\right)\frac{2\kappa_2\gamma_0}{N_{01}},\tag{20}$$

where N_{01} is the norm of the E_{01} mode in the TWT.

For the simulation, we chose the following parameters of the electron beam and E_{01} mode: electron beam energy ~2.2 MeV ($\gamma_0\simeq5.31$), electron current inside the TWT $I_b\sim500$ A, electron beam radius ~0.5 cm, microwave frequency $f_0=17\times10^9$ Hz ($\lambda\simeq1.76$ cm), and microwave power input in the TWT 10 kW. The value of the parameter d was found from the dispersion curve of the corrugated waveguide, where $l_0=1$ mm, the radius $r_0\simeq1.8$ cm, and $\beta_{\rm ph}\simeq0.982$. The dispersion curve was calculated using the URMEL code. In our case $d\sim5.8$ mm and $k_s d=2\pi/3$. Then we have $\kappa_2\simeq0.102$ from Eq. (19) and $\eta_2\simeq3.2\times10^{-3}$ from Eq. (20) (in our case the norm of the wave $N_{01}\simeq10$). For initial microwave power ~10 kW in the TWT the corresponding dimensionless amplitude of the microwave electric field is $a_s\simeq6.8\times10^{-4}$.

Figure 5 shows the computed curves of the microwave power versus distance along the TWT. The two curves correspond to initial electron beam energies 2.2 and 1 MeV. As one can see from Figs. 1 and 5, the bunching length of a 2.2 MeV electron beam is ~1.5 times shorter in TWT than in

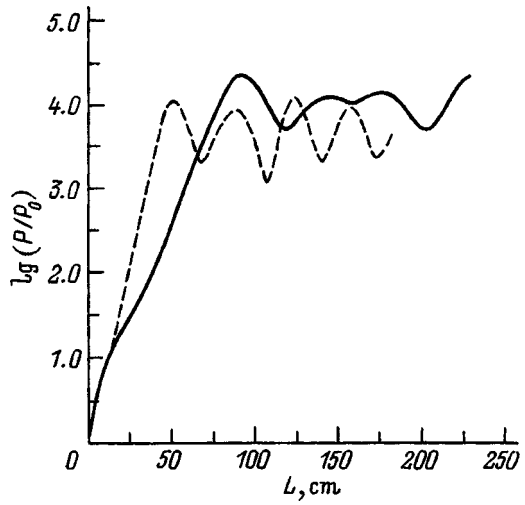

FIG. 5. Microwave power in a TWT versus the interaction length with the beam: $\gamma_0 = 5.31$ (solid curve) and 3.0 (dashed curve).

the FEL. The electron distribution in phase space $\{\gamma, \psi\}$ for the maximum value of the bunching parameter $B = 0.61$ (before saturation of the wave in the TWT) is shown in Fig. 6. It is evident from Figs. 3 and 6 that the energy spread in the bunches is larger in the TWT than in the FEL. It is also seen from Fig. 5 that the bunching length in the TWT decreases substantially with decreasing initial beam energy.

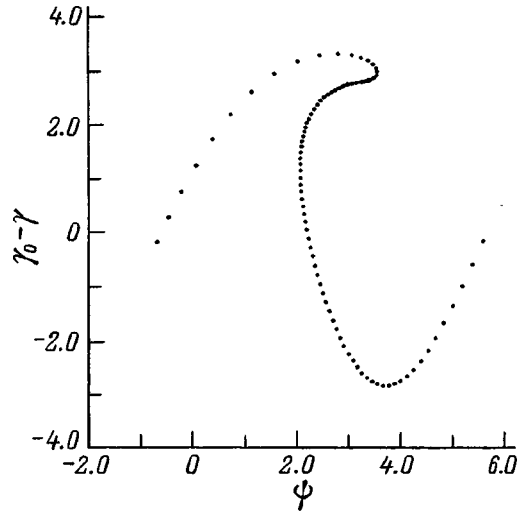

FIG. 6. Phase space distribution of a bunched beam in a TWT at the point $z = 88.3$ cm, corresponding to the maximum value of the bunching parameter.

The dependence of the microwave power at the TWT exit on the energy spread (2.2 MeV) is quite weak. This dependence becomes substantial when the initial electron energy decreases to 1 MeV.

CONCLUSIONS

Our simulation showed that the high degree of bunching of a 1–2 MeV electron beam can be quite easily achieved in a short traveling-wave tube.

Bunching of an electron beam (2.2 MeV, 500 A) occurs in a ~ 1.5 times shorter distance in a TWT than in a FEL. This is because the spatial gain in the TWT is much higher than in a FEL. The energy spread in the bunches formed in a TWT is larger than in a FEL. The bunching effect in a TWT is virtually independent of the initial energy spread in the beam and in a FEL this dependence is strong.

The bunching efficiency in a TWT decreases with increasing initial electron energy. Thus, a TWT can be used effectively to bunch an electron beam in the energy range from 1 to 2 MeV, where the TWT length can range from 0.5 to 1 m.

This work was performed in the Laboratory of Nuclear Problems at the Joint Institute for Nuclear Research. This work was supported by MNS (Soros, Grant No. JLD100) and by the Russian Fund for Fundamental Research (Grant No. 96-02-17395).

[1] A. M. Sessler, in *Proceedings of the Workshop on the Laser Acceleration of Particles*, edited by C. Voshi and T.Katsouleas, AIP Conference Proceedings, 1982, Vol. 91, pp. 154–159.
[2] W. Schnell, ''Radio-frequency acceleration for linear colliders,'' CERN-LEP-RF/86-27, 1986; ''The drive Linac for a two-stage rf linear collider,'' CERN-LEP-RF/88-59, 1988.
[3] G. Fiorentini, T. Houk, and C. Wang, ''Design of a reacceleration experiment using the Choppertron,'' UCRL–JC–111391, Livermore, USA, 1993.
[4] W. B. Colson and A. M. Sessler, Annu. Rev. Nucl. Part. Sci. **35**, 25 (1985).
[5] H. D. Shay, R. A. Ryne, S. S. Yu, and E. T. Scharlemann, Nucl. Instrum. Methods Phys. Res. A **304**, 262 (1991).
[6] J. Gardelle, J. Labrouche, and P. le Taillander, Phys. Rev. E **50**, 4973 (1994).
[7] J. Gardelle, J. Labrouche, and J. L. Rullier, Preprint CESTA/4, 1996.
[8] J. Gardelle, J. Labrouche, G. Marchese *et al.*, Preprint CESTA/5, 1996.
[9] J. Gardelle, J. Labrouche, and J. L. Rullier, in *Proceedings of the EPAC'96*, Sitges, Barcelona, 1996, Vol. 1, pp. 298–300.
[10] N. S. Ginzburg and A. S. Sergeev, Zh. Tekh. Fiz. **61**, 133 (1991) [Sov. Phys. Tech. Phys. **36**, 665 (1991)].
[11] A. M. Sessler, D. H. Whittum, J. S. Wurtelle *et al.*, Nucl. Instrum. Methods Phys. Res. A **306**, 592 (1991).
[12] V. L. Bratman, N. S. Ginzburg, N. F. Kovalev *et al.*, in *Relativistic Radio-Frequency Electronics*, edited by A. V. Gaponov-Grekhov, Institute of Applied Physics, USSR Academy of Sciences, 1979, pp. 249–274.

Translated by M. E. Alferieff

Calculation of the shape of the mass peaks of hyperboloid mass spectrometers with one-dimensional unipolar sorting of the ions

E. V. Mamontov and D. V. Kiryushin

Ryazan State Radio Engineering Academy, 391000 Ryazan, Russia
(Submitted November 18, 1997)
Zh. Tekh. Fiz. **69**, 103–106 (February 1999)

The properties of the particular solutions of the Hill equation are used to obtain expressions for the envelopes of charged-particle trajectories in a hyperboloid analyzer with ion sorting along one coordinate in its positive range. Analytical relations for calculating the shape of the mass peaks are obtained on the basis of these expressions. The results of analytical calculations are compared with a computer simulation. The parameters for calculating the sensitivity and resolution of the one-dimensional analyzer are determined according to the mass peaks. © *1999 American Institute of Physics.* [S1063-7842(99)01902-9]

The possibilities of producing a dynamic mass spectrometer with an analyzer in the form of two hyperboloids of revolution with radii $r_1 > r_2$, in which the charged particles are sorted along one coordinate z, are discussed in Refs. 1 and 2. In the sorting process, the analyzed particles with mass m_0 execute almost periodic oscillations in the positive region of the sorting coordinate $z > 0$. Estimates made in Refs. 1 and 2 indicate that it is best to use a one-dimensional, unipolar regime of particle sorting by specific charge. The instrumental function — the shape of the mass peak of the instrument — gives a more complete idea of the analytical possibilities of the sorting method. For a one-dimensional unipolar mass spectrometer (OUMS), the instrumental function is the dependence of the ion confinement factor η on the normalized mass $M = m/m_0$ (Ref. 1).

The shape of the mass peak can be constructed by computer simulation of the charged-particle sorting processes. But, in so doing, the complete relationship between the different sorting parameters and the analytical indicators of the mass spectrometer is not established. The one-dimensional unipolar method of ion sorting makes it possible to obtain quite simple and accurate analytical representations for the shape of the mass peaks on the basis of the characteristic features of the particle motion near the stability boundary $a_0(q)$. Under the conditions of field-free phase input and a small spread of the initial coordinates of the ions $\Delta z/z \ll 1$, characteristic for the one-dimensional unipolar mass analyzer, the thermal velocities v are the diversity factor of trajectories along the sorting axis z of the particles with fixed mass m. Some ion trajectories with different masses and different velocities are shown in Fig. 1. A particle is stable if during n_c sorting cycles its instantaneous coordinate z falls within the electrode system of the analyzer $r_1 > z > r_2$. To establish this fact it is sufficient to know the behavior of the extremal values $Z_{\max}(n)$ and $Z_{\min}(n)$, which are the envelopes of the charged-particle trajectories.

Ion motion in an ac field in a square potential with the analyzer powered by a pulsed square voltage is described by the Hill equation[3]

$$\frac{d^2z}{dt^2} + [a + 2q\Phi(t)]z = 0, \tag{1}$$

where $\Phi(t)$ is the normalized step function with period $2T$.

The general solution of Eq. (1) can be represented as a linear combination of two independent particular solutions[3]

$$z(t) = Az_1(t) + Bz_2(t), \tag{2}$$

where A and B are constants determined from the initial conditions.

For small $\Delta m/m$, when the working point lies near the stability boundary $a_0(q)$, as the number of sorting periods n_c increases, the positions of the extremal values of the functions $z_1(t)$ and $z_2(t)$ coincide with increasing accuracy. For example, for independent particular solutions $ce_0(t)$ and $fe_0(t)$ with $q = 0.8$ and $n_c = 10$, the discrepancies in the position of the extremal positions does not exceed 0.75×10^{-2} of a sorting period. The error in determining the extremal values themselves is 3×10^{-4}. This feature of the particular solutions makes it possible to determine the values of the envelopes $Z_{\max}(t)$ and $Z_{\min}(t)$ as a sum of the extremal values of the functions $z_1(t)$ and $z_2(t)$.

To find the extremal values of the trajectories we shall employ the method of characteristic solutions.[4] We choose as

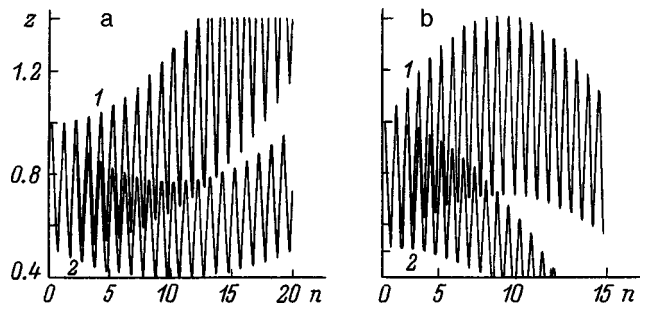

FIG. 1. Ion trajectory in a hyperboloid mass spectrometer with one-dimensional unipolar sorting of the ions: $M = 1.002$ (a), 0.998 (b); *1* — $v = 0.0$ (a), v_T (b); *2* — $v = -v_T$ (a), 0 (b).

characteristic points $t_{\max}$ or $t_{\min}$, which coincide with the extrema of the functions $z_1(t)$ or $z_2(t)$ with entrance phases φ_{01} and φ_{02},

$$t_{\max n}=2Tn; \quad t_{\min n}=T\frac{2n+1}{2}. \tag{3}$$

In accordance with the method of characteristic solutions, the coordinates z_n and velocities v_n of the particles after the nth sorting cycle are determined by the values of these parameters z_{n-1} and v_{n-1} after the $(n-1)$th cycle by the system of equations[4]

$$z_n=\Psi_{i3}z_{n-1}+\Psi_{i4}v_{n-1}, \quad v_n=\Psi_{i1}z_{n-1}+\Psi_{i2}v_{n-1}, \tag{4}$$

where the coefficients can be calculated according to the following formulas:

for entrance phase $\varphi_{01}=0$

$$\Psi_{11}=-\sqrt{\alpha}\Omega\sin\sqrt{\alpha}\Theta\cosh\Theta+\frac{\sqrt{\alpha}\Omega}{\alpha}\times\left[\sqrt{\alpha}+\frac{1}{\sqrt{\alpha}}+\left(\frac{1}{\sqrt{\alpha}}-\sqrt{\alpha}\right)\cos\sqrt{\alpha}\Theta\right]\sinh\Theta,$$

$$\Psi_{14}=\frac{1}{\sqrt{\alpha}\Omega}\sin\sqrt{\alpha}\Theta\cosh\Theta+\frac{1}{2\sqrt{\alpha}\Omega}\times\left[\sqrt{\alpha}+\frac{1}{\sqrt{\alpha}}-\left(\frac{1}{\sqrt{\alpha}}-\sqrt{\alpha}\right)\cos\sqrt{\alpha}\Theta\right]\sinh\Theta,$$

for entrance phase $\varphi_{02}=\pi$

$$\Psi_{21}=\Omega\sinh\Theta\cos\sqrt{\alpha}\Theta-\frac{\Omega}{2}\times\left[\sqrt{\alpha}+\frac{1}{\sqrt{\alpha}}-\left(\frac{1}{\sqrt{\alpha}}-\sqrt{\alpha}\right)\cosh\Theta\right]\sin\sqrt{\alpha}\Theta,$$

$$\Psi_{24}=\frac{1}{\Omega}\sinh\Theta\cos\sqrt{\alpha}\Theta+\frac{1}{2\Omega}\times\left[\sqrt{\alpha}+\frac{1}{\sqrt{\alpha}}+\left(\frac{1}{\sqrt{\alpha}}-\sqrt{\alpha}\right)\cosh\Theta\right]\sin\sqrt{\alpha}\Theta,$$

for entrance phases φ_{01} and φ_{02}

$$\Psi_2=\Psi_3=\cosh\Theta\cos\sqrt{\alpha}\Theta-\frac{1}{2}\left[\sqrt{\alpha}-\frac{1}{\sqrt{\alpha}}\right]\sin\sqrt{\alpha}\Theta\sinh\Theta,$$

where $\Omega=\sqrt{2U_me/mr_1^2}$, $\alpha=U_{m1}/U_m$ is the pulsed voltage parameter, and Θ is the solution of the equation for the boundary $a_0(q)$ of the stability zone.[1]

The solutions of the system (4), which are represented as a sum of two independent solutions, have the form

$$Z_1(n)=A_i\cosh\omega_1 n+B_i\sinh\omega_1 n, \quad m>m_0;$$

$$Z_2(n)=A_i\cos\omega_2 n+B_i\sin\omega_2 n, \quad m<m_0. \tag{5}$$

Depending on the values of the constants A_i and B_i, the functions $Z_1(n)$ and $Z_2(n)$ describe the envelopes of the minima or maxima of the trajectories for entrance phases φ_{01} and φ_{02}. For $\Delta m/m<10^{-2}$, the values of the parameters $\omega_1=\tanh^{-1}\Psi_2$ and $\omega_2=\tan^{-1}\Psi_2$ can be adequately represented in the form

$$\omega_1\simeq\omega_2\simeq\omega=\sqrt{\gamma\Theta\Delta m/m}, \tag{6}$$

where $\gamma=(1/2\sqrt{\alpha}-3\sqrt{\alpha}/2)\sin\sqrt{\alpha}\Theta\cosh\Theta+1/2(3-\alpha)\times\cos\sqrt{\alpha}\Theta\sinh\Theta$.

The constant A_i in Eqs. (5) for the envelopes of the maxima $Z_{\max}(n)$ equals the initial coordinate Z_{01} for entrance phase φ_{01}, and for the envelopes of the minima $Z_{\min}(n)$ it equals the initial coordinate Z_{02} for entrance phase φ_{02}. To determine the constants B_i, we take account of the fact that for $\rho>10^2$ the relative changes in the coefficients Ψ_{14} and Ψ_{24} with m deviating from m_0 do not exceed 2.5×10^{-4}, so that they can be assumed to be constant. As follows from Eq. (4), for a zero initial coordinate the envelopes of trajectories vary linearly with increasing n:

for φ_{01}

$$Z_{\max}(n)=\Psi_{14}vn, \quad Z_{\min}(n)=\sqrt{\Psi_{14}\Psi_{24}}vn,$$

for φ_{02}

$$Z_{\max}(n)=\sqrt{\Psi_{14}\Psi_{24}}vn, \quad Z_{\min}(n)=\Psi_{24}vn. \tag{7}$$

According to Eq. (7), the expression for the envelope of the minima for φ_{01} is identical to the expression for the envelope of the maxima for φ_{02}. For small $\Delta m/m$ Eqs. (5) become

$$Z(n)=B_i\omega n. \tag{8}$$

Equating expressions (7) and (8), we obtain the values of the constants B_i:

for the envelopes of the maxima

$$B_1=\frac{\Psi_{14}v}{\omega} \quad \text{for } \varphi_{01},$$

$$B_3=\frac{\sqrt{\Psi_{14}\Psi_{24}}v}{\omega} \quad \text{for } \varphi_{02},$$

for the envelopes of the minima

$$B_2=\frac{\sqrt{\Psi_{14}\Psi_{24}}v}{\omega} \quad \text{for } \varphi_{01},$$

$$B_2=\frac{\Psi_{24}v}{\omega} \quad \text{for } \varphi_{02}.$$

We shall use relation (5) to calculate the mass peaks of an OUMS. In terms of the envelope functions, the conditions for particle confinement can be written in the form

$$Z_{\max}(n)<r_1, \quad Z_{\min}(n)>r_2. \tag{9}$$

These conditions correspond to the range of initial ion velocities $v_{\min}$–$v_{\max}$ for which particles with mass m are confined in the analyzer for n_c sorting periods. With allowance for the values of the constants A_i and B_i in Eq. (5), the limiting velocities should be determined for masses $m<m_0$ and $m>m_0$ and entrance phases φ_{01} and φ_{02}.

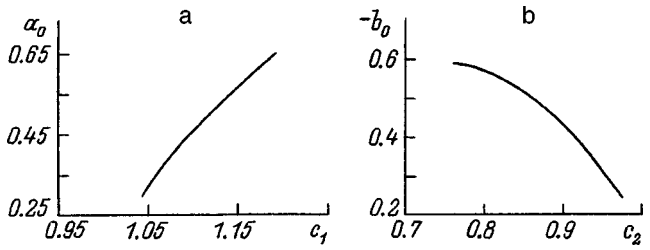

FIG. 2. Solution of the nonlinear equations.

For $m<m_0$ and φ_{01} the equation for $v_{\min}$ has the form

$$Z_{02}\cos\omega n_c+\frac{\sqrt{\Psi_{14}\Psi_{24}}v_{\min}}{\omega}\sin\omega n_c=r_2.$$

Introducing $\omega n_c=\xi_c$, $r_2/r_1=\varepsilon$, and $r_2/z_{02}=c_2$, we have

$$v_{\min}=\frac{\varepsilon r_1}{\sqrt{\Psi_{14}\Psi_{24}}c_2 n_c}\frac{c_2-\cos\xi_c}{\sin\xi_c}\xi_c. \tag{10}$$

To calculate the maximum velocity $v_{\max}$ we take into account the fact that the envelope $Z_{\max}(n)$ in the sorting interval ξ_c increases monotonically for $\xi_c<\xi_1$, while for $\xi_c>\xi_1$ it has a maximum at the point $\xi_1=\tan^{-1}B_{01}/Z_{01}$, where B_{01}/Z_{01} is determined below. In the interval $0\leqslant\xi_c\leqslant\xi_1$ the maximum velocity is found from the equation

$$Z_{01}\cos\xi_c+\frac{\Psi_{14}v_{\max}}{\omega}\sin\xi_c=r_1.$$

Transforming and introducing $r_1/z_{01}=c_1$, we obtain

$$v_{\max}=\frac{r_1}{\Psi_{14}c_1 n_c}\frac{c_1-\cos\xi_c}{\sin\xi_c}\xi_c. \tag{11}$$

In the interval $\xi_c>\xi_1$, taking into account the value ξ_1, the equation for $v_{\max}$ becomes

$$\cos\tan^{-1}B_{01}/Z_{01}+\sin\tan^{-1}B_{01}/Z_{01}=c_1. \tag{12}$$

The numerical solution of Eq. (12) for the parameter $a_0=B_{01}/Z_{01}$ is presented in Fig. 2a. The value found for a_0 is used to calculate the maximum velocity as

$$v_{\max}=\frac{a_0 r_1}{c_1\Psi_{14}n_c}\xi_c. \tag{13}$$

Expressions for the maximum and minimum velocities in the mass range $m>m_0$ are determined similarly:

$$v_{\min}=\frac{\varepsilon r_1}{\sqrt{\Psi_{14}\Psi_{24}}c_2 n_2 n_c}\frac{c_2-\cosh\xi_2}{\sinh\xi_c}\xi_c \quad \text{for } \xi_c<\xi_2,$$

$$v_{\min}=\frac{b_0 r_1\varepsilon}{\sqrt{\Psi_{14}\Psi_{24}}c_2 n_c}\xi_c \quad \text{for } \xi_c>\xi_2,$$

$$v_{\max}=\frac{r_1}{\Psi_{14}c_1 n_c}\frac{c_1-\cosh\xi_c}{\sinh\xi_c}\xi_c, \tag{14}$$

where $\xi_1=\tanh^{-1}B_{02}/Z_{02}$, and $b_0=B_{02}/Z_{02}$ is the solution of the nonlinear equation similar to Eq. (12) and is presented in Fig. 2b.

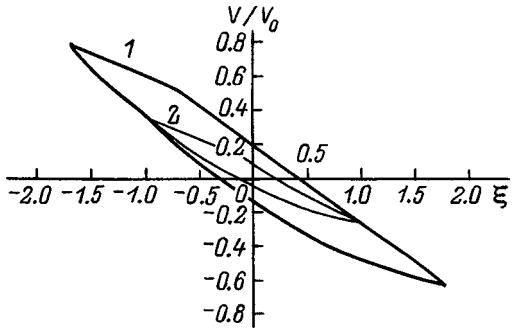

FIG. 3. Regions of confinement of analyzed particles with $c_1=1.2$ (*1*) and 1.1 (*2*).

Relations (10), (11), (13), and (14) together describe the region of initial velocities for which the ions are confined in the analyzer for entrance phase φ_{01}. For entrance phase φ_{02} the limiting velocities calculated using these relations must be multiplied by the factor $\sqrt{\Psi_{14}\Psi_{24}}$. The confinement regions constructed using expressions (10), (11), (13), and (14) are displayed in Fig. 3 for the sorting parameters $\lambda=0.266$ and $\varepsilon=0.3$ and the two values $c_1=1.1$ and 1.2. It can be shown that for $c_1<1.3$, which values are of practical significance, the confinement regions are closed. The bounded nature of the particle confinement regions determines the finite extent of the mass peaks, which is an important property of OUMS, following from the characteristic features of unipolar ion sorting. The points of intersection of the velocity limits $v_{\min}$ and $v_{\max}$ in the region of small masses ξ_{01} and in the region of large masses ξ_{02} determine the width $\xi_{02}-\xi_{01}$ of the mass peak. Symmetry of the mass peak, in the sense of its extent in the direction of masses which are larger and smaller than m_0, obtains for $c_1\approx c_2$

$$\xi_{01}=\xi_{02}=\xi_0\approx 3.16\sqrt{c_0-1}. \tag{15}$$

Using Eq. (15) we shall obtain a relation for the number n_c of sorting periods as a function of the resolving power ρ_0, determined according to the zero level,

$$n_c=4.5\varepsilon c_1^2\sqrt{c_1-1}\sqrt{\rho_0}. \tag{16}$$

For $\varepsilon=0.3$, $c_1=1.1$, and $\lambda=0.32$ we obtain $n_c=0.52\sqrt{\rho_0}$.

For a strictly bounded mass peak, the sorting velocity in OUMS is much higher than in other types of hyperboloid mass spectrometers.

The velocity range $v_{\min}-v_{\max}$ determines the number of particles with fixed mass m which are confined in the analyzer. Using the fact that component of the thermal velocity in the direction of the sorting axis conforms to a normal distribution and using the expressions for $v_{\min}$ and $v_{\max}$ as the limits of integration, we obtain for the confinement factor

$$n(\xi)=\frac{1}{\sqrt{2\pi}v_T}\int_{V_{\min}}^{V_{\max}}\exp(-v^2/v_T^2)dv. \tag{17}$$

Making the substitution

$$M=1+\frac{\Delta m}{m}=\frac{\xi^2}{\gamma\Theta}+1$$

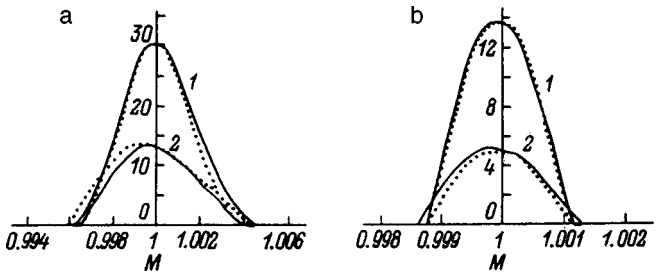

FIG. 4. Mass peaks of a one-dimensional unipolar mass spectrometer for $n_c=10$ and $c_1=1.1$ (a), 1.2 (b); $\lambda=0.327$ (a), 0.276 (b). Solid curves — analytical calculation, dashed curves — computer simulation, *1* — for entrance phase φ_{02}, *2* — for entrance phase φ_{01}.

expression (17) becomes the function $\eta(M)$.

The mass peaks calculated using the relations obtained for the instrumental function are presented in Fig. 4. To estimate the computational error associated with the finite spread of the initial particle coordinates and the curvature of the electrodes, which are neglected in Eq. (9), a computer simulation was performed of one-dimensional unipolar ion sorting processes. The simulation results, which are presented in Fig. 4, indicate that the accuracy of the analytical expressions for the mass peaks is adequate.

Setting in Eq. (17) $\xi=0$ and making a number of simplifications, we obtain formulas for the confinement factor for particles with the analyzed mass that characterizes the sensitivity of the OUMS:

$$\eta_1 \approx \eta_0 \frac{\varepsilon(c_0^2-1)}{\sqrt{(c_0-1)\rho_0}} \qquad \text{for} \qquad \varphi=\varphi_{01}, \tag{18}$$

$$\eta_2 \approx \eta_0 \frac{(c_0^2-1)}{c_0^2\sqrt{(c_0-1)\rho_0}} \qquad \text{for} \qquad \varphi=\varphi_{02}, \tag{19}$$

where $\eta_0=8.9\sqrt{U_m e/m}/v_T$.

According to Eqs. (18) and (19), a one-dimensional analyzer is characterized by a weak dependence of the confinement factor η on the resolving power ρ_0. This makes it possible to obtain high resolution $\rho_0 \geqslant 10^3$ without greatly decreasing the sensitivity of the mass spectrometer. Comparing expressions (18) and (19) shows that the sorting efficiency with entrance phase φ_{02} is $1/\varepsilon c_0^2$ times higher than with the entrance phase φ_{01}. This is also reflected in the different intensity of the peaks in Fig. 4.

CONCLUSIONS

The positions of the extrema of the particular solutions of the Hill equations near the stability boundary $a_0(q)$ for $n_c>10$ coincide to a high degree of accuracy. This feature of the trajectories and of the method of characteristic solutions makes it possible to calculate the envelopes of trajectories of charged particles with different initial coordinates and initial velocities. This is the basis for finding the shape of the mass peaks of a one-dimensional unipolar mass spectrometer. The mass peaks constructed using the analytical expressions agree well with the mass peaks obtained by computer simulation.

A distinguishing feature of the mass peaks of an OUMS is that they are strictly mass-limited. The confinement factor of a one-dimensional analyzer is essentially independent of the resolving power of the mass spectrometer. This makes it possible to obtain a parameter $\rho_0>10^3$ without appreciably degrading the sensitivity of the instrument.

[1] E. V. Mamontov, Vestn. Ryazanskoĭ Radiotekh. Akad., No. 3, 116 (1997).
[2] E. V. Mamontov, *Dynamic Mass Spectrometer with One-Dimensional Separation, 14the IMSC*, Tampere, 1997.
[3] N. W. McLachlan, *Theory and Application of Mathieu Functions*, Clarendon Press, Oxford, 1947 [Russ. trans., IL, Moscow, 1953].
[4] É. P. Sheretov and V. I. Terent'ev, Zh. Tekh. Fiz. **42**(5), 953 (1972) [Sov. Phys. Tech. Phys. **42**, 755 (1972)].

Translated by M. E. Alferieff

Effect of ion sputtering on the statistical properties of a surface

A. V. Merkulov

A. F. Ioffe Physicotechnical Institute, Russian Academy of Sciences, 194021 St. Petersburg, Russia

O. A. Merkulova

St. Petersburg State Technical University, 195250 St. Petersburg, Russia

(Submitted July 10, 1997)
Zh. Tekh. Fiz. **69**, 107–111 (February 1999)

The modification of a gallium arsenide surface during irradiation by heavy cesium ions Cs^+ is investigated by measuring the surface height distribution with an atomic force microscope. Both increases and decreases in the rms height σ, an integral parameter of the surface, are observed to occur. It is established that for all experimental samples the roughness of the gallium arsenide surface increases in a 1–100 nm lateral range. Analysis of the structure function yields an estimate of the characteristic lateral dimensions of the surface structures arising during ion etching. © *1999 American Institute of Physics.* [S1063-7842(99)02002-4]

INTRODUCTION

Ion etching in combination with surface-sensitive methods is one of the basic methods used to investigate the depth distributions of the host and impurity elements of semiconductor devices. However, ion bombardment changes the surface topography. Low-energy ion etching of the surface gives rise to cone formation and, in some cases, at glancing angles of incidence a groove structure forms.[1] To understand these changes in greater detail, it is necessary to study the effect of various conditions of irradiation on the modification of the microrelief. In previous works these features were studied mainly by electron microscopy[2] or Auger-electron spectroscopy, x-ray electron spectroscopy, and secondary-electron spectroscopy.[3] But these methods do not adequately reflect the three-dimensional topography of the surface. The advent of the scanning tunneling microscope and atomic force microscope (AFM) has made it possible to obtain a three-dimensional image of a surface that can be used for quantitative characterization of the changes produced in the the surface morphology by ion bombardment. AFM measurements make it possible to obtain high lateral and height resolution, making the AFM an ideal tool for investigating quite smooth semiconductor surfaces. However, in such investigations[4–6] are often limited their work to only measuring the rms height, which does not carry any information about the structure of the surface. Our objective in the present work was to find out which statistical parameters of the microrelief provide an adequate description of the surface topography of semiconductor structures obtained by ion bombardment. The statistical approach to the investigation of such structures will make it possible in the future to model both the surfaces arising in the course of ion bombardment and the physicochemical processes accompanying ion irradiation.

EXPERIMENTAL PROCEDURE

We investigated samples of gallium arsenide doped with indium δ layers grown by molecular beam epitaxy (sample 1) and samples of gallium arsenide doped with germanium δ layers grown by magnetron sputtering (samples 2–4). We note that the surfaces of the samples 2–4 are not as smooth as the surface of sample 1, probably because of the shortcomings the magnetron sputtering method. Their rms heights are 7.6–18 and 1.4 nm, respectively. To study the development of surface topography as a function of the ion irradiation dose the samples were irradiated with Cs^+ ions with energy $E_p = 3$ keV and angle of incidence of 40° with respect to the surface normal. The height distribution of the surface microrelief was measured with an Autoprobe-CP atomic force microscope with a tip radius of about 10 nm. The statistical characteristics of the microrelief were calculated from the map obtained for the height distribution. The resolution of the AFM surface maps was 512×512 pixels. Varying the scanning length (the measurement base line L), the discretization step was measured automatically. For comparative analysis, measurements were performed on $5 \times 5\,\mu$m surface regions with a 10 mm discretization step.

RESULTS AND DISCUSSION

In such measurements it is ordinarily assumed that the statistical parameters of the surface carry only qualitative or relative information and that they all depend on the measurement scale, i.e., on the resolution of the instrument and the measurement base line.[7] It is also necessary to take into consideration the existence of instrumental effects of AFM measurements. The parameters of the AFM surface maps before and after ion irradiation are presented in Fig. 1. They were used to calculate the roughness characteristics of a surface, the height probability density $P(h)$, and the rms roughness σ given by

$$\sigma = \sqrt{\frac{1}{N-1} \sum_{i=1}^{N} (h_i - \overline{h})^2}, \tag{1}$$

where h_i is the height at a point, $\overline{h}$ is the average height of the surface, and N is the number of points.

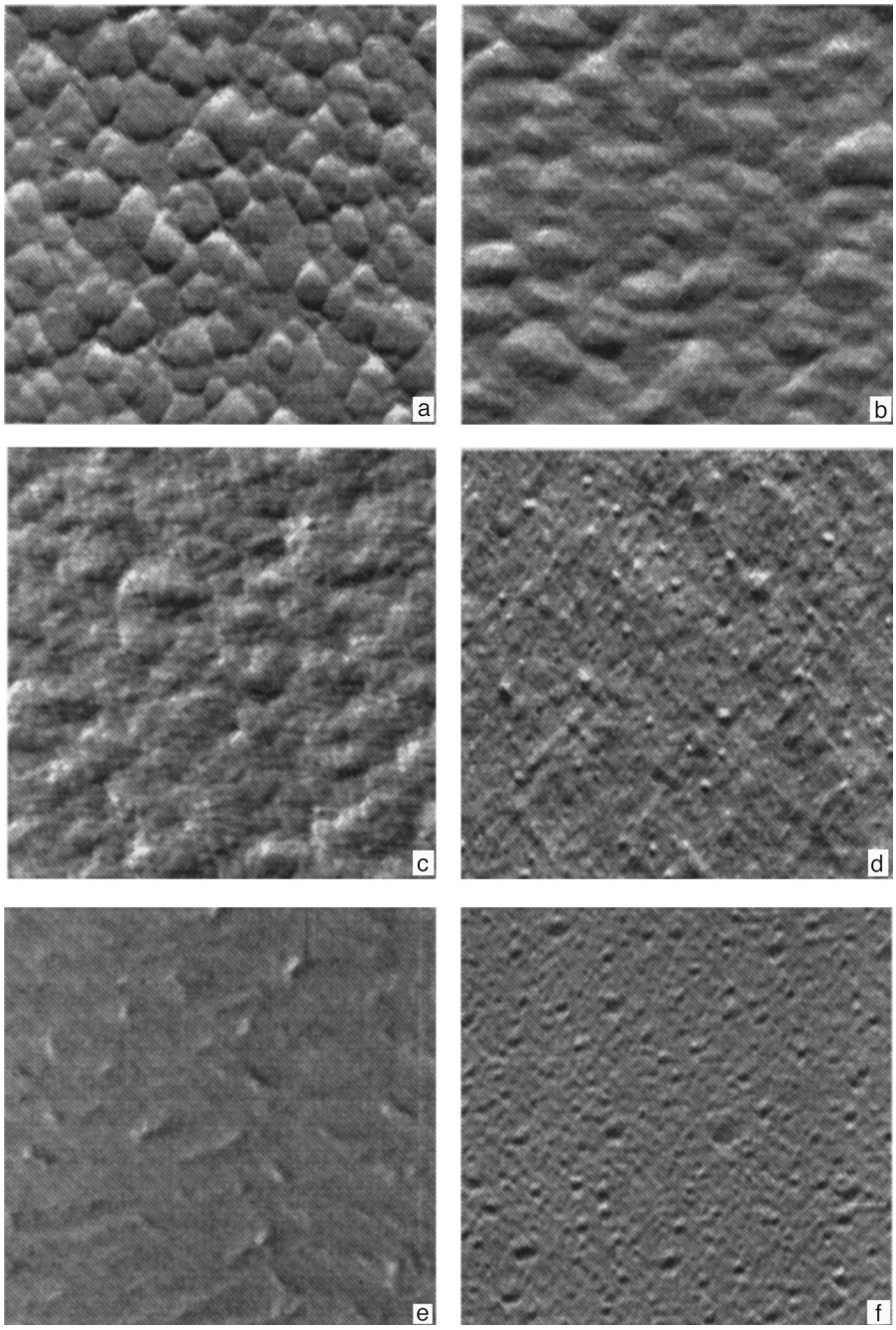

FIG. 1. AFM surface maps for samples 2 and 1 and various ion radiation doses: a–d — sample 2, e–f — sample 1; a, e — initial surface; dose, cm^{-2}: b — 3.3×10^{17}, c — 6.6×10^{17}, d — 2.7×10^{18}, f — 4.6×10^{17}.

It was found that on the surface scale considered, all surfaces possess a close to Gaussian height probability density, which in turn can be approximated by an orthogonal set of Hermite functions.[8] Figure 2 shows the height probability densities approximated by Hermite polynomials for surfaces modified by different ion doses. The dose dependence of the rms roughness is shown in Fig. 3 and is of an exponential character. An effect of this kind (exponential dependence of the rms roughness σ on the ion irradiation dose) was observed for irradiation of InP with low-energy Ar^+ ions,[6] but for InP surfaces the authors observed only exponential growth of σ, while in the present case both exponential growth and exponential decrease of σ during the ion modification process are observed. Therefore it can be inferred that ion etching has a polishing effect on samples grown by magnetron sputtering and initially possessing larger height variances, while the roughness of a sample obtained by molecular-beam epitaxy, conversely, becomes worse.

Together with the height characteristics, we calculated the lateral parameters of the surface roughness, which carry information about the structure of the surface, the quasi-two-dimensional correlation and structure functions of the surface

$$\mathrm{Cor}(\tau)=\langle h(x)h(x+\tau)\rangle_\tau, \tag{2}$$

$$\mathrm{Ctr}^2(\tau)=\langle (h(x+\tau)-h(x))^2\rangle_\tau. \tag{3}$$

Here $\langle \ldots \rangle$ indicates statistical averaging over a length. The quasi-two-dimensional averages mean that in calculating these functions the averaging was performed over each row of the measurements, after which everything was averaged.

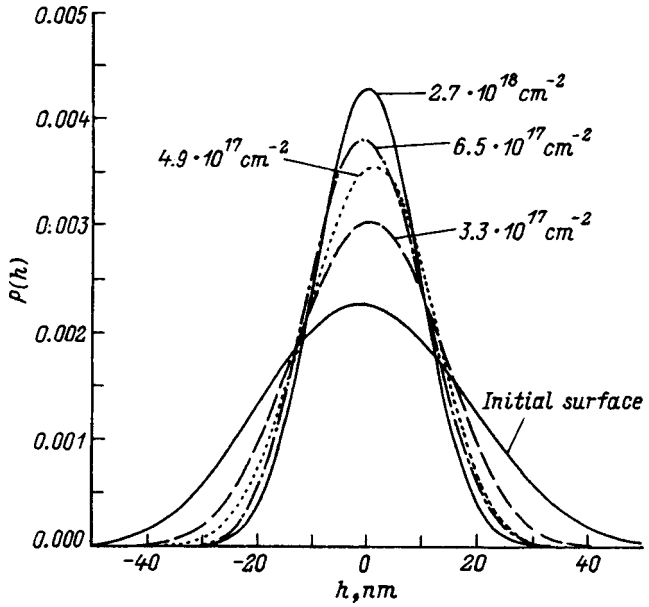

FIG. 2. Probability density $P(h)$ of the heights of surfaces modified by various ion irradiation doses (sample 2).

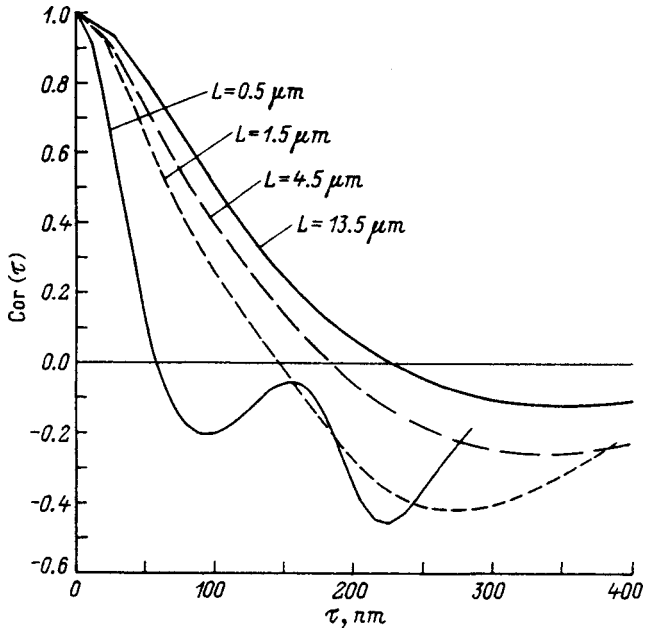

FIG. 4. Correlation functions of sample 1 (initial surface), measured for various base line lengths L.

In Ref. 7 it is shown that the values of the two-dimensional and quasi-two-dimensional lateral functions of a surface are almost equivalent, and that the computational time required for them differs very strongly. It should be noted that the values of the correlation function depend on the measurement length and the discretization step. Measurements over a distance exceeding the correlation length, defined as the intersection of the correlation function with zero, by more than a factor of 10 can be taken as reliable.[8] This fact is illustrated in Fig. 4, which displays examples of correlation functions of sample 1 which were measured for various discretization steps and, correspondingly, different base lines L.

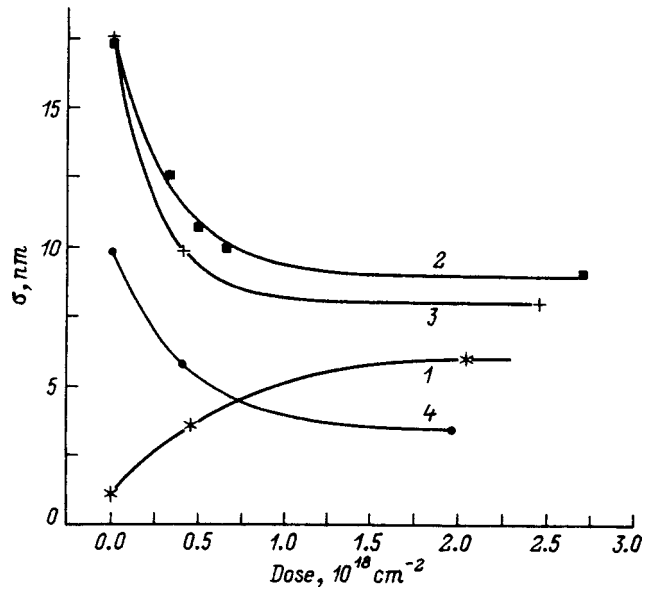

FIG. 3. The rms height versus ion irradiation dose for different samples (the numbers on the curves correspond to the numbers of the samples).

We shall use a fractal approach to describe the surfaces investigated. On account of physical limitations, the surface can exhibit fractal behavior only on limited length scales. It is known that for self-affine surfaces, i.e., surfaces which are invariant under a scale transformation in the lateral direction, the following relation holds:

$$\mathrm{Str}(\tau) \simeq |\tau|^H, \tag{4}$$

where H is a self-affine exponent or Hurst parameter.

In addition, there exists the concept of the fractal dimension of a surface $D=3-H$, and for physical surfaces D lies in the range $2 \leqslant d \leqslant 3$. The parameter D is a measure of the surface roughness.[7] The structure function of a fractal surface constructed in log–log coordinates should be linear and its slope proportional to the fractal dimension of the surface. The structure functions measured for sample 1 in different scanning regions are shown in Fig. 5. The curves coincide with one another in the crossing region $\tau = 1-100$ nm. Their slope does not depend on the measurement scale, so that they quantitatively characterize the surface state. The change in the fractal dimension during ion etching was investigated. For sample 1 the parameter D increases from 2.088 to 2.215; the accuracy of the values obtained is $\delta = \pm 0.007$. All of the surfaces investigated exhibit a similar behavior. Figure 6 shows the structure functions and fractal dimensions of the surfaces of sample 2 for the initial surface and for surfaces irradiated with various ion doses. The dose dependence of the fractal dimension (Fig. 7) makes it possible to conclude that in the length range 1–100 nm the fractal dimension increases during etching for all experimental samples, i.e., under bombardment by cesium ions the surface roughness of gallium arsenide increases on these length scales. This increase in roughness corresponds to the development of prominences with characteristic diameters of up to 100 nm; the appearance of such prominences is clearly seen in the

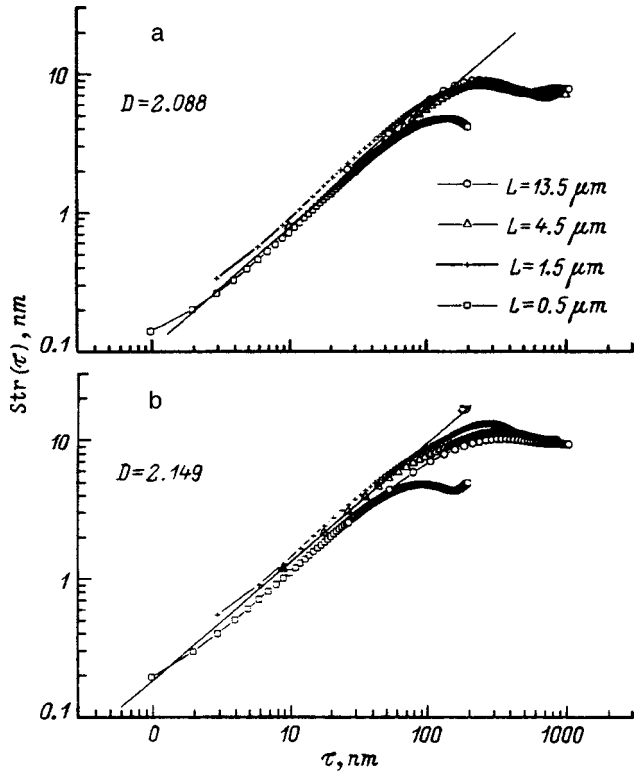

FIG. 5. Structure functions of sample 1, measured with various base lines L, for surfaces before (a) and after (b) ion etching.

AFM maps (Fig. 1d,f). The measured values of σ, however, characterize the larger-scale roughness. For sample 1 this roughness increases, while for samples 2–4 it decreases, indicating the presence of a process that smoothens the surface. A similar behavior of the statistical parameters of a surface under ion irradiation, i.e., a decrease in roughness on a large scale and an increase on a small scale, was observed in Ref. 9. The title of this work ''Ion etching: does the roughness increase or decrease?'' attests to the ambiguity of the measured integral statistical parameters. It can be concluded on the basis of the investigations performed that in ion etching there exist at least two different processes that modify the surface roughness: 1) ion polishing of the surface, and 2) the formation of random surface structures. Thus, the behavior of the structure function assists in estimating the characteristic lateral dimensions of the processes accompanying ion etching.

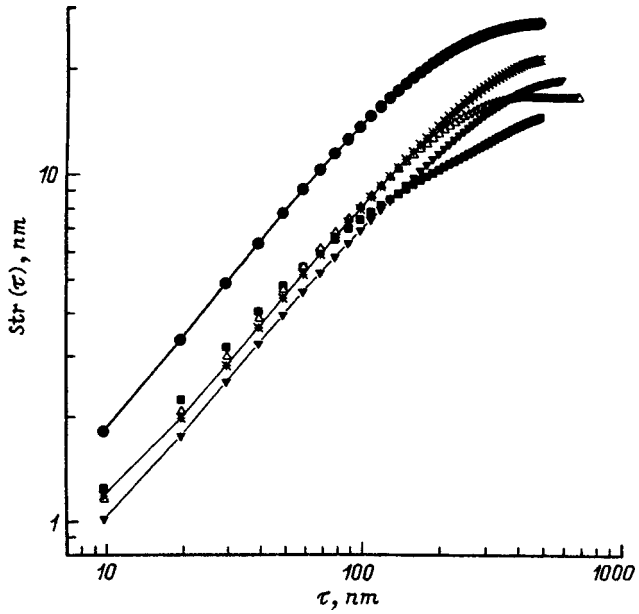

FIG. 6. Structure functions of sample 2, measured for various ion irradiation doses: ● — initial surface ($D=2.100$),* — 3.27×10^{17} cm^{-2} ($D=2.130$),▼ — 4.91×10^{17} cm^{-2}($D=2.153$), △ — 6.55×10^{17} cm^{-2} ($D=2.163$),■ — 2.70×10^{18} cm^{-2}($D=2.222$).

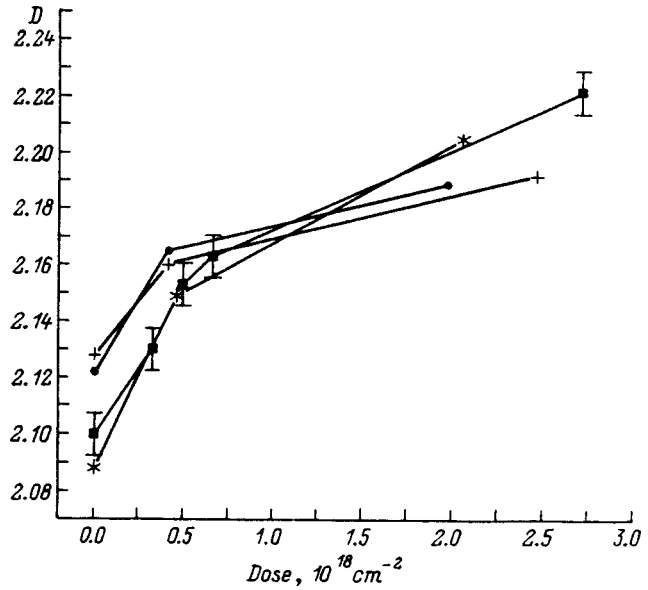

FIG. 7. Fractal dimension D versus ion irradiation dose: * — sample 1, ■ — sample 2, + — sample 3, ● — sample 4.

CONCLUSIONS

In the present work we investigated the modification of a gallium arsenide surface during irradiation with heavy cesium ions Cs^+ by measuring the distribution of the surface heights of the samples, using an atomic force microscope, followed by statistical analysis. Both increases and decreases in the integral parameter σ, the rms surface height, were observed. The lateral statistical characteristics of the surfaces, such as the correlation and structure functions, were analyzed. It was found that the correlation length, determined as the intersection of the correlation function with zero, in the interesting range of lengths depends on the measurement base line. The structure function constructed in log–log coordinates possesses a linear segment, whose slope does not depend on the measurement conditions but is determined solely by the surface roughness on this segment. It was established that in the lateral range 1–100 nm the surface roughness of gallium arsenide increases for all samples investigated. The investigations performed show that in ion etching there exist at least two different processes that modify the surface roughness. Analysis of the structure function made it possible to estimate the characteristic lateral

extent of the processes accompanying ion etching and to determine the degree of detailing of each of them in subsequent modeling.

[1] J. B. Mahnerbe, Crit. Rev. Solid State Mater. Sci. **24**(3), 141 (1994).
[2] O. Auciello and R. Kelly (eds.), *Ion Bombardment Modification of Surfaces. Fundamentals and Applications*, Elsevier, New York, 1984.
[3] Yoshukazu Homma, Hamao Okamota, and Yoshukazu Ishii, Jpn. J. Appl. Phys. **24**(8), 934 (1985).
[4] C. M. Demanet, K. Vijaya Sankar, J. B. Mahnerbe *et al.*, Surf. Interface Anal. **24**, 497 (1996).
[5] C. M. Demanet, K. Vijaya Sankar, and J. B. Mahnerbe, Surf. Interface Anal. **24**, 503 (1996).
[6] C. M. Demanet, K. Vijaya Sankar, J. B. Mahnerbe, and N. G. Van der Berg, Surf. Interface Anal. **23**, 433 (1995).
[7] N. Almqvist, Surf. Sci. **355**, 221 (1996).
[8] J. A. Ogilvi and J. R. Foster, J. Phys. D **22**, 1243 (1989).
[9] Z. Csahok, Z. Farkas, M. Menyharg *et al.*, Surf. Sci. Lett. **364**, 600 (1996).

Translated by M. E. Alferieff

Dosed extraction of hydrogen from a layered thin-film system

Yu. N. Borisenko, V. T. Gritsyna, S. V. Litovchenko, and T. S. Maslova

Kharkov State University, 310077 Kharkov, Ukraine
(Submitted April 7, 1997; resubmitted April 6, 1998)
Zh. Tekh. Fiz. **69**, 112–115 (February 1999)

Radiation-stimulated interfacial gas release in an Ag–glass thin-film system is investigated. It is established that under proton irradiation hydrogen accumulates in bubbles, which are the interfacial gas reservoirs, at the interface. The gas bubbles formed are studied and their parameters are determined by optical microinterferometry. It is shown that 15–50 μm in radius bubbles contain $2\times10^{9}-2\times10^{11}$ hydrogen molecules. Hydrogen is extracted from the reservoir by rupturing the thin-film dome of a bubble with a 2×10^{13} W·cm^{-2} laser beam. © *1999 American Institute of Physics.* [S1063-7842(99)02102-9]

INTRODUCTION

The most promising material in modern nuclear power is hydrogen, which can be used both by itself as a fuel and as an activator of a chemical reaction of other gaseous reactants. Since the optimal hydrogen content in the gas mixture can be hundredths of a percent,[1,2] careful dosing of the hydrogen is required.

Getters — titanium, palladium, and metal hydrides, whose sorption of hydrogen is reversible — are used as the hydrogen reservoir. Hydrogen is extracted from a getter by standard thermal desorption, the variation of whose parameters gives rise to substantial difficulties in dosing out the hydrogen. Specifically, the hydrogen desorption rate from a getter at fixed temperature decreases with time because of ''exhaustion'' of the gas reservoir. During annealing, hydrogen can diffuse not only into the exterior volume but also into the intercrystallite cracks and gaps forming in the getter as a result of its ''swelling'' in the process of gas absorption.[3] Finally, gas which has reached the outer surface of the getter can migrate along the surface (spillover effect) over distances of tens of centimeters[4] without reaching the working chamber. As a result, there is a mismatch between the characteristics of hydrogen diffusion in the getter matrix and the hydrogen desorption into the exterior volume, making it difficult to effect a dosed release of hydrogen.

The present lack of reliable methods of dosed extraction of hydrogen makes it necessary to search for unconventional solutions based on new technologies. Specifically, irradiation of thin-film systems by hydrogen ions has shown elevated gas release in the interface zone.[5] It has been suggested that hydrogen be released into the interfacial zone, where the gas bubbles that form in this case will become interfacial gas reservoirs.

In the present work the mechanism of ion-stimulated interfacial gas release in a thin-film system is investigated and the possibilities of using the method of stimulated gas release for dosed extraction of embedded hydrogen into an exterior volume are analyzed.

EXPERIMENT

Thin silver films deposited on $24\times24\times0.2$ mm glass substrates were investigated. The surfaces of the substrates were cleaned using an alkali and potassium bichromate and then washed with distilled water. The cleaned substrates were placed in a vacuum chamber and ~100 nm thick films were deposited by thermal vaporization at 10^{-4} Pa pressure. The thin-film system (TFS) obtained was irradiated in an electrostatic accelerator with 1 MeV hydrogen ions with fluence $1\times10^{13}-1\times10^{15}$ ions·cm^{-2} and flux density 1.6×10^{12} ions·cm^{-2}s^{-1}. The gas bubbles formed at the interface were studied and their parameters were determined in a Linnik interferometer. Next, the amount of gas in the bubbles and the gas extracted into an exterior volume using laser radiation were calculated.

RESULTS AND DISCUSSION

1) *Physical principles of the method of stimulated gas release.* It was established that during proton irradiation small spherical formations, whose dimensions increase with the irradiation dose, appear on the film–substrate interface (Fig. 1). Their appearance is explained by the fact that as the does increases, hydrogen implanted in the substrate during bombardment (the proton range in the TFS is ~10μm) starts to migrate into the substrate and then emerges into the surrounding medium through various sinks. Some hydrogen migrates to the film–substrate interface, which is one of these sinks.

Gas accumulates near the substrate surface and emerges at the interface when the pressure due to the gas makes it possible to overcome the film–substrate adhesive force. It is obvious that the irradiation doses at which spherical formations appear on the interface should be progressively higher with increasing strength of the initial adhesion, as is in fact observed experimentally.[5] This and the fact that the bubble diameters are much greater (by three orders of magnitude) than the film thickness attest to formation of gas bubbles predominantly in the interphase space.

One possible source of bubble formation at the interface are gas inclusions in the glass. To determine the nature of the

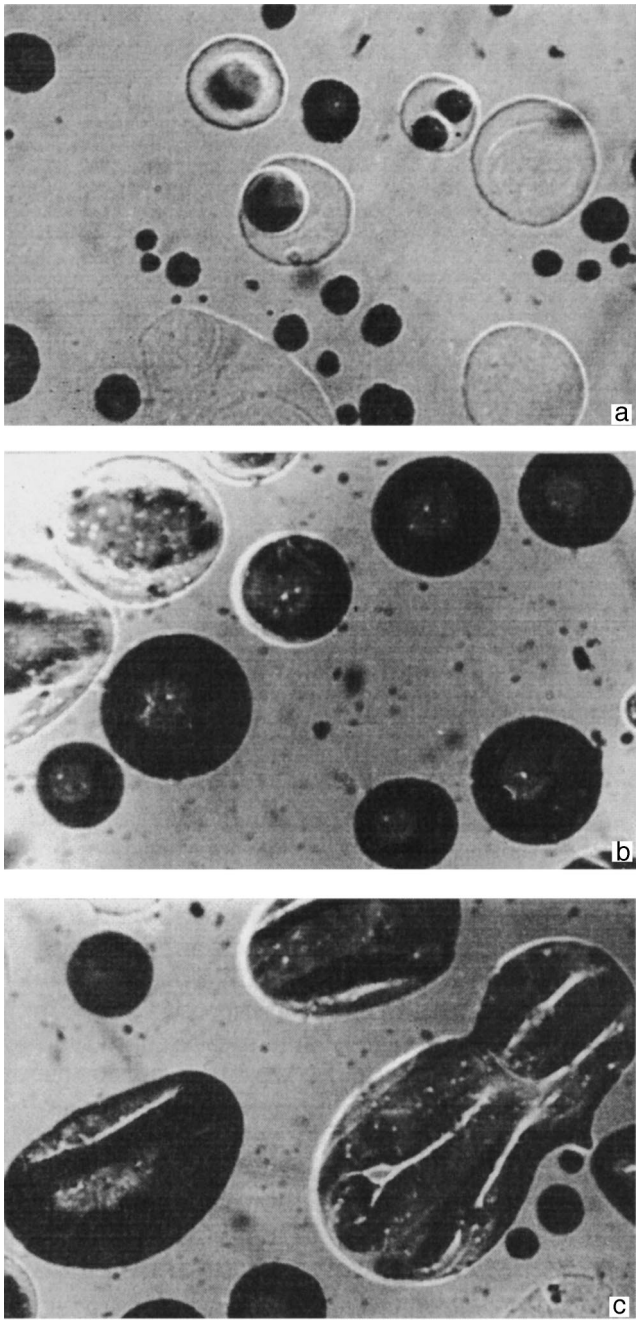

FIG. 1. Photomicrographs of films after proton irradiation with fluence 2×10^{13} (a), 2×10^{14} (b), 1×10^{15} ions$\cdot$cm^{-2} (c); $\times400$.

gas in the bubbles the films were irradiated with both hydrogen and helium atoms, which affect the gas inclusions in the glass substrate by essentially the same mechanism. Under irradiation with helium ions with fluence 1×10^{16} ions $\cdot$cm^{-2} there were no gas bubbles at the interface, while under irradiation with protons the gas bubbles appeared even at fluences 2×10^{13} ions$\cdot$cm^{-2}. This is explained by the well-known difference in the behavior of hydrogen and helium implanted in a substrate.[6,7] Under proton irradiation the implanted gas strives to escape from the substrate, as a result of which a stationary flux of hydrogen from the substrate against the direction of the incident beam is established some time after irradiation starts. At the same time, the implanted helium is retained in the substrate, and as a result, gas-filled bubbles, which increase in size with the irradiation dose, are formed in the implanted layer.[8] Thus, the results of the experiments attest to emergence of hydrogen at the interface under proton irradiation. Gaseous inclusions in the substrate do not participate in bubble formation at the interface.

Analysis of Fig. 1 confirmes the homogeneous nucleation of gas bubbles, whose size increases with the dose. Larger bubbles form at the expense of small neighboring bubbles, with sphericity being restored by minimization of the surface area of a bubble. As the dose increases, bubbles continue to increase in size on account of the diffusion flux of hydrogen escaping from the substrate and by absorption of small neighbors. At the same time, some neighboring bubbles which are close in size can coalesce, forming ''dumbbell-shaped'' formations. Bubbles burst when their diameter reaches 0.2–0.3 mm.

The average diffusion flux density $j_{\rm dif}$ and the relative amount of gas escaping from the substrate onto the interface $\beta=j_{\rm dif}/j_{\rm f}$, where $j_{\rm f}$ is the incident ion flux density, can be found by studying the bubble growth kinetics. Under the experimental conditions $j_{\rm dif}=4\times10^{11}$ atoms$\cdot$cm^{-2}s^{-1} and $\beta=0.25$ atoms/ion, which confirms the statements made above about the behavior of hydrogen in a substrate.

2) *Calculation of the amount of gas in bubbles.* Statistical analysis of microinterferograms of various sections of the surface of an irradiated film (Fig. 2) established the following: The bubble diameters at fluences of 1×10^{14}, 3×10^{14}, and 1×10^{15} ions$\cdot$cm^{-2} were 5–30, 30–60, and 60–100 μm, respectively; the bubble surfaces are predominantly spherical, as is indicated by the rectilinear character of the dependence of the squared diameters of the interference rings on their numbers; the ratio of the bubble radius r to the radius of curvature R_c of a bubble is a constant for all bubbles and equals $r/R_c=\Psi=0.10\pm0.01$. The radius R_c is given by the relation

$$R_c=\frac{R_m^2-R_n^2}{\lambda(m-n)}, \tag{1}$$

where R_m and R_n are the radii of Newton's rings, m and n are the numbers of the rings, and λ is the wavelength of the incident light.

It follows from the sphericity of the bubbles and the constancy of Ψ that the film–substrate structure is uniform over the interface, and the smallness of the relative extensions ($\Delta r/r\sim10^{-3}$) attests to the elastic character of the deformation of the film.[9]

The amount of gas in bubbles was calculated using the Mendeleev–Clapeyron formula, in which P is calculated from the well-known expression relating the gas pressure in a bubble and the elastic characteristics of the film:[10]

$$P=\frac{2d}{R_c}\left(\sigma_0+\frac{2}{3}\frac{E}{1-\mu}\frac{\Psi^2}{4}\right), \tag{2}$$

where d is the film thickness, σ_0 is the internal tensile stress in the film (which is determined by x-ray extensometry and is equal to 4×10^7 Pa), E is Young's modulus of the film material, and μ is Poisson's ratio.

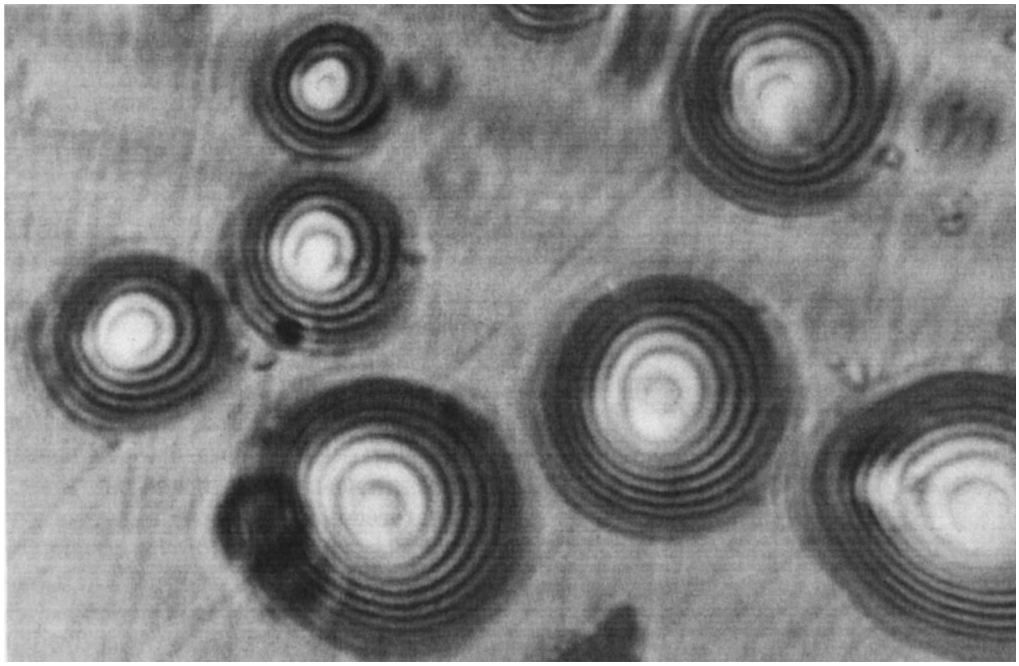

FIG. 2. Interferogram of a film surface after proton irradiation with fluence 2×10^{14} ions$\cdot$cm^{-2}; $\times1000$.

The volume V of a gas bubble can be calculated from the formula for a spherical segment with radius R_c. Thus, the total amount of gas in a bubble is determined as

$$N=\frac{\pi d r^2\Psi^2}{2kT}\left(\sigma_0+\frac{2}{3}\frac{E}{1-\mu}\frac{\Psi^2}{4}\right). \tag{3}$$

To improve the accuracy of the calculation of R_c, bubbles 10–100 μm in diameter were used. Such bubbles give a sufficiently large number of Newton rings (more than 2). The calculations, which were confirmed by subsequent mass-spectrometric quantitative monitoring, showed that a bubble contains from 2×10^9(for $r=15\,\mu$m) to 2×10^{11} (for $r=50\,\mu$m) hydrogen molecules. It should be noted that the amount of gas in bubbles was computed on the assumption that the deformation of the silver film is elastic, which is true[9] for relative extensions up to 4×10^{-3}, which correspond to $\Psi=0.15$. Further extension results in plastic deformation and destruction of the film. The value of Ψ is limited by preparing the TFS with allowance for the well-known dependence of the parameters of gas bubbles on the adhesion strength.[11] The prescribed adhesion characteristics are achieved by varying the technological conditions of film deposition (deposition rate, substrate temperature, and so on). Specifically, $\Psi=0.15$ corresponds to adhesion strength 0.5×10^5 Pa.[12]

Another parameter that determines the working capacity of TFSs as a gas reservoir is the thickness of the thin-film coating. The minimum thickness is determined by the requirement that the coating remain continuous, and it should not be less than 50 nm. The maximum coating thickness is determined by the requirement that the coating have a long lifetime under pressure (10^6–10^8 s) and derives from the need to maintain in the bubble formation zone a ratio of the geometric parameters of the TFS — coating thickness d and radius of curvature R_c — such that the stresses arising in the thin-film coating under the gas pressure are primarily tangential stresses, which do not produce rapid destruction of the coating. According to the kinetic theory of the fracture of solids, which describes well the fracture of a metallic spherical shell by internal pressure,[13] the fracture time τ is determined by the longevity equation

$$\tau=\tau_0\exp\frac{U_0-\gamma\sigma_{\tan}^{\max}}{kT}, \tag{4}$$

where τ_0 is the acoustic passage time of a cell (for metals $\sim10^{-13}$ s), U_0 is the activation energy of the fracture process, γ is the slope, and $\sigma_{\tan}^{\max}$ is the maximum value of the tangential stresses, which is determined by the relation

$$\sigma_{\tan}^{\max}=\frac{P}{\sqrt{3}}\frac{R_c}{2d}. \tag{5}$$

Calculations using Eq. (4) show that the shell of a bubble will have a quite long lifetime (greater than 10^8 s) if $R_c/d>180$. For the minimum radius of the bubbles investigated 5 μm, this ratio holds for $d<280$ nm.

3) *Extraction of hydrogen from bubbles.* After a bubble of the required size and containing a prescribed amount of gas is selected, the thin-film dome of the bubble is ruptured by a laser beam. The minimum laser intensity I_f required to rupture a metallic thin-film shell can be determined from the relation

$$I_f=\frac{\sigma_f\cdot c}{R}, \tag{6}$$

where c is the speed of light, R is the radiation reflection coefficient of the thin-film shell (for metals ~0.5), and σ_f is the fracture stress, determined from the longevity equation by the relation

$$\sigma_f = \frac{1}{\gamma}\left(U_0 - kT \ln \frac{\tau_f}{\tau_0} \right), \tag{7}$$

where τ_f is the fracture time at the impact location ($\sim 10^{-8}$ s for a short laser pulse).

Calculations using Eq. (6) show that a laser with intensity of at least 2×10^{13} W·cm^{-2} is required to guarantee fracture of the metallic thin-film dome of a bubble. This corresponds to the values used in practice in pulsed laser treatment of metals in the hydrodynamic regime.[14]

In summary, the proposed sequence of operations — proton irradiation of a thin-film system, analysis and calculation of interfacial gas bubbles, and fracture of the thin-film dome of a selected bubble by a laser beam — makes possible the dosed extraction of hydrogen into the exterior volume. Precise dosing of the extraction is accomplished by using intermediate gas microreservoirs, which can be investigated and counted.

[1] G. Alefeld and J. Volkl (Eds.), *Hydrogen in Metals*, Springer-Verlag, Berlin–New York, 1978 [Russian trans., Mir, Moscow, 1981, Vol. 2, 430 pp.].
[2] D. Yu. Gamburg and N. F. Dubrovnik (Eds.), *Handbook of Hydrogen*, Khimiya, Moscow, 1989, 679 pp.
[3] L. V. Basteev, M. A. Obolenskiĭ, and V. V. Soloveĭ, *Activation of Hydrogen and Hydrogen-Containing Energy Carriers*, Naukova Dumka, Kiev, 1993, 162 pp.
[4] V. V. Soloveĭ, L. V. Basteev, A. M. Prochnimak, and V. V. Popov, Vopr. At. Nauk. Tekh. Ser. Yad. Tekh. Tekhnol. (Kharkov), No. 1, 28 (1991).
[5] Yu. N. Borisenko, V. T. Gritsyna, and V. F. Pershin, Vopr. At. Nauk Tekh. Ser. Fiz. Radiats. Povrezh. Radiats. Materialoved. (Kharkov), No. 1, 97 (1974).
[6] D. Kaletta, Radiat. Eff. **47**, 237 (1980).
[7] G. Carter, D. C. Armour, S. E. Donelly, and D. S. Ingram, Radiat. Eff. **53**, 143 (1980).
[8] I. M. Neklyudov, V. F. Rybalko, G. D. Tolstolutskaya, and V. G. Dzenkovskiĭ, Poverkhnost', No. 12, 48 (1983).
[9] L. S. Palatnik, G. V. Fedorov, and A. I. Il'inskiĭ, Fiz. Met. Metalloved., No. 5, 815 (1961).
[10] J. W. Beams, *Structure and Properties of Thin Films*, Wiley, New York, 1959, pp. 183–192.
[11] Yu. N. Borisenko, V. T. Gritsyna, and T. V. Ivko, Zh. Tekh. Fiz. **59**(12), 121 (1989) [Sov. Phys. Tech. Phys. **34**, 1445 (1989)].
[12] Yu. N. Borisneko, V. T. Gritsyna, and T. V. Ivko, J. Adhesion Sci. Technol. **9**, 1413 (1995).
[13] V. R. Regel', A. I. Slutsker, and É. E. Tomashevskiĭ, *Kinetic Nature of the Strength of Solids* [in Russian], Nauka, Moscow, 1974, 560 pp.
[14] J. F. Ready, *Lasers in Modern Industry*, Society of Manufacturing Engineers, Dearborn, Michigan, 1979 [Russian trans., Mir, Moscow, 1981, 638 pp.].

Translated by M. E. Alferieff

Elasticity of a cryo-insulation polymer foam coating in the temperature range 8–293 K

L. A. Bulavin, Yu. F. Zabashta, A. Ya. Fridman, and A. I. Kostyuk

Taras Shevchenko Kiev State University, 252127 Kiev, Ukraine
(Submitted September 12, 1997; resubmitted April 20, 1998)
Zh. Tekh. Fiz. **69**, 116–118 (February 1999)

An apparatus is developed for investigating the dynamic deformation properties of cryo-insulation coatings in the temperature range 8–293 K. One type of cryo-insulation material — polyurethane foam — is chosen as the object of investigation. Test measurements on a polyurethane foam ''pack'' (metal substrate with a polyurethane foam coating) are performed at 0.01 Hz in the temperature range 8–293 K. A jump in the temperature dependence of the dynamic shear modulus (by two orders of magnitude) is observed in the temperature range 54–63 K. This feature is attributed to the solidification of the air present in the pores of the polyurethane foam. Such a transition results in cementation of the polyurethane skeleton of the coating by the nitrogen and oxygen ''ice'' that is formed. © *1999 American Institute of Physics.* [S1063-7842(99)02202-3]

Cryo-insulation polymer foam coatings employed in aviation and space technology are used, as a rule, to insulate tanks containing liquid hydrogen. However, as far as we know, there are virtually no published works on the properties of cryo-insulation polymer foam coatings at low temperatures, including the temperature of liquid hydrogen. To construct and operate aircraft, it is primarily necessary to have data on the elasticity of cryo-insulation material in the indicated temperature interval. In the present paper we describe a method which we have developed for performing such measurements in the temperature range 8–293 K.

To investigate dynamic deformation properties of cryo-insulation coatings in the temperature range 8–293 K, we developed and built an apparatus (Fig. 1) which contains a cryostatic system (including a KG-100 helium cryostat), an inverted torsion pendulum,[1] an apparatus for lifting the cryostat, a system of transitional flanges, and a working ''vessel,'' located in a helium bath, into which the working part of the pendulum containing the sample is inserted. As one can see from Fig. 1, the measuring head of the inverted torsion pendulum with inertial rods *1* is mounted on a massive metallic plate *2*. A glass vacuum cap *7* is placed on the measuring head. The base of the cap is hermetically clamped to the plate by means of quite thick (12 mm) elastic rubber *13*. A rod with the sample *5* passes through a circular opening in the plate. The rod with the sample is located inside the pendulum tube, welded to the system of transitional flanges (central flange), which in turn is hermetically secured, by the top flange, at the bottom to the metallic plate by means of vacuum rubber gaskets *12*.

The tube with the rod holding the sample *5* is placed in the working ''vessel'' *6* of the helium cryostat *9*, welded to the bottom flange, which is likewise hermetically secured to the flange of the helium cryostat.

The ''vessel'' is made of German silver and is enclosed in a copper jacket (up to 2/3 of the height) so as to produce a thermal bridge. A resistance thermometer and a nichrome heating coil *8* followed by insulation are mounted successively on the outer part of the ''vessel,'' covered with thin, thermally stable insulation.

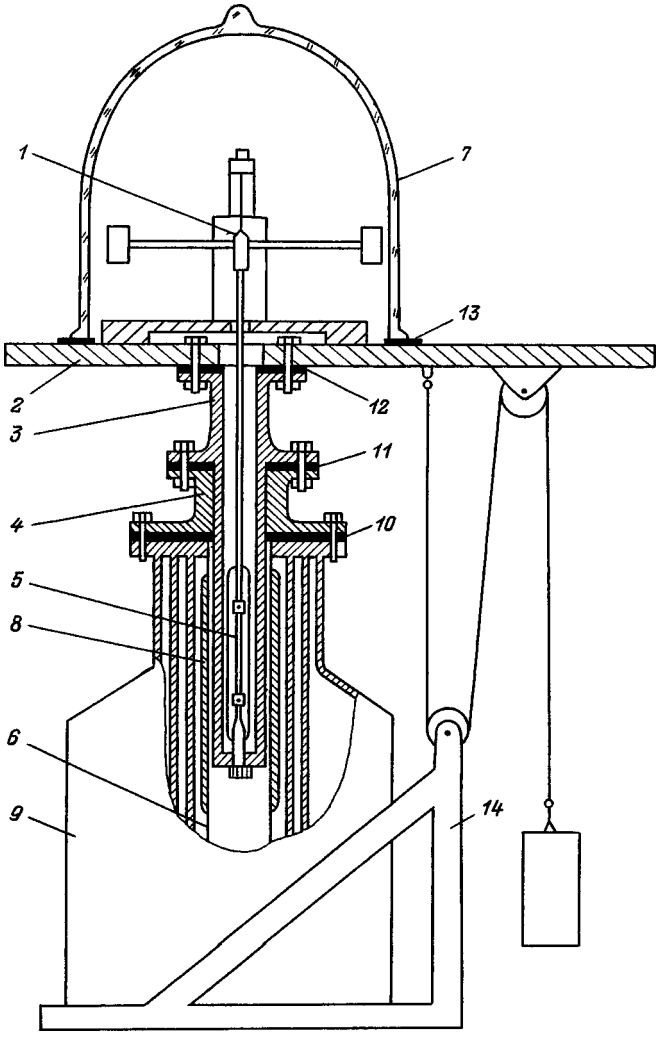

FIG. 1. Setup for investigating the dynamic deformation properties of cryo-insulation polymer foam coatings in the temperature interval 8–293 K.

Tubes for feeding and removing helium are located on the bottom flange. Helium is poured from a transport Dewar using transfer siphons.[2]

The entire system (vessel cavity, space below the cap and inside the tubes *3* and *4* with transitional flanges) is completely sealed hermetically by means of vacuum gaskets *10–12* and clamping screws and is evacuated to the required pressure (0.12 Torr) with a roughing pump. Air is evacuated to prevent icing of the working part of the pendulum with the sample as the temperature is lowered and with further cryogenic suction of air into the system from the outside. It should be noted that the comparatively low vacuum used is dictated by the specific structure of polymer foams: A large pressure drop could destroy the integrity of the pores of the foam.

A lifting device *14* was used to move the cryostat in the vertical direction. After helium was poured into the helium bath of the cryostat (the cryostat was first cooled with liquid nitrogen poured into the nitrogen bath), a minimum temperature 6–8 K was established in 190 min. Next, the temperature was gradually raised at a definite rate. Attainment and stabilization of a prescribed temperature in the working chamber of the ''vessel'' were accomplished with an electric heater *8* and a resistance thermometer, which is one arm of the ac current bridge. The automatic temperature regulation circuit is described in Ref. 1.

The temperature of the medium surrounding the sample was measured with a TPK-N436-68 semiconductor thermometer, fabricated at the Special Design and Technology Office of IPAN, Ukrainian National Academy of Sciences. The accuracy of temperature stabilization was as follows: 4.00–0.05, 30.00–0.10, 100.00–0.50, 200.00–0.80 K.

One form of the cryo-insulation material — polyurethane foam (closed porosity 90%) was chosen as the object of investigation. We investigated this material experimentally in previous work by the internal-friction method using an inverted torsion pendulum in the temperature range 93–373 K.[3]

Our apparatus for investigating the dynamic deformation properties at ultralow temperatures was used for test measurements of the elasticity of a ''pack'' of polyurethane foam (aluminum substrate with a polyurethane foam coating) — batch ÉKG-532-04. The working frequency was 0.01 Hz and the temperature range was 8–300 K. It is well known that the elastic properties, just as other physical properties, of a material are determined by its structure. It is also well known that foam plastic in the form of a block and foam plastic deposited on a substrate as a coating possess different structures. Our aim was to measure the elastic characteristics of the latter. Accordingly, the following method was used to prepare the samples.

A layer of foam plastic is deposited on a metal substrate by the technology used for manufacturing objects. Samples in the form of parallelepipeds were cut from the pack formed (substrate + coating) in such a way that the long side of the parallelepipeds was arranged along the thickness of a sheet (pack). Correspondingly, the samples obtained, like the pack, consisted of a substrate (4.3 mm thick) and foam plastic (30 mm thick). For the tests, a sample was placed in clamps in a manner so that the substrate–foam boundary would be flush with the top face of the bottom clamp.

The measurements yielded φ versus t — the rotation angle of the pendulum as a function of time. The conventional theory of a torsion pendulum was used to determine the shear modulus G from this relation.[4] The equations of motion of the pendulum were written in the form

$$I\frac{d^2\varphi}{dt^2} = -C\varphi, \tag{1}$$

where I is the moment of inertia of the loads and C is the torsional stiffness of the system (suspension + sample).

Since $\varphi = \varphi_0 e^{i\omega t}$, we obtained for the torsional stiffness C from Eq. (1)

$$C = \omega^2 I. \tag{2}$$

The stiffness C of the system was written as a sum

$$C = C_1 + C_2, \tag{3}$$

where C_2 is the stiffness of the system without the sample and C_1 is the stiffness of the sample.

The quantity C_2 was determined experimentally: In the absence of the sample the stiffness C_1 of one sample determined from the experiment is, according to Eqs. (2) and (3),

$$C_1 = \omega^2 I - C_2. \tag{4}$$

To determine the relation between the shear modulus G and the stiffness C_1, we solved a problem of the theory of elasticity concerning the torsion of a rod with a square cross section[5]

$$C_1 = \frac{P\alpha JG}{l}, \tag{5}$$

where J is the moment of inertia of the section, l is the working length of the sample, and α is a coefficient that takes into account the warping of the section and depends on the ratio of the transverse dimensions of the sample.

The values so obtained for the shear modulus G as a function of temperature are presented in Fig. 2. The main feature of this curve is the jump in the modulus by approxi-

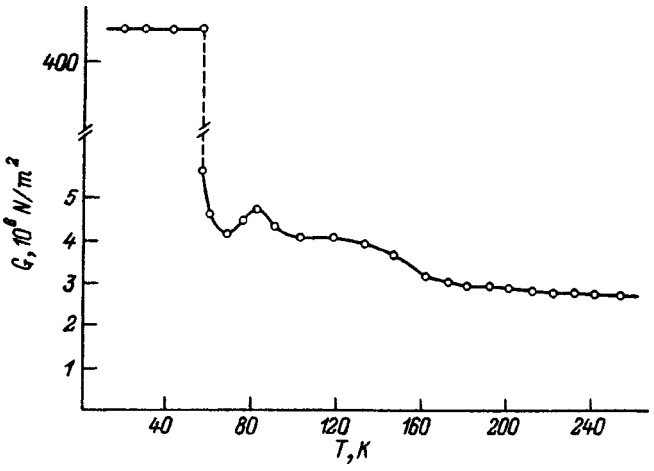

FIG. 2. Temperature dependence of the dynamic shear modulus G of the polyurethane foam pack.

mately two orders of magnitude at temperature 57 K. Since this jump occurs in the range of freezing of nitrogen and oxygen in air, it can evidently be asserted unequivocally that this jump is due to the indicated phenomenon. In principle, this jump could be due to external icing of the sample, despite our efforts to evacuate air from the system. To check this supposition, we performed a control experiment on a sample fabricated from the substrate material. There is no jump in modulus in the corresponding temperature dependence $G(T)$ in the temperature interval where a jump in modulus was observed for the pack (Fig. 2). Therefore it can be concluded that the observed jump in the modulus is due to the solidification of the air contained in the pores in the polyurethane foam coating, which results in cementation of the polyurethane skeleton of the coating by the nitrogen and oxygen ''ice'' formed. In addition, a vacuum arises in the pores of the polyurethane foam, and the cryo-insulation coating should acquire the properties of vacuum insulation.

The increase in the modulus and the corresponding improvement of the thermal insulation properties of the coating that we observed experimentally provide an additional argument in favor of using polymer foam coatings for insulating tanks containing liquid hydrogen.

[1] A. Z. Golik and A. F. Lopan, Ukr. Fiz. Zh. **12**, 991 (1967).
[2] B. I. Formozov, *Experimental Technique in the Physics of Superconductors* [in Russian], Vysshaya Shkola, Kiev, 1978, 198 pp.
[3] A. I. Seigniy, Yu. F. Zabasta, and A. Ya. Fridman, Int. J. Hydrogen Energy **20**, 401 (1995).
[4] V. S. Postnikov, *Internal Friction in Metals*, Metallurgiya, Moscow, 1969, 350 pp.
[5] L. D. Landau and E. M. Lifshitz, *Theory of Elasticity*, Pergamon Press [Russ. original, Mir, Moscow, 1982, 250 pp.].

Translated by M. E. Alferieff

Effect of the laser sputtering parameters on the orientation of a cerium oxide buffer layer on sapphire and the properties of a $YBa_2Cu_3O_x$ superconducting film

P. B. Mozhaev, G. A. Ovsyannikov, and Ĭ. L. Skov

Institute of Radio Engineering and Electronics, Russian Academy of Sciences, 103907 Moscow, Russia; Technical University of Denmark, Lyngby DK-2800, Denmark

(Submitted May 27, 1997; resubmitted October 14, 1997)
Zh. Tekh. Fiz. **69**, 119–123 (February 1999)

The effect of the laser sputtering parameters on the crystal properties of CeO_2 buffer layers grown on a $(1\bar{1}02)$ sapphire substrate and on the properties of superconducting $YBa_2Cu_3O_x$ thin films are investigated. It is shown that (100) and (111) CeO_2 growth is observed, depending on the sputtering conditions. A buffer layer with the desired unidirectional orientation can be obtained by varying the heater temperature, the pressure in the chamber, and the energy density of the laser beam at the target. © *1999 American Institute of Physics.* [S1063-7842(99)02302-8]

INTRODUCTION

The combination of a sapphire substrate with $(1\bar{1}02)$ orientation (*r* orientation) and a CeO_2 buffer layer appears to be one of the most promising variants for obtaining epitaxial films of the high-temperature superconductor $YBa_2Cu_3O_x$ (YBCO). The cubic lattice of CeO_2, with a lattice constant of 0.541 nm, matches well with the lattice constants of YBCO (the mismatch along the *a*, *b*, and *c* axes is 0.15, 1.4, and 1.7%, respectively), which allows epitaxial growth of YBCO. Sputtering of a CeO_2 buffer layer on sapphire, which is done by laser,[1] electron-beam,[2,3] and rf sputtering,[3,4] gives a dense, monolithic film, which prevents the chemical interaction (which ordinarily suppressing the superconductivity) of the aluminum substrate with the YBCO film. The high dielectric properties of sapphire make this combination one of the most promising ones for fabricating microwave superconducting components and devices. It is known, however, that CeO_2 on sapphire can grow both in the (100) and (111) orientations, and these two orientations often coexist (Refs. 3, 5, and 6).[1)] Purely (111) and (100) CeO_2 orientations have been obtained by varying the properties of the sapphire surface by chemical treatment.[3] The existence of two domain subsystems with relative disorientation of about 30° in the (111) plane have been noted in the (111) CeO_2 buffer layer.[3,5] It has been pointed out that the formation of a (111) CeO_2 film was due to the formation of an oxygen-deficient AlO_x phase on the substrate surface. The effect of the growth conditions during cathodic sputtering on the (111) CeO_2 content was noted in Ref. 6. In the present work we investigate d the structure of CeO_2 buffer layers grown on sapphire under different laser sputtering conditions, and we studied the structural and electrophysical parameters of YBCO films grown by laser sputtering on these CeO_2 buffer layers of different orientation and structure.

EXPERIMENTAL PROCEDURES

A laser sputtering setup[8] was used to deposit YBCO and CeO_2. A KrF excimer laser (wavelength 248 nm) with energy density on target up to $3\ J/cm^2$ was used. The laser beam was moved along the surface of a stoichiometric ceramic target ($YBa_2Cu_3O_7$ and CeO_2) using a rotating mirror and two motors. A constant pressure of 0.03–1 mbar was maintained in the chamber. The substrate was placed 42.5 mm from the target on a susceptor heated by a halogen lamp. The temperature of this susceptor during deposition was monitored with a thermocouple and maintained constant to within 1 °C in the range 750–900 °C. To improve thermal contact with the heater, the substrate was glued to the susceptor using silver paste. When the deposition of CeO_2 was completed, the substrate was cooled to room temperature at the maximum rate; after deposition of YBCO, the cooling was conducted in three stages: at maximum rate to temperature 400 °C at the deposition pressure, in oxygen at atmospheric pressure to 350 °C over 2 h, and at the maximum rate to room temperature. The thicknesses of the deposited films were 16 nm for the CeO_2 buffer layer and 60 nm for the film of the high-temperature superconductor.

The structure of the films obtained was investigated by x-ray diffractometry ($\Theta/2\Theta$ and Θ scanning). The parameter *IR*, equal to the ratio of the intensities of the (111) and (200) peaks of the $\Theta/2\Theta$ scanning diffraction pattern, $IR = I(111)/I(200)$, was used to estimate the fraction of the (111) orientation in the buffer layer. The lattice parameter *c* of the YBCO film was calculated according to the positions of the $(00l)$ peaks of YBCO in the $\Theta/2\Theta$-scanning diffraction patterns; the parameter of the cubic lattice of CeO_2 was calculated according to the (200) peak using the $(1\bar{1}02)$ peak of sapphire as the standard.[9] The quality of the YBCO films was estimated according to the half-width $\Delta(2\Theta)_{(005)}$ of the (005) peak from the $\Theta/2\Theta$ scanning and the $FWHM_{(005)}$ from the Θ scanning, the quality of the CeO_2 films was estimated according to the width $\Delta(2\Theta)_{(200)}$ of the (200) peak from the $\Theta/2\Theta$ scanning. For the YBCO films, the stresses in a film were calculated according to the system of peaks $(00l)$ with allowance for the instrumental broadening.

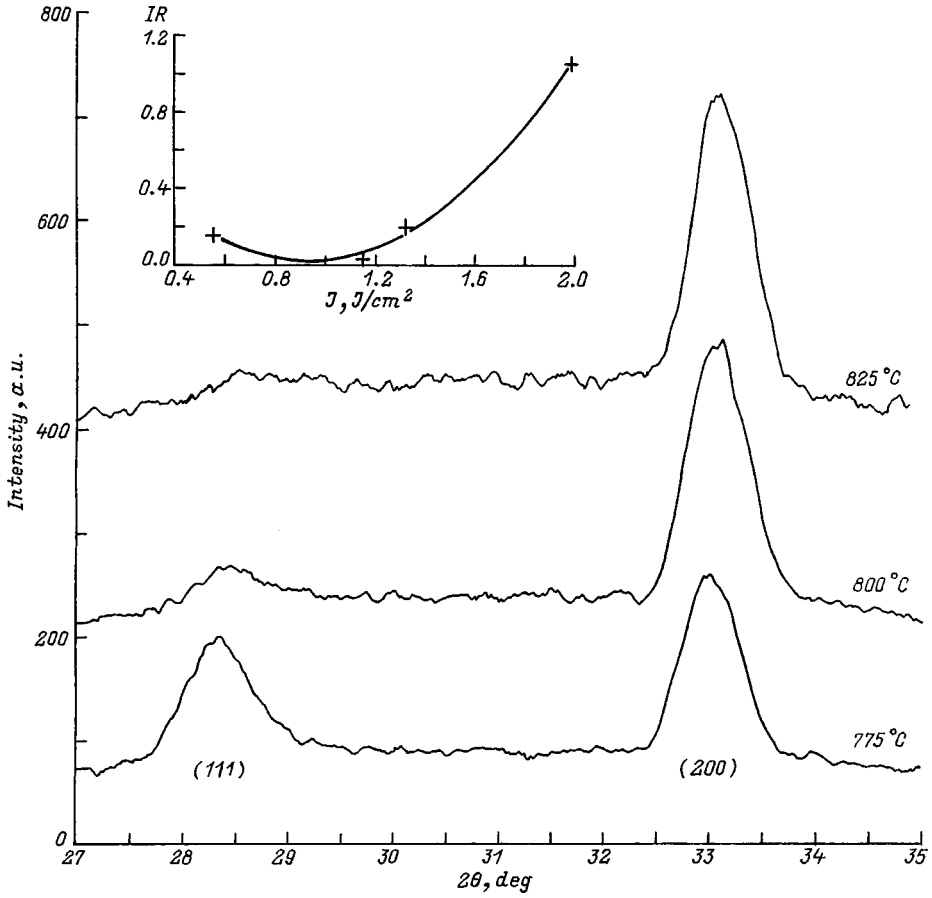

FIG. 1. Diffraction patterns obtained by $\Theta/2\Theta$ scanning of CeO_2 buffer layers on (1$\underline{1}$02) sapphire. The layers were deposited by laser sputtering at different substrate temperatures. The oxygen pressure in the chamber was 0.06 mbar and the laser energy density at the target was 1.1 J/cm^2. Inset: Fraction of the (111) buffer layer as a function of the laser energy density at the target. The oxygen pressure in the chamber was 0.03 mbar and the substrate temperature was 780 °C.

The desired value of the relative variance of the interplanar spacing (stress)

$$\Delta d/d = -(\Delta(2\Theta))_{\text{volt}} \tan\Theta \quad (1)$$

was assumed to give the minimum variance of the film thickness t, calculated from the equation

$$t = \lambda/((\Delta(2\Theta))_{\text{th}} \cos\Theta) \quad (2)$$

for each $(00l)$ peak.[10] In the formulas presented above Θ is the Bragg diffraction angle, d is the interplanar spacing, $\lambda = 0.15405$ nm is the wavelength of the Cu$K_{\alpha 1}$ radiation, $(\Delta(2\Theta))_{\text{th}}$ and $(\Delta(2\Theta))_{\text{volt}}$ are the contributions to the broadening of the peaks from the small thickness of the film and the stresses in the film, respectively, and Δd is the variation of the lattice constant over the thickness of the film. To determine the contributions of the peaks, the nonadditive character of their contribution to the observed broadening $\Delta(2\Theta)$ was taken into account. The computed thickness for the value found for the stress was in good agreement with the thickness determined from the known rate of deposition for all the experimental samples. The film surfaces were studied in a scanning electron microscope (SEM). To observe nonconducting buffer layers, the films were coated with a thin (less than 2) layer of platinum. The electrical properties of the YBCO films (critical temperature T_c, width ΔT_c of the superconducting transition) were determined from the temperature dependence of the resistance of a film.

RESULTS

Figure 1 shows the diffraction patterns obtained at three different temperatures by $\Theta/2\Theta$ scanning of a CeO_2 buffer layer deposited on sapphire with the *r* orientation. Increasing the deposition temperature with other laser sputtering parameters held constant decreases the content of the (111) orientation; the (111) peak virtually vanishes at 825 °C. Increasing the thickness of the buffer layer while maintaining the deposition conditions unchanged appreciably increases *IR*. Particles of irregular shape are observed on the surface of CeO_2 films in the photomicrographs obtained with a scanning electron microscope; the density of these particles on the surface increases with decreasing temperature (from less than 10^7 cm^{-2} at 825 °C to 5×10^8 cm^{-2} at 775 °C), which suggests that the particles are CeO_2 crystallites with the (111) orientation.

Table I gives the parameters of the buffer layer as a function of the pressure in the chamber, the substrate temperature, and the energy density of the beam on the target surface. At 0.06 mbar pressure and low energy density the (111) orientation of CeO_2 predominates. Increasing the energy density up to 1 J/cm^2, like a pressure decrease, decreases *IR*. However, as the energy density increases further, the (111) orientation fraction once again increases (inset in Fig. 1).

The measured lattice constant of the buffer layer (Table I) for samples with the (111) orientation comprising a substantial fraction of the film is somewhat higher than the pub-

TABLE I. Deposition of a CeO_2 buffer on a sapphire substrate with the *r* orientation by the laser sputtering method (film thickness 20 nm).

Sample	T, °C	p, mbar	I, J/cm^2	IR	$a_{(200)}$	$\Delta(2\Theta)_{(200)}$
*A*002, *A*003	775	0.06	1.1	0.55	5.421	0.8
*A*006, *A*007	800	0.06	1.1	0.12	5.410	0.63
*A*010	825	0.06	1.1	0.08	5.412	0.55
*A*013, *A*016	800	0.06	0.55	117	(5.447)	4.64
*A*017, *A*019	800	0.03	0.55	0.12	5.413	0.57
*A*024	800	0.11	1.1	0.18	5.406	0.5
*A*026, *A*028*	825	0.03	1.1	0.85	5.409	0.42

*Film thickness 33 nm.

TABLE II. Deposition of $YBa_2Cu_3O_x$ on a CeO_2 buffer layer on a sapphire substrate by laser sputtering.

Sample	T_H, °C	p_{02}, mbar	I, J/cm^2	T_{c0}, K	ΔT_c, K	$c_{(005)}$	FWHM$_{(005)}$	$\Delta d/d$
*A*019	750	0.8	1.2	85.3	1.3	11.668	0.87	0.001
*A*017	800	0.8	1.2	88.9	0.9	11.667	0.65	<0.0001
*A*007	825	0.8	1.2	88.2	1.2	11.666	0.75	0.0009
*A*025	800	0.8	0.8	85.6	1.8	…	…	…
*A*026	800	0.8	1.8	88.8	0.8	11.665	0.76	<0.0001

lished value. An increase in IR is accompanied by an increase in the lattice constant and the width of the (200) peak; this is probably due to an increase in the density of defects in the film. The broadening of the (200) peak of films with lattice constant close to the tabulated value is 0.05–0.06 nm and it is due mainly to the finite thickness of the film: A film thickness of 20 nm gives 0.5° broadening in accordance with Eq. (2). When the oxygen pressure during deposition is increased to 0.11 mbar, the lattice constant decreases and the structural perfection of the film increases. This behavior presupposes an oxygen deficiency in buffer layers containing the (111) orientation and deposited at low oxygen pressure in the chamber. This phenomenon agrees well with the results of Ref. 3 concerning the nucleation of the (111) orientation accompanying oxygen depletion of the sapphire surface, but in our case the deposition parameters resulting in an oxygen deficiency in the growing film operate during the entire deposition time, a circumstance which can account for the observed increase in the content of the (111) orientation with increasing film thickness.

A change in the rate of the reaction leading to the oxidation of cerium atoms on the substrate surface can be suggested as a mechanism for the effect of the deposition conditions on the orientation of the growing film. For thermodynamically equilibrium processes, the intensity of oxidation is determined by the oxygen pressure and temperature on the substrate surface. An increase in the temperature or pressure results in more complete oxidation of the growing film and promotes formation of the (100) orientation. A similar result was reported in Ref. 11, where an increase in the oxygen pressure during laser deposition of yttrium-stabilized ZrO_2 on sapphire made it possible to change the orientation of the obtained film from (111) to (100). In our laser sputtering geometry, the substrate is located at the boundary of the region of intense luminescence of the sputtered material (flame). The film grows under bombardment by the sputtered material, whose particles have a substantial energy. Increasing the laser energy density on target increases the energy with which the atoms and molecules arrive at the substrate, thereby increasing the effective temperature at the substrate surface. Decreasing the pressure in the chamber for certain values of the energy density on target leads to a similar effect, decreasing the scattering of atoms and molecules along the path from target to substrate. Both phenomena, which intensify oxidation, suppress the formation of the (111) orientation. A change in pressure in the chamber, on the one hand, increases the oxygen pressure and, on the other hand, decreases the energy of the arriving particles. This can explain the observed increase in IR and simultaneous decrease of the lattice constant and width of the (200) peak with pressure increasing to 0.11 mbar (Table I). Increasing the laser energy density on target results not only in a higher effective temperature on the substrate but also a rapid increase in the deposition rate, which, on the one hand, increases the thickness of the film with the same number of pulses and, on the other hand, results in incomplete oxidation of Ce atoms arriving at the substrate. Both effects increase the content of the (111) orientation in the buffer layer (inset in Fig. 1).

It should be noted that laser sputtering is not a thermodynamically equilibrium process, since the main mass of the material to be deposited arrives at the substrate in a very short time after the pulse. For such high fluxes, the oxygen pressure at the surface of the substrate is not constant, and for several milliseconds after the pulse it is lower than the pressure in the chamber. This could explain the presence of crystallites with the (111) orientation in films obtained by laser sputtering, since in Refs. 2 and 4 the pressures and average deposition rates close to our values in the cathodic rf sputtering regime gave purely (100)-oriented films with the same substrate temperature.

The deposition of YBCO on a CeO_2 buffer layer on sapphire was optimized with respect to the temperature and the laser energy density at the target (Table II). The best values of the temperature at which the resistance vanished and the best value of the width of the transition into the superconducting state (between levels of 0.1–0.9 times the resistance above the transition) were obtained with a deposition temperature of 800 °C. As the substrate temperature increases, the lattice constant c of YBCO decreases; this can be attributed to the high oxygen saturation of the film during growth. However, the half-width of the (005) peak, measured by the Θ-scanning method, has a minimum near 800 °C, indicating that the degradation of the superconducting parameters of the film is related with the increase in disorder in the crystal lattice. The estimate made of the stresses in the film on the basis of the system of $(00l)$ peaks shows a minimum temperature of 800 °C. For this temperature, the broadening of the peaks can be completely attributed to the small thickness of the film. Apparently, the decrease in critical temperature with an increase in the temperature above 800 °C is due to the introduction of additional disorder into the crystal lat-

tice. An increase of the energy density at the target affects the parameters of the film similarly to an increase in temperature: The lattice constant c decreases, attesting to further saturation of the lattice with oxygen, and the half-width of the rocking curve increases, indicating an increase in the density of defects in the film. The curves of the electrical parameters of the film as a function of the energy density at the target have a bell shape with an optimum near 1.5 J/cm^2. When the energy density at the target drops below the ablation threshold (1.2 J/cm^2), the superconducting properties of the film degrade sharply, possibly because of the nonuniform sputtering of the target and the nonstoichiometric composition of the film obtained. Comparing the superconducting parameters obtained for the films with the results of the investigation of the buffer layers shows that the critical temperatures of films on the buffer layers with different values of IR differ very little, in agreement with the results of Refs. 3 and 7. Therefore, for the buffer layers investigated the electrophysical and structural properties of the YBCO films depended primarily on the deposition parameters. The best superconducting properties were observed for films of the highest crystalline quality.

CONCLUSIONS

We investigated the effect of the laser sputtering parameters on the crystal properties of CeO_2 buffer layers on a sapphire substrate with the r orientation and on the electrophysical properties of supercondu cting $YBa_2Cu_3O_x$ thin films. It was shown that the formation of the (111) orientation of the buffer layer is due to a deficiency of oxygen in the deposited film, as is indicated by the increased lattice constant and width of the peaks for films deposited at low oxygen pressure. The nucleation of (111) crystallites can apparently occur during growth of the film. This can be explained by an oxygen deficiency in the growing film. The properties of YBCO films depend more on the deposition parameters than on the structure of the buffer layer. The best electrophysical properties were obtained in films with the lowest content of defects and the lowest stress level. The effective substrate temperature and the oxygen pressure at the substrate surface apparently have the greatest influence on film formation. The effective substrate temperature is influenced by the temperature of the heater, the energy of the laser pulse, the pressure of the gas mixture in the chamber, and the geometric arrangement of the substrate. The second parameter is determined by the gas composition of the atmosphere during deposition and, probably, the flux of material onto the substrate.

We thank F. Kra for assisting in the observations in the scanning microscope and I. M. Kotelyanskiĭ and I. K. Bdikin for a helpful discussion of the results.

This work was supported in part by the Russian Fund for Fundamental Research, the Russian Government Program ''Topical Problems Condensed-Matte r Physics'' (division ''Superconductivity''), programs of the INTAS and INKO-Copernicus ES, and the Danish Research Academy.

[1)]High electrical parameters of films grown on a mixed-orientation CeO_2 buffer layer, despite some degradation of the crystal structure of the film, has been was reported in Ref. 7.

[1] M. W. Denhoff and J. P. McCaffrey, J. Appl. Phys. **70**, 3986 (1991).
[2] M. Maul *et al.*, Physica B **194–196**, 2285 (1994).
[3] I. M. Kotelyanskiĭ *et al.*, Sverkhprovodimost: Fiz., Khim., Tekh. **7**(7), 1306 (1994).
[4] J. M. Owens *et al.*, IEEE Trans. Appl. Supercond. **AS-5**, 1650 (1995).
[5] A. G. Zaitsev, R. Kutzner, and R. Woerdenweber, Appl. Phys. Lett. **67**, 2723 (1995).
[6] D. W. Face, R. J. Small, and C. W. Wilker, Proceedings of ISEC'93 (1993), pp. 297–298.
[7] A. G. Zaitsev *et al.*, IEEE Trans. Appl. Supercond. **AS-7**, 1482 (1997).
[8] P. B. Mozhaev *et al.*, Sverkhprovodimost: Fiz., Khim., Tekh. **8**, 288 (1995).
[9] M. S. Raven *et al.*, Semicond. Sci. Technol. **7**, 462 (1994).
[10] J. P. Gong *et al.*, Phys. Rev. B **50**, 3280 (1994).
[11] X. D. Wu and R. E. Muenchausen, Mod. Phys. Lett. B **5**, 1267 (1991).

Translated by M. E. Alferieff

BRIEF COMMUNICATIONS

Taking aberrations into account in experiments testing the relativistic theory of the Doppler effect

V. O. Beklyamishev†

(Submitted February 3, 1997; resubmitted February 18, 1998)
Zh. Tekh. Fiz. **69**, 124–126 (February 1999)

The interpretation of experimental results [L. A. Pobedonostsev, Sov. Phys. Tech. Phys. **34**, 303 (1989)] on a test of the relativistic formula for the Doppler effect and the mistaken conclusion drawn by one author of the experiment that the special theory of relativity (STR) is unsound [L. A. Pobedonostsev, Galilean Electrodyn. **6**(6), 117 (1995)] are criticized. It is suggested that the construction of the slit collimator be altered so as to take into account the aberration of light. © *1999 American Institute of Physics.* [S1063-7842(99)02402-2]

INTRODUCTION

According to the special theory of relativity, when a light source and detector are in motion relative to one another, the wavelength detected is given by the formula

$$L' = L\Gamma\left(1 - \frac{v}{c}\cos\phi\right), \tag{1}$$

where

$$\Gamma = (1 - v^2/c^2)^{-1/2}, \tag{2}$$

v is the velocity of relative motion, ϕ is the angle between the direction of the velocity v and the direction of observation, L is the wavelength of the radiation in the rest frame K of the source, and L' is the wavelength of the radiation in the moving frame K', to which the photodetector is tied.

In 1938 Ives and Stillwell performed an experiment in which the radiation was observed simultaneously at two symmetric angles ϕ and $\phi + 180°$, where the angle ϕ was close to zero. Thus the longitudinal Doppler effect was checked. In this experiment, ionized hydrogen molecules were accelerated in a ''cathode tube'' up to 28 keV. The accelerated molecules in the observation zone collided with unaccelerated molecules and ''decayed'' into free protons and excited hydrogen atoms. The blue-shifted spectral line $L'(c)$ was observed in the direction of motion of the emitting atoms and the red-shifted line $L'(k)$ was observed in the opposite direction, where

$$L'(c) = L\Gamma[1 - (v/c)\cos\phi], \tag{3}$$

$$L'(k) = L\Gamma[1 + (v/c)\cos\phi]. \tag{4}$$

Correspondingly, the blue and red shifts relative to the wave L are

$$d(c) = L - L'(c) = L[1 - \Gamma + (v/c)\Gamma\cos\phi], \tag{5}$$

$$d(k) = L'(k) - L = L[\Gamma - 1 + (v/c)\Gamma\cos\phi]. \tag{6}$$

Hence follows the difference D of the shifts

$$D = d(k) - d(c) = 2L(\Gamma - 1). \tag{7}$$

Since $\Gamma > 1$ in the general case, it follows from expression (7) that the red shift $d(k)$ is greater than the blue shift $d(c)$. Ives and Stillwell measured this asymmetry. The the experiment was later repeated for an energy of 40 keV. The results of these works[3,4] agreed completely with Eq. (1).

Then, in 1938 Ives discovered experimentally and measured the transverse Doppler effect,[5] and the relativistic formula (1) was confirmed in this case as well. Now, an experiment in which photons are observed at intermediate values of the angle ϕ was needed to complete the picture.

In 1986, a group of investigators at the V. G. Khlopin Radium Institute in St. Petersburg performed such an experi-

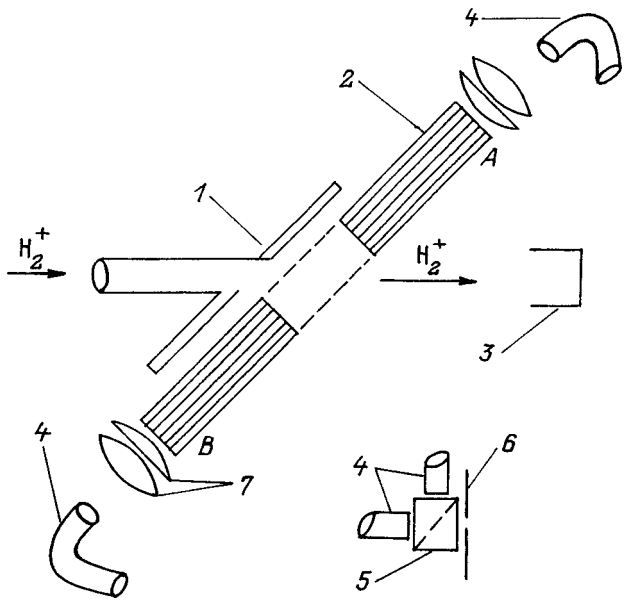

FIG. 1. Schematic diagram of the experimental setup of Ref. 1: *1* — flange, *2* — multislit collimator, *3* — Faraday cylinder, *4* — optical fiber, *5* — Lummer cube, *6* — spectrograph slit, *7* — converging lens.

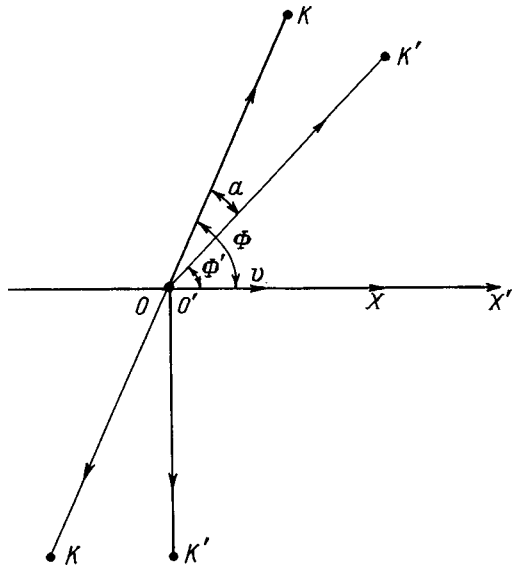

FIG. 2. Diagram for determining the aberration angle a.

ment, in which the radiation was observed at angles of 77 and 257°. However, the results of this experiment, at first glance, contradicted the relativistic formula (1). A reasonable explanation of this was not found, and the affair ended with L. A. Pobedonostsev announcing in Ref. 2 that the experimental data confirm the classical formula for the Doppler effect and do not confirm the relativistic formula. Given the experimental successes of special relativity, such an announcement seemed audacious. A deeper study of the problem revealed that the aberration of the radiation was neglected in the interpretation of the experimental results.

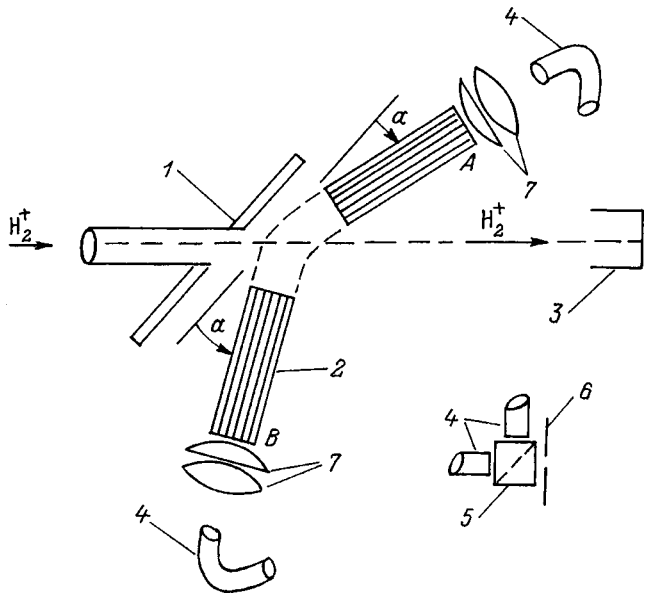

FIG. 3. Diagram of the setup with a modified slit collimator consisting of two independent parts A and B, which can be rotated relative to one another by the aberration angle a. The notation is the same as in Fig. 1.

TABLE I.

E, keV	v/c	Γ	$\sin\phi'$	a
2000	0.04618	1.001068	0.97572	±2.58
1750	0.04315	1.000932	0.97491	±2.41
1500	0.04000	1.000801	0.97512	±2.23
300	0.01788	1.0001598	0.97982	±1.00
275	0.01722	1.0001482	0.97834	±0.96
260	0.01665	1.0001386	0.97857	±0.93
250	0.01632	1.0001331	0.98012	±0.92
225	0.01549	1.0001199	0.97885	±0.87
210	0.01496	1.0001119	0.97893	±0.84
200	0.01460	1.0001066	0.97941	±0.82
180	0.01385	1.0000959	0.97930	±0.78
175	0.01366	1.0000933	0.97766	±0.76
150	0.01264	1.0000799	0.97878	±0.71

CONSTRUCTION OF A SLIT CALORIMETER WITH ALLOWANCE FOR THE ABERRATION OF LIGHT

Figure 1 shows a diagram of a slit collimator, consisting of 29 parallel plates, each plate being 116 mm long, 20 mm wide, and 0.2 mm thick. The distance between the plates is 0.5 mm — this is the width of each slit through which light propagates to the photodetector. The stack of plates has a through opening, through which a beam of ionized hydrogen molecules is passed.

Let us single out one slit of the collimator and imagine it to be tied to the inertial frame K'. Two radiation fluxes pass through the slit: the flux from the hydrogen atoms at rest and the hydrogen atoms moving with velocity $-v$ (relative to the inertial frame K'). Let us fix the second reference frame K to the hydrogen atom emitting a wave with wavelength L. According to the special theory of relativity, if the light beam in the rest frame K is directed at an angle ϕ, then in the moving frame K' this same beam propagates at an angle $\phi'=\phi-a$, where a is the aberration angle (Fig. 2).

To picture the aberration more clearly, an analogy can be drawn with aberration in astronomy, where a telescope must be tilted by the aberration angle a in order to observe a star. Otherwise, the radiation source is simply invisible. Likewise, the collimator slit must be inclined at an angle a, which can be approximately expressed as (see Eq. (20) on p. 81 of Ref. 5)

$$a=v\sin\phi', \quad v\ll c. \tag{8}$$

The relativistic formula (1) can hold only if this condition is satisfied. Thus, either the initial construction of the slit collimator, both arms of which (A and B) had a constant orientation at angles of ϕ' and $\phi'+180°$, must be changed so that a correction can be made in the observation angle for the arms A and B independently or the corresponding correction must be taken into account in the interpretation of the measurements results. Thus, in our specific case, which is displayed in Fig. 3, the arm A is rotated by the angle a counterclockwise and the arm B is rotated by the same angle clockwise. The computed values of the aberration correction a for different values of the velocity v are presented in Table I.

†Deceased.

[1] L. A. Pobedonostsev, Zh. Tekh. Fiz. **59**(3), 84 (1989) [Sov. Phys. Tech. Phys. **34**, 303 (1989)].
[2] L. A. Pobedonostsev, Galilean Electrodyn. **6**, 117 (1995).
[3] U. E. Ives and G. R. Stilwell, J. Opt. Soc. Am. **28**, 215 (1938).
[4] U. E. Ives and G. R. Stilwell, J. Opt. Soc. Am. **31**, 369 (1941).
[5] V. A. Ugarov, *The Special Theory of Relativity* [in Russian], Moscow, Nauka, 1969, p. 304.

Translated by M. E. Alferieff

Stochastic ionization of a relativistic hydrogenlike atom

D. U. Matrasulov

Division of Thermophysics, Uzbekistan Academy of Sciences, 700135, Tashkent, Uzbekistan
(Submitted April 28, 1997; resubmitted March 13, 1998)
Zh. Tekh. Fiz. **69**, 127–129 (March 1999)

The stochastic ionization of a relativistic hydrogenlike atom in a monochromatic field is investigated. Using Chirikov's criterion for stochasticity, an analytical formula is obtained for the critical value of the external field for which stochastic ionization of a relativistic atom occurs. © *1999 American Institute of Physics.* [S1063-7842(99)02502-7]

INTRODUCTION

Deterministic classical systems with chaotic dynamics and their quantum dynamics have been a subject of intense study for the last few decades. An important problem here is the behavior of a highly excited atom in a monochromatic field. A large number of works, both theoretical (see, for example, Refs. 1–4) and experimental (Refs. 2 and 5), are devoted to this problem.

From the standpoint of general physics, this problem falls at the intersection of several different directions of investigation, so that various fields find general application here. The first and probably most important of these subjects is chaos. Indeed, even the simplest theoretical model — a classical one-dimensional Kepler atom in a monochromatic field — shows that the appearance of chaotic motion makes a large contribution to the classical excitation process. On the other hand, a Rydberg atom is, to a high degree, a quantum object. For this reason, the study of its chaotic dynamics makes it possible to investigate the possibility of the existence of quantum chaotic phenomena.

Thus far, most works on chaotic dynamics and overlapping of resonances have been limited to nonrelativistic systems. However, as recent works show, some relativistic systems likewise can manifest chaotic dynamics.[6–9] Examples are relativistic electrons propagating in a spatially nonuniform field of an electron laser, a relativistic electron in the electric field of an electrostatic wave packet,[6] a relativistic electron in the field of two stationary Coulomb centers,[8] and a relativistic harmonic oscillator in the presence of beats.[9]

In the present paper the results mentioned above concerning the stochastic ionization of a nonrelativistic hydrogenlike atom are extended to the relativistic case for a relativistic one-dimensional hydrogenlike atom. It is known[1–3] that in the case of a nonrelativistic hydrogen atom interacting with an oscillating field, the one-dimensional model makes it possible to describe quite well the dynamics of stochastization of the electron motion and to obtain an ionization threshold very close to the experimental value, i.e., valid also for a three-dimensional hydrogen atom. In the case of a relativistic atom, however, the application of the one-dimensional model makes it possible to avoid the difficulties due to the openness of the trajectories in relativistic Kepler motion[10] and the appearance of additional degrees of freedom.[11] A detailed substantiation of the application of the one-dimensional model for the investigation of stochastic ionization of the hydrogen atom can be found in Ref. 2.

Applying Chirikov's criterion to the relativistic Hamiltonian, we obtain an analytical expression for the critical external field in which stochastic ionization of a relativistic atom occurs. We use the system of units where $m_e=h=c=1$.

HAMILTONIAN IN ACTION–ANGLE VARIABLES

Consider a relativistic electron moving in a one-dimensional Kepler field $Z\alpha/x$ of a charge Z ($\alpha=137^{-1}$). The momentum of this electron is

$$p=\sqrt{\left(\varepsilon+\frac{Z\alpha}{x}\right)^2-1},$$

where ε is the total energy of the electron.

We introduce the action according to the standard definition

$$n=\int_{x_2}^{x_1} p\,dx=\pi a\sqrt{1-\varepsilon^2},$$

where

$$a=\frac{\varepsilon Z\alpha}{1-\varepsilon^2},$$

and x_1 and x_2 are the turning points.

Expressing ε in terms of n for the unperturbed Hamiltonian, we obtain

$$H_0=\varepsilon=\frac{n}{\sqrt{n^2+\pi^2Z^2\alpha^2}}. \tag{1}$$

The characteristic frequency corresponding to this Hamiltonian is

$$\omega_0=\frac{dH_0}{dn}=\frac{\pi^2Z^2\alpha^2}{(n^2+\pi^2Z^2\alpha^2)^{\frac{3}{2}}}. \tag{2}$$

It is easy to show that in the limit of small Z the Hamiltonian (1) and the frequency (2) become the well-known nonrelativistic expressions for the Hamiltonian and frequency, respectively.[1,3]

Consider now the interaction of our atom with a monochromatic perturbation field of the form

$$V(x,t)=\varepsilon x\cos(\omega t), \tag{3}$$

where ε and ω are, respectively, the amplitude and frequency of the field.

We now write Eq. (3) in action–angle variables. For this, we expand $V(x,t)$ in a Fourier series

$$V(x,t)=\varepsilon\sum_{-\infty}^{\infty} x_k(n)\cos(k\theta-\omega t), \tag{4}$$

where the Fourier component of the coordinate is determined by the integral

$$x_k=\int_0^{2\pi} d\theta e^{ik\theta}x(\theta,n)$$

$$=-\frac{a}{k}\,J'(\xi k)=-\frac{n\sqrt{n^2+Z^2}}{k}J_k'(\xi k), \tag{5}$$

where $J_k'(y)$ are the derivatives of Bessel functions of y, and

$$\xi=\frac{\sqrt{n^2+Z^2\alpha^2}}{n}.$$

Thus, the complete Hamiltonian of a relativistic hydrogenlike atom interacting with the perturbation field (3) can be written in action–angle variables as

$$H=\frac{n}{\sqrt{n^2+\pi^2Z^2\alpha^2}}+\varepsilon\sum_{-\infty}^{\infty} x_k(n)\cos(k\theta-\omega t). \tag{6}$$

OVERLAPPING OF RESONANCES

For sufficiently weak electric fields, on the basis of the Kolmogorov–Arnol'd–Moser theory, most electron trajectories in action–angle space will be slightly distorted by the perturbation. The maximum distortion of the orbits occurs at resonances, i.e., at locations where the phase $k\theta-\omega t$ is stationary.[12] Therefore the resonance values of the frequency and action are related by the relation

$$k\omega_0-\omega=0 \tag{7}$$

Using Eq. (2) and (7), we obtain the resonance value of the action corresponding to the kth subharmonic

$$n_k=\left[\left(\frac{\pi^2kZ^2\alpha^2}{\omega^2}\right)^{\frac{2}{3}}-\pi^2Z^2\alpha^2\right]^{\frac{1}{2}}. \tag{8}$$

It is known that the chaotic dynamics of systems with a Hamiltonian of the form (6) can be investigated approximately using the Chirikov criterion.[12,13] According to this criterion, chaotic motion arises if two neighboring resonances overlap, i.e., if

$$\frac{\Delta n_k}{\delta n_k}>1, \tag{9}$$

where Δn_k is the width of the kth resonance and $\delta n_k=n_{k+1}-n_k$ is the distance between the kth and the $(k+1)$th resonances.

Using Eq. (8), we obtain for the distance between the resonances

$$\delta n_k=\left(\frac{kZ^2}{\omega}\right)^{\frac{2}{3}}\frac{1}{3kn_k}.$$

According to Refs. 6–8 and 13, the width of the kth resonance is given by

$$\Delta n_k=4\left(\frac{\varepsilon x_k}{\omega_0'}\right)^{\frac{1}{2}}, \tag{10}$$

where

$$\omega_0'=\frac{d\omega_0}{dn}=\frac{3n_kZ^2\alpha^2}{(n_k^2+Z^2\alpha^2)^{\frac{5}{2}}}.$$

We note that the expressions for Δn_k and δn_k in the nonrelativistic limit become the well-known expressions for the nonrelativistic Δn_k and δn_k, respectively.[1–3]

Using the expression for a and the asymptotic formula[3] $J_k'(ek)\approx 0.411k^{-\frac{5}{2}}$ (for $k\gg 1$) for the derivative of the Bessel function, we obtain for the width of the resonance

$$\Delta n_k\approx[\varepsilon k^{-\frac{8}{3}}Z^{-3}(n_k^2+\pi^2Z^2\alpha^2)]^{1/2}.$$

Substituting the expressions for Δn_k and δn_k into Eq. (9), we obtain

$$\varepsilon^{\frac{1}{2}}k^{-\frac{1}{3}}Z^{-\frac{3}{2}}n_k(n_k^2+\pi^2Z^2\alpha^2)^{\frac{1}{2}}>1.$$

This inequality gives the critical value of the field amplitude for which stochastic ionization of a relativistic electron moving in the Coulomb field of a charge $Z\alpha$ occurs:

$$\varepsilon_{\rm cr}=k^{\frac{2}{3}}(\pi Z\alpha)^3n_k^{-2}(n_k^2+\pi^2Z^2\alpha^2)^{-1}.$$

For small Z the latter formula can be expanded in a power series in $Z\alpha/n_k$ as follows:

$$\varepsilon_{\rm cr}=k^{\frac{2}{3}}Z^3n_k^{-4}\left(1-\frac{Z^2\alpha^2}{n_k^2}+\ldots\right)$$

or

$$\varepsilon_{\rm cr}=\varepsilon_{\rm un}\left(1-\frac{Z^2\alpha^2}{n_k^2}+\ldots\right),$$

where $\varepsilon_{\rm un}$ is the critical field corresponding to the nonrelativistic case.[1]

As one can see from this formula, the critical field required for stochastic ionization of a relativistic hydrogenlike atom is less than in the nonrelativistic case.

In summary, we have derived an analytical formula for the critical field required for stochastic ionization of a relativistic hydrogenlike atom in the form of a function of the charge Z and the action n_k. Since a hydrogenlike atom is a strongly quantum object, the study of its excitation by a monochromatic field will make it possible to investigate the possibility of existence of relativistic quantum chaos phenomena. A more detailed analysis of the problem examined

above must be based on a solution of the nonstationary Dirac equation and the classical equations of motion.

I am deeply grateful to V. I. Matveev for a discussion and helpful remarks.

[1] R. V. Jensen, Phys. Rev. A **30**, 386 (1984).
[2] R. V. Jensen, S. M. Susskind, and M. M. Sanders, IEEE J. Quantum Electron. **201**, 1 (1991).
[3] G. Casati, I. Guarneri, and D. L. Shepelyansky, IEEE J. Quantum Electron. **24**, 1420 (1988).
[4] N. B. Delone, V. P. Kraĭnov, and D. L. Shepelyanskiĭ, Usp. Fiz. Nauk **140**, 355 (1983) [Sov. Phys. Usp. **26**, 551 (1983)].
[5] J. E. Bayfield and P. M. Koch, Phys. Rev. Lett. **33**, 258 (1974).
[6] A. A. Chernikov, T. Tel, G. Vattay, and G. M. Zaslavsky, Phys. Rev. A **40**, 4072 (1989).
[7] D. G. Luchinsky, P. V. McClintock, and A. B. Neiman, Phys. Rev. E **53**, 4240 (1996).
[8] S. P. Drake, C. P. Dettman, and N. J. Cornish, Phys. Rev. E **53**, 1351 (1996).
[9] Jung-Hoon Kim and Hai-Woong Lee, Phys. Rev. E **53**, 4242 (1996).
[10] L. D. Landau and E. M. Lifshitz, *The Classical Theory of Fields*, Pergamon Press, New York [Russ. original, Nauka, Moscow, 1988].
[11] M. Born, *The Mechanics of the Atom*, G. Bell and Sons, London, 1927 [Russ. trans., ONTI, Kharkov, 1934].
[12] B. V. Chirikov, Phys. Rep. **52**, 265 (1979).
[13] G. M. Zaslavskiĭ and B. V. Chirikov, Usp. Fiz. Nauk **105**, 3 (1971) [Sov. Phys. Usp. **14**, 549 (1972)].

Translated by M. E. Alferieff

Alignment on moiré fringes of finite width during optical processing of images of a periodic amplitude grating which are distorted by the reconstructed wave front

A. I. But' and A. M. Lyalikov

Ya. Kupala Grodno State University, 230023 Grodno, Belarus
(Submitted September 24, 1997; resubmitted February 3, 1998)
Zh. Tekh. Fiz. **69**, 130–132 (February 1999)

A method of alignment on moiré fringes of finite width for visualization of the deflection angles of rays reconstructed by a hologram of a phase object is described. It is suggested that the resulting moiré pattern be obtained by superposing two distorted images of amplitude gratings with different period. The result of an experimental test of the method is presented. © *1999 American Institute of Physics.* [S1063-7842(99)02602-1]

It has been proposed[2] that the moiré effect in the superposition of images of defocused gratings be used to increase the sensitivity of the quantitative method of investigating phase inhomogeneities that is based on obtaining a distorted image of the defocused amplitude grating during reconstruction of the wave front by a hologram.[1] The images of the distorted gratings were formed by waves reconstructed in the complex-conjugate orders of diffraction. A moiré pattern aligned on an infinitely wide fringe was observed in the plane of superposition of the grating images. However, alignment of the pattern of moiré or interference fringes on a fringe of infinite width has the substantial drawback that the sign of the fringe number is not unique.[3]

In moiré or holographic interferometry, alignment on fringes of finite width is accomplished by turning the interferograms or holograms and by recording them with different periods.[4] Carrying such methods of alignment directly over to the method of visualization of phase objects using an amplitude grating[2] will lead to a number of errors in the visualized moiré pattern which are associated with a shift or nonidentical sensitivities of the superposed grating images.

In the present work we consider a modification of the moiré method of visualizing angles of deflection of light rays reconstructed by a hologram of a phase object.[2] It is suggested that for purposes of alignment on a fringe of finite width the resulting moiré pattern should be obtained by superposing two distorted images of amplitude gratings with a different period.

Figure 1 shows a scheme of the setup used for optical processing of holograms of a phase object. This scheme makes it possible to regulate the width of the fringes in the resulting moiré pattern. The setup contains two channels for forming images of amplitude gratings *1* and *5* in the planes *8* and *9*, located near the hologram *10*. The lines of the amplitude gratings *1* and *5* with different periods are oriented vertically for visualizing the projection of the angles of deflection of the reconstructed beams on the x axis and they are oriented horizontally for visualizing on the y axis. The amplitude gratings are illuminated with collimated beams of light simultaneously in two channels of the illuminating part of the setup, and telescopic systems with $1\times$ magnification are used to form images of the gratings *1* and *5* at different distances L_1 and L_2 from the holograms *10*. Since the sensitivity of this method is determined by the ratios L_1/T_1 and L_2/T_2, where T_1 and T_2 are the periods of the amplitude gratings *1* and *5*, respectively, for $T_1 \neq T_2$ with identical sen-

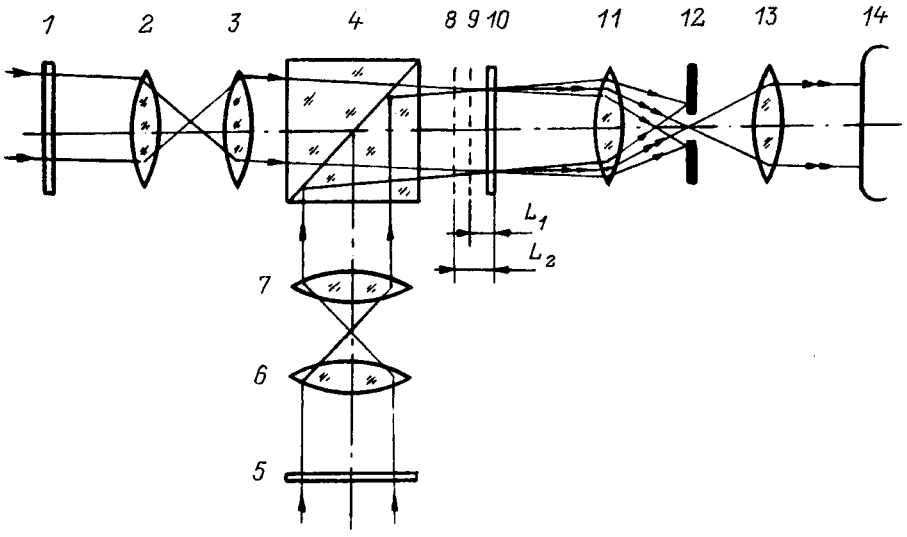

FIG. 1. Diagram of a setup for optical processing of a hologram of a phase object: *1,5* — amplitude gratings; *2,3* and *6,7* — telescopic systems; *4* — beam-splitting cube; *8,9* — image planes of an amplitude grating; *10* — hologram of a phase object; *11,13* — objective; *12* — filtering diaphragm; *14* — plane of observation of the moiré pattern.

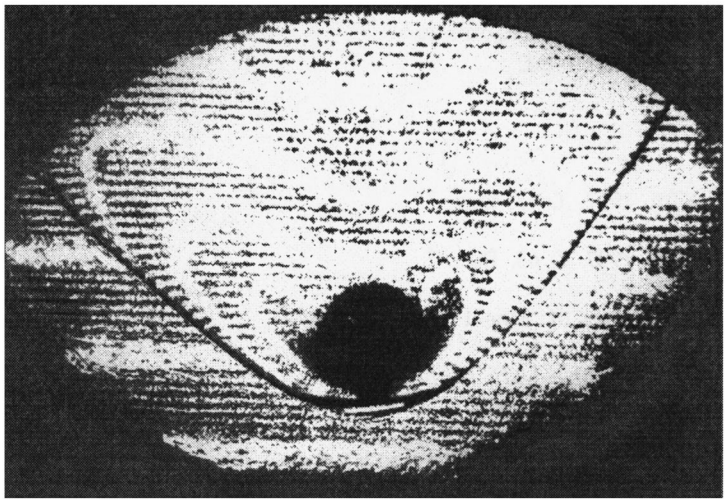

FIG. 2. Moiré pattern with alignment on finite fringes.

sitivity in both channels the equalities $L_1/T_1=L_2/T_2=C$ should hold. In Fig. 1, the position of the planes *8* and *9* of the images of the amplitude gratings are presented for the case $T_1<T_2$. The hologram *10* is illuminated by a beam-splitting cube *4* in a manner such that the waves diffracted by it in the ± 1st orders propagate in the same direction. A filtering diaphragm *12* separates these waves, which are amplitude-modulated by the gratings *1* and *5*, in the back focal plane of the objective *11*. It is obvious that the necessary condition for such spatial filtering is $(T_1,T_2)\gg P$, where P is the period of the fringes of the hologram.[2]

Let the amplitude transmission of the hologram of the phase object be described by the expression[3]

$$\tau(x,y)\sim 1+\cos\left[\frac{2\pi x}{P}+\Phi(x,y)\right], \tag{1}$$

where x and y are coordinates in the plane of the hologram, the y axis is parallel to the holographic fringes, and $\Phi(x,y)$ is the distortion introduced in the phase by the experimental object.

For example, it can be shown[2] for vertical orientation of the lines of the amplitude gratings *1* and *5* that the illuminance distributions produced in the plane *14* (which is optically coupled with the hologram *10* by the objective lens *13*) by each channel of the illuminating part of the setup separately are

$$I_{+1}(x,y)\sim 1+\cos\left[\frac{2\pi x}{T_1}+2C\pi\varepsilon_x\right], \tag{2}$$

$$I_{-1}(x,y)\sim 1+\cos\left[\frac{2\pi x}{T_2}-2C\pi\varepsilon_x\right]. \tag{3}$$

The periodicities of the images of the gratings are distorted by the x component of the angles of deflection from the rectilinear distribution of the light rays reconstructed by the hologram, i.e., ε_x. For incoherent superposition of the distorted images of the gratings (2) and (3), the resulting illuminance distribution in the plane *14* will be described by the sum $I_{+1}(x,y)+I_{-1}(x,y)$. In this case, the illuminance distribution in the resulting pattern, describing the low-frequency modulation of the illuminance, is determined by the term

$$\cos\left[\frac{\pi x(T_2+T_1)}{T_2T_1}\right]\cos\left[\frac{\pi x(T_2-T_1)}{T_2T_1}+2C\pi\varepsilon_x\right]. \tag{4}$$

The regions of low visibility of the images of the superposed amplitude gratings will be observed when the second cosine vanishes. The equation for the family of moiré fringes in this case is

$$\frac{x(T_2-T_1)}{T_2T_1}+2C\varepsilon_x=N+1/2,\quad N=0,1,2,\ldots. \tag{5}$$

Thus, when two images of amplitude gratings with a different period that are distorted by the wave fronts reconstructed by the hologram are superposed, a moiré aligned on finite fringes oriented parallel to the images of the fringes of the gratings will be observed. The period of the alignment fringes is determined from Eq. (4) as $T_1T_2/(T_2-T_1)$.

We underscore an important advantage of this method of optical processing of images of amplitude gratings over the method proposed in Ref. 2. In the optical processing scheme of Ref. 2, the wave fronts reconstructed by the hologram pass through the objective lenses of the detecting part of the setup at different angles and along different paths, which can result in various distortions of the images of the gratings which are not associated with the phase object under study, i.e., it can cause aberrations. In the scheme displayed in Fig. 1, by aligning the beam-splitting cube *4* the wave fronts reconstructed in complex-conjugate orders can be directed through the objectives *11* and *13* along the same path, and the aberrations inherent in the method of Ref. 2 can thereby be eliminated.

Figure 2 displays a moiré pattern with alignment on vertical fringes of finite width. This pattern visualizes the x component of the angles of deflection of the light beams

reconstructed by the hologram of a sphere moving on a ballistic trajectory.

In summary, the method proposed for alignment on fringes of finite width makes it possible to eliminate the errors in the visualized moiré pattern that are due to the shift and unequal sensitivities of the superposed images of amplitude gratings. It should be noted that in the present work the same hologram (provided by I. S. Zeĭlikovich) of a sphere on a ballistic trajectory as in Refs. 1 and 2 was used.

[1] A. I. But' and A. M. Lyalikov, Zh. Tekh. Fiz. **63**(3), 39 (1997) [Sov. Phys. Tech. Phys. **42**, 287 (1997)].
[2] A. I. But' and A. M. Lyalikov, Zh. Tekh. Fiz. **63**(7), 134 (1997) [Sov. Phys. Tech. Phys. **42**, 845 (1997)].
[3] C. Vest, *Holographic Interferometry*, Wiley, New York, 1979 [Russ. trans., Mir, Moscow, 1982, 504 pp.].
[4] A. K. Beketova, A. F. Belozerov, A. N. Berezkin *et al.*, *Holographic Interferometry of Phase Objects*, Nauka, Leningrad, 1979, 232 pp.

Translated by M. E. Alferieff

On the destruction of the superconducting state of a multiconductor composite

A. N. Balev, N. A. Lavrov, V. K. Ozhogina, and V. R. Romanovskiĭ

Kurchatov Institute Russian Science Center, 123182 Moscow, Russia
(Submitted February 2, 1998)
Zh. Tekh. Fiz. **69**, 133–136 (February 1999)

The kinetics of thermal instability in the form of an initially arising local region of normal conductivity is investigated using a model of a discrete superconducting medium in which the components are assumed to interact thermally across a thermally thin intermediate layer. It is found that certain characteristic features of the transient processes occurring at currents close to the minimum current for propagation of the normal zone must be taken into account in an experimental determination of the normal-zone propagation velocities in multiconductor composites. © *1999 American Institute of Physics.* [S1063-7842(99)02702-6]

The irreversible transition of a superconductor to the normal state is due to its thermal bistability. The Joule heating of the superconductor as a result of the formation of a local region with normal conductivity in it can be accompanied by the propagation of a characteristic heat wave.[1,2] As a rule, the kinetics of the normal zone can be described by a one-dimensional heat-conduction equation. In a number of practical applications this approach is not only justified but it makes it possible to write down analytical expressions which are convenient for estimating the velocity of a heat wave in a single conductor.[1–4] Recently, however, particular attention has been paid to transient processes in superconducting multiconductor current-carrying elements (CCEs). The processes occurring in them exhibit a number of characteristic features which are a direct consequence of the discrete character of the change in their thermal and electrophysical properties.

Ordinarily, the phenomena responsible for the initial formation of a resistive region in multiconductor CCEs are omitted in the investigation of the processes leading to the appearance and propagation of a normal zone in these composites. In this case, it is assumed *a priori* that instability initiated in a single component of the composite certainly will result in complete destruction of superconducting properties of the entire CCE. At the same time, the presence of additional transverse heat flow due to contact heat transfer between all components of the CCE apparently will modify this supposition. This concerns chiefly the range of currents close to the so-called minimum normal-zone propagation current, where the processes occurring depend strongly on the conditions of dissipation of the heat released. For this reason, a correct formulation and the solution of this problem are important not only for understanding the general physical laws of the destruction of the superconducting properties of multiconductor superconducting media but also for preparing and performing the corresponding experiments.

It is convenient to solve such problems for the kinetics of the normal zone in a heat-insulated CCE, for which the minimum normal-zone propagation current is zero. The most complete analysis of the conditions leading to the destruction of superconductivity should be based on the solution of the corresponding system of nonstationary equations, which adequately describe the transient character of the processes occurring and their dependence on the local properties of all elements of the composite.

Let us consider the propagation of the normal zone inside an uncooled discrete superconducting region, whose elements are thermally thin superconducting composite conductors, which are in thermal contact with one another and are separated from one another by a finite thermal resistance. Let a thermal instability be initiated initially by a powerful external heat source, which produces local regions of normal conductivity in one or several elements of the composite. To simplify the analysis let us assume that the current in each conductor is constant. We shall describe the process of symmetric redistribution of heat inside the composite by a system of equations of the form

$$C\frac{\partial T_k}{\partial t}=\frac{\partial}{\partial x}\lambda\frac{\partial T_k}{\partial x}+\frac{I^2}{S^2}\rho(T_k)-\begin{cases}\dfrac{P}{SR}(T_1-T_2), & k=1,\\ \dfrac{P}{SR}(2T_k-T_{k-1}+T_{k+1}), & k=\overline{2,\,N-1},\\ \dfrac{P}{SR}(T_N-T_{N-1}), & k=N\end{cases} \tag{1}$$

with the initial and boundary conditions

$$T_k(x,0)=\begin{cases}T_1, & 0<x<x_0, \quad k=k_i, \quad i=1,2,\ldots,\\ T_0, & x_0\leqslant x\leqslant l, \quad k=k_i,\\ T_0, & 0\leqslant x\leqslant l, \quad k\neq k_i,\end{cases}$$

$$\frac{\partial T_k}{\partial x}(0,t)=0, \quad T_k(l,t)=T_0. \tag{2}$$

Here $k=1,\ldots,N$ is the number of the conductor in the composite; C is the volume specific heat of the kth element; λ is

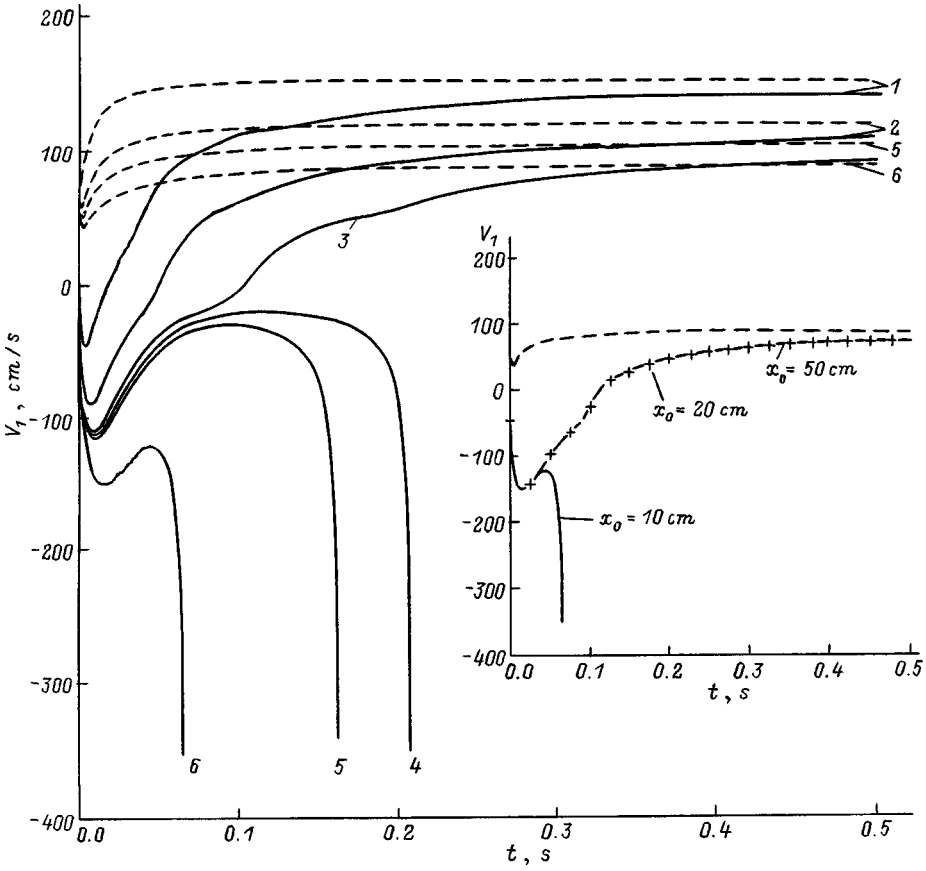

FIG. 1. Time variation of the longitudinal velocity of the normal zone for various values of the current: $I=100$ (*1*), 80 (*2*), 72 (*3*), 71 (*4*), 70 (*5*), 60 A (*6*).

the thermal conductivity of the element in the longitudinal direction; S is the cross-sectional area; P is the contact perimeter between two neighboring conductors; R is the thermal contact resistance; I is the transport current in each conductor; T_0 is the temperature of the surrounding medium; T_1 is the initial temperature of a thermal perturbation of extent x_0; and, $\rho(T_k)$ is the effective resistivity of the superconducting composite, which takes into account the existence of regions where the current is divided between sections located in the kth conductor in the superconducting and normal states,[3,4]

$$\rho(T_k)=\rho_0(T_k)\times\begin{cases}1, & T_k>T_{SC},\\ (T_k-T_C)/(T_{SC}-T_C), & T_C\leqslant T_k\leqslant T_{SC},\\ 0, & T_k<T_C=T_{SC}-(T_{SC}-T_0)I/T_C,\end{cases}$$

where ρ_0 is the resistivity of the matrix and I_C and T_{SC} are the critical parameters of the superconductor.

The finite-difference method was used to determine the instantaneous temperature distribution in all elements of the composite and the corresponding propagation velocity of regions with normal conductivity.[5] The boundary of the resistive region separating the superconducting and nonsuperconducting states inside a single composite was determined by solving the equation $T_k(x_{n,k},t)=T_{SC}$. The results of numerical experiments reflecting the qualitative laws of the transition of a discrete superconducting composite to the normal state in the presence of a current in it close to the minimum current for propagation of the normal zone, are presented in Figs. 1 and 2. In the calculations it was assumed without loss of generality that the diameter of a single conductor is 0.12 cm, $l=200$ cm, $R=1$ cm$^2\cdot$K/W, $P=0.01$ cm, $T_0=4.2\,K, T_{SC}=9.5$ K, and initially the normal zone arises as a result of local heating, equal to $T_1=10$ K. The initial thermo- and electrophysical parameters corresponding to a niobium–titanium superconductor in a copper matrix were determined according to Ref. 6.

The solid lines in Fig. 1 show the time variation of the instantaneous values of the longitudinal propagation velocity of the normal zone in the first conductor, where it was assumed that an instability with extent $x_0=10$ cm arises ($k_i=1$) initially. Here, for comparison, the longitudinal propagation velocities of the isotherm T_{SC} in an isolated composite are displayed by dashed curves (see also the dashed curve in the inset). Formally, these states also correspond to the limit $R\to\infty$. The normal-zone velocities with $I=60$ A as a function of the initial extent of the perturbation are presented in the inset in Fig. 1. Figure 2 shows the computational results for the longitudinal velocity $V_1(t)$ of the normal zone in the first conductor of the CCE and the development of the transient process $N(t)$ in its cross section. The number of conductors in which local regions of normal conductivity arise initially was varied.

The computational results show that the kinetics of the normal zone in a multiconductor CCE, carrying a current which is just slightly higher than the minimum normal-zone

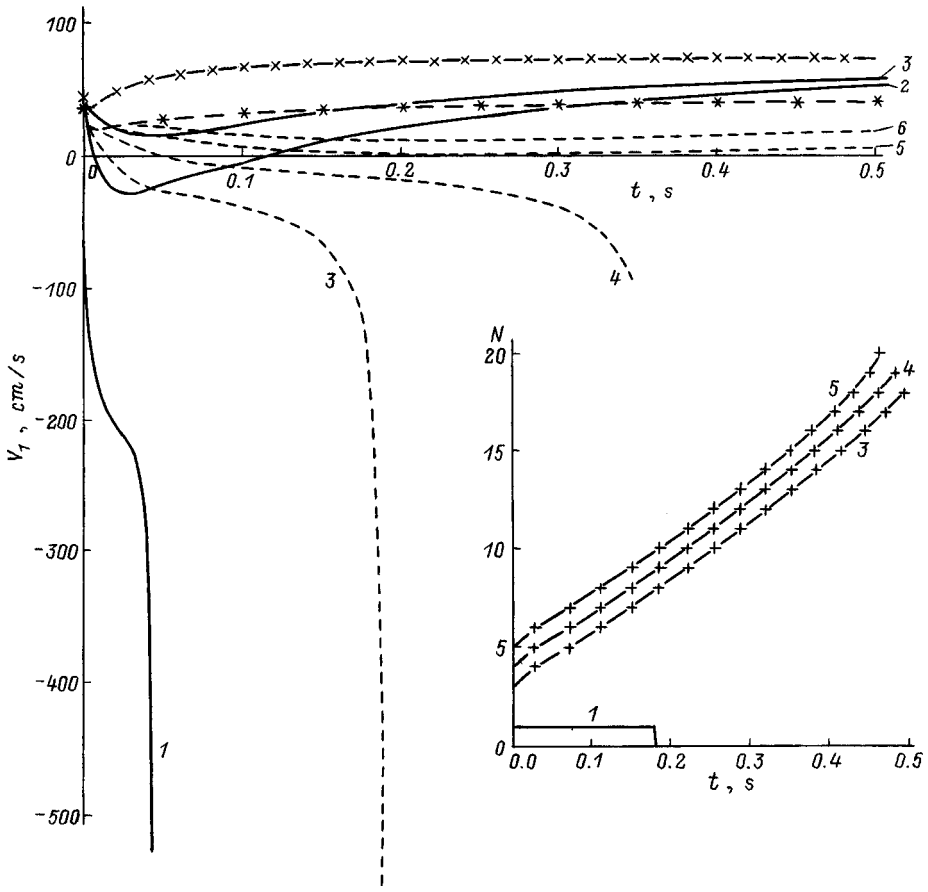

FIG. 2. Kinetics of a normal zone with $x_0=10$ cm in a single conductor ($I=50$ (×), 30 A (*)) and in a multiconductor CCE for different numbers of conductors in which local regions with normal conductivity arise initially ($I=30$ (dashed curves), 50 (solid curves), 70 A (inset)): $k_i=1$ (*1*), 1, 2 (*2*); 1, 2, 3 (*3*); 1, 2, 3, 4, (*4*); 1, 2, 3, 4, 5 (*5*); 1, 2, 3, 4, 5, 6, (*6*).

propagation current, depends largely on the character of the initial conditions of the perturbation. Thus, for $I\leqslant 70$ A even a strong extended perturbation ($2x_0=20$ cm) in a single element of the composite does not produce a transition of the element to the normal state. In this case, superconductivity will be destroyed primarily by more-extended heat sources. In addition, the presence of heat transfer between conductors greatly increases the formation time of a heat wave in both the longitudinal and transverse directions of propagation of the normal zone (more accurately, the time of asymptotic approach to the corresponding limiting values increases). Specifically, one can see that for $I=60$ A and $2x_0=40$ cm there is no quasistationary state, even when the total extent of the normal-conductivity region (taking account of the symmetry of the process) reaches almost 1 m. On the whole, the tendencies noted above become more noticeable, the weaker the current under otherwise the same conditions. Current regimes where even a local transition of several conductors simultaneously to the normal state is not accompanied by irreversible destruction of the superconducting properties of the entire composite are possible.

It is obvious that as the thermal resistance increases, the kinetics of the transient process in the longitudinal direction of the CCE will approach processes which destroy superconductivity in a single conductor. However, in this case the characteristic features discussed above will affect most the character of the processes occurring in the cross section of the conductor. For this reason, as the thermal coupling between the conductors becomes worse, the time of a transition to a steady value of the normal-zone velocity in the transverse section of a multiconductor CCE will increase, and the range of currents for which initiation of instability in several conductors simultaneously will be required to obtain an irreversible transition of the entire composite to the normal state, will also increase.

In summary, our investigation shows that in experiments whose purpose is to determine the normal-zone propagation velocities in a multiconductor superconducting region in both the longitudinal and transverse sections, a number of features characteristic for the development of a transient process in the range of currents close to the minimum normal-zone propagation current occur. In this case: 1) the extent and power of the heater simulating an external thermal perturbation should be many times greater than the analogous parameters required for initiating thermal instability in a single conductor; 2) current regimes where local destruction of the superconducting properties in several conductors is necessary for an irreversible transition of the entire composite to the normal state; and, 3) the presence of heat transfer between conductors increases the formation time of the quasistationary state, which in turn can result in a substantial increase of the dimensions of the CCEs which ensure that the desired values of the normal-zone velocities can be determined correctly.

This work was supported by the Russian Fund for Fundamental Research (Project No. 96-02-16122a).

[1] W. H. Cherry and J. I. Gittleman, Solid-State Electron. **1**, 287 (1960).
[2] R. F. Broom and E. H. Rhoderick, Br. J. Appl. Phys. **11**, 292 (1960).
[3] V. A. Al'tov, V. B. Zenkevich, M. G. Kremlev, and V. V. Sychev, *Stabilization of Superconducting Magnet Systems* [in Russian], Énergoatomizdat, Moscow, 1984, 312 pp.
[4] M. Wilson, *Superconducting Magnets*, Oxford University Press, London, 1983 [Russ. trans., Mir, Moscow, 1985, 407 pp.].
[5] V. M. Paskonov, V. I. Polezhaev, and L. A. Chudov, *Numerical Modeling of Heat and Mass Transfer Processes* [in Russian], Nauka, Moscow, 1984, 286 pp.
[6] I. G. Kozhevnikov and L. A. Novitskiĭ, *Thermophysical Properties of Materials at Low Temperatures* [in Russian], Mashinostroenie, Moscow, 1982, 328 pp.

Translated by M. E. Alferieff

Effect of the microstructure of a metal on the emission spectrum excited during destruction of current-carrying conductors by an MHD instability

K. B. Abramova, I. P. Shcherbakov, and A. I. Rusakov

A. F. Ioffe Physicotechnical Institute, Russian Academy of Sciences, 194021, St. Petersburg, Russia
(Submitted February 20, 1998)
Zh. Tekh. Fiz. **69**, 137–140 (February 1999)

The spectral characteristics of the radiation emitted during the destruction of copper conductors with different microstructures by a high-density current are investigated experimentally. The proposed mechanisms leading to radiation generation and the experimental results corresponding to these mechanisms are discussed. © *1999 American Institute of Physics.* [S1063-7842(99)02802-0]

The passage of high current densities $j \sim 5 \times 10^7$ A/cm^2 along conductors results in deformation and destruction of the conductors by MHD instabilities.[1] This process is accompanied by a bright flash of light whose spectrum contains a series of lines and bands, i.e., extensive information about the system and dynamics of the electronic levels of both the metal itself and individual atoms of the metal. In Ref. 2, the emission spectrum excited by MHD destruction of copper conductors was investigated. The emission bands observed were identified, and the processes leading to the excitation of these bands were examined.

It is well known that bombardment of the surface of a metal by charged particles with energies of several kiloelectron volts excites cathodo- and ionoluminescence.[3,4] Radiative decay of single-particle and collective excitations makes the main contribution to the cathodoluminescence. It was assumed even in the first work on cathodoluminescence of copper that the emission observed is due not only to the radiative transition of electrons from the Fermi level ε_F to lower-lying hole states but also to electron–hole recombination from states above ε_F, i.e., cathodoluminescence is of an above-edge character.[3] The luminescence peaks should coincide with the peaks in the density of states below ε_F. Qualitatively, the mechanism leading to the appearance of a strong electric field in the destruction process due to the passage of a high density current along a conductor is very simple. The growth of a sausage-type perturbation up to an amplitude equal to the radius of the conductor leads to the appearance of gaps.[5] On account of the response of the circuit, the voltage across the gaps is many times higher than the initial voltage, and a strong electric field arises in the gaps. Acceleration of electrons and ions in the fields produced in this manner should result in the appearance of cathodo- and ionoluminescence, just as under stationary conditions. However, for the same particle energy, fast electrons excite the electronic subsystem of the crystal more strongly than do slow ions. Therefore electrons make the main contribution to emission in this process.

Destruction by a strong current can result in the excitation of plasmon luminescence. Plasmon radiation has been observed under electronic bombardment of aluminum, silver, and a number of other metals. On the basis of the estimates made in Ref. 6, the plasmon luminescence for copper should lie in the UV range, and in the present work we shall not consider it.

In the process of destruction by a strong current, together with the excitation caused by high-energy electrons, there arises emission due to the destruction process itself.[7] The proposed mechanism of this emission is as follows.[1] In viscous fracture, plastic zones with high dislocation density form near the crack tips. After the load is removed, a dislocational recovery of the deformed layer occurs in connection with the annihilation of pairs of dislocations of opposite sign and with the emergence of mobile dislocations on the surface. Real dislocations in metals have a complicated structure, so that their complete annihilation is unlikely. In each dislocation reaction, only the annihilation of individual parallel segments is possible. The annihilation of such segments is accompanied by a release of substantial energy, reaching several electron volts over the interatomic distance along the axis. For annihilation of dislocations in copper, crossing of the terms of the internal *d* electrons, localized near dislocation nuclei, with states of unoccupied *s*—*p* bands is possible. Nonadiabatic transitions arising during crossing result in the appearance of holes in quasilocal *d* states near dislocations formed as a result of dislocation reactions.

Individual luminescence bands arising during the destruction of conductors by high-density currents[2] have been excited and detected in other processes also: 1) a cathodoluminescence band (λ_{max}=5550 Å) has been observed under electron irradiation of a copper sample,[3] 2) a photoluminescence band (λ_{max}=5800 Å) has been observed upon laser irradiation of a copper sample,[9] and 3) a mechanoluminescence band (λ_{max}=7300 Å) has been observed on the back cleavage surface (purely mechanical load).[8]

A detailed investigation of the luminescence due to purely mechanical loading is most interesting from our standpoint. The reason is that if the dislocation mechanism is valid, then mechanoluminescence makes it possible not only to investigate dislocation processes near a metal surface but it also serves as a unique source of information about the nature of surface electronic states. Other methods of excita-

tion of the luminescence of metals (by light or charged particles) are in principle incapable of leading to the excitation of such luminescence, since in these cases bulk states are excited in the metal, while surface states are essentially unaffected.

It seems to us possible and important to assess the validity of one of the basic assumptions of the dislocation model of the mechanoluminescence of metals. According to this model,[8,10] the maximum luminescence intensity can be determined from the formula

$$I = \eta N_m \frac{S_t}{dt},$$

where I is the mechanoluminescence intensity, η is the quantum yield of mechanoluminescence, N_m is the density of mobile dislocations, S_t is the thickness of the plastic zone, t is the luminescence time, and d is the lattice parameter.

It is evident from this formula that for the same metal two quantities remain unchanged for any conditions of loading. These are η, the quantum yield of luminescence, and d, the lattice parameter. The thickness S_t of the plastic zone can be different for different methods of loading; it will be greatest for isotropic stretching. The emission time in the formula occurs in the denominator, so that the more rapid the loading, the higher the mechanoluminescence intensity should be. The density N_m of mobile dislocations is ultimately determined by the initial dislocation density N in the sample. Correspondingly, the initial material with a high initial dislocation density must emit more photons than material with a lower initial density.

In Ref. 11, the intensity of mechanoluminescence was investigated as a function of the initial microstructure of the sample. The total emission was detected and compared. Spectral measurements of the radiation were not performed because of its low intensity. To confirm the assumptions of the dislocation model, it is important to check the existence of a dependence of the mechanoluminescence spectrum on the initial microstructure of the sample.

In the experiments described in the present paper, destruction of copper conductors was accomplished by passing along them an electric current with density $0.7–1.0\times10^7$ A/cm^2. The conductors consisted of a piece of copper wire 70 mm long and 0.5 mm in diameter, made from ''technically pure'' M0-grade copper wire. The power source was of a 400 μF capacitor bank charged to 1.5 kV. The rate of loading was $V=1\times10^3$ m/s, and the emission duration was $t=20\mu$s. The radiation investigated was focused on the input slit of a diffraction spectrometer. An FPP31L autoscanning charge-transfer photoelectric linear transducer was placed in the focal plane of the spectrometer. Signals from the transducer were fed into an analog-to-digital converter and then into a computer. This made it possible to perform measurements of the spectral characteristics of the light flash in the range 5400–8100 Å with a spectral resolution of 6 Å during the destruction of a sample.

The previously published[2] continuous radiation spectrum accompanying MHD destruction of copper was measured in a wider range 4500–9000 Å. However, the measurements were performed at only 20 points of this spectral range, and it was necessary to destroy 10 samples in order to obtain the average intensity at each point.

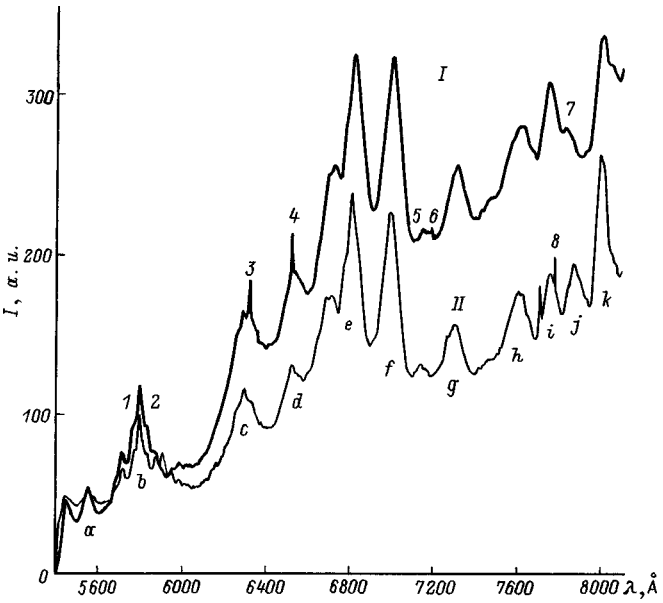

FIG. 1. Emission spectrum of copper: *I* — Rolled M0-grade copper wire, *II* — annealed M0-grade copper wire; *1* — CuI 5700, *2* — CuI 5782, *3* — SII 6312, *4* – SbII 6503, *5* — NiI 7122, *6* — FeI 7207, *7* — Bi 7838, *8* — OI 7772; a — cathodoluminescence band λ_{max}=5550 Å, b — photoluminescence band λ_{max}=5800 Å, c — excitonic luminescence band of copper oxide with λ_{max}=6350 Å, g — mechanoluminescence band λ_{max}=7300 Å.

The present measurements were performed in greater detail and on a qualitatively new experimental level. In the first place, the entire emission spectrum was measured in a single experiment. In the second place, the measurements were performed at 500 points in the spectral range 5400–8100 Å. Finally, not only the continuous emission spectrum but also the line spectrum were measured. This made it possible to increase the accuracy and reliability of the results.

Two of a large number of characteristic curves obtained are presented in Fig. 1. Curve *I* is the characteristic emission spectrum produced by the destruction of M0-grade rolled copper wire. The following bands are excited: A cathodoluminescence band *a*,[3] a band *b* corresponding to photoluminescence of copper,[9] an excitonic luminescence band *c* of copper oxide,[12] and a mechanoluminescence band *g* due to recombination of electrons in surface electron states and bands *d*, *e*, and *f* observed during spallation of the back side,[6,8] and the bands *h*, *i*, and *k*, which are yet to be identified. The sharp peaks in some bands and marked in the figure by the numbers *1–8* correspond to the most intense atomic lines of copper and impurities present in the sample.[13]

Curve *II* is the emission spectrum of an M0-grade copper wire, annealed in advance and destroyed under the same conditions. It is known that dislocations with oppositely directed Burgers vectors, lying in the same slip plane, mutually annihilate as they approach one another. If such dislocations lie in different slip planes, then climb is required in order for them to annihilate one another. Annealing promotes dislocation climb, and in this manner the dislocation density decreases.[14] Photographs of the microstructure of annealed

and rolled samples were obtained in Ref. 11.

Comparing the spectra presented in Fig. 1 it is evident that the cathodoluminescence bands a[3] and the photoluminescence bands b of copper[9] repeat one another. This is probably due to the fact that these bands arise as a result of the excitation of bulk states, which undergo small changes during annealing. In other sections of the spectrum of the curves *I* and *II* the intensities are different, i.e., changes have occurred in the relative intensity of the luminescence bands of different nature.

The most interesting section of the spectrum for us is the mechanoluminescence band g. As expected, the intensity of the band g was found to be lower for destruction of an annealed sample than for an unannealed sample. These results confirm the dislocation model of mechanoluminescence: Annealing decreased the dislocation density and the intensity of the band due to the excitation of hole states in nonadiabatic transitions arising at the moment of annihilation of dislocations and when dislocations emerge at the surface.

The intensities of the bands d, e, and f, which have also been observed in spallation of the back side,[7] decreased. These bands were not excited with other methods of acting on a metal, such as cathodo-, iono-, and photoirradiation. Therefore, like the mechanoluminescence band g, they also are excited only when the sample is destroyed. The decrease in the intensity of these bands with the destruction of an annealed sample could signify that the intensity of these bands, just as the intensity of the g band, is determined by the density of defects in the sample.

As one can see from the figure, the intensity of the atomic spectrum also changed. Annealing had no effect on the lines *1*, *2*, *5*, and *6*, while the lines *3*, *4*, and *7* vanished, and the line 8 appeared. The vanishing of the lines *3*, *4*, and *7* could signify that the density of sulfur, antimony, and bismuth impurities decreased in the annealing process. The appearance of line *8* and band *j* is probably due to the oxidation and adsorption of oxygen during annealing.

In summary, analysis of the emission spectra arising with the destruction of conductors by a high-density current shows the following.

1. The change in microstructure during annealing decreases the probability of excitation of surface electronic states, which determine the appearance of the mechanoluminescence band.

2. The change in microstructure during annealing has no effect on the bulk electronic states, which determine the appearance of the cathodoluminescence and photoluminescence bands.

It should be underscored that thus far the dynamics of the appearance of and change in the spectral bands in time have not been investigated. Such investigations would yield information about the dynamics of the change in the surface and bulk electronic states in a metallic sample during its deformation and destruction and also about the dynamics of the emergence of mobile dislocations on the surface.

This work was supported by the Russian Fund for Fundamental Research under Grant No. 97-02-18097.

[1] K. B. Abramova, N. A. Zlatin, and B. P. Peregud, Zh. Éksp. Teor. Fiz. **69**, 2007 (1975) [Sov. Phys. JETP **42**, 1019 (1975)].
[2] K. B. Abramova, B. P. Peregud, and Yu. N. Perunov, Opt. Spektrosk. **58**, 809 (1985) [Opt. Spectrosc. **58**, 496 (1985)].
[3] A. Bonnot, J. M. Debever, and J. Hanus, Solid State Commun. **10**, 173 (1972).
[4] M. Zivitz and E. W. Thomas, Phys. Rev. **13**, 2747 (1976).
[5] B. A. Trubnikov, in *Plasma Physics and Problems of Controlled Thermonuclear Fusion* [in Russian], 1958, Vol. 4, pp. 87–91.
[6] M. I. Molotskiĭ, Fiz. Tverd. Tela (Leningrad) **20**(6), 1651 (1978) [Sov. Phys. Solid State **20**, 956 (1978)].
[7] M. I. Molotskiĭ and B. P. Peregud, Zh. Tekh. Fiz. **51**(3), 618 (1981) [Sov. Phys. Tech. Phys. **26**, 369 (1981)].
[8] K. B. Abramova, V. L. Valitskiĭ, N. A. Zlatin *et al.*, Zh. Éksp. Teor. Fiz. **71**, 1873 (1976) [Sov. Phys. Tech. Phys. **44**, 983 (1976)].
[9] A. Mooradian, Phys. Rev. Lett. **22**, 185 (1969).
[10] B. R. Chandra, M. S. Ryan, R. Seema, Simon, and M. H. Ansari, Cryst. Res. Technol. **31**, 495 (1996).
[11] K. B. Abramova, I. P. Shcherbakov, I. Ya. Pukhonto, and A. M. Kondyrev, Zh. Tekh. Fiz. **66**(5), 190 (1996) [Sov. Phys. Tech. Phys. **41**, 511 (1996)].
[12] F. I. Kreĭgol'd and B. S. Kulinkin, Opt. Spektrosk. **33**, 706 (1972).
[13] A. N. Zaĭdel', V. K. Prokof'ev, S. M. Raĭskiĭ, and E. Ya. Shreĭder, *Tables of Spectral Lines* [in Russian], Moscow, 1962, 607 pp.
[14] V. L. Idenbom and A. N. Orlov, Usp. Fiz. Nauk **76**, 557 (1962) [Sov. Phys. Usp. **5**, 272 (1962)].

Translated by M. E. Alferieff

Piezoelectric textures of polycrystalline zinc selenide

V. P. Migal', M. A. Rom, and O. N. Chugaĭ

Kharkov Aviation Institute, 310070 Kharkov, Ukraine
(Submitted March 18, 1998)
Zh. Tekh. Fiz. **69**, 141–143 (February 1999)

The preliminary results of an investigation of the structure and electrophysical properties of CVD-grown polycrystalline ZnSe are reported. A weak multicomponent texture is observed which bears upon the piezoelectric effect, the characteristic features of the electric polarization, and the characteristic elastic oscillations of samples of regular shape. © *1999 American Institute of Physics.* [S1063-7842(99)02902-5]

Zinc selenide crystals find wide application in optical instrumentation and, especially, in laser technology,[1] as materials with a favorable combination of optical, mechanical, and thermal properties. A high-voltage photo-emf,[2] diffraction of light as by a periodic phase structure,[3] and other anomalous properties closely related with the ordered arrangement of two-dimensional structural defects have been observed in individual single crystals of zinc chalcogenides. We report here the first observation of piezoelectric textures formed in polycrystalline ZnSe during the growth of the crystals.

Polycrystalline wafers grown by chemical vapor deposition (CVD) were used for the investigations. The wafers had a small absorption coefficient ($\beta \leqslant 2\times10^{-3}$ cm^{-1}) at a wavelength of 10.6 μm. They were selected according to the characteristic size l_0 of the crystallites (see Table I) which is determined by the conditions under which the polycrystalline samples are obtained, primarily the temperature in the chemical reaction zone.[4] Samples in form of a disk ($D=20-25$ mm and $h=1-4$ mm) and a square parallelepiped ($4\times4\times10$ mm) were investigated. The planes of the samples were oriented parallel or perpendicular to the surface of the initial wafer. Their piezoelectric and dielectric parameters were determined by the standard method.[5] Rectilinear polar figures (RPFs) (110) and (111) were obtained in CuK_α radiation ''in reflection'' by varying the angle of inclination of the sample in the range 0–65° with a 5° step. Fast linear displacement of the sample and accumulation of intensity with a 10° step were used. The main orientations were calculated by the method used for weak textures, which is described in Ref. 6. The data presented in Table I are characteristic for a series of samples prepared from various wafers.

TABLE I.

Parameter Texture orientation fraction, %	Sample		
	S-180	S-120	S-50
⟨111⟩	36	5.5	2.3
{111}*	55	24	12
⟨110⟩	⋯	1.2	⋯
{110}	⋯	2.3	⋯
⟨100⟩	⋯	⋯	1.9
{100}	⋯	⋯	3.8
⟨100⟩+⟨211⟩	3.3	18	⋯
{100}+{211}	⋯	12.5	⋯
{100}+{211}+{311}	5.7	⋯	⋯
Textureless component	⋯	36.5	80
l_0, μm	180	120	50
ε_{33}^T	9.78	9.43	13.2
$\tan\delta$	0.80	0.039	0.27
$d_{31}\cdot10^{-12}$, C/N	0.68	0.52	0.59
k_p	0.035	0.027	0.031
$Q\cdot10^3$	12	1.8	2.3
K_ε	1.2	1.1	1.05

*Bounded component

Figure 1 shows a typical RPF for the experimental samples. The distribution of the polar density is complicated and indicates the presence of a weak multicomponent texture. The results of an analysis of the RPFs of samples with different characteristic grain size are presented in Table I. It is evident from the table that the quantitative ratios of the predominant orientations for samples with different l_0 are different. In addition, the fraction of the textureless component varies inversely as a function of this parameter. For all samples, the texture axis is normal to the surface of the initial wafer. We underscore especially the presence of axial components, since axial texture is characteristic for piezoelectric ceramics.[7]

A direct manifestation of the piezoelectric properties of the experimental polycrystalline samples is the excitation of characteristic elastic oscillations by an ac electric field, i.e., piezoelectric resonances. Disks from different series differ strongly from one another in terms of the number of piezoelectric resonances in the frequency range 40–200 kHz. For example, the spectrum for the samples with the lowest fraction of the textureless component (the samples S-50) contains only one strong piezoelectric resonance with a frequency close to 103 kHz. For samples from the other series, additional oscillations, whose frequencies can be less than or greater than the indicated frequency, are characteristically present in the spectrum (Fig. 2). An isolated piezoelectric resonance is observed in the spectra of all disks, without exception, as the strongest resonance. The form of the corresponding optical-polarization topogram (Fig. 2a) attests to the fact that this is the first harmonic of the radial

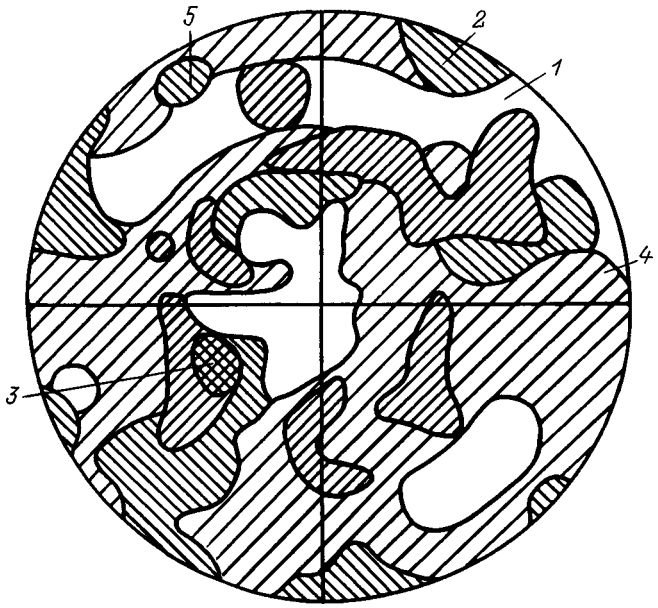

FIG. 1. The (110) polar figure of polycrystalline ZnSe (S-180), reflection (220). Designations of the polar density: *1* — 0, *2* — 0.4–0.8, *3* — 2–4, *4* — 0.1–0.3, *5* — 0.9–2.

oscillations.[8] It is well known that such oscillations are characteristic of piezoceramic disks polarized perpendicular to their plane. On this basis, the piezoelectric effect in the experimental polycrystalline samples can be linked to the axial components of the texture, which, as we have said, have the same orientation of the axis.

Table I gives some of the main piezoelectric parameters of the experimental polycrystalline samples. One can see that samples which do not have a the textureless component exhibit the highest Q for radial oscillations, electromechanical coupling coefficient k_p, piezoelectric modulus d_{31}, dielectric loss tangent $\tan\delta$, and anisotropy of the permittivity. The coefficient $K_\varepsilon=\varepsilon_{33}^T/\varepsilon_{11}^T$ is taken as a measure of the latter. For all samples, the piezoelectric modulus d_{31} is less than the piezoelectric modulus d_{14} of ZnSe single crystals [$d_{14}=1.1\times10^{-12}$ C/N (Ref. 9)]. The anomalously high Q of the piezoelectric resonances is interesting.

To all appearances, the anisotropy of the elastic properties and the plastic deformation of the crystallites play a large role in the structural ordering of polycrystalline ZnSe. Thus, when many crystallites grow simultaneously, each one is influenced its immediate environment and is subjected to elastic deformation. Assuming all strain components ε_{ij} to be equal, a small fraction of the free energy of the deformed state of a crystal belonging to the cubic system[10] will be related to the shear components, i.e., $\varepsilon_{12}=\varepsilon_{21}$, $\varepsilon_{13}=\varepsilon_{31}$, and $\varepsilon_{23}=\varepsilon_{32}$, if $c_{11}/2+c_{12}>2c_{44}$ for the elastic moduli, just as in the case of zinc selenide crystals.[9,11] Hence it follows that the crystallites whose orientation in the acting force field gives rise mainly to the indicated strain components will have the lowest free energy (and hence an advantage in the rate of growth).

The mechanical stresses acting on individual crystallites can exceed the elastic limit. This leads to plastic deformation of the crystallites with formation of slip bands and twins, which were observed in the experimental samples by optical microscopy. A planar-stressed state forms in the wafer. For this reason, crystallites, whose slip and twinning planes make acute angles with the plane of the wafer, are most strongly subjected to plastic deformation. Since slip and twinning in ZnSe crystals of the sphalerite modification can occur in the same planes $\{111\}$, the formation of an axial component of the texture $\langle111\rangle$ in the experimental samples can be explained by plastic deformation of the crystallites. It is possible that the piezoelectric properties of polycrystallites

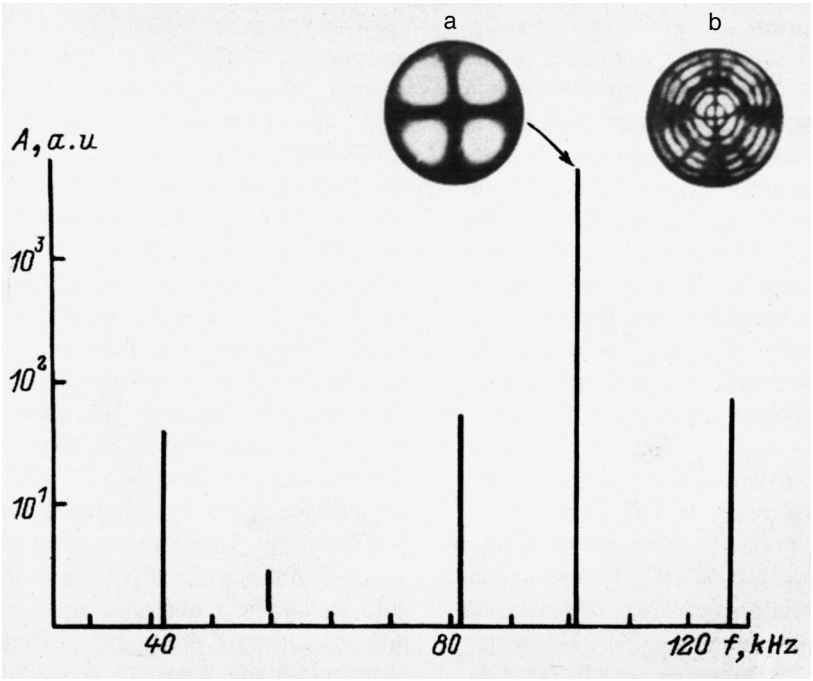

FIG. 2. Spectrum of piezoelectric resonances of a polycrystalline ZnSe disk; a, b — optical-polarization topograms of the oscillations obtained on different disks.

are due to this component, since twinning along the $\{111\}$ planes in the indicated crystals often occurs according to the $6'mm'$ law with conservation of polarity of the twinning axis [111] (Ref. 12). This can explain the observation of piezoelectric resonances, fragments of whose optical-polarization topograms are characterized by a sixfold symmetry axis (Fig. 2b), in many disks in the frequency range 0.4–1.5 MHz.

When the total fraction of oriented crystallites is sufficiently high, their effect on the piezoelectric properties becomes more complicated because of the appearance of additional piezoelectric resonances. Samples which do not contain a textureless component, naturally, possess the highest content of crystallites ''participating in the piezoelectric effect,'' as a result of which the parameters Q, k_p, and d_{31} reach their highest values.

In summary, during synthesis of polycrystalline ZnSe wafers by the CVD method, piezoelectric textures are formed together with multicomponent orientational textures. This greatly enlarges the range of application of these materials.

[1] G. T. Petrovskiĭ, S. N. Borozdin, V. A. Demidenko *et al.*, Opt. Zh., No. 11, 77 (1993).
[2] J. Baillou, P. Bugnet, J. Dauney *et al.*, J. Phys. D **12**, 451 (1979).
[3] V. Ya. Emelin, N. V. Klassen, and Yu. A. Osip'yan, *Abstracts the Fifth All-Union Conference on the Physics and Technical Applications of II–VI Semiconductors* [in Russian], Vilnius, 1983, Vol. 1, p. 56.
[4] M. N. Vladyko, A. A. Kolchin, V. A. Tatarchenko *et al.*, Vysokochistye Veshchestva, No. 2, pp. 217–221 (1988).
[5] *Piezoceramic Materials. Technical Conditions* [in Russian], OST 11 0444-87.
[6] M. M. Borodkina and É. N. Spektor, *X-Ray Diffraction Analysis of Textures of Metals and Alloys* [in Russian], Metallurgiya, Moscow, 1981, 272 pp.
[7] A. V. Shubnikov, I. S. Zheludev, V. P. Konstantinova *et al.*, *Investigation of Piezoelectric Textures*, Soviet Academy of Sciences Press, Moscow, 1955, 189 pp.
[8] L. Bergman, *Ultrasonics*, Bell, London, 1938 [Russ. trans., Inostr. Lit., Moscow, 1957, 726 pp.].
[9] D. Berlincourt, H. Jaffe, and L. R. Shiozawa, Phys. Rev. **129**, 1009 (1963).
[10] L. D. Landau and E. M. Lifshitz, *The Theory of Elasticity*, 3rd ed., Pergamon Press, Oxford, 1986 [Russ. original, Nauka, Moscow, 1987, 248 pp.].
[11] B. H. Lee, J. Appl. Phys. **41**, 2988 (1970).
[12] M. P. Kulakov, V. D. Kulakovskiĭ, and A. V. Fadeev, Izv. Akad. Nauk SSSR, Neorg. Mater. **12**, 1867 (1976).

Translated by M. E. Alferieff